

# Experimental and numerical investigation of fuel flexibility and pollutant emissions in novel combustion technologies using renewable synthetic fuels

**Thesis presented by Marco Ferrarotti**

in fulfilment of the requirements of the PhD Degree in Engineering  
Sciences and Technology (ULB & UMONS - "Docteur en Sciences de  
l'ingénieur et technologie")

Academic year 2019-2020

Supervisor : Professor Alessandro PARENTE  
Université Libre de Bruxelles  
Co-supervisor : Professor Ward DE PAEPE  
Université de Mons

## Thesis jury :

Gérard DEGREZ (Université libre de Bruxelles, Chair)  
Axel COUSSEMENT (Université libre de Bruxelles, Secretary)  
Laurent BRICTEUX (Université de Mons)  
D.J.E.M. ROEKAERTS (TUDelft)  
Giancarlo SORRENTINO (Università Federico II di Napoli)  
Enrico CRESCI (WS Wärmeprozessstechnik GmbH)

# Experimental and numerical investigation of fuel flexibility and pollutant emissions in novel combustion technologies using renewable synthetic fuels

A thesis presented by

Marco Ferrarotti

in fulfilment of the requirements for the degree of  
Doctor in Engineering Sciences and Technology

Université Libre de Bruxelles

Université de Mons

Belgium, September 2020

Supervisors:

Prof. Alessandro Parente (Université Libre de Bruxelles, Belgium)

Prof. Ward de Paepe (Université de Mons, Belgium)

Doctoral committee:

Gérard Degrez (Université libre de Bruxelles, Belgium), Chair

Axel Coussement (Université libre de Bruxelles, Belgium), Secretary

Laurent Briceux (Université de Mons, Belgium)

D.J.E.M. Roekaerts (TUDelft, The Netherlands)

Giancarlo Sorrentino (Università Federico II di Napoli, Italy)

Enrico Cresci (WS Wärmeprozessstechnik GmbH, Germany)





*To Alice and Giulio*



# Acknowledgements

At the end of this exciting, fulfilling, thrilling and unpredictable journey, also called *PhD*, there is a multitude of people that I would like to thank.

First of all, I would like to thank Prof. Parente, who gave me the opportunity to undertake this experience. He believed in me since the time of the Master thesis. He followed me with constant support, positive energy and passion to make me grow as a scientist.

I am glad to have been part of an amazing department, such as ATM, not made by colleagues, but friends. In particular, I would like to thank Simone, Magnus, Marianna, Andrea, Steven, Ruggero and Maryam for the scientific collaborations, but also for all the laughs.

I would like to thank my co-supervisor Prof. de Paepe. Even if we started to collaborate after the beginning of my PhD, he followed my work with constancy, helping to structure better my work.

I cannot forget to thank the ATM Lab's team for helping me during the installation and testing of the facility. In particular, my sincere gratitude goes to Adrien Fita-Codina for his constant technical support in installing, trouble-shooting and continuously improving the facility.

I would like to express my gratitude to all my friends, my parents and my brother for the support and encouragement.

Last but not least, to Alice: thank you for being my person, for supporting me in every moment of my life and for making me smile when I needed the most. But above all, for your love and your patience. To Giulio, thanks for choosing us as your parents.

This work has been supported by a FRIA fellowship of the F.R.S.-FNRS.



# Abstract

By 2050, Europe needs to have drastically decoupled its economic growth from its emissions of  $\text{CO}_2$ . This is a direct response to the compelling evidence from the increasing risks of climate change brought about by the anthropogenic Greenhouse Gas (GHG) emissions and pollutant emissions ( $\text{NO}_x$ ). A replacement of significant percent of fossil fuels with renewable energy sources will be needed. However, energy production from most renewable energy sources, is typically intermittent and unpredictable. This requires a reliable mid-long term energy storage to synchronize production and demand. The Power-to-Fuel option or chemical storage can be the key for a sustainable energy system. Indeed, converting the excess of renewable energy into second generation fuels will unlock a long-term and high-density energy storage, ensuring also a reduction of the carbon footprint. These "green" non-conventional fuels are blends of  $\text{CH}_4$ ,  $\text{H}_2$ ,  $\text{CO}$  and  $\text{NH}_3$ . However, to achieve Power-to fuel, the development of an efficient combustion technology, coupled with virtually zero pollutant emissions, stable working conditions with different load and fuel and significant energy saving is required. In the last years, a so-called MILD or flameless combustion has drawn attention for its ability of meeting the mentioned targets. However, the studies available in literature are conducted on Jet in hot co-flow-like systems or they face conventional fuels, such as natural gas or methane. The examples using non-conventional fuels are scarce and limited to few operating conditions.

In this framework, this PhD thesis focuses on a threefold aspect.

Experimental campaigns investigated fuel flexibility of flameless combustion in the ULB furnace. A progressive addition of hydrogen in methane enhanced combustion features, reducing the ignition delay time and increasing the reactivity of the system, possibly losing its flameless behaviour. Indeed, a threshold of 25%  $\text{H}_2$  was defined for reaching flameless/MILD

conditions, characterized by still low pollutant emissions and temperature peak. This is in line with the goal of introducing “green” hydrogen into the natural gas pipeline (up to 20%) to reduce CO<sub>2</sub> emissions. Further experimental campaigns tested the role of the injection geometry (varying the air injector ID) and fuel lance length to reduce NO emissions and retrieve flameless/MILD conditions for high hydrogen content. Finally, ammonia/hydrogen blends were tested. Results suggests that stoichiometry has a major impact on NO emissions. An optimal window, minimizing both NO and NH<sub>3</sub>-slip emissions was defined using  $\phi = 0.9$ . To qualitatively describe the observed trends, a simplified reactors network was considered. The analysis highlighted the most important reactions correlated to NO formation and the reason of the NO reduction at stoichiometry condition.

On the other side an affordable and reliable numerical model was optimized and tested in the Adelaide Jet in Hot Co-flow burner. The latter is a simplified burner capable of mimicking MILD combustion conditions. A set of RANS simulations were run using the Partially Stirred Reactor (PaSR) approach, investigating different mixing model formulations: a static, a fractal-based and a dynamic formulation, based on the resolution of transport equations for scalar variance and dissipation rate. A study about the role of combustion models and kinetic mechanisms on the prediction of NO formation was also conducted. Finally, an analysis of the choice of a Heat Release Rate (HRR) marker for MILD (HM1 flame) and not MILD (HM3 flame) conditions was carried out. Once having awareness of the capability of the proposed numerical model, simulations were conducted to define the key aspects in simulating a flameless furnace, varying the composition of the fuel, considering methane/hydrogen and ammonia/hydrogen blends. In particular, for the latter case, existing kinetic schemes showed a major over-estimation of NO emissions, reason why an optimization study was conducted in a simplified reactor (well stirred reactor) using a Latin Hypercube Sampling.

Finally, the first-of-its-kind digital twin based on CFD simulations for a furnace operating in flameless combustion conditions was created. A reduced-order model (ROM) based on the combination of Proper Orthogonal Decomposition (POD) and Kriging was developed for the prediction of spatial fields (i.e. temperature) as well as pollutant in the exhausts.

# Contents

<b>Acknowledgements</b>	<b>i</b>
<b>Abstract</b>	<b>iii</b>
<b>Contents</b>	<b>v</b>
<b>List of Figures</b>	<b>xi</b>
<b>List of Tables</b>	<b>xxv</b>
<b>Nomenclature</b>	<b>xxix</b>
<b>1 Introduction</b>	<b>1</b>
1.1 Global warming and energy transition . . . . .	2
1.2 Formation mechanisms for NO emissions . . . . .	5
1.3 Non-conventional or diluted combustion . . . . .	10
1.3.1 Experimental studies and industrial applications . .	13
1.3.2 Challenges dealing with flameless/MILD combustion	16
1.4 Objectives . . . . .	19
1.5 Outlines . . . . .	21



<b>2</b>	<b>Experimental Setup</b>	<b>23</b>
2.1	Test bench . . . . .	24
2.2	Measurements techniques . . . . .	25
2.2.1	Temperature measurements . . . . .	25
2.2.2	Chemiluminescence Imaging . . . . .	28
2.2.3	Gas Analyser . . . . .	29
2.3	Fuels . . . . .	30
2.3.1	Hydrogen and ammonia-enrich fuels . . . . .	31
2.4	Mass and energy balances . . . . .	34
2.5	Uncertainty quantification . . . . .	39
<b>3</b>	<b>Fuel flexibility in the ULB furnace</b>	<b>41</b>
3.1	Introduction and literature review . . . . .	43
3.2	Methane/Hydrogen blends . . . . .	44
3.2.1	Settings and processing method . . . . .	45
3.2.2	Main features of flameless combustion of CH <sub>4</sub> -H <sub>2</sub> mix- tures with air injector ID25 . . . . .	47
3.2.3	Main features of flameless combustion of CH <sub>4</sub> -H <sub>2</sub> mix- tures varying the air injector ID . . . . .	58
3.2.4	Main features of flameless combustion of CH <sub>4</sub> -H <sub>2</sub> mix- tures varying the fuel lance length . . . . .	65
3.3	Ammonia/Hydrogen blends . . . . .	69
3.3.1	Pollutant emissions for NH <sub>3</sub> /H <sub>2</sub> blends . . . . .	69
3.3.2	Characterisation of ammonia/hydrogen blends in WSR with EGR . . . . .	73
3.4	Summary and conclusion . . . . .	78

<b>4</b>	<b>Mathematical models</b>	<b>81</b>
4.1	RANS for turbulent combustion modeling . . . . .	82
4.1.1	Closure for RANS equations . . . . .	83
4.2	Combustion model . . . . .	84
4.2.1	Eddy Dissipation Concept . . . . .	86
4.2.2	Partially Stirred Reactor . . . . .	87
4.3	Radiation Modeling . . . . .	91
4.3.1	Absorption coefficient . . . . .	92
<b>5</b>	<b>Validation of the PaSR model in a Jet in Hot Co-flow flame</b>	<b>95</b>
5.1	Introduction and literature review . . . . .	97
5.2	Description of the AJHC Database . . . . .	98
5.3	Numerical setup . . . . .	100
5.4	Results and discussion . . . . .	102
5.4.1	Preliminary Analysis . . . . .	102
5.4.2	Effect on the choice of the mixing model . . . . .	103
5.4.3	NO predictions . . . . .	119
5.4.4	HRR marker analysis . . . . .	124
5.5	Summary and conclusions . . . . .	134
<b>6</b>	<b>CFD analysis of the ULB flameless furnace</b>	<b>137</b>
6.1	Introduction . . . . .	139
6.2	Methane/hydrogen blends . . . . .	140
6.2.1	Numerical details . . . . .	140
6.2.2	Results . . . . .	142
6.3	Ammonia/hydrogen blends . . . . .	158
6.4	Summary and conclusion . . . . .	162

<b>7</b>	<b>Reduced-order model from CFD simulations</b>	<b>165</b>
7.1	Introduction and literature review . . . . .	167
7.2	Methods . . . . .	168
7.2.1	Proper Orthogonal Decomposition . . . . .	168
7.2.2	Kriging . . . . .	169
7.2.3	Data-set . . . . .	169
7.3	Reduced order model development . . . . .	170
7.3.1	Reconstruction of test data . . . . .	171
7.3.2	Prediction of new data . . . . .	173
7.4	ROM developed from the training data-set determined by leave-k-out analysis . . . . .	176
7.5	Summary and conclusions . . . . .	180
<b>8</b>	<b>Conclusions and future work</b>	<b>183</b>
8.1	Summary and conclusions . . . . .	184
8.2	Recommendations . . . . .	187
	<b>Appendices</b>	<b>189</b>
<b>A</b>	<b>Correlations used to calculate the furnace energy balance</b>	<b>A1</b>
<b>B</b>	<b>Uncertainty quantification</b>	<b>B1</b>
<b>C</b>	<b>Additional information about numerical modeling</b>	<b>C1</b>
<b>D</b>	<b>Additional experimental studies for CH<sub>4</sub>-H<sub>2</sub></b>	<b>D1</b>
D.1	Effect of equivalence ratio . . . . .	D1
D.2	Dilution effect on a pure hydrogen flame . . . . .	D3
	<b>Publications</b>	

**Bibliography**



# List of Figures

1.1	Estimated anthropogenic warming and possible future scenarios depending on different CO <sub>2</sub> and non-CO <sub>2</sub> emissions targets [1]. . . . .	3
1.2	Total annual anthropogenic greenhouse gas (GHG) emissions for the period 1970 to 2010 by gases [2]. . . . .	4
1.3	Simplified schematization of the NO formation pathways: thermal NO (green), prompt NO (red), fuel NO (purple), N <sub>2</sub> O (blue) and NNH (yellow) routes [3]. . . . .	5
1.4	Reaction path diagram from prompt NO formation under slightly fuel-rich conditions. Adapted from [4]. . . . .	7
1.5	Arrhenius plot for the reaction $\text{NNH} + \text{O} \rightleftharpoons \text{NH} + \text{NO}$ . The rate constant $k$ profiles are drawn from the following sources: Klippenstein et al. [5], Bozzelli et al. [6], Konnov et al. [7] and Hayhurst et al. [8]. Adapted from [3] . . . . .	8
1.6	Reaction path diagram for oxidation of NH <sub>3</sub> . Adapted from [4].	9
1.7	Conceptual diagram of Diluted Combustion. . . . .	10
1.8	Schematic diagram of the stability limits for different combustion modes. Zone A: stable flames regime; Zone B: unstable flames regime; Zone C: flameless regime. Source: [9].	12
1.9	Combustion regimes defined with inlet temperature and temperature raise. Source: [10]. . . . .	13

2.1	Schematic of the furnace (left), vertical cross section (top right) and burner nozzle (bottom right). For sake of clarity, only a part of the probe ports are shown. . . . .	26
2.2	Schematic P&ID of the test bench. . . . .	27
2.3	Schematic diagram of the suction pyrometer. . . . .	28
2.4	Thermal and mass diffusivity of different fuels mixed with air at various equivalence ratio, at 300 K and under atmospheric pressure. The equivalence ratios for $\text{CH}_4$ and $\text{NH}_3$ are not indicated, since they overlap with each other. . . . .	32
2.5	Equilibrium temperature of $\text{NH}_3$ , $\text{CH}_4$ and $\text{H}_2$ in air at $P=1$ atm and $T_0 = 300$ K, calculated with OpenSMOKE [11] and the POLIMI kinetic scheme [12, 13]. Courtesy of M. Cafiero-ULB. . . . .	33
2.6	Sketch of the system considered to evaluate the global energy balance of the furnace. . . . .	36
2.7	Sketch of the system considered to evaluate the energy balance of the heat exchanger. . . . .	38
2.8	Idealized problem to quantify the radiative power transmitted through the window. . . . .	39
3.1	Averaged $\text{OH}^*$ distribution based on 10 (a), 100 (b), 150 (c) and 300 (d) frames. Units in mm and counts. . . . .	47
3.2	(a)-(b)-(c)-(d)-(e)-(f) Instantaneous frames taken at different times, (g) averaged and (h) Abel-inverted $\text{OH}^*$ distributions. Units in mm and counts. . . . .	48
3.3	Photographs of “flame” (a) and “flameless” (b) modes and NO emissions. Canon EOS 80D 1/70 s exposure time. . . .	49
3.4	Photographs of M100H0 (a), M75H25 (b), M50H50 (c), M25H75 (d) and M0H100 (e). The visible reaction zone is highlighted. Canon EOS 80D 1/70 s exposure time. $\text{CH}_4$ - $\text{H}_2$ blends. ID25. . . . .	50

3.5	Contours of temperatures measured at different spatial coordinates (black dots) varying the $H_2$ percentage. The contours represent only a part of the furnace. Units in mm and $^{\circ}C$ . Test-case T1. . . . .	50
3.6	Averaged temperature measured at (a) $z=100$ mm, (b) $z=150$ mm, (c) $z=200$ mm, (d) $z=300$ mm, (e) $z=400$ mm and (f) $z=600$ mm, varying the $H_2$ percentage. Averaged experimental uncertainty of 10 K. Test-case T1. . . . .	51
3.7	Averaged $OH^*$ distribution varying the $H_2$ percentage. The flame lift-off is highlighted. Units in mm and counts. Test-case T1. . . . .	52
3.8	Standard deviation distribution for $OH^*$ varying the $H_2$ percentage. Units in mm and counts. Test-case T1. . . . .	52
3.9	$NO$ and $CO_2$ emissions varying the $H_2$ percentage. $CH_4-H_2$ blends. ID25. . . . .	56
3.10	Averaged $CH^*$ distribution varying the $H_2$ percentage. Units in mm and counts. $CH_4-H_2$ blends. ID25. . . . .	58
3.11	Standard deviation distribution for $CH^*$ varying the $H_2$ percentage. Units in mm and counts. $CH_4-H_2$ blends. ID25. . . . .	59
3.12	Photographs of M50H50 for air injector ID25 (a), ID20 (b) and ID16 (c). The visible reaction zone is highlighted. Canon EOS 80D 1/70 s exposure time. Test-cases T1-T2-T3. . . . .	61
3.13	Contours of temperature measured at different spatial coordinates for M50H50 and ID25, ID20, ID16. The contours represent only a part of the furnace. Units in mm and $^{\circ}C$ . Test-cases T1-T2-T3. . . . .	61
3.14	Averaged temperature measured at (a) $z=100$ mm, (b) $z=150$ mm, (c) $z=200$ mm, (d) $z=300$ mm, (e) $z=400$ mm and (f) $z=600$ mm for ID20, varying the $H_2$ percentage. Averaged experimental uncertainty of 10 K. Test-case T2. . . . .	62
3.15	Averaged $OH^*$ distribution for ID20, varying the $H_2$ percentage. Units in mm and counts. Test-case T2. . . . .	62



3.16	Averaged temperature measured at (a) $z=100$ mm, (b) $z=150$ mm, (c) $z=200$ mm, (d) $z=300$ mm, (e) $z=400$ mm and (f) $z=600$ mm for ID16, varying the $H_2$ percentage. Averaged experimental uncertainty of 10 K. Test-case T3. . . . .	63
3.17	Averaged $OH^*$ distribution for ID16, varying the $H_2$ percentage. Units in mm and counts. Test-case T3. . . . .	63
3.18	NO emissions varying the $H_2$ percentage and the ID air injector. Test-cases T1-T2-T3. . . . .	64
3.19	Conceptual sketch of the injection system, increasing the fuel lance length of 25 mm (L25) (b) and 50 mm (L50) (c) respect to the standard configuration (L0) (a). . . . .	66
3.20	CFD profiles of oxygen mass fraction, extracted at a relative distance of 50 mm (a) and 100 mm (b) from the fuel lance exit. Four different lance length are compared. M50H50, ID16. . . . .	66
3.21	Averaged temperature profiles extracted along the axis and shown in function of $z+$ for (a) M50H50 , (b) M25H75 and (c) M0H100. Averaged experimental uncertainty of 10 K. Test-cases T5-T6. . . . .	67
3.22	Averaged $OH^*$ distribution for L25, varying the $H_2$ percentage. Units in mm and counts. Test-cases T5-T6. . . . .	68
3.23	NO emissions varying the $H_2$ percentage and the fuel lance length L. Test-cases T5-T6. . . . .	68
3.24	Photographs of $NH_3$ - $H_2$ combustion for (a) N10H90, (b) N20H80, (c) N40H60, (d) N50H50 and (e) N60H40. ID25, $\phi = 1$ . Canon EOS 80D 1/70 s exposure time. . . . .	70
3.25	Averaged temperature measured at (a) $z=100$ mm, (b) $z=150$ mm, (c) $z=200$ mm and (d) $z=400$ mm for N50H50, varying the air ID and $\phi$ . Averaged experimental uncertainty of 10 K. . . . .	71
3.26	Averaged $OH^*$ distribution for ID16 $\phi=0.8$ (a) and $\phi=1$ (b) and for ID25 $\phi=0.8$ (c) and $\phi=1$ (d). Units in mm and counts. N50H50. . . . .	71
3.27	(Left) NO and (Right) $NH_3$ -slip emissions varying the $NH_3$ percentage in the fuel (vol.) and the equivalence ratio $\phi$ for ID 25 mm. $NH_3$ -slip averaged relative uncertainty of 8%. . . . .	72

3.28	(Left) NO and (Right) NH <sub>3</sub> -slip emissions varying the NH <sub>3</sub> percentage in the fuel (vol.) and the equivalence ratio $\phi$ for ID 16 mm. NH <sub>3</sub> -slip averaged relative uncertainty of 8%. . . . .	73
3.29	Schematic representation of the adopted reactor network. . . . .	74
3.30	Pollutant emission estimates from the WSR network, for $\phi=1.0$ (left) and $\phi=0.8$ (right) at different fuel composition. . . . .	75
3.31	NO sensitivity analysis for NH <sub>3</sub> /H <sub>2</sub> mixtures at different fuel compositions for $\phi=1$ . ID16. . . . .	76
3.32	ROPA and flux analysis for NH <sub>3</sub> -H <sub>2</sub> mixtures. ID16. . . . .	77
4.1	Conceptual drawing of the EDC model. . . . .	86
5.1	Schematic of the Adelaide Jet in Hot Co-flow burner, taken from [14]. . . . .	99
5.2	2D sketch of the Adelaide Jet in Hot Co-flow burner (left) adapted from Galletti et al. [15], and detail of the numerical grid with sample positions (right). . . . .	101
5.3	Sensitivity analysis of turbulence models (using KEE) and kinetic schemes (using $k-\epsilon$ $C_{\epsilon 1}=1.6$ ) on the mean temperature profiles, at $z=30$ mm (a-d), $z=120$ mm (b-e) and along the centerline (c-f). Case $Re=10k$ and 3% O <sub>2</sub> , adopting $C_{mix}=0.5$ . . . . .	103
5.4	Sensitivity analysis of $C_{mix}$ using a static approach on the mean temperature profiles, at $z=30$ mm (a), $z=60$ mm (b), $z=120$ mm (c) and along the centerline (d). Case $Re=10k$ and 3% O <sub>2</sub> . Modified $k-\epsilon$ and KEE. . . . .	105
5.5	Sensitivity analysis of $C_{mix}$ using a static approach on the mean H <sub>2</sub> O profiles, at $z=30$ mm (a), $z=60$ mm (b), $z=120$ mm (c) and along the centerline (d). Case $Re=10k$ and 3% O <sub>2</sub> . Modified $k-\epsilon$ and KEE. . . . .	106
5.6	Sensitivity analysis of $D$ using a fractal approach on the mean temperature profiles, at $z=30$ mm (a), $z=60$ mm (b), $z=120$ mm (c) and along the centerline (d). Case $Re=10k$ and 3% O <sub>2</sub> . Modified $k-\epsilon$ and KEE. . . . .	107

5.7	Comparison between different mixing models based on mean temperature, mean CO and OH mass fraction profiles. Re=10k and 3% O <sub>2</sub> in the co-flow. Modified k- $\epsilon$ and KEE. . . . .	108
5.8	Radial $C_{mix}$ distribution as a function of (a) different mixing models (z=120 mm, Re=10k, 3% O <sub>2</sub> ), (b) axial position (Re=10k, 3% O <sub>2</sub> , “Dyn Chen”) and (c) Y <sub>O<sub>2</sub></sub> in the co-flow (Re=10k, “Dyn Chen”, z=120 mm). . . . .	110
5.9	Comparison between RANS and LES (Li et. al [16]). Re=10k, 3% O <sub>2</sub> . Modified k- $\epsilon$ and KEE. . . . .	110
5.10	Comparison between different mixing models based on mean temperature for different co-flow oxygen levels (3%, 6% and 9%). Re=10 k. Modified k- $\epsilon$ and KEE. . . . .	111
5.11	Comparison between different mixing models based on mean OH mass fraction for different co-flow oxygen levels (3%, 6% and 9%). Re=10 k. Modified k- $\epsilon$ and KEE. . . . .	112
5.12	Comparison between different mixing models based on mean CO mass fraction for different co-flow oxygen levels (3%, 6% and 9%). Re=10 k. Modified k- $\epsilon$ and KEE. . . . .	113
5.13	Chemical time scale ( $\tau_c$ ) distribution for different co-flow oxygen levels (3%, 6% and 9%). Re=10 k. Modified k- $\epsilon$ , KEE and “Dyn JM”. Only the area of interest of the simulation domain is shown. . . . .	114
5.17	Mixing time constant $C_{mix,eq}$ distribution for the different fuel jet Reynolds number cases (5k, 10k and 20k). Only the area of interest of the simulation domain is shown. . . . .	115
5.14	Comparison between different mixing models based on mean temperature for different fuel jet Reynolds number (5k, 10k and 20k). Modified k- $\epsilon$ and KEE. . . . .	116
5.15	Comparison between different mixing models based on mean OH mass fraction for different fuel jet Reynolds number (5k, 10k and 20k). Modified k- $\epsilon$ and KEE. . . . .	117
5.16	Comparison between different mixing models based on mean CO mass fraction for different fuel jet Reynolds number (5k, 10k and 20k). Modified k- $\epsilon$ and KEE. . . . .	118

5.18	Experimental and numerical NO mass fraction profiles at axial locations $z=60$ mm (a), $z=120$ mm (b), and $z=200$ mm (c). “Dyn JM” and KEE. . . . .	120
5.19	Experimental and numerical NO mass fraction profiles at axial locations $z=60$ mm (a), $z=120$ mm (b), and $z=200$ mm (c). “Dyn JM” and KEE. . . . .	121
5.20	Experimental and numerical NO mass fraction profiles at axial locations $z=60$ mm (a), $z=120$ mm (b), and $z=200$ mm (c). “Dyn JM” and full GRI-2.11. . . . .	122
5.21	Experimental and numerical NO mass fraction profiles at axial locations $z=60$ mm (a), $z=120$ mm (b), and $z=200$ mm (c). “Dyn JM” and full GRI-2.11 and: a single $\kappa$ for all the species (blue solid lines); $\kappa_{NO}=1$ and the “standard” $\kappa$ for all the species but NO (red dashed lines). . . . .	123
5.22	(Left) Contribution of each pathway to the peak of NO formation at $z=200$ mm with a single $\kappa$ and with $\kappa_{NO}=1$ . (Right) Effect of $\kappa_{NO}=1$ on the formation of NO from each route. “Dyn JM” and full GRI-2.11. . . . .	124
5.23	HM1 case: best correlated species at various axial locations. Lower $Z_s^+(X_\alpha)$ values mean better correlation. . . . .	128
5.24	HM1 case: best correlated net reaction rates at various axial locations. Lower $Z_s^+(\dot{\omega}_r)$ values mean better correlation. . .	128
5.25	HM3 case: best correlated species at various axial locations. Lower $Z_s^+(X_\alpha)$ values mean better correlation. . . . .	130
5.26	HM3 case: best correlated net reaction rates at various axial locations. Lower $Z_s^+(\dot{\omega}_r)$ values mean better correlation. . .	130
5.27	HM1 case: best correlated markers at various axial locations. Lower $Z_s^+(\nu)$ values mean better correlation. Here $\nu$ comprehends both $X_\alpha$ and their combinations. . . . .	131
5.28	HM3 case: best correlated markers at various axial locations. Lower $Z_s^+(\nu)$ values mean better correlation. Here $\nu$ comprehends both $X_\alpha$ and their combinations. . . . .	132

5.29	Trends of normalized HRR, top-two mole fractions and combinations at 60 mm, 120 mm and 550 mm respectively. First row refers to HM1 case, second row to HM3. . . . .	132
5.30	HM1 and HM3 contour plots of HRR compared to species products contours. The three zones are split as follows: from 0 to 150 mm, from 150 mm to 450 mm and from 450 mm to 550 mm. . . . .	133
6.1	Streamlines, colored according to the velocity magnitude for pure methane combustion in the ULB furnace. Units in meters per second. . . . .	139
6.2	Computational domain and grid resolution from the selected grid (case without window). . . . .	141
6.3	Comparison of the measured and computed wall temperature profiles at six different points along the $z$ coordinate. . . . .	143
6.4	Sensitivity of temperature predictions to kinetic scheme and PaSR constant $C_{mix}$ for pure methane. (a) $z=100$ mm, (b) $z=200$ mm, (c) $z=300$ mm, (d) $z=400$ mm, (e) $z=500$ mm and (f) $z=600$ mm. Averaged experimental uncertainty of 10 K, which is the radius of the marker. M100H0, $\phi=0.8$ and ID16. Std k- $\epsilon$ . . . . .	144
6.5	Contour of $\kappa$ (a), Damköhler number (b) and flame index (c) for M100H0, $\phi=0.8$ , ID16. Std k- $\epsilon$ , $C_{mix}=0.5$ , GRI-2.11. . . . .	145
6.6	Sensitivity of temperature predictions to the $\kappa$ parameter for pure methane. (a) $z=100$ mm, (b) $z=200$ mm, (c) $z=300$ mm, (d) $z=400$ mm, (e) $z=500$ mm and (f) $z=600$ mm. Averaged experimental uncertainty of 10 K, which is the radius of the marker. M100H0, $\phi=0.8$ and ID16. Std k- $\epsilon$ . . . . .	145
6.7	Contour of $\kappa$ (a), Damköhler number and (b) for M50H50, $\phi=0.8$ , ID16. Std k- $\epsilon$ , $C_{mix}=0.3$ , GRI-2.11. . . . .	147
6.8	Contour of flame index (a), predicted OH (b) and experimental OH* (c) for M50H50, $\phi=0.8$ , ID16. Std k- $\epsilon$ , $C_{mix}=0.3$ , GRI-2.11. . . . .	147

- 6.9 Sensitivity of temperature predictions to kinetic scheme for M50H50,  $\phi=0.8$ , ID16. (a)  $z=100$  mm, (b)  $z=150$  mm, (c)  $z=200$  mm, (d)  $z=250$  mm, (e)  $z=300$  mm and (f)  $z=400$  mm.  $C_{mix}=0.5$ , std k- $\epsilon$ . Averaged experimental uncertainty of 10 K, which is the radius of the marker. . . . . 148
- 6.10 Sensitivity of temperature predictions to different  $\tau_{mix}$  definitions for M50H50,  $\phi=0.8$ , ID16. (a)  $z=100$  mm, (b)  $z=150$  mm, (c)  $z=200$  mm, (d)  $z=250$  mm, (e)  $z=300$  mm and (f)  $z=400$  mm. GRI-2.11, std k- $\epsilon$ . Averaged experimental uncertainty of 10 K, which is the radius of the marker. . . . . 148
- 6.11 Sensitivity of temperature predictions to different turbulence models for M50H50,  $\phi=0.8$ , ID16. (a)  $z=100$  mm, (b)  $z=150$  mm, (c)  $z=200$  mm, (d)  $z=250$  mm, (e)  $z=300$  mm and (f)  $z=400$  mm. GRI-2.11,  $C_{mix}=0.3$ . Averaged experimental uncertainty of 10 K, which is the radius of the marker. . . . . 150
- 6.12 Sensitivity of temperature predictions to inlet air turbulence intensity for M50H50,  $\phi=0.8$ , ID16. (a)  $z=100$  mm, (b)  $z=150$  mm, (c)  $z=200$  mm, (d)  $z=250$  mm, (e)  $z=300$  mm and (f)  $z=400$  mm. GRI-2.11,  $C_{mix}=0.3$ , std k- $\epsilon$ . Averaged experimental uncertainty of 10 K, which is the radius of the marker. . . . . 150
- 6.13 Sensitivity of temperature predictions to radiation modeling for M50H50,  $\phi=0.8$ , ID16. (a)  $z=100$  mm, (b)  $z=150$  mm, (c)  $z=200$  mm, (d)  $z=250$  mm, (e)  $z=300$  mm and (f)  $z=400$  mm. GRI-2.11,  $C_{mix}=0.3$ , std k- $\epsilon$ . Averaged experimental uncertainty of 10 K, which is the radius of the marker. . . . . 152
- 6.14 Contour of  $\kappa$  (a), Damköhler number and (b) flame index for M0H100,  $\phi=0.8$ , ID16. Std k- $\epsilon$ ,  $C_{mix}=0.5$ , KEE. . . . . 152
- 6.15 Sensitivity of temperature predictions to different kinetic schemes for M0H100,  $\phi=0.8$ , ID16. (a)  $z=100$  mm, (b)  $z=150$  mm, (c)  $z=200$  mm, (d)  $z=250$  mm, (e)  $z=300$  mm and (f)  $z=400$  mm.  $C_{mix}=0.5$ , std k- $\epsilon$ . Averaged experimental uncertainty of 10 K, which is the radius of the marker. 153

6.16	Sensitivity of temperature predictions to different $\tau_{mix}$ definitions for M0H100, $\phi=0.8$ , ID16. (a) $z=100$ mm, (b) $z=150$ mm, (c) $z=200$ mm, (d) $z=250$ mm, (e) $z=300$ mm and (f) $z=400$ mm. GRI-2.11, std k- $\epsilon$ . Averaged experimental uncertainty of 10 K, which is the radius of the marker. . . . .	154
6.17	Sensitivity of temperature predictions to different turbulence models for M0H100, $\phi=0.8$ , ID16. (a) axial, (b) $z=100$ mm, (c) $z=150$ mm, (d) $z=200$ mm, (e) $z=250$ mm and (f) $z=300$ mm. GRI-2.11, $C_{mix}=0.5$ . Averaged experimental uncertainty of 10 K, which is the radius of the marker. . . . .	155
6.18	Measured and predicted NO emissions on dry basis in the exhaust gases, using different methods. PP means post-processing tool. ID16, $\phi=0.8$ . . . . .	156
6.19	Percentage contribution of each pathway to NO emissions varying the hydrogen content in the fuel blend using a brute-force sensitivity analysis. GRI-2.11, ID16. . . . .	157
6.20	Sensitivity of temperature predictions to different kinetic schemes, Stagni et al. [13] and Glarborg et al. [4]. (a) Axial, (b) $z=100$ mm, (c) $z=150$ mm and (d) $z=200$ mm. $C_{mix}=0.5$ , std k- $\epsilon$ . Averaged experimental uncertainty of 10 K. N50H50, $\phi=1$ , ID16. . . . .	159
6.21	Dry NO pollutant emissions predicted using different kinetic schemes. The gray area represents the uncertainty propagation of the LHS study for Stagni et al. [13]. ID16, $\phi=1$ (left) and $\phi=0.8$ (right). Relative experimental uncertainty 2%. . . . .	159
6.22	Effect of the recirculation degree ( $k_v$ ), the residence time, and kinetics uncertainties on the pollutant emission estimates from the WSR network, for equivalence ratio of 1.0 (left) and 0.8 (right) at different fuel composition. ID16. . . . .	160
6.23	Latin Hypercube Sampling samples for reactions R80, R85 and R39. Here, the grey scale represents in black the points with maximum NO deviation from the nominal mechanism, in white the points with minimum NO deviation. . . . .	161
7.1	Reduced-order model generation: identification of invariant and system-dependent information. . . . .	171

7.2	Leave-one-out reconstruction errors, visualized in the input parameter space. The sizes of the circles are proportional to the error. Different colours are used for the 3 different values of the air injector size. . . . .	172
7.3	Average NRMSE for the reconstruction of an increasing number of left-out simulations. Vertical bars represent the standard deviation of the error associated to different combinations of $k$ left out simulations. . . . .	173
7.4	Leave-one-out reconstruction errors, visualized in the input parameter space. The sizes of the circles are proportional to the error. Different colours are used for the 3 different values of the air injector size. . . . .	174
7.5	Average NRMSE for the prediction of an increasing number of left-out simulations. Vertical bars represent the standard deviation of the error associated to different combinations of $k$ left out simulations. . . . .	175
7.6	Leave- $k$ -out relative errors for the prediction of scalar quantities such as wall temperature, flame length, value and location of the $Y_{OH}$ peak. Vertical bars represent standard deviations of the error associated to different combinations of $k$ left out simulations. . . . .	176
7.7	List of CFD cases varying the three operating conditions. .	177
7.8	NRMSE for the prediction of the test data by a ROM based on POD and Kriging. . . . .	178
7.9	(left) True temperature field from CFD simulation for ID16, 60% $H_2$ and $\phi=0.93$ . (right) Predicted temperature field for the same operating conditions. . . . .	178
7.10	(left) True OH field from CFD simulation for ID25, 65% $H_2$ and $\phi=0.91$ . (right) Predicted OH field for the same operating conditions. . . . .	179
A1	Idealized problem to quantify the radiative power transmitted through the window. . . . .	A2
A2	View factors for aligned parallel rectangles [17]. . . . .	A2



B1	Graphical visualization of the measurand uncertainties that need post-processing. . . . .	B2
B2	Relative impact of MFC and impurities on the final fuel uncertainty. For sake of clarity only the pure component cases are reported. . . . .	B4
B3	Relative impact of MFC, dry air composition and air moisture (a) on the final combustion air and cooling air uncertainties. (b) Relative impact of each sources of Table B1 on the MFC uncertainty. Two examples are reported for combustion air (100% H <sub>2</sub> and 100% CH <sub>4</sub> ). . . . .	B5
C1	Predicted temperature profiles for the coarse, medium and fine grids, varying the axial location (a) z=100 mm, (b) z=200, (c) z=300 mm and (d) z=400 mm for a 40%-60% CH <sub>4</sub> -H <sub>2</sub> fuel blend and $\phi=1$ . ID16, case without window. .	C2
C2	Predicted temperature profiles for the case with window and without window, varying the axial location (a) z=100 mm, (b) z=200 mm, (c) z=300 mm and (d) z=400 mm for a 40%-60% CH <sub>4</sub> -H <sub>2</sub> fuel blend and $\phi=1$ . ID16. . . . .	C3
C3	Contour of temperature for a 45° domain without window (left) and a 180° domain with window (right) on the symmetry plane. Case 40%-60% CH <sub>4</sub> -H <sub>2</sub> fuel blend and $\phi=1$ . ID16. . . . .	C4
C4	Comparison between two different formulations of $\tau^*$ based on mean temperature, mean CO and OH mass fraction profiles. Re=10k and 3% O <sub>2</sub> in the co-flow. AJHC, Modified k- $\epsilon$ and KEE. . . . .	C5
C5	Comparison between two different formulations of $\tau^*$ for M50H50, ULB furnace. (a) z=100 mm, (b) z=150 mm, (c) z=200 mm, (d) z=250 mm, (e) z=300 mm and (f) z=400 mm. GRI-2.11, $C_{mix}=0.3$ , std k- $\epsilon$ . Averaged experimental uncertainty of 10 K, which is the radius of the marker. . . .	C6

C6	Comparison between two different formulations of $\tau^*$ for M0H100, ULB furnace. (a) $z=100$ mm, (b) $z=150$ mm, (c) $z=200$ mm, (d) $z=250$ mm, (e) $z=300$ mm and (f) $z=400$ mm. GRI-2.11, $C_{mix}=0.3$ , std k- $\epsilon$ . Averaged experimental uncertainty of 10 K, which is the radius of the marker. . . .	C6
D1	Averaged OH* distribution varying the equivalence ratio. Test-case T4. Units in mm and counts. . . . .	D2
D2	Pollutant emission varying the equivalence ratio. Test-case T4. . . . .	D2
D3	Pollutant emissions in function of the nitrogen dilution level. Test-case T7. . . . .	D3



# List of Tables

2.1	LHV for various CH <sub>4</sub> -H <sub>2</sub> blends . . . . .	31
2.2	LHV for various NH <sub>3</sub> -H <sub>2</sub> blends . . . . .	31
2.3	Fundamental combustion characteristics of ammonia, hydrogen and methane. . . . .	34
3.1	A summary of the fuels used in the main working groups operating in flameless. . . . .	44
3.2	Operating conditions of the experimental tests on the CH <sub>4</sub> -H <sub>2</sub> mixtures. . . . .	45
3.3	Main operating parameter for the experimental campaign with the air injector diameter ID 25 mm. $\phi=0.8$ . . . . .	49
3.4	Recirculation ratio $k_v$ estimated using CFD simulations, varying the hydrogen content. Test-case T1. . . . .	53
3.5	Classification of the cases as MILD combustion, according to the two different estimations of $T_{in}$ . $T_{max}$ refers to the maximum measured temperature. Test-case T1. . . . .	55
3.6	Furnace energy balance for the investigated cases. Test-case T1. . . . .	56
3.7	Formation (F), quenching (Q) and release (R) reactions for OH* and CH*. Only a part of the quenching reactions is reported. . . . .	57
3.8	Air injection velocity varying the air injector ID. Test-cases T1-T2-T3. . . . .	60

3.9	Recirculation ratio $k_v$ estimated using CFD simulations for air injection diameter ID25 and ID16, varying the hydrogen content. Test-cases T1-T3. . . . .	60
3.10	Classification of the cases as MILD combustion, varying the hydrogen content and the air injector ID. . . . .	64
3.11	Operating conditions of the experimental tests on the $\text{NH}_3\text{-H}_2$ mixtures. . . . .	69
3.12	List of sensitive reactions for $\text{NH}_3\text{-H}_2$ blends. . . . .	72
4.1	Coefficients of the scalar dissipation rate equation by various authors [18]. . . . .	91
5.1	Physical properties of the jet (Central jet velocity is for the $\text{Re}=10\text{k}$ case). . . . .	99
5.2	List of the investigated cases for AJHC. . . . .	100
5.3	CPU time consumption of various mixing models. . . . .	106
6.1	Comparison of the measured and computed temperature, $\text{O}_2$ and $\text{CO}_2$ (on a dry basis) mole fraction values at the outlet. . . . .	143
6.2	Details about identified sensitive reactions. . . . .	160
7.1	Digital twin's prediction errors for different scalar quantities of the furnace such as wall temperature, flame length , position of the peak of $Y_{OH}$ , value of the peak of $Y_{OH}$ , furnace outlet mass fractions of $\text{H}_2\text{O}$ , $\text{CO}_2$ and $\text{CO}$ . . . . .	179
B1	MFC uncertainty data summary. SP set-point, FS full-scale. . . . .	B2
B2	Uncertainty quantification for the fuel, combustion air and cooling air, varying the $\text{H}_2$ content. Flow rates in $\text{Nm}^3/\text{h}$ . . . . .	B4
B3	Energy balance with uncertainty quantification ( $U_{95}$ ) for the investigated cases. . . . .	B7





# Nomenclature

## Acronyms

<i>AJHC</i>	Adelaide Jet in hot Co-flow
<i>BFG</i>	Blast furnace gas
<i>CCS</i>	Carbon capture and storage
<i>CDS</i>	Colorless Distributed Combustion
<i>CFD</i>	Computational fluid dynamics
<i>CMC</i>	Conditional moment closure
<i>DO</i>	Discrete ordinate
<i>EDC</i>	Eddy dissipation concept
<i>EGR</i>	Exhaust gas recirculation
<i>FGM</i>	Flamelet Generated Manifold
<i>FLOX</i>	Flameless oxidation
<i>FS</i>	Full scale
<i>FTIR</i>	Fourier Transform InfraRed
<i>GHC</i>	Greenhouse Gas
<i>HiTAC</i>	High Temperature Air Combustion
<i>HRR</i>	Heat release rate
<i>ICCD</i>	Intensified charge-coupled device



<i>ID</i>	Inner diameter
<i>IPCC</i>	Intergovernmental Panel on Climate Change
<i>LES</i>	Large eddy simulations
<i>LHV</i>	Low heating value
<i>MILD</i>	Moderate or Intense Low-oxygen Dilution
<i>MxHy</i>	Molar composition for a blend CH <sub>4</sub> -H <sub>2</sub>
<i>NG</i>	Natural gas
<i>NRMSE</i>	Normalized root mean squared errors
<i>NxHy</i>	Molar composition for a blend NH <sub>3</sub> -H <sub>2</sub>
<i>PaSR</i>	Partially stirred reactor
<i>PDF</i>	Probability Density Function
<i>POD</i>	Proper orthogonal decomposition
<i>RANS</i>	Reynolds averaged Navier-Stokes
<i>RMS</i>	Root Mean Square
<i>ROM</i>	Reduced order model
<i>ROP</i>	Rate of production
<i>RSM</i>	Reynolds Stress Model
<i>SNCR</i>	Selective non-catalytic reduction
<i>UQ</i>	Uncertainty quantification
<i>WSGG</i>	Weighted-sum- of-grey-gas
<i>WSR</i>	Well stirred reactor
<b>Greek Symbols</b>	
$\chi$	Mixture fraction dissipation rate
$\delta_{ij}$	Kronecker symbol

$\epsilon$	Emissivity or turbulent dissipation rate
$\epsilon_\phi$	Scalar dissipation rate
$\epsilon_{he}$	Efficiency of the heat exchanger
$\gamma_\lambda$	Mass fraction of the reactive structures in EDC model
$\kappa$	Mass fraction of the reactive structures in PaSR model
$\lambda_k$	Eigenvalues of the Jacobian matrix
$\mu$	Molecular viscosity
$\mu_t$	Turbulent viscosity
$\Omega$	Solid angle
$\omega_k$	Source term for species $k$
$\phi$	Equivalence ratio
$\rho$	Density
$\sigma$	Stefan-Boltzmann constant
$\tau$	Residence time for the WSR
$\tau^*$	Residence time in the fine structure
$\tau_c$	Chemical time scale
$\tau_{mix}$	Mixing time scale
$\xi$	Flame index

### Roman Symbols

$\dot{m}$	Mass flow rate
$\dot{n}$	Volumetric flow rate
$\widetilde{Y_k}$	Species mass fraction in the cell
$\widetilde{Z''^2}$	Mixture fraction variance

$A$	Pre-exponential factor
$a_j$	Weight for WSGG
$c_p$	Specific heat at constant pressure
$C_{\epsilon 1}, C_{\epsilon 2}$	Model constants in turbulent kinetic energy dissipation rate transport equation
$C_\gamma, C_\tau$	EDC model constants
$C_\mu$	Model constant in standard k- $\epsilon$ turbulence model
$C_{D1}, C_{D2}, C_{P1}, C_{P2}$	Constants in transport equation for the mixture fraction dissipation rate
$C_{mix}$	Model constant in PaSR
$D$	Dilution level
$D_m$	Molecular mass diffusion
$D_t$	Turbulent mass diffusion
$Da$	Damköhler number
$E_b$	Blackbody emissive power
$f$	Ratio N <sub>2</sub> /air
$F_{ij}$	View factor between surfaces $i$ and $j$
$Gr$	Grashof number
$h$	Enthalpy
$h$	Heat transfer coefficient
$h_f^0$	Enthalpy of formation
$I_\nu$	Radiation intensity
$k$	Turbulent kinetic energy
$k_v$	Recirculation ratio
$L$	Fuel lance length

$N_f$	Frame
$Nu$	Nusselt number
$P$	Power
$P_f$	Production of scalar fluctuation
$P_k$	Production of turbulent kinetic energy
$Pr$	Prandtl number
$q$	Heat flux
$Ra$	Rayleigh number
$Re$	Reynolds number
$S_r$	Radiation source
$Sc$	Schmidt number
$T$	Temperature
$t$	Time
$u_i$	Velocity on $i$ -component
$U_{95,x}$	Uncertainty on the measurement of X with a 95% probability
$x$	Traversal coordinate
$Y$	Mass fraction
$Y_k^0$	Species mass fraction in the fine structure
$Y_k^0$	Species mass fraction in the surrounding fluid
$Z$	Mixture fraction
$z$	Axial coordinate
$Z_s^+$	Metric

### Subscripts

$a$ or $air$	Air
--------------	-----

<i>conv</i>	Convective
<i>cool</i>	Cooling
<i>exh</i>	Exhaust
<i>f</i> or <i>fuel</i>	Fuel
<i>rad</i>	Radiative
<i>rec</i>	Recirculating
<i>si</i>	Self-ignition
<i>st</i>	Stoichiometric
<i>th</i>	Thermal
<i>walls</i>	External walls

### **Superscripts**

"	Fluctuations
~	Favre-averaged

# Chapter 1

## Introduction

*This chapter introduces the global framework of this PhD thesis. First the current environmental issues related to greenhouse gas emissions, especially from power and industrial applications, are described. In this context, the role of fossil fuels in the short- and long-term energy transition is discussed as well as the different formation mechanisms for NO emissions. Secondly, the concept of Diluted/Flameless/MILD combustion is introduced and a detailed literature review is provided. The main experimental and numerical issues dealing with this combustion mode are also revised. Finally, the scope of this PhD is described. It arises from the increasing necessity of flexible combustion technologies capable of dealing with non-conventional fuels keeping low pollutant emissions.*

## 1.1 Global warming and energy transition

Energy is undoubtedly the single most important factor impacting the prosperity of our society. Global energy consumption is predicted to continue increasing, and at least 60% of the world's energy will still be provided by combustion of bio- and fossil-derived fuels in 2040 [19]. However, by 2050, Europe needs to decouple drastically its economic growth from its emission of carbon dioxide ( $\text{CO}_2$ ). Indeed, the human influence on the climate system is clear and growing, with impact observed across all countries. The Intergovernmental Panel on Climate Change (IPCC) is 95% certain that humans are the main cause of current global warming [2]. As reported in the Synthesis Report (SYR) 2014 [2], the final part of the IPCC's Fifth Assessment Report (AR5), the global average surface temperature warmed by around  $0.85^\circ\text{C}$  between 1880 and 2012. This temperature rise has already affected the climate and ecosystems leading to increment of droughts, floods, sea level rise and biodiversity loss [20]. Besides, the wide spread use of combustion systems has also adverse effects on air pollution (particulate matter,  $\text{NO}_x$ ,  $\text{SO}_x$ ).  $\text{NO}_x$  is a general term for the nitrogen oxides, namely nitric oxide (NO) and nitrogen dioxide  $\text{NO}_2$ . When released in atmosphere  $\text{NO}_x$  emissions can further react to produce photochemical smog, acid rain as well as enhance tropospheric ozone production and stratospheric ozone depletion [21].

Figure 1.1 shows the observed monthly global mean surface temperature change and estimated anthropogenic global warming over the coming years (solid orange line up to 2017) [1]. Orange dashed arrow and horizontal orange error bar show respectively the central estimate and likely range of the time at which  $1.5^\circ\text{C}$  is reached if the current rate of warming continues. The grey, blue and purple surfaces show the likely range of warming responses, computed with a simple climate model [1]. They represent a stylized pathway in which net  $\text{CO}_2$  emissions and non- $\text{CO}_2$  radiative forcing decline following a linear trend from 2020 to reach net zero in reported year in the legend (except for the purple surface where the non- $\text{CO}_2$  emission remains constant). The alarming message of this Figure is clear, our society must take actions to limit the consequences of the climate change. Figure 1.2 shows the total anthropogenic greenhouse gas (GHC) emissions in gigatonne of  $\text{CO}_2$  equivalent per year during the period 1970 - 2010 [2]. It appears clear that the  $\text{CO}_2$  production by combustion of fossil fuels and industrial processes has increased from 55% to 65%, with an almost doubled quantity of  $\text{CO}_2$  rate per year. The Paris Agreement [22] could prove

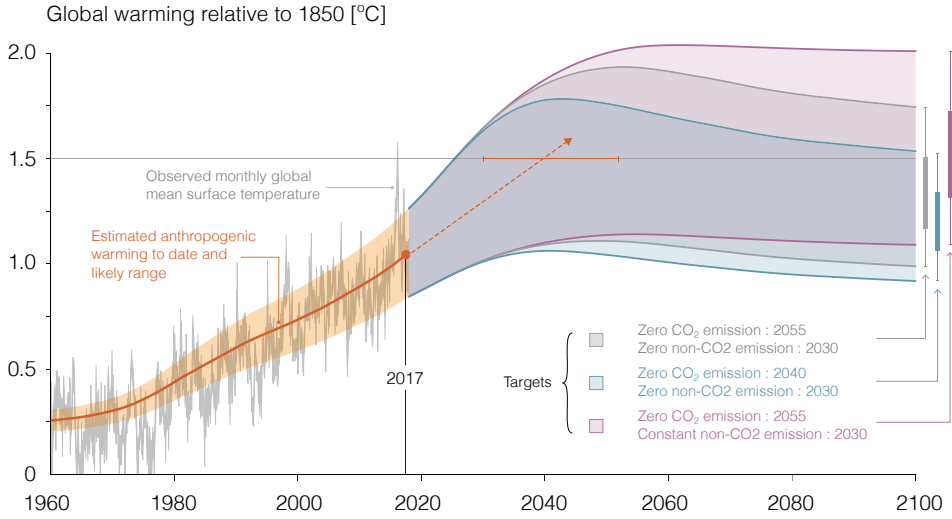


**Figure 1.1:** Estimated anthropogenic warming and possible future scenarios depending on different CO<sub>2</sub> and non-CO<sub>2</sub> emissions targets [1].

to be an historic milestone in the fight against global warming, aiming at holding the global temperature increase well below 2 °C above the pre-industrial levels (2 Degrees Scenario: 2DS) and pursuing efforts to limit the temperature increase to 1.5 °C.

To achieve the mentioned goals, two targets must be pursued: (i) a smarter and more efficient use of the available resources, in such a way to reduce energy waste and CO<sub>2</sub> emissions, and (ii) a systematic control of pollutant emissions, which are formed as byproduct. Moreover a replacement of a significant percent of fossil fuels with renewable energy sources will be needed. However, energy production from most renewable energy sources, such as wind, solar, tidal and wave is typically intermittent and unpredictable. This requires a reliable mid-long term energy storage to synchronize production and demand. The Power-to-Fuel option or chemical storage can be the key for a sustainable energy system rather than batteries. Indeed, converting the excess of renewable energy into second generation fuels will unlock a long-term and high-density energy storage. Indeed, the building structure of these fuels is hydrogen (H<sub>2</sub>), which can be produced from electrolysis of water using the electricity excess from renewables. However, storage and



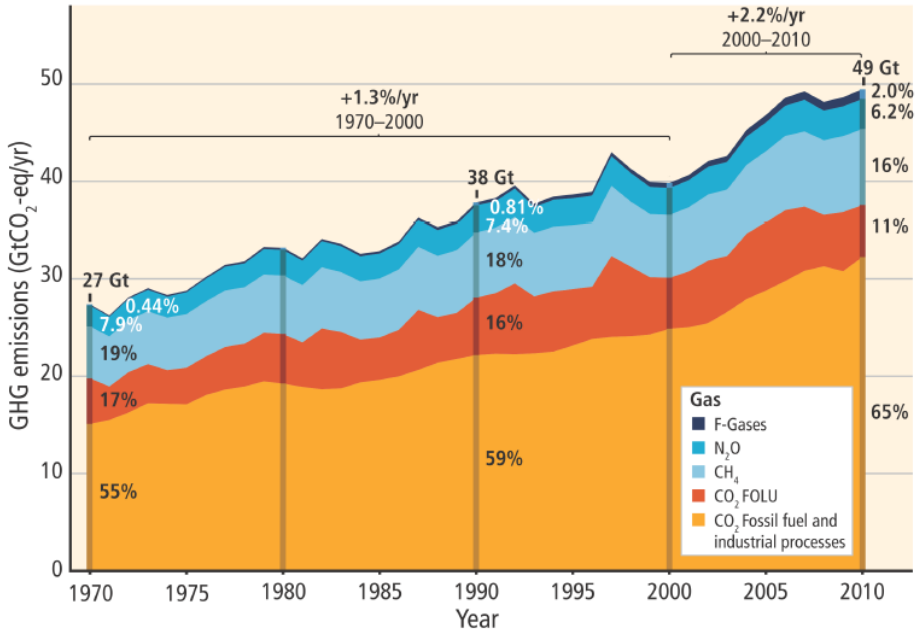


**Figure 1.2:** Total annual anthropogenic greenhouse gas (GHG) emissions for the period 1970 to 2010 by gases [2].

transport of hydrogen remain important unsolved challenges for its sustainable utilization. To overcome these issues, hydrogen can be combined with carbon dioxide to obtain a higher energy density fuels, such as methane ( $\text{CH}_4$ ). To this purpose, carbon dioxide might come from carbon capture and storage (CCS) system, contributing to a reduction of the carbon footprint. Moreover, the usage of  $\text{CH}_4/\text{H}_2$  will contribute to further reduce  $\text{CO}_2$  emissions. On the other side, hydrogen might also be converting into ammonia ( $\text{NH}_3$ ), a carbon free fuel, reacting with nitrogen ( $\text{N}_2$ ). Ammonia has a great advantage compared to hydrogen, being in liquid form at room temperature ( $25^\circ\text{C}$ ) when pressurized to 10.1 bar or temperature of  $-33.4^\circ\text{C}$  at atmospheric pressure [23].

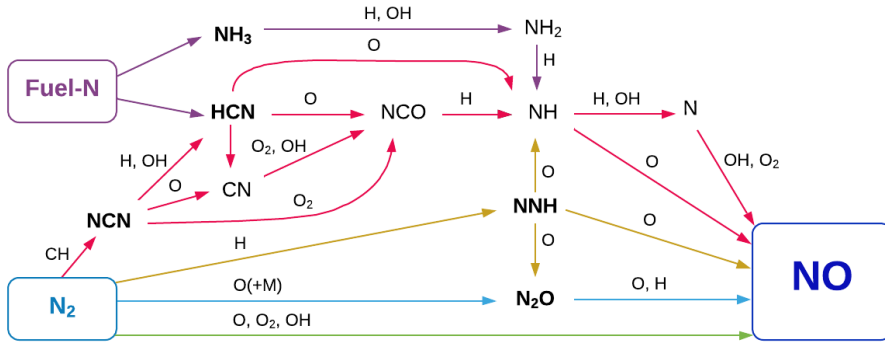


**Figure 1.3:** Simplified schematization of the NO formation pathways: thermal NO (green), prompt NO (red), fuel NO (purple),  $\text{N}_2\text{O}$  (blue) and NNH (yellow) routes [3].

## 1.2 Formation mechanisms for NO emissions

This section tries to explain the main formation mechanisms for NO emissions. Indeed, understanding the physics behind pollutant emissions is crucial to prevent them.

Several separate mechanisms leading to formation of nitrogen oxides have been identified in literature [4], involving either fixation of the molecular nitrogen contained in the combustion air or oxidation of organic nitrogen chemically bound in the fuel (Figure 1.3). For gaseous fuels with no fuel-bound nitrogen (e.g. methane), formation of NO arises from fixation of  $\text{N}_2$  in the combustion air. This process involves the attack of reactive radicals, such as  $\text{O}$ ,  $\text{CH}_x$ , and  $\text{H}$  on the triple bond in the molecular nitrogen. These reactions form either NO or a reactive nitrogen intermediate, e.g. cyanides,  $\text{N}_2\text{O}$ , NNH that might be oxidized to NO eventually. For fuels with a considerable content of organically bound nitrogen, i.e.  $\text{NH}_3$  and most solid fuels, oxidation of fuel-bound nitrogen constitutes the dominant source of nitrogen oxides. In conventional regime, the thermal NO or Zeldovich [24] mechanism is the most important source of NO. This route is predominant at temperatures higher than 1800 K and with sufficient oxygen available. At 1800 K the formation rate doubles for every 35 K temperature rise [25]. Because of this strong temperature dependence, most NO-reducing tech-

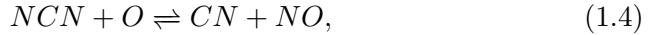
nologies try to cut off temperature peak and/or keep the residence time in high temperature regions low, avoiding local high oxygen concentration. The initiating step is the attack of an oxygen atom on the triple bond in  $N_2$  [24] (green line in Figure 1.3)



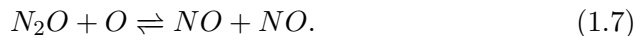
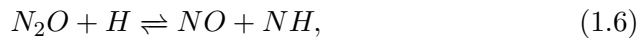
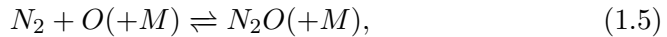
Reaction 1.1 has a high activation energy, being the rate limiting step. Once formed, the nitrogen atom reacts with the following reactions:



The Fenimore's prompt NO [26] is typical of rich system characterized by temperatures above the thermal route threshold and it is a dominant source of NO in turbulent hydrocarbon/air diffusion flames [27]. Early modeling studies [28] identified the reaction of CH with  $N_2$  as the most important initiation step. However, this does not form HCN and N, but rather NCN and H as recently discovered [29]. The NCN species can subsequently react with O radicals to form NO directly:



or it can undergo a reaction path that eventually leads to form NO (Figure 1.4). Prediction of prompt NO formation requires an accurate rate constant for the reaction of CH with  $N_2$ , along with the capability to predict the concentration of CH and the selectivity in the oxidation of NCN [4]. Several studies [30, 31] show that the inclusion of additional routes ( $N_2O$  and NNH) is critical for predicting NO accurately. The  $N_2O$  pathways plays an essential role in fuel-lean systems with temperature below 1800 K and high pressure. It is constituted by the following reversible reactions [32] involving a third-body (blue line in Figure 1.3):



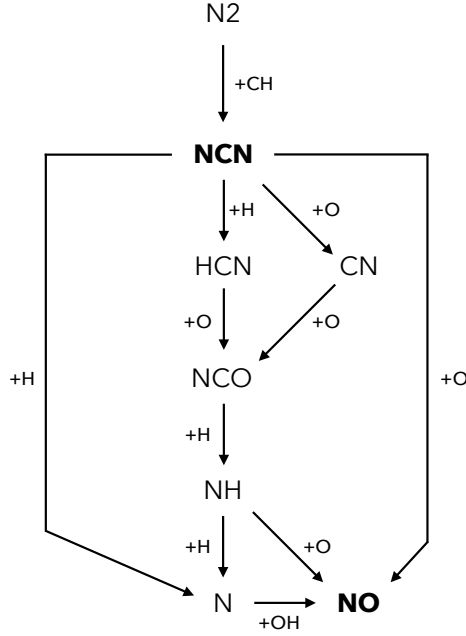
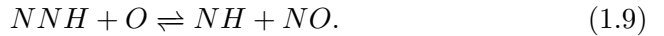


**Figure 1.4:** Reaction path diagram from prompt NO formation under slightly fuel-rich conditions. Adapted from [4].

Lastly, the NNH mechanism is most significant when non-conventional fuels with relevant hydrogen content are oxidized. While the  $N_2O$  mechanism is quite well established, the magnitude of NO formation via NNH remains controversial [4]. The mechanism for forming NO via NNH consists of the reaction sequence [6]:



Hayhurst et al. [8] performed measurements of NO in a laminar, premixed, flat  $CH_4/H_2$  flame and observed high NO concentration. They confirmed the presence of such route, which corrected the underestimation of NO given by the Zeldovich route alone. Konnov et al. [7] observed that the NNH route represents the dominant source of NO at 1500 K, not only in rich conditions, but also in lean mixtures and at stoichiometric conditions. An Arrhenius expression for the rate constant of the reaction between NNH and O was proposed. They derived a range of variability for the activation temperature

$T_a$ , based on the uncertainty in the value of the heat of formation of NNH between 1400 and 2500 K, which affects the equilibrium of Reaction 1.8. However, a later study of Klippenstein et al. [5] quantified such heat of formation with negligible uncertainty, so that the yield of NO from the NNH route becomes proportional to the rate constant of Reaction 1.9. While the uncertainty in the heat of formation of NNH may alter the NO predicted by a factor of 2, reported rate constants for Reaction 1.9 vary by more than an order of magnitude, as shown by the Arrhenius plot of Figure 1.5, and significantly affect the resulting NO predictions [4].

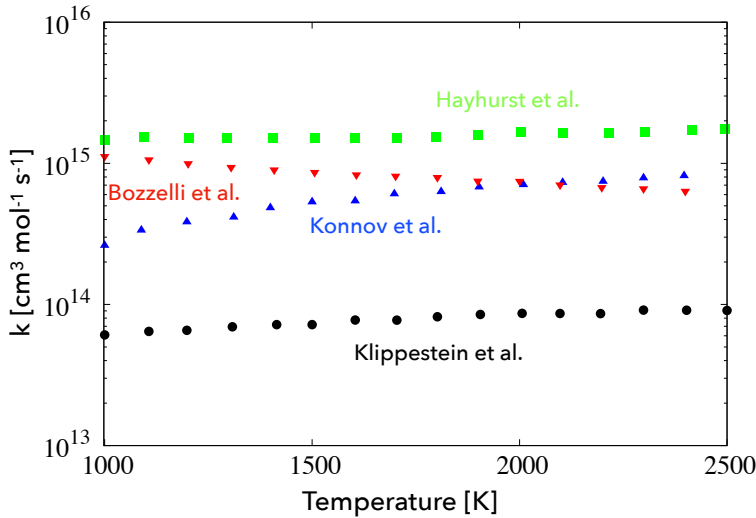


**Figure 1.5:** Arrhenius plot for the reaction  $\text{NNH} + \text{O} \rightleftharpoons \text{NH} + \text{NO}$ . The rate constant  $k$  profiles are drawn from the following sources: Klippenstein et al. [5], Bozzelli et al. [6], Konnov et al. [7] and Hayhurst et al. [8]. Adapted from [3]

For solid or gaseous fuels having a certain amount of fuel-bound nitrogen,  $\text{NH}_3$  plays a major role in forming NO.  $\text{NH}_3$  can be available directly in the fuel stream or it may be the result of the devolatilization of solid fuel or from conversion of cyanides at higher temperature [33]. The research on the ammonia oxidation started several decades ago. The high-temperature pyrolysis mechanism was first experimentally characterized starting from the 1980s [34]. Studies on oxidation focused first on  $\text{NH}_3$  flame chemistry [35] and on its use within the Thermal DeNO<sub>x</sub> process [36] for the selective non-

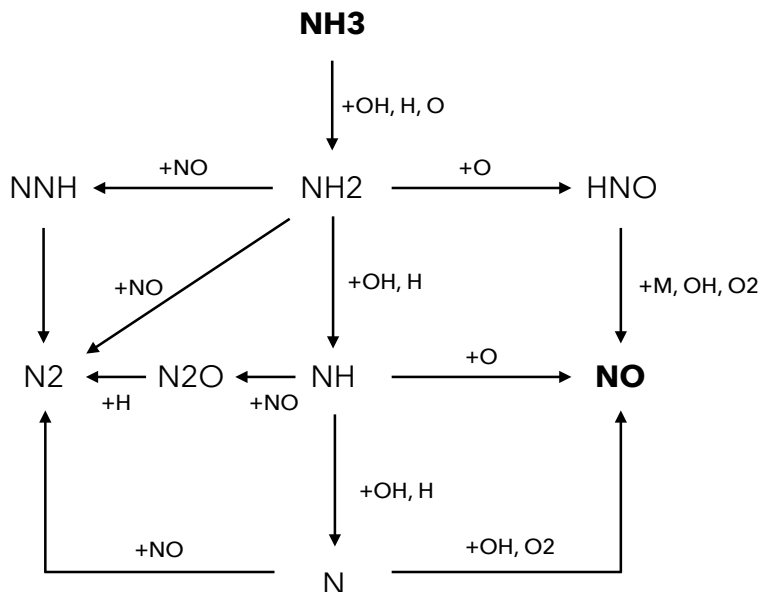


**Figure 1.6:** Reaction path diagram for oxidation of  $\text{NH}_3$ . Adapted from [4].

catalytic reduction (SNCR) of nitrogen oxides. Later, oxidation chemistry was studied at a fundamental level through targeted experiments [37] and theoretical methodologies [5]. The work of Miller et al. [38] was a pioneer study to describe ammonia oxidation with detailed kinetics. Since then, many studies were released [4]. Figure 1.6 shows the reaction pathways of  $\text{NH}_3$  oxidation and fuel NO formation and reburn [4]. In particular,  $\text{NH}_3$  is converted to  $\text{NH}_2$  by reaction with the radical pool, which, in turn, may be converted to  $\text{NH}$  and  $\text{N}$ . These reactions become more competitive with increasing temperature. Subsequently, the  $\text{NH}_i$  radicals may react with  $\text{NO}$ , leading to  $\text{N}_2$ , or with  $\text{O}$ ,  $\text{OH}$ , or  $\text{O}_2$ , forming  $\text{NO}$ . The selectivity for forming  $\text{NO}$  or  $\text{N}_2$  in oxidation of ammonia is determined by the competition of the amine radicals for reacting with  $\text{NO}$  or with the  $\text{O}/\text{H}$  radical pool (or  $\text{O}_2$ ).

### 1.3 Non-conventional or diluted combustion

To achieve the Power-to-Fuel objective, the development of a high efficiency technology, coupled with virtually zero pollutant emissions, stable working conditions with different loads and fuels and significant energy saving is required. In the last years, a so-called non conventional or diluted combustion [39] has drawn attention for its ability of meeting the mentioned targets. The key aspect is the dilution of fuel and oxidizer streams with a ballast of inert gases before they react so that the oxygen concentration in the reactants is substantially reduced with respect to the standard contents in atmospheric air. This combustion technology has undergone different changes during its year of progressing with, obviously, different shades of meaning (Figure 1.7). Among them, the author can recall HiTAC, flameless, MILD and Colorless Distributed Combustion (CDC).

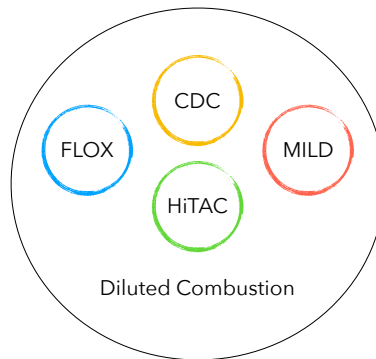


**Figure 1.7:** Conceptual diagram of Diluted Combustion.

In 1971, Weinberg [40] perceived that the use of heat of recirculation could be used to preheat the mixtures and extend their flammability limits. Moreover, the author understood that this could lead to sustain combustion without any assistance from an external heat source and an attractive solution for burning low grade fuels. Later, researchers focused more on preheating regenerative systems applied to air and the term *High Temperature Air Combustion* (HiTAC) was coined. Katsuki et al. [41] pointed out that the air temperature at which a gaseous fuel is automatically ignited and in which combustion is sustained should be called *High*. The result is a distributed intense combustion with little to none visible signature and bluish green or/and green color flame. The authors also underlined the

new low-NO concept for HiTAC to satisfy the more and more tightening regulations for emissions standards.

Wünning and Wünning [9] introduced the term FLameless OXidation (FLOX<sup>®</sup>), emphasizing the importance to reach a combustion regime able to avoid temperature peaks (hot-spots) to suppress thermal NO formation. It requires enough inert combustion products to be entrained in the reaction region to dilute and pre-heat the mixture air-fuel above the auto-ignition temperature. As a result, a flame front is no longer identifiable, thus the name *flameless*. Moreover the combustion process is no longer restricted to the flame front region, rather extended to a larger portion of the combustion chamber. The system is characterized by a more uniform temperature field than traditional combustion systems. By avoiding temperature peaks, thermal NO formation is largely suppressed and the effect on the furnace materials is beneficial. Soot formation is also suppressed, due to the lean conditions and the large CO<sub>2</sub> concentration in the exhausts. In contrast to stabilized flame combustion, flameless oxidation is mixture and temperature controlled, and it is achieved with specific flow and temperature conditions. A prerequisite for a stable flame in traditional combustion systems is represented by the balance between flow velocity and flame velocity. Creating flow conditions for flame stabilization is an essential burner design criterion, for both premixed and diffusion flame. Wünning and Wünning [9] defined a parameter named recirculation ratio ( $k_v$ ) to describe the characteristic of the recirculation in the reaction zone, as follows:

$$k_v = \frac{\dot{m}_{rec}}{\dot{m}_a + \dot{m}_f}, \quad (1.10)$$

where  $\dot{m}_{rec}$  is the net mass flow rate of recirculated flue gas, whereas  $\dot{m}_f$  and  $\dot{m}_a$  are the fuel and air mass flow rates, respectively. Different combinations of recirculation ratios and temperatures result in different combustion modes as shown in Figure 1.8 for natural gas combustion. Stable flames (zone A) are achievable over the whole range of combustion chamber temperatures, but only in a narrow recirculation ratio window. As recirculation ratio is increased, the flames become unstable, and even extinguish if the temperature is below the autoignition temperature (the horizontal line), as seen in the “No reactions” zone. However, if the furnace temperature is above the self-ignition temperature and the exhaust gas recirculation is sufficiently high ( $k_v \geq 3$  for natural gas combustion [9]), the fuel can react in the very steady form of flameless oxidation (zone C) with an abatement of the noise of about 15 dB(A) [42].



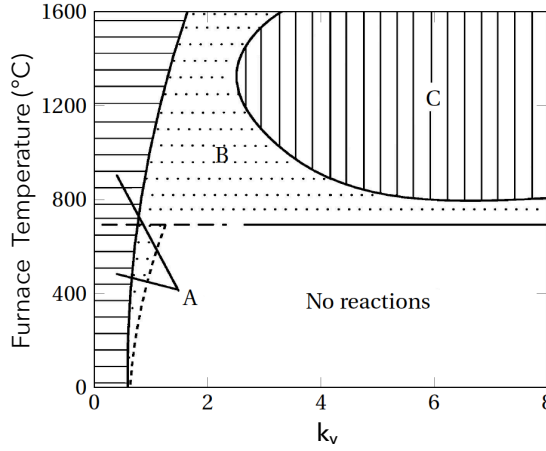


**Figure 1.8:** Schematic diagram of the stability limits for different combustion modes. Zone A: stable flames regime; Zone B: unstable flames regime; Zone C: flameless regime. Source: [9].

The MILD (Moderate or Intense Low-oxygen Dilution) acronym was coined by Cavaliere and de Joannon [10] in 2004, considering a Well Stirred Reactor (WSR). The term should be used to indicate a burning regime in which the inlet temperature of the reactant mixture is higher than the mixture self-ignition one ( $T_{si}$ ). Furthermore, the maximum allowable temperature increase with respect to inlet temperature during combustion is lower than the mixture self-ignition temperature (expressed in Kelvin). The resultant diagram is displayed in Figure 1.9. The process of preheating of reactants becomes fundamental for this combustion technique to be sustainable. Moreover, the term “MILD” is used to stress the mild changes and gradual evolution which this combustion mode can guarantee.

Another term used by authors such as Gupta and Arghode [43, 44] and which is based on the principle of HiTAC is Colorless Distributed Combustion (CDC). The name colorless is due to negligible visible emission from the flame as compared to the conventional ones. A particular aspect of the volume CDC is that air and fuel jets are injected separately in non-premixed mode into the combustion chamber at high momentum to entrain hot gases to a desirable degree and with controlled shear layer mixing. Fuel start to auto-ignites in a volume distributed mode after only complete mixing with the hot chemically reactive mixture and air. In classic HiTAC technology, on the contrary, air is first diluted with internal or external hot gases, so

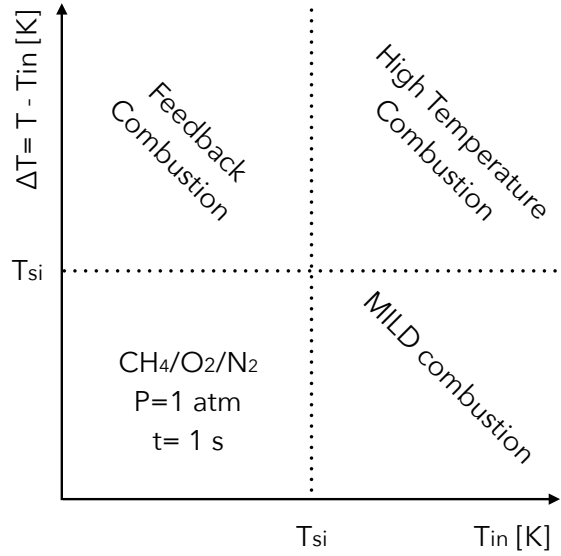


**Figure 1.9:** Combustion regimes defined with inlet temperature and temperature raise. Source: [10].

that it is above the auto ignition temperature prior to its mixing with the fuel [45].

### 1.3.1 Experimental studies and industrial applications

Flameless combustion appears very well suited for those industrial processes which require high and homogeneous temperature distribution within the combustion chamber (e.g. in glass and ceramic industry, steel thermal treatments). For these processes, the energy recovery represents a primary issue to ensure acceptable energy efficiency. Energy saving can be achieved with either recuperative or regenerative burners according to the exchange area and heating rate required. These burners are usually designed to operate both in flame and flameless mode, by varying the reactants feeding mode. The combination of recuperative burners with radiant tubes is a widely applied solution in many thermal treatments of material surfaces, to avoid any contact or contamination of the flue gases with the stock surface to be treated [39].

The first experimental evidence regarding the structure of the combustion

zone in flameless combustion was provided by Plessing et al. [46], who measured temperature and species concentration with optical techniques in flame and flameless conditions. The maximum temperatures decreased, from 1900 to 1650°C, when switching from flame to flameless mode. In addition OH radicals were present in lower concentration (below 10 ppm) in flameless regime, thus reducing NO prompt formation.

Choi and Katsuki [47] investigated the feasibility of flameless oxidation in industrial glass furnaces. They found that combustion was sustained even with low calorific value fuels and low oxygen concentrations, if the combustion air was preheated above the fuel self-ignition temperature. Results also showed that NO<sub>x</sub> formation was controlled by the mixing process between fuel and the preheated air. Flamme [48] investigated the application of flameless combustion to glass melting furnaces operating with process temperature around 1600°C and air preheating temperatures up to 1350°C. Experimental results on a 300 kW furnace showed that the replacement of conventional burners with recuperative burners led to dramatic reduction of NO<sub>x</sub> emission, from 1500 ppm down to values safely below 100 ppm.

The application of flameless combustion in different fields than thermal treatment processes is also very attractive. The advantages of a clean and quite combustion process could be exploited by several fields of application, including power generation, micro co-generation and low-temperature applications. Flamme [49] showed the applicability of recuperative burners to gas turbine to overcome the oscillating problems typical of lean premixed combustion occurring in gas turbines. Kruse et al. [50] have proposed newer combustor configurations for possible applications in gas turbine engines at higher pressure (2-5 bar). A reverse flow configuration was used to achieve better mixing. It consists of an ignition chamber at the top, a combustion chamber attached with an air-fuel supply system at the bottom of the furnace. The combustion chamber is heated up to 1100 K with the help of the ignition chamber and consequently switched to flameless mode using the principle of Plessing et al. [46]. The combustion chamber operates at a thermal intensity of 6 MW/m<sup>3</sup> which represents the lower end limit of gas turbines. Initially, measurements were taken at 1 bar pressure as a reference case with methane as fuel. Low NO<sub>x</sub> and CO emissions were observed in this case. Then the pressure was increased to 2.5 and 5 bar and equivalence ratios were varied in the range of  $\phi = 0.22-0.8$ . At higher pressures, the NO<sub>x</sub> formation pathways were changed and residence time was increased. Moreover, higher NO<sub>x</sub> emissions were observed for this condition due to the increased residence time of the reactants. However, a reduced air nozzle

diameter helped to reduce the overall  $\text{NO}_x$  emissions.

During the last 50 years diluted combustion technologies have been deeply tested with natural gas (NG), since this fossil fuel is one of the most important non-renewable energy source together with petroleum and coal. However, the energy transition and the Power-To-Fuel scenario will require the massive diffusion of non-conventional fuels. The capability to spread the reaction in a very wide volume preventing the formation of a flame front, as well as the high recirculation rate and the consequent preheating of reactants through the exhaust gases guarantee a reliable combustion of fuels with very variable LHV. Moreover, usually it is not necessary to introduce complicated or onerous changes to the geometry of the system, but attention must be paid to correctly balance momentum rates of jets, recirculation rates, temperatures and flammability limits of the mixture. Especially during the last 15 years several group of research started to investigate the behaviour of alternative fuels in MILD combustion, mainly focusing on the field of industrial furnaces. For instance, a variety of fuel mixtures using methane, ethylene ( $\text{C}_2\text{H}_4$ ), propane ( $\text{C}_3\text{H}_8$ ) and their dilution with  $\text{CO}_2$  or  $\text{N}_2$  were investigated by Dally et al. [51]. Weber et al. [52] examined in 2005 the fundamental and industrial application aspects of combustion of natural gas, heavy and lightfuel oils, and coal in a furnace at 0.58 MW thermal input using highly preheated air at  $1300^\circ\text{C}$ . Derudi et al. [53] focused their attention on experimental results obtained in a laboratory-scale burner, using non-conventional fuels obtained as industrial by-product, e.g. the coke oven gas (COG), whose hydrogen content can reach up to 60% by volume. Parallel studies on laboratory apparatus using methane/hydrogen mixtures were performed by Sabia et al. [54] and Ayoub et al. [55] to better understand the  $\text{H}_2$  effects on the MILD combustion. Mosca [56] investigated MILD combustion of B50, a low LHV fuel whose composition is obtained by mixing 50% COG by vol% with 50% blast furnace gas (BFG) on a 30 kW furnace. Sabia et al. [57] showed that an efficient recirculation of the exhausts produces a robust MILD combustion condition enabling combustion of low calorific fuels. Chinnici et al. [58] analyzed the thermal performance of a syngas-fuelled hybrid solar receiver combustor operated under MILD combustion regime. It was found that the type of fuel influences significantly the rate of radiative heat transfer and the ratio of radiative to convective heat transfer rates, and therefore the configuration must be optimized for each type of fuel. The study of fuels derived from biomass, such as biogas (usually rich in  $\text{CH}_4$  and  $\text{CO}_2$  and produced by anaerobic digestion with anaerobic organisms or fermentation

of biodegradable materials) or some forms of syngas (primarily consisting of  $H_2$  and  $CO$  and produced by gassification of biomass at high temperature), became interesting in the MILD combustion field. Colorado et al. [59] investigated the effect of biogas on the performance of an experimental furnace equipped with a self-regenerative flameless burner and compared the results with the performance of the system fueled with natural gas. More recently in 2013, Hosseini et al. [60] wrote a review on biogas, its resources, and its use on MILD combustion, encouraging the use of this fuel with this technique because more efficient and economically feasible.

Nowadays, the scientific community is facing the possible use of ammonia as energy carrier and its subsequent combustion. Sorrentino et al. [61] studied  $NH_3$  oxidation in a MILD cyclonic burner. They showed that operative parameters such as equivalence ratio, thermal power and inlet preheating level affected  $NO_x$  emissions. More specifically, the best operational window identified to minimize  $NO_x$  emissions was very narrow and it ranged from stoichiometric to slightly fuel-rich conditions, where the conversion efficiency is decreased due to the formation of some unburned components such as  $NH_3$  and  $H_2$ . Therefore it is very important to identify strategies to increase the optimal operational window, in terms of feeding mixture composition, where the  $NO_x$  levels are minimized.

### 1.3.2 Challenges dealing with flameless/MILD combustion

The aim of this section is to provide a brief literature review about the main challenges dealing with flameless/MILD combustion. Additional relevant information will be reported at the beginning of each chapter.

To better understand the nature of any combustion process, a key aspect is the identification of the region where the heat is released. This is especially true for flameless combustion where no visible flame is present. The Heat Release Rate (HRR) represents the amount of heat released per unit of time and space due to chemical reactions. Its spatial distribution directly influences important physical phenomena such as flame-turbulence interactions, sound generation and its interaction with flames. The mathematical expression of HRR is:

$$HRR = \sum_{\alpha=1}^N \dot{\omega}_{\alpha} h_{f,\alpha}^0 \quad (1.11)$$

where  $N$  is the number of species,  $\dot{\omega}_{\alpha}$  is the reaction rate of the  $\alpha$ -th

chemical species, and  $h_{f,\alpha}^0$  is its standard enthalpy of formation. Clearly, a direct measurement of the HRR would involve the accurate determination of a significant number of scalars simultaneously [62]. Due to such a high complexity, it would be more practical to measure a quantity (i.e. a species mass fraction or a reaction) that presents some correlation with this rate over the relevant range of flame and flow parameters [63], to qualitatively estimate the local HRR.

Chemiluminescence of natural excited species, e.g  $\text{OH}^*$ ,  $\text{CH}^*$ , (where  $*$  denotes an electronically excited state) and Laser-Induced Fluorescence (LIF) [63–66] are generally techniques used to identify the reaction zone and its topology. However, the choice of the scalars able to identify the reaction region can be influenced by the specific chemical-physical behaviour of the combustion process, determined in turn both by operative conditions and fuel mixture [62, 63]. For instance, Vagelopoulos et al [67] showed that the  $\text{CH}$  marker provides a reasonable correlation with the HRR only for undiluted reactant mixtures with equivalence ratios,  $\phi$ , of 0.8-1.2, whereas Najm and co-workers [63, 64] showed that the formyl radical,  $\text{HCO}$ , is a good HRR-marker for stoichiometric or slightly rich ( $\phi = 1.2$ ) methane and dimethyl ether-air laminar flames. Moreover, the flame stretch effects coming from flame-vortex interaction do not significantly influence this correlation [63]. According to the authors, the robust correlation between HRR and  $\text{HCO}$  concentration may be attributed to three main reasons: (1)  $\text{HCO}$  is a major intermediate species in oxydation of  $\text{CH}_4$  to  $\text{CO}_2$ ; (2) its concentration is directly dependent on its production rate; (3)  $\text{HCO}$  production is directly dependent on the concentration of  $\text{CH}_2\text{O}$ , that in turn directly depends on the reaction  $\text{CH}_3 + \text{O} \rightleftharpoons \text{CH}_2\text{O} + \text{H}$ , which shows the largest fractional influence on heat release rate [64]. Nevertheless, Swaminathan and co-workers [62, 68] highlighted the difficulty of accurately measuring  $\text{HCO}$  concentration due to its low signal to noise ratio, thus suggesting the usage of the more reliable product of  $\text{OH}$  and  $\text{CH}_2\text{O}$  local signals. Indeed, such species are involved as reactants in  $\text{HCO}$  formation from formaldehyde through the reaction  $\text{OH} + \text{CH}_2\text{O} \rightleftharpoons \text{HCO} + \text{H}_2\text{O}$ . This reconstructed LIF-signal was demonstrated to be a clear HRR-marker for the investigated conditions. Up to now, a wide number of different analysis [69] on flame topology has relied on this assumption.

However, due to the very diluted conditions, the same reactions or marker might fail in correlating with the HRR in MILD conditions. Recent studies have tried to clarify this aspect. Sidey et al. [65] compared the presence of  $\text{OH}$ ,  $\text{OH}^*$  with the flame primary heat release region under MILD con-

ditions, suggesting that the sole OH may not be a comprehensive HRR marker for this regime. Minamoto et al. [70] investigated undiluted and diluted (MILD) methane-air flames, and multicomponent fuel mixtures under both laminar and turbulent conditions, using Direct Numerical Simulations (DNS) data. The authors showed that: (1) a large fractional contribution of a reaction to the HRR does not automatically imply that this will have a good correlation with the HRR; thus, the rate of the aforementioned reaction,  $CH_3 + O \rightleftharpoons CH_2O + H$ , which often shows a high fractional influence on HRR, is not necessarily well correlated with the HRR. (2) the HRR correlation is strongly dependent on the equivalence ratio. As a consequence, alternative markers were proposed. The product of H and  $CH_2O$  concentrations, corresponding to reaction  $H + CH_2O \rightleftharpoons HCO + H_2$ , instead of OH and  $CH_2O$  ones was suggested for turbulent MILD and conventional premixed methane-air flames. The viability of H- $CH_2O$  product LIF signal was demonstrated in [68]. Nevertheless, additional studies are still required to add further understanding on the adequacy of the various HRR markers under MILD/diluted conditions for non-conventional fuels (i.e. methane/hydrogen blends).

Flameless/MILD combustion is characterized by a stronger competition between chemistry reaction and fluid dynamics, leading to a relatively low Damköhler number, due to the strong mixing and the reduced temperature level. As a consequence, a reliable numerical model must consider both phenomena (chemistry and fluid dynamic) and the usage of a detailed kinetic scheme appears mandatory. This makes the usage of Computational Fluid Dynamics (CFD) models more complex, involving multi-physics and multi-scales. CFD was widely used in the last years to optimize burner performances by investigating geometrical details, such as injection nozzle configurations and internal devices for flue gas recirculation. Different approaches were evaluated by Christo et al. [71], Parente et al. [72] in the framework of RANS (Reynolds-averaged Navier-Stokes) simulations adopting Eddy Dissipation Concept (EDC) [73] model. Recently, Evans et al. [74] showed that adjusting the EDC coefficients  $C_\tau$  and  $C_\gamma$  from their default value results in significantly improved performance under MILD combustion. Afterwards, Parente et al. [75] proposed functional expression showing the dependency of the EDC coefficients on dimensionless flow parameters, such as Reynolds and Damköhler number. This expression was further investigated by Romero-Anton [76] simulating a Delft Lab Scale furnace (9 kW) burning natural gas. Beside the EDC model, the Partially Stirred Reactor (PaSR) [77] combustion model was proposed for MILD combus-

tion [78]. PaSR model is conceptually similar to EDC, but it is characterized by a different definition of the reacting volume fraction, which becomes a function of the chemical and the mixing time-scales.

Furthermore, in flameless combustion fuel and air streams are highly diluted by recirculated burnt gas, which contains carbon dioxide and water, increasing the infrared radiative flux [79]. For this reason, radiation must be well modeled dealing with flameless combustion, adding another degree of complexity to the problem.

However, although CFD tools have significantly progressed in recent years, their use in real time is still unrealistic, especially for combustion regimes such as flameless/MILD combustion, characterized by stronger competition between chemistry reaction and fluid dynamic. In this framework, analytical, numerical and experimental knowledges must be combined to create a physics-based reduced-order models (ROMs), to embed the critical aspects of a detailed simulation into simplified relationships between the inputs and outputs that can be used in real time. The development of virtual models, also referred to as digital twins, of industrial systems opens up a number of opportunities, such as the use of data to anticipate the response of a system and brainstorm malfunctioning, and the use of simulations to develop new technologies, i.e. virtual prototyping. Digital twins are a disruptive technology that creates a living model of a physical system that can also be used for predictive maintenance. The digital twin will continually adapt to changes in the environment or operation using real-time sensory data and can forecast the future of the corresponding physical system and act as soft sensor [80]. Importantly, digital twins can also be used for non-destructive testing, which can undoubtedly benefit industrial protagonists. For the above reasons, the need for digital twins is becoming imperative. Combining CFD simulations with experimental real-time data coming from sensors of a real industrial system might foresee a change in its state [81].

## 1.4 Objectives

Due to the unpredictable and intermittent behaviour of renewable energies, the synchronization of production and demand requires a reliable mid-long term energy storage. The Power-to-Fuel option can be the key for a sustainable power production: converting the excess of renewable energy into so called “electro-fuels”, will unlock a long-term and high-density energy



storage to be used when renewable production is not sufficient. Indeed,  $H_2$  can be produced by electrolysis but it shows some unsolved challenges for storage and transport. To overcome these issues,  $H_2$  can be combined with  $N_2$  to obtain  $NH_3$ , a carbon-free fuel, or to  $CO_2$  to obtain  $CH_4$ . The energy transition will also involve a massive usage of other green fuels, such as the ones deriving from biomass gasification (i.e. syngas) or anaerobic fermentation (i.e. biogas). As a results, the resulting non-conventional fuels will be blends of  $H_2$ ,  $CH_4$ ,  $NH_3$ ,  $CO$  and  $CO_2$  in variable proportions, introducing flame stability issues. Recently, the combustion community has shown great interest in flameless combustion to meet load and fuel flexibility as well as low pollutant emissions. However, in spite of the reasonable number of experimental investigations involving natural gas or methane, the amount of detailed studies available for furnaces operating under flameless or MILD combustion using non-conventional fuel is scarce and limited to few operating conditions. For ammonia flameless combustion, the author can even count only few works (see Chapter 3). Literature still needs further analysis to deeply test the fuel flexibility of flameless combustion.

Considering the multi-physics and multi-scale aspects of flameless combustion, CFD simulation may be a key aspect to optimize burner performances reducing costs and time related to the manufacturing and testing new prototypes. However, the numerical model should be comprehensive and well validated. Currently, there is no existing model specifically for flameless combustion and most traditional combustion models fail in this job because of the challenges listed in Section 1.3.2. EDC was generally applied in most of the simulations because it can be used with detailed chemistry, but it requires an adjustment of the constants to make it suitable for flameless. On the other hand, PaSR model was also proposed for flameless/MILD combustion and it can be seen as a more general version of EDC. It is characterized by a different definition of the reacting volume fraction, which becomes a function of the chemical and the mixing time-scales. Then, the estimation of these two variables becomes crucial to ensure accurate predictions from the model.

With these considerations in mind, the investigations carried out in this PhD thesis tackled the following aspects:

- Test fuel flexibility of flameless combustion burning non-conventional fuels, such as blends of  $CH_4/H_2$  and  $NH_3/H_2$ , while keeping low pollutant emissions. Experiments have also the aim of bridging the gap between laboratory and industrial scales.

- Optimize the PaSR combustion model to create a numerical model robust enough to handle multiple fuels in a non-conventional combustion mode.
- Build a digital twin of a furnace, starting from CFD simulations, for instantaneous evaluation.

## 1.5 Outlines

This PhD thesis is a contribution towards the understanding of flameless combustion using non-conventional fuels. The approach used in the current work foresees a strong link between experiments and modeling, therefore the corresponding chapters contain references to each other.

A detailed description of the furnace used in the current work and a brief description of the principles of measurements techniques are presented in Chapter 2. Chapter 3 instead, collects the experimental campaigns carried out on the ULB furnace using blends of  $\text{CH}_4\text{-H}_2$  and  $\text{NH}_3\text{-H}_2$ .

Chapter 4 provides a brief description of turbulent combustion modeling, which will be used in Chapter 5 and 6. In particular, Chapter 5 offers the validation and optimization of the PaSR combustion model in a Jet in hot co-flow burner (AJHC). In Chapter 6, PaSR model is applied to the ULB furnace, simulating some of the cases investigated experimentally in Chapter 3, focusing on temperatures and pollutant predictions.

Chapter 7 provides the key issues in developing a digital twin able to reproduce the main features of the ULB furnace.

Finally, the main conclusions and findings of this study are summarized, suggestions and recommendations for future studies are made in Chapter 8.



## Chapter 2

# Experimental Setup

*This chapter firstly presents the furnace used in this work, which consists of a commercial WS REKUMAT M150 recuperative Flame-FLOX burner and an insulated combustion chamber. Secondly, the main measurements techniques, such as suction pyrometer, chemiluminescence imaging and exhaust gases analyser are presented. Thereafter, the main characteristics and issues related with non-conventional fuels, such as hydrogen and ammonia-enriched blends are discussed. Finally, the last sections provide details about the energy balance of the furnace and the uncertainty quantification of measured data.*

*This chapter is partially based on the following publication:*

**M. Ferrarotti**, M. Fürst, E. Cresci, W. De Paepe, A. Parente, “Key Modeling Aspects in the Simulation of a Quasi-industrial 20 kW Moderate or Intense Low-oxygen Dilution Combustion Chamber”, *Energy&Fuels*, 2018, 32, 10228-10241.

**M. Ferrarotti**, W. De Paepe, A. Parente, “Reactive structures and pollutant emissions for methane/hydrogen mixtures in flameless regime”, *Combustion&Flames*, In preparation.

## 2.1 Test bench

The experimental flameless combustion furnace designed for this study is shown in Figure 2.1. It is composed of a cubic combustion chamber ( $1100 \text{ mm} \times 1100 \text{ mm} \times 1100 \text{ mm}$ ) insulated with a 200 mm thick high-temperature ceramic foam layer, resulting in inner dimensions of  $700 \text{ mm} \times 700 \text{ mm} \times 700 \text{ mm}$ . This assists in the establishment and stability of the flameless regime, limiting the heat loss through the walls. A commercial WS REKUMAT M150 recuperative Flame-FLOX burner (nominal power of 20 kW) is mounted at the bottom of the combustion chamber (Figure 2.1) (top right). The burner has an integrated metallic finned heat exchanger to extract energy from the flue gases and to preheat the combustion air. However, the preheating level cannot be controlled, being just the result of an energy balance. Furthermore, due to hardware limit, the temperature of the air entering the combustion chamber can only be derived analytically (see Section 2.4).

The test bench 2.1 shows a configuration similar to industrial furnaces, allowing to vary: geometry, injection system, air excess and load. The fuel is injected via a centrally located nozzle (inner diameter ID 8 mm) and surrounded by a coaxial air jet, whose dimensions can be varied to adjust the air jet entrainment (ID 16-20-25 mm) (Figure 2.1 (bottom right)). However, with such burner configuration, flameless combustion can not be sustained directly when the furnace is at ambient temperature. For that reason, industrial flameless recuperative burners have a “flame mode”, where the fuel is injected close to the air jet to generate a classical flame attached to the burner during the heating of the furnace. Then, when the lowest temperature in the furnace (lower corner) exceeds the self-ignition temperature of the mixture fuel-air, the burner switches to its “flameless mode”: all the fuel is delivered through the coaxial injection and flameless combustion is achieved.

The unit is equipped with an air cooling system (Figure 2.1)(top right) consisting of four cooling tubes (outer diameter OD of 80 mm), with a length of 630 mm inside the furnace. Varying the air flow allows the combustion chamber to operate at different stable conditions, thus simulating the effect of a variable load. On each vertical wall of the combustion chamber, an opening is available for measurements. One side is equipped with a  $110 \text{ mm} \times 450 \text{ mm}$  quartz window allowing optical measurements. In particular, the transmissivity of the quartz glass (GE124) is above 90% within

the wavelength 200-2000 nm, which also enables to collect  $\text{OH}^*$  and  $\text{CH}^*$  chemiluminescence. The other three opening are blocked using the same insulation material and they host ports for temperature measurements.

Figure 2.2 reports the flow control scheme of the fuel feeding system. It is composed by gas bottles, a set of Brooks Mass Flow Controller (MFC) SLA-585XX for different ranges and fuels ( $\text{CH}_4$ ,  $\text{NH}_3$ ,  $\text{H}_2$ ,  $\text{CO}_2$  and  $\text{N}_2$ ) and a static mixer to create an homogeneous fuel blend. A natural gas (NG) line is also feeding the burner by means of a three-ways valve. Combustion air and cooling air are supplied by two blowers and their flow rates are also controlled by MFCs.

## 2.2 Measurements techniques

This section presents the main measurements techniques used in the framework of this thesis, focusing on temperature probes, chemiluminescence imaging and pollutant emissions.

### 2.2.1 Temperature measurements

Temperature inside the chamber is measured at different locations. As mentioned before, three sides of the furnace are closed with insulated plates. In one of those (Figure 2.1), twelve equally spaced thermocouple ports, at a related distance of 50 mm, are installed. In particular, an air-cooled suction pyrometer equipped with a 0.5 mm diameter B-type thermocouple (Platinum Rhodium 30% / Platinum Rhodium 6%) is used to measure the in-flame temperature profiles. It works with a Venturi tube connected to a compressed air circuit at a maximum pressure of 6 bar(g). The thermocouple is protected from chemical attack and from radiation heat exchange with the surrounding walls by two concentric sintered alumina shields. The inox part of the probe has a diameter of 12 mm, while the outer ceramic shield has a diameter of 10 mm [82]. The injector, driven by compressed air, ensures suction of gases at a high speed ( $\approx 100$  m/s), which heats the thermocouple tip via convective heat transfer, so that the equilibrium thermocouple temperature is nearly that of the gases without the need for correction. The associated response time is about 10 s. The differential voltage signal is continuously sampled at 10 Hz and automatically converted to temperature units with a National Instrument cold-junction

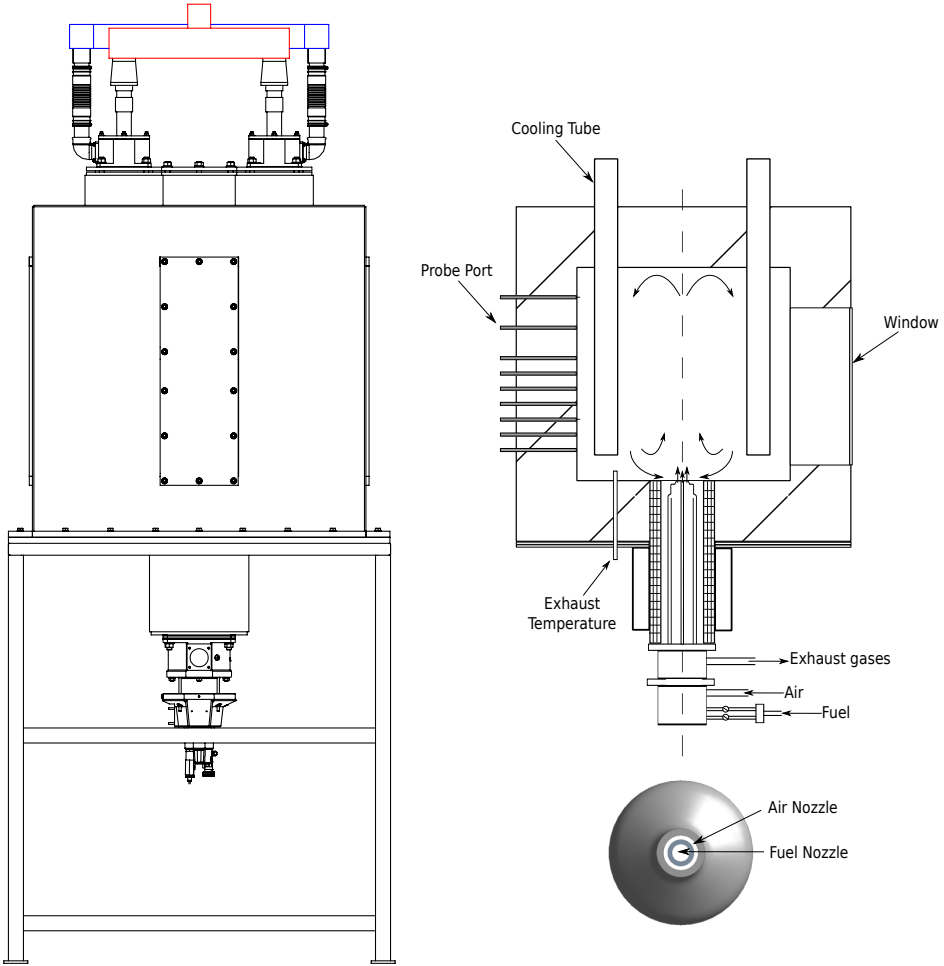


**Figure 2.1:** Schematic of the furnace (left), vertical cross section (top right) and burner nozzle (bottom right). For sake of clarity, only a part of the probe ports are shown.

compensated acquisition card. According to the specifications of the manufacturer, the associated uncertainty is 0.5% of the reading. On another side of the furnace, six K-type thermocouples (Nickel-Chromium / Nickel-Alumel) are mounted, flush against the insulation, to measure the inner wall temperature (uncertainty of 2.2 °C or 0.75% of the reading). Finally, the exhaust gases temperature (before the heat exchanger) is given by a

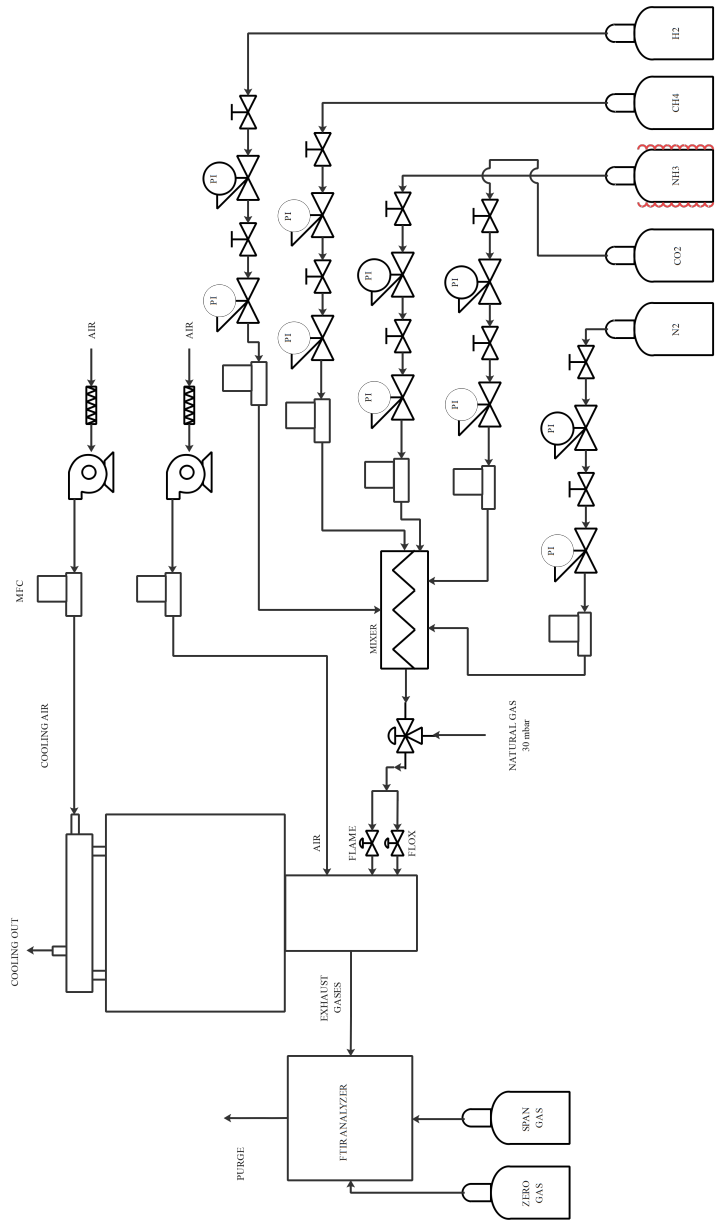


**Figure 2.2:** Schematic P&ID of the test bench.



shielded N-type thermocouple (Nicrosil / Nisil) positioned on the central plane and shifted 200 mm with respect to the axis, on the bottom wall (Figure 2.1). Other K-type thermocouples measure temperature of the main operating parameters, such as fuel, cooling air, combustion air and exhaust gases after the heat exchanger.

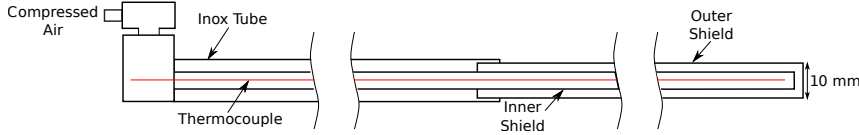


**Figure 2.3:** Schematic diagram of the suction pyrometer.

### 2.2.2 Chemiluminescence Imaging

Chemiluminescence is the radiation emitted by electronically excited molecules in flames when these molecules return to a lower energy state. The wavelength of the radiation is characteristic for the particular molecule and the particular transitions the molecule undergoes.  $\text{OH}^*$  and  $\text{CH}^*$  are examples of molecules exhibiting a simple spectrum with major peaks at 310 nm and 438 nm, respectively. Since these species are mainly produced in the reaction zone, chemiluminescence can be used as a marker of the reaction zone and heat release rate [83, 84]. It is also used to show dynamic behaviour of flames and to identify flame structure and flame stabilization mechanisms [85] in combustion research. Moreover, quantitative results, such as Damköhler numbers and heat release rate, can be obtained from  $\text{OH}^*$  and  $\text{CH}^*$  following [86] and [87], respectively. From a practical viewpoint, flame chemiluminescence detection is a simple method that can be used in many combustion systems.

In this thesis, the chemiluminescence imaging technique was applied to identify flame characteristics in flameless combustion. Indeed, previous studies [55, 56, 65, 88–91] shown the potential of  $\text{OH}^*$  imaging in detecting the reactive region even in diluted conditions. On the other hand, the usage of  $\text{CH}^*$  as marker is still controversial. For instance, Medwell et al. [92] used  $\text{CH}^*$  to retrieve the flame lift-off in MILD conditions, while Zhou et al. [93] reported a moderated suppression of  $\text{CH}^*$  under the same conditions. During the present work,  $\text{CH}^*$  imaging was performed to test the

previous statement and to provide data for future works aimed at estimating the local equivalence ratio, starting from the  $\text{OH}^*/\text{CH}^*$  ratio [94, 95]. Because of the dilution feature of the flameless combustion regime, chemiluminescence signal from reaction zones is very low compared to a classical flame mode, and largely smaller than the continuous radiation in the visible range coming from hot refractory walls in a furnace, inducing its colorless characteristics. However heat release by combustion is still present in the combustion chamber in reaction zones where slight chemiluminescence is emitted. As it occurs in ultraviolet and purple-visible spectral ranges,  $\text{OH}^*$  and  $\text{CH}^*$  chemiluminescence imaging permits to avoid high continuous visible-red and infrared radiation from the walls of the furnace object of the study. Then, an intensified CCD (ICCD) camera allows to record chemiluminescence images even in flameless combustion regime to obtain and analyse the topology of the reaction zones. In the current configuration, imaging are recorded with an intensified charge-coupled device (ICCD) camera (LaVision  $1392 \times 1040$  pixels - 16 bits) equipped with a UV 78 mm f/3.8 lens and two interferential filters to collect  $\text{OH}^*$  ( $310 \pm 10$  nm) and  $\text{CH}^*$  ( $438 \pm 24$  nm). The camera has a maximum acquisition frequency of 17 Hz. The setup can be moved along the three axes thanks to a movable structure coupled with three stepper motors. To avoid the overheating of the system by wall radiations, it was placed sufficiently far from the window, still ensuring, however, a field of view big enough to capture the reactive region.

### 2.2.3 Gas Analyser

As described in Figure 2.2, the exit of the combustion chamber is equipped with a thermocouple and a heated sampling probe to allow for flue gas temperature and composition measurements, avoiding condensation. A Fourier Transform InfraRed (FTIR) analyser (HORIBA MEXA-ONE-FT) is used to measure major species ( $\text{CH}_4$  and  $\text{CO}_2$ ) as well as pollutants ( $\text{NH}_3$ ,  $\text{CO}$ ,  $\text{NO}$  and  $\text{NO}_2$ ). Since, oxygen is transparent to IR sources, a paramagnetic analyser is used, after condensing water from the exhaust gases. With FTIR spectroscopy, uncertainty depends on the choice of the concentration ranges and it has different sources, such as zero noise (1% of full scale (FS)), linearity (1% FS) and water interference (1% FS).

## 2.3 Fuels

Even if natural gas (NG) is a very common fuel in literature, the present thesis focuses on the study of non-conventional fuels in flameless conditions. For this reason, NG is currently used only for preheating the furnace until reaching the auto-ignition temperature of the main fuel. Besides, this also avoid the common issues related to this gas:

- species composition fluctuations day by day, which decreases the repeatability of the tests;
- the inability to know the NG components concentrations in the day of the test;
- the uncertainties introduced in the numerical simulations to correctly represent the species inside NG and their combustion.

During this work, two blends of non-conventional fuels (in variable composition) are used:  $\text{CH}_4\text{-H}_2$  and  $\text{NH}_3\text{-H}_2$ . Tables 2.1-2.2 show the typical lower heating values (LHV) associated with these fuel blends.

As already mentioned in the Introduction, hydrogen can be produced via water electrolysis with low carbon or renewable power or biogas/biomethane reforming and biomass gasification/pyrolysis. However, electrolysis remains relatively expensive at this stage due to the high capital costs of the technology which require larger markets and further development to reach industrial scale-up and bring costs down. The current absence of an adopted policy and regulatory framework for electrolysis is inhibiting market development. However, costs are expected to decrease dramatically with the uptake of power-to-gas/power-to-hydrogen. Furthermore, with the forecasted increase in wind energy generation for example (it is expected to reach around 40% of EU energy generation in 2040 [96]), electricity costs are also expected to decrease [97]. The usage of pure hydrogen would require large investments, since a replacement of existing steel pipelines to non-permeable materials with a leakage control and the conversion or replacement of end-user appliance are required. On the other hand, the utilization of methane/hydrogen blends into existing natural gas pipelines and with current end-user appliance is possible up to a concentration of 20% [97], thus reducing  $\text{CO}_2$  emissions.

%CH <sub>4</sub> [vol]	%H <sub>2</sub> [vol]	LHV [MJ/Nm <sup>3</sup> ]
100	0	35.8
50	50	23.3
0	100	10.8

**Table 2.1:** LHV for various CH<sub>4</sub>-H<sub>2</sub> blends

%NH <sub>3</sub> [vol]	%H <sub>2</sub> [vol]	LHV [MJ/Nm <sup>3</sup> ]
100	0	14.1
50	50	12.4
0	100	10.8

**Table 2.2:** LHV for various NH<sub>3</sub>-H<sub>2</sub> blends

Ammonia would help to overcome the issues related to hydrogen storage and transportation. Indeed, ammonia is in liquid form at room temperature (25 °C) when pressurized to 10.1 bar or temperature of -33.4 °C at atmospheric pressure [23]. Furthermore, since its boiling temperature and condensation pressure are almost the same as those of propane, transport ship designed for propane can generally be used for ammonia as well [23]. The process of manufacturing ammonia was invented about 100 years ago by F. Haber and C. Bosh. It uses an iron-based catalyst at high pressure (100-300 atm) and high temperature (400-500 °C) to combine hydrogen and nitrogen. Even if researchers are still focusing in optimizing ammonia combustion [98–101] and its pollutant emissions, there are already examples of prototype generating power, such as a micro gas turbine fuelled with ammonia/methane and pure ammonia in Japan [23]. However, ammonia also presents some safety issues, being considered a high health hazard, since it is corrosive to the skin, eyes and lungs. Once it turns to gas, ammonia is colourless with a sharp, penetrating, intensely irritating odour.

The following section revises the property of hydrogen and ammonia in fuel blends.

### 2.3.1 Hydrogen and ammonia-enrich fuels

Molecular hydrogen (H<sub>2</sub>) has significant higher thermal, mass and momentum diffusivities compared to other typical fuels and air. Figure 2.4 shows the thermal diffusivity of three different fuels mixed with air at various equivalence ratios, as well as the mass diffusivity of the respective fuel in

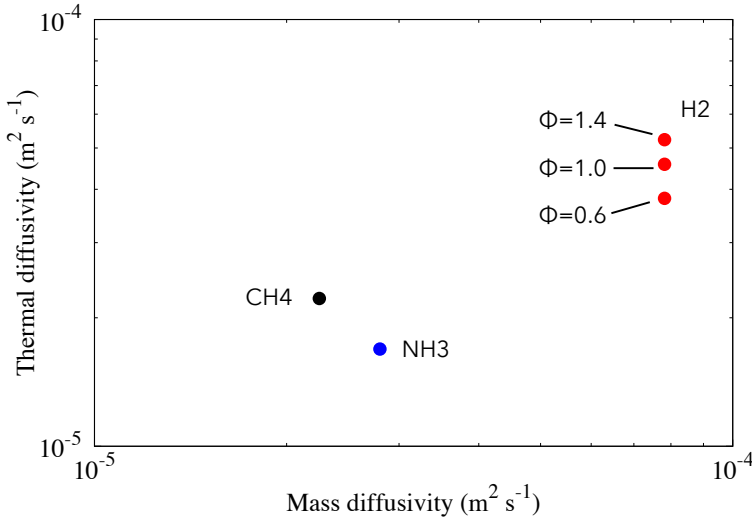


**Figure 2.4:** Thermal and mass diffusivity of different fuels mixed with air at various equivalence ratio, at 300 K and under atmospheric pressure. The equivalence ratios for  $\text{CH}_4$  and  $\text{NH}_3$  are not indicated, since they overlap with each other.

the mixture. Methane and ammonia have comparable mass and thermal diffusivities, which do not change in function of the equivalence ratio and their values are similar to those of air. Their Lewis number (i.e. the ratio between thermal and mass diffusivity) is relatively constant and close to unity. This number indicates indirectly how sensitive the combustion intensity for a given fuel is to fluid dynamic strain and flame front curvature (i.e., stretch). The thermal diffusivity of  $\text{H}_2$ , on the other hand, is approximately one order of magnitude larger than that of air, which leads to a considerable variation of the thermal diffusivity for  $\text{H}_2$ -air mixtures depending on their equivalence ratio. The high thermal diffusivity of  $\text{H}_2$ -air mixtures compared to the mass diffusivity of oxygen ( $\text{O}_2$ ) and nitrogen ( $\text{N}_2$ ) leads, furthermore to a Lewis number larger than unity for fuel rich mixtures, while it is lower than unity for fuel lean mixtures, due to the high mass diffusivity of  $\text{H}_2$  [102]. The special chemical, thermodynamic and transport properties of  $\text{H}_2$  affect both combustion and transport processes and lead therefore to unique flame properties for  $\text{H}_2$  flames compared to other fuels. Figure 2.5 shows the equilibrium temperature for three different fuels.  $\text{H}_2$  is, at all equivalence ratios, characterized by much higher

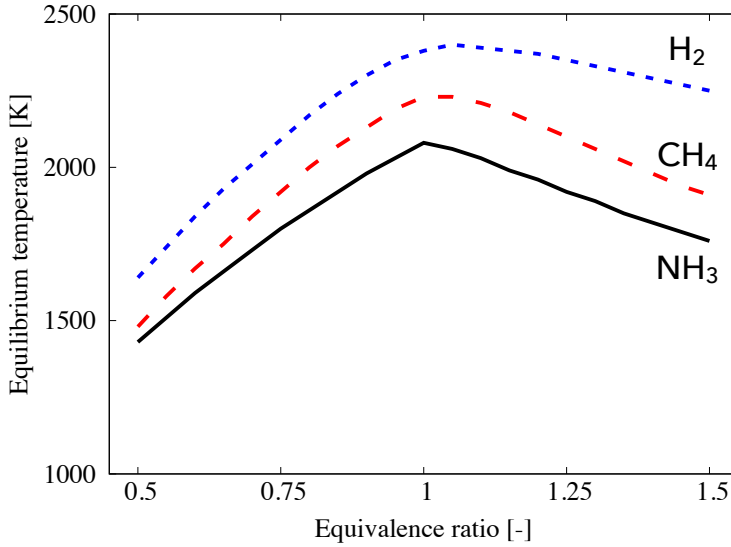


**Figure 2.5:** Equilibrium temperature of  $\text{NH}_3$ ,  $\text{CH}_4$  and  $\text{H}_2$  in air at  $P=1$  atm and  $T_0 = 300$  K, calculated with OpenSMOKE [11] and the POLIMI kinetic scheme [12, 13]. Courtesy of M. Cafiero-ULB.

flame temperatures compared to  $\text{CH}_4$  and  $\text{NH}_3$ .

More important differences can be outlined considering the fundamental combustion characteristics presented in Table 2.3. Indeed, the difference in terms of equilibrium temperature becomes even bigger considering the laminar flame speed  $S_L$  (i.e. the speed at which a laminar premixed flame propagates through an unburned quiescent mixture).  $\text{H}_2$  has a significantly higher laminar flame speed, which can be at least one order of magnitude larger than for other fuels. The high laminar flame speed of  $\text{H}_2$  is caused by its large molecular diffusivity, as well as by the higher chemical reactivity which intensifies the formation of a radical pool [103]. Hence, the laminar flame speed of a hydrogen-enriched mixture increases with increasing its concentration. The presence of  $\text{H}_2$  in fuel-mixtures also affects indirectly the laminar flame speed. Indeed, hydrogen enhances the sensitivity of  $S_L$  to stretch and curvature, which in turn have an effect on the density of the burnt and unburnt gases. Finally, both last variables are connected to the definition of  $S_L$ .  $\text{CH}_4$ - $\text{H}_2$ -air flames become diffuse-thermal unstable, when the  $\text{H}_2$  mole fraction in the mixture exceeds 45%, while pure  $\text{CH}_4$  flames

are diffuse thermal stable [103]. The preferential diffusion of  $H_2$  leads to a locally increased equivalence ratio and increased consumption rate per unit area in positive curved flame regions. This leads to the formation of cusps and enhanced flame surface area generation, leading to an overall increased turbulent flame speed [104].

Another important combustion property, of special relevance for  $H_2$  combustion, is the ignition delay time, which is relevant for the control of auto-ignition. A typical definition for the ignition-delay time is the time delay between a sudden pressure increase, for example in a shock tube experiment, and the following rapid increase in hydroxyl (OH) emissions [105]. The ignition delay time of hydrogen is similar to other fuels below 1000 K, but becomes much shorter at higher temperatures. To control it, a sufficient level of mixing is required [106].

On the other hand, ammonia shows a very low laminar flame speed, about 20% of the one typical of methane (Table 2.3) and high ignition delay time [23]. Furthermore, the flammability range for  $NH_3$ /air mixture is narrower and the ignition temperature is higher, indicating that ammonia has low flammability. Therefore, its blending with or cracking into hydrogen is frequently suggested [99].

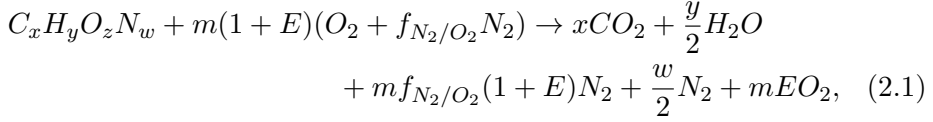
Property	$NH_3$	$H_2$	$CH_4$
Flammability Limit (Eq. ratio)	0.63-1.4	0.1-7.1	0.50-1.7
Max laminar flame speed (m/s)	0.07	2.91	0.37
Min auto-ignition temperature (K)	923	824	885

**Table 2.3:** Fundamental combustion characteristics of ammonia, hydrogen and methane.

## 2.4 Mass and energy balances

As mentioned in Section 2.3, the fuels used during this thesis are mainly composed by  $CH_4$ ,  $NH_3$  and  $H_2$ . The combustion reaction has to be written in a general form to manage all fuels in a simple way. Therefore, the main idea is to use an equivalent molecule  $C_xH_yO_zN_w$  for the considered fuel,

whose oxidation is the following:



where  $x, y, z$ , are the coefficients for the equivalent molecule,  $E$  is the air excess,  $f_{N_2/O_2}$  or  $f$  is the ratio between the molar fraction of  $N_2$  and  $O_2$  in air (3.76). Let us define  $m$  as the number of oxygen moles required to ensure the complete combustion of one mole of equivalent fuel:

$$m = x + y/4 - z/2. \quad (2.2)$$

The coefficients are easily found by weighted mean of the number of the considered atom in each species  $i$  using the corresponding molar fraction as weight. For  $x$  one could write:

$$x = \sum_{i=1}^{N_s} \left( (N_C)_i x_i \right), \quad (2.3)$$

where  $N_C$  is the number of carbon atoms. The fuel flow rate injected into the chamber is then calculated as:

$$\dot{n}_f = \frac{P_{th}}{LHV}, \quad (2.4)$$

where  $P_{th}$  is the required thermal power and LHV is the low calorific value, calculating applying the Hess' law to the chemical reaction in Eq. 2.1 considering water in gaseous state (thereby its standard enthalpy of formation too). On the other hand, combustion air flow rate becomes:

$$\dot{n}_{air} = \dot{n}_f \left( m(1 + f)(1 + E) \right), \quad (2.5)$$

where  $m(1 + f)$  is the stoichiometric coefficient for air. Finally, the equivalence ratio  $\phi$  can be defined as:

$$\phi = \frac{\dot{n}_f / \dot{n}_{air}}{(\dot{n}_f / \dot{n}_{air})_{st}}. \quad (2.6)$$

Following Figure 2.6, a global energy balance of the flameless furnace can be set as:



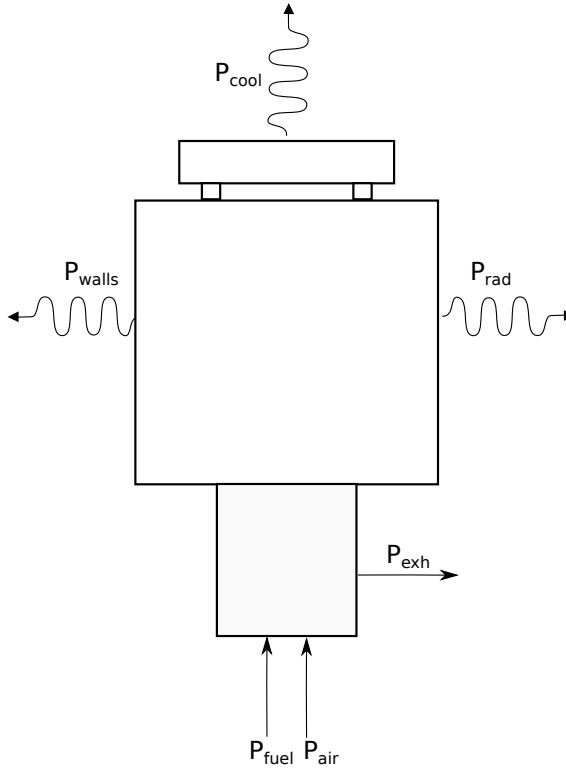


**Figure 2.6:** Sketch of the system considered to evaluate the global energy balance of the furnace.

$$P_{th} + P_{fuel} + P_{air} = P_{cool} + P_{walls} + P_{rad} + P_{exh} + \Delta P, \quad (2.7)$$

where  $P_{th}$  is the power generated by combustion,  $P_{fuel}$  and  $P_{air}$  are the sensible heat of fuel and combustion air (usually negligible). On the right-hand side of Eq. 2.7,  $P_{cool}$  is the power transferred to the cooling system,  $P_{walls}$  are the losses through the walls,  $P_{rad}$  is the radiative power transmitted through the window,  $P_{exh}$  is the enthalpy associated with the exhaust gases, while  $\Delta P$  considers the losses not taken into account to satisfy the balance. Each sensible power ( $P_{cool}$  and  $P_{exh}$ ) can be determined by the generic equation:

$$P_i = \dot{n}_i \int_{T_1}^{T_2} c_{p,i} dT, \quad (2.8)$$

where  $T_1$  is the cooling air inlet temperature or the reference temperature

( $T_{ref} = 298.15$  K), while  $T_2$  is either the exhaust temperature before the heat exchanger or the cooling air outlet temperature. Finally,  $c_{p,i}$  is the specific heat capacity at constant pressure of the fluid  $i$ . The latter is approximated with a 4th degree polynomial according to the NASA's JANAF tables [107]. The process efficiency of the furnace is evaluated considering the useful heat subtracted by the cooling system and the radiative heat lost through the window <sup>1</sup> as:

$$\eta_p = \frac{(P_{cool} + P_{rad})}{P_{th}}. \quad (2.9)$$

Looking at Figure 2.6, combustion air enters the furnace after being pre-heated through the heat exchanger by the exhaust gases. Considering that the air temperature after the heat exchanger ( $T_{air,out}$ ) can not directly be measured due to hardware limit, one could retrieve it analysing the following energy balance on the heat exchanger (Figure 2.7):

$$\left( \dot{n}_{exh} \int_{T_{exh,out}}^{T_{exh,in}} c_{p,exh} dT \right) \epsilon_{he} = \left( \dot{n}_{air} \int_{T_{air,in}}^{T_{air,out}} c_{p,air} dT \right), \quad (2.10)$$

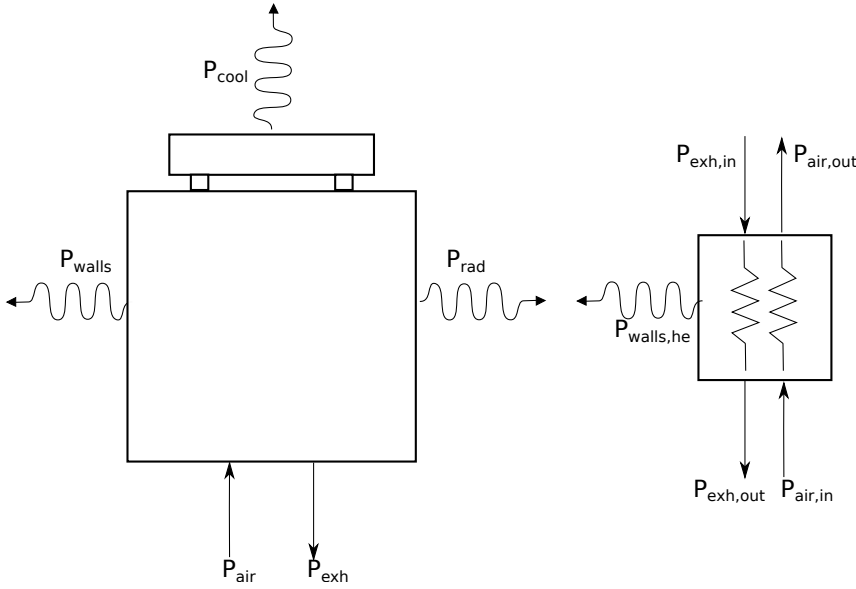
where  $\dot{n}_{exh}$  and  $\dot{n}_{air}$  are the exhaust gases and cooling flow rates, while  $\epsilon_{he}$  is an efficiency accounting for a non adiabatic heat exchanger ( $P_{walls,he}$ ). According to the manufacturer data, the latter can be set as 0.9.

Figure 2.8 shows an idealized sketch to estimate the radiative power transmitted trough the window ( $P_{rad}$ ). The solution of the problems relies on the following assumptions: (1) steady-state conditions, (2) furnace interior and exterior surroundings are large, isothermal surfaces, (3) furnace insulation layers are adiabatic and diffuse-gray with uniform radiosity. The open-end ideal surfaces ( $A_1$  and  $A_2$ ) and the two sides of the insulation (both named as  $A_R$ ) form a diffuse-gray enclosure. The hypothetical areas  $A_1$  and  $A_2$  behave as black surfaces at the respective temperatures of the large surroundings to which they are exposed. Since  $A_R$  is adiabatic, it behaves as a re-radiating surface and its emissivity has no effect on the analysis. The net radiation passing through the window ( $A_2$ ) can be finally written as:

$$P_{rad} = \frac{E_{b1} - E_{b2}}{\frac{1 - \epsilon_1}{\epsilon_1 A_1} + \frac{1}{A_1 F_{12} + [(1/A_1 F_{1R}) + (1/A_2 F_{2R})]^{-1}} + \frac{1 - \epsilon_2}{\epsilon_2 A_2}}, \quad (2.11)$$

---

<sup>1</sup>Indeed, if the window was closed by insulation material, the operator shall increase the cooling heat flux to keep the same operating parameters constant.



**Figure 2.7:** Sketch of the system considered to evaluate the energy balance of the heat exchanger.

where  $F_{ij}$  is the view factor between surfaces  $i$  and  $j$  and  $\epsilon_i$  is the emissivity of the surface  $i$ <sup>2</sup>.  $E_{bi}$  is the black body emissive power  $\sigma T_i^4$ , where  $\sigma = 5.67 \times 10^{-8} \text{ W/m}^2\text{K}^4$ . The view factor  $F_{12}$  can be determined using the relation between aligned parallel rectangles (see Appendix A), while using the summation rule on  $A_1$ , one could find:

$$F_{1R} = 1 - F_{12}, \quad (2.12)$$

and from symmetry of the enclosure  $F_{2R} = F_{1R}$ .

Finally, the energy loss trough the walls ( $P_{walls}$ ) considers the convective and radiative heat exchange as:

$$P_{walls} = A(h_{conv} + h_{rad})(T_{walls} - T_{sur}), \quad (2.13)$$

where  $A$  is the external furnace wall surface,  $T_{walls}$  is the wall temperature,  $T_{sur}$  is the temperature of the surrounding air and  $h_{rad}$  and  $h_{conv}$  are the radiative and convective heat transfer coefficients, respectively. More informations about the estimate of the heat transfer coefficients can be found in Appendix A.

---

<sup>2</sup> $\epsilon_2$  can be assumed equal to 1, being the surrounding

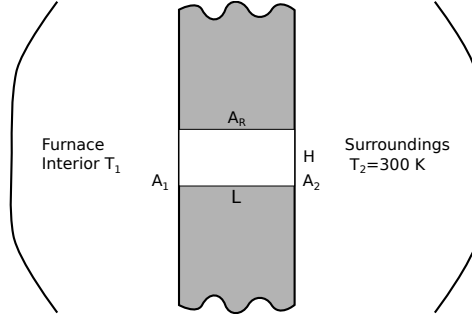


**Figure 2.8:** Idealized problem to quantify the radiative power transmitted tough the window.

## 2.5 Uncertainty quantification

When a physical quantity is measured (called “measurand”), its uncertainty comes out in two ways: (1) from the statistical methods used to analyse it, which is called Type A uncertainty, and (2) from any other method, called Type B uncertainty. Often, but not systematically, Type A uncertainties represent the stochastic behaviour of the measurand (i.e. its repeatability), and Type B uncertainties represent the lack of accuracy of the measurement system. Let consider a physical quantity  $X$  be measured through  $n$  independent repetitions  $x_i$  having for mean value  $\bar{x}$ . If  $n \rightarrow \infty$  then  $\bar{x} \rightarrow \bar{x}_\infty$  and therefore  $\bar{x}$  is our best estimate of  $\bar{x}_\infty$ , with an uncertainty  $u_{\bar{x}}$  being the standard deviation of the mean. For an assumed normal distribution of  $X$  and an infinite sample of measurements, the region  $\bar{x} \pm u_{\bar{x}}$  represents a 68.3% probability that  $\bar{x}_\infty$  falls in between it. This is called Type A uncertainty [108]:

$$u_{typeA} = u_{\bar{x}} = \sqrt{\frac{1}{n(n-1)} \sum_{i=1}^N (x_i - \bar{x})^2}. \quad (2.14)$$

However,  $\bar{x}_\infty$  is not the true value of the physical quantity  $X$ . Indeed, a measurement tool must first be calibrated in all conditions of interest in order to capture a sensible value of a specific physical quantity. Type B uncertainty encompasses linearity, linearisation, repeatability, temperature or pressure drift, reference, and least count (LC) uncertainties (i.e. the smallest variation that can be captured by the measurement tool), all obtained through a calibration process of the sensor or provided by the

manufacturer [109]:

$$u_{typeB} = \sqrt{u_{ref}^2 + u_{LC}^2 + u_{lin}^2 + u_{fit}^2 + u_{drift}^2 + u_{repeat}^2}. \quad (2.15)$$

Concerning manufacturer uncertainties, if no precision is made on the probability level and distribution type, they are conventionally assumed to be of uniform distribution and at a 100% probability level [109]:  $u_{man,X} = \sqrt{3} \cdot u_X$ .

The global uncertainty becomes:

$$u_{global} = \sqrt{u_{typeA}^2 + u_{typeB}^2}, \quad (2.16)$$

Finally, the uncertainty on the measurement of  $X$  with a 95% probability is denoted as  $U_{95,X}$ :

$$U_{95,X} = 1.96 \cdot u_{global}. \quad (2.17)$$

Finally, when a physical quantity is computed from several measurands, there is no concept of Type A or Type B uncertainties, since the variable is not directly measured by a sensor. Let us consider the physical quantity  $Z$  computed from the measurands  $Y_i$ :  $Z=f(Y_1, \dots, Y_n)$ . The uncertainty on  $Z$  will be proportional to the global uncertainty (i.e. Type A and Type B) on  $Y_i$  by the rate of change of  $Z$  with respect to  $Y_i$ . Given that second-order derivative factors can be neglected, and assuming that  $Y_i$  are uncorrelated between them, one obtains the uncertainty on  $Z$  through the first-order Taylor series approximation of  $Z$ :

$$u_Z = \sqrt{\sum_{i=1}^N \left( \frac{\partial f}{\partial Y_i} \right)^2 \cdot u_{Y_i}^2}. \quad (2.18)$$

## Chapter 3

# Fuel flexibility in the ULB furnace

*The aim of this Chapter is to provide further understanding on the behaviour of non-conventional blends, testing  $\text{CH}_4\text{-H}_2$  and  $\text{NH}_3\text{-H}_2$  blends on the ULB flameless burner. Both fuels would allow to reduce the carbon footprint, introducing, however, operative issues, such as very high temperature and NO emissions. First, methane/hydrogen blends are presented, focusing on measures to reduce the maximum temperature and NO emissions, increasing the air injection velocity or the fuel lance length. Second, ammonia/hydrogen blends are analysed, varying the percentage of ammonia up to extinction and the equivalence ratio to define an optimal working window to minimize NO and  $\text{NH}_3$ -slip emissions. Finally a Well Stirred Reactor (WSR) analysis allowed to explain the measured trend, highlighting the most impacting reactions.*

*This chapter is partially based on the following publication:*

**M. Ferrarotti**, W. De Paepe, A. Parente, “Reactive structures and pollutant emissions for methane/hydrogen mixtures in flameless regime”, Combustion&Flames, In preparation.

**M. Ferrarotti**, A. Bertolino, R. Amaduzzi, A. Parente, “On the influence of kinetic uncertainties on the accuracy of numerical modelling of an industrial flameless furnace fired with  $\text{NH}_3/\text{H}_2$  blends: a numerical and experimental study”, Frontiers in Energy Research, Under review.

**Author's contribution to the publications** The author developed the experimental facility and the measurements techniques. He also performed the experimental tests and post-processing for both methane/hydrogen and ammonia/hydrogen cases. He also helped in conceptualizing the idea of WSR for ammonia/hydrogen blends, providing the main operating parameter of the reactor. The kinetic analysis on the WSR was performed by A. Bertolino. The author helped in interpreting the results.

### 3.1 Introduction and literature review

Flameless combustion is a flow controlled combustion technique because it requires internal recirculation of burnt gas in the combustion chamber. The recirculation efficiency is commonly measured by the recirculation ratio  $k_v$  defined as the ratio of recirculated mass flow of combustion products and the mass flow of the injected fresh reactants [9]. The injected fuel and air flows are the driving force for the in-furnace flow field. This involves a complex three-dimensional fluid dynamics pattern, with vortices and recirculation loops. For these reasons, Jet in hot co-flow (JHC) burners (Adelaide JHC [14] or Delft JHC [110], more information in Chapter 5) only reveal part of the important flow and combustion characteristics in a furnace. Indeed, internal flow field is crucial for establishing flameless combustion in a furnace [111, 112]. Therefore, this gap must be bridged with experiments in real burner in lab-scale or quasi-industrial furnaces.

In the last years, detailed measurements have been conducted in a number of test benches operating in flameless combustion, such as at RWTH Aachen [46, 51, 113], University of Adelaide [30], Technical University of Lisbon [88, 114], University of Mons [56, 115], TUDelft [89], Università Federico II di Napoli [57, 61, 116] and at CORIA [55].

Nevertheless, the above mentioned studies focused mostly on conventional fuels, such as natural gas and methane, and only a few used non-conventional fuels, such as biogas [57], blast furnace gas (BFG) [56], methane/hydrogen blends [55] and ammonia [61] (Table 3.1). Furthermore, there are only few comprehensive studies investigating the effect of operating parameters, such as equivalence ratio, injection velocity, loads and thermal power on NO emissions and turbulence/chemistry interactions.

The present work investigates hydrogen and ammonia-enriched flames (methane/hydrogen and ammonia/hydrogen blends) and their combustion performances in terms of pollutant emissions and turbulence/chemistry interactions. Furthermore, the effect of the air injection velocity and recirculation ratio  $k_v$  is also shown as a measure to retrieve flameless combustion conditions going towards a pure hydrogen flame. In-flame temperatures, OH\* and CH\* chemiluminescence and pollutant emissions analysis are employed.

The remainder of this chapter is organised as follows. The methane/hydrogen campaigns are described in Section 3.2, focusing on the effect of the air



**Table 3.1:** A summary of the fuels used in the main working groups operating in flameless.

Group	Power [kW]	Fuel
Aachen	5-10	Methane
Adelaide	7.5-20	Natural gas
Lisbon	6-13	Methane
Mons	30	Methane, BFG
Naples	0.1-10	Methane, propane biogas, ammonia
CORIA	20	Methane/hydrogen
TUDeft	9	Natural gas

injection diameter and the fuel lance length. Section 3.3 is devoted to pollutant emissions in ammonia/hydrogen blends. Finally, Section 3.3.2 wants to explain the measured trends of Section 3.3 using a Well Stirred Reactor (WSR) network.

## 3.2 Methane/Hydrogen blends

The goal of this section is to test the performances of the ULB flameless furnace for progressively decarbonated fuel blends, ranging from pure methane to pure hydrogen. Furthermore, the study investigates different techniques to mitigate the higher temperature and pollutant emissions due to the introduction of hydrogen in the fuel. Following Table 3.2, different air injectors sizes (Air ID), equivalence ratio ( $\phi$ ), fuel lance extra length (L) and nitrogen dilution (D) were tested and evaluated. An input thermal power of 15 kW was chosen considering multiple aspects. The first is to remain within safe operating temperatures for the furnace components, considering in particular the junctions between furnace insulation, metallic structure and quartz window. The second is to prevent the main reaction zone from positioning itself too close to the top wall of the furnace, where the optical access is limited. The cooling power subtracted via the air cooling system was set to 5.1 kW to ensure an exhaust gases temperature of

around 950 °C before the heat exchanger<sup>1</sup>.

Test	$P_{th}$ [kW]	$P_{cool}$ [kW]	$\phi$ [-]	H <sub>2</sub> [%vol]	Air ID [mm]	L [mm]	D [%]
T1	15	5.1	0.8	0-100	25	0	0
T2	15	5.1	0.8	0-100	20	0	0
T3	15	5.1	0.8	0-100	16	0	0
T4	15	5.1	0.7-1	50	16	0	0
T5	15	5.1	0.8	0-100	16	25	0
T6	15	5.1	0.8	0-100	16	50	0
T7	15	5.1	0.8	100	16	25	0-50

**Table 3.2:** Operating conditions of the experimental tests on the CH<sub>4</sub>- H<sub>2</sub> mixtures.

Experiments were performed at steady-state conditions, after a warming period of about 3 h, during which the same burner was used in normal flame conditions, acting on the fluid dynamic of the injection. In the following, "MxHy" term represents the operating conditions where the fuel is a mixture of x % (vol.) of CH<sub>4</sub> and y % (vol.) of H<sub>2</sub>.

### 3.2.1 Settings and processing method

The suction pyrometer (shown in Chapter 2) was used to extract in-flame temperature at different vertical positions, among the set of twelve equally spaced (50 mm distant) ports (Figure 2.1). Indeed, the aim was to have a finer spatial resolution in the high gradient region of the furnace. The differential voltage signal was continuously sampled at 10 Hz and automatically converted to temperature units with a National Instrument cold-junction compensated acquisition card. The acquisition time was set to 40 s and an averaged value was then calculated.

Thanks to a movable support system, chemiluminescence images were taken at the height of the reaction region<sup>2</sup> due to the limited size of the field of view of the camera. Considering the size of the window (1100×450 mm), the accessible area on the symmetry plane of the furnace goes from 40 mm to 500 mm from the burner exit<sup>3</sup>. A series of  $N_f$  frames was taken at a global acquisition frequency of 17 Hz. The images post-processing includes:

<sup>1</sup>For the case 50/50 CH<sub>4</sub>/H<sub>2</sub>  $\phi=0.8$

<sup>2</sup>which changes case by case

<sup>3</sup>furnace total height of 700 mm

- noise subtraction. A background image was taken with the flame extinguished and hot walls for both OH\* and CH\*. Afterwards, it was subtracted from the raw images to remove the wall radiation interferences;
- average of the  $N_f$  frames;
- an Abel inversion [117], based on the symmetrized and smoothed image, was used for data transformation from the line-of-sight-integrated image of chemiluminescence emissions to radial distributions. The smoothing was performed with a 20-pixel filter.

A preliminary analysis focused on determining the number of frames  $N_f$  needed to have a statistically converged average, considering M75H25. Figure 3.1 compares different  $N_f$  values, i.e. 10, 100, 150, 300. It clearly states that 150 frames are enough to reach statistical convergence and, therefore, this value was used for the entire analysis. Secondly, Figure 3.2 shows the post-processing sequence, comparing selected different frames ((a)-(f)), among the 150, along with averaged and Abel-inverted distributions. Considering flameless combustion is characterized by a weak chemiluminescence signal, the camera maximum exposure time (80 ms) was considered. The selected frames ((a)-(f)) show a sequence of ignition-extinction processes for a flameless combustion case. Indeed, the reactive region is not a unique and smooth surface, but it is formed by different auto-ignition kernels. This is in line with the work of Huang [89], who investigated methane flameless combustion with high frequency OH\*. According to his results, three types of autoignition events can be identified: individual autoignition kernel, which is formed and convected downstream and might or not lead to an intense zone; multiple autoignition kernels, which appear in a region at nearly the same time. Finally, both the individual and multiple autoignition kernels can develop into an autoignition kernel cluster [89]. Looking at Figure 3.2 (g)-(h), it also appears that the major effect of the Abel-inversion is the symmetrisation of the profile. This might be either a consequence of a narrow depth of field or the fact that combustion is happening on the axial plane. Differences might be noticed if the reaction zone was detected on the recirculation loop induced by the top wall. In light of these considerations, Abel-inversion will not be considered hereafter.

Pollutant emissions were sampled at 1 Hz and averaged considering 60 s of acquisition time. After removing the water content measured by the FTIR,

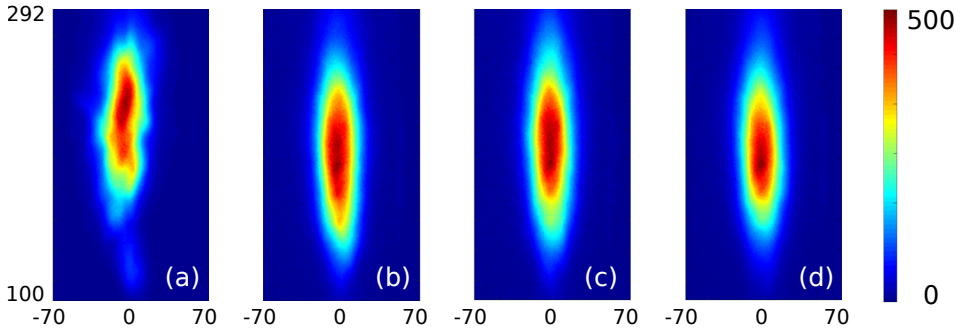


**Figure 3.1:** Averaged  $\text{OH}^*$  distribution based on 10 (a), 100 (b), 150 (c) and 300 (d) frames. Units in mm and counts.

the pollutant emissions were normalized at 3% of  $\text{O}_2$  as normal practise for a gas fired process.

### 3.2.2 Main features of flameless combustion of $\text{CH}_4\text{-H}_2$ mixtures with air injector ID25

The first experimental campaign was aimed at analysing the performances of the burner using a standard air-injector dimension, ID 25 mm (hereafter called ID25), once varying the percentage of hydrogen in the blend (Case T1 of Table 3.2). The equivalence ratio was set to 0.8. The main operating conditions are summarized in Table 3.3. It appears clear the higher the hydrogen content (in molar basis) the lower the LHV and therefore the higher the needed flow rate and the injection velocity. The behaviour is not linear, therefore passing from 50% to 75%  $\text{H}_2$  would imply a bigger increment in terms of fuel flow rate and velocity respect the case from 0 to 25%. On the other hand, the required air flow rate decreases incrementing the hydrogen content, in accordance with the stoichiometry of the reaction.

The furnace was preheated in “flame” mode using a partially premixed combustion until reaching the self-ignition temperature even in the lower corners. At that point, the fuel was delivered through the coaxial injection, activating the “flameless” mode. Figure 3.3 shows a comparison between the two modes in terms of photographs taken with a Canon EOS 80D 1/70 s exposure time and NO emissions for M100H0. It appears clear how the flame is visible and attached in the first case, while reactions occur away

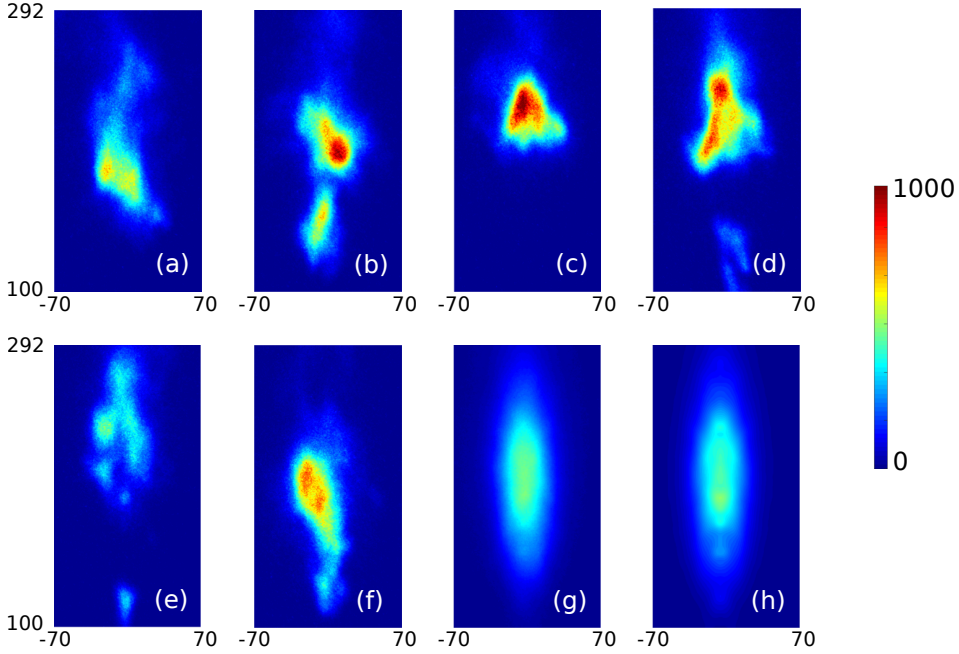


**Figure 3.2:** (a)-(b)-(c)-(d)-(e)-(f) Instantaneous frames taken at different times, (g) averaged and (h) Abel-inverted OH\* distributions. Units in mm and counts.

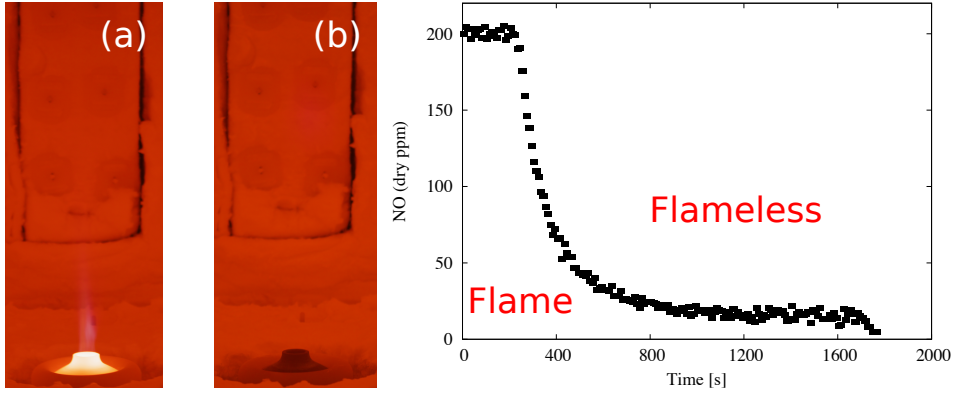
from the burner so that the burner itself becomes relatively cooled, for the second mode. Furthermore, the combustion reaction has a quite diminished visibility that stems from a decrease in the radiation extending up to the ultraviolet range [113]. This is also clear from the NO emission plot. In “flame” mode, NO are high (200 ppm) following essentially the thermal pathway, while they become single digit switching to flameless, which is characterized by smooth temperature gradients, without peaks.

Figure 3.4 shows photographs taken with the same camera, varying the percentage of hydrogen in the fuel (from 100% CH<sub>4</sub> (a) to 100% H<sub>2</sub> (e)). A visible flame structure appears with M75H25 and it is progressively shifted upstream with M50H50 and M25H75. Finally, M0H100 shows its characteristic invisible flame.

Figures 3.5-3.6 offer a comparison in terms of contours and averaged tem-

**Table 3.3:** Main operating parameter for the experimental campaign with the air injector diameter ID 25 mm.  $\phi=0.8$ .

$\%H_2$ [vol]	$\dot{n}_f$ [ $Nm^3/h$ ]	$v_f$ [m/s]	$\dot{n}_{air}$ [ $Nm^3/h$ ]	$v_{air}$ [m/s]
0	1.51	9.86	17.95	44.92
25	1.83	11.95	17.67	44.22
50	2.32	15.15	17.24	43.15
75	3.17	20.72	16.51	41.29
100	5.01	32.72	14.86	37.27

**Figure 3.3:** Photographs of “flame” (a) and “flameless” (b) modes and NO emissions. Canon EOS 80D 1/70 s exposure time.

peratures measured at different spatial location using the suction pyrometers ports, as shown in Figure 2.1. It must be underlined that these ports are equally spaced (each 50 mm) and located in a space between  $z = 100$  and  $z = 600$  mm along the axial direction. This means that a complete mapping of the temperature in the furnace is not possible. Figure 3.7 investigates the position and shape of the reactive region using averaged chemiluminescence  $OH^*$  images. A lift-off distance is also defined by searching along the vertical axis ( $z$ ), the height from the burner exit where 5% of the  $OH^*$  maximum intensity is reached. Figure 3.8 shows the standard deviation ( $\sigma$ ) associated to the  $OH^*$  averaged images of Figure 3.7.

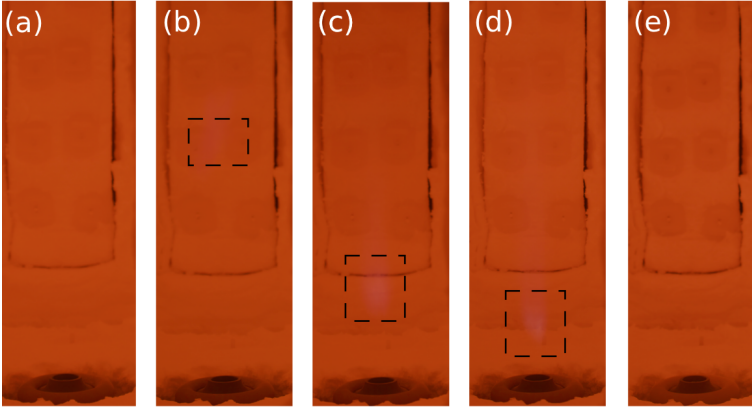


**Figure 3.4:** Photographs of M100H0 (a), M75H25 (b), M50H50 (c), M25H75 (d) and M0H100 (e). The visible reaction zone is highlighted. Canon EOS 80D 1/70 s exposure time. CH<sub>4</sub>-H<sub>2</sub> blends. ID25.

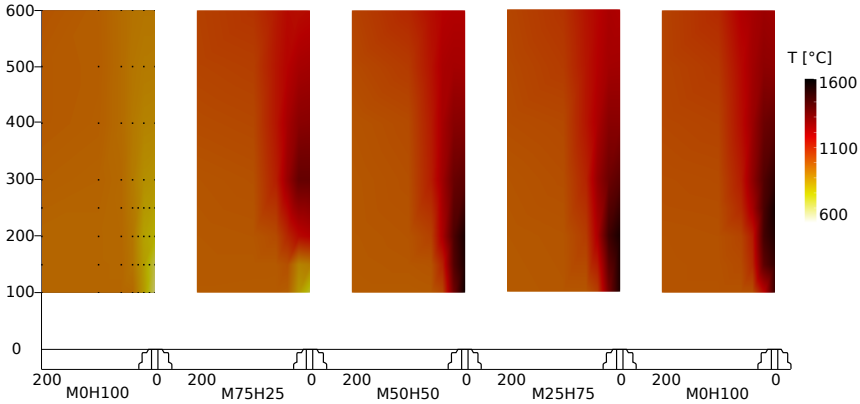


**Figure 3.5:** Contours of temperatures measured at different spatial coordinates (black dots) varying the H<sub>2</sub> percentage. The contours represent only a part of the furnace. Units in mm and °C. Test-case T1.

Finally, the definition of MILD combustion provided by Cavaliere et al. [10] was analysed.

$$T_{max} - T_{in} < T_{si}. \quad (3.1)$$

The original formulation proposed by Cavaliere et al. [10] investigated

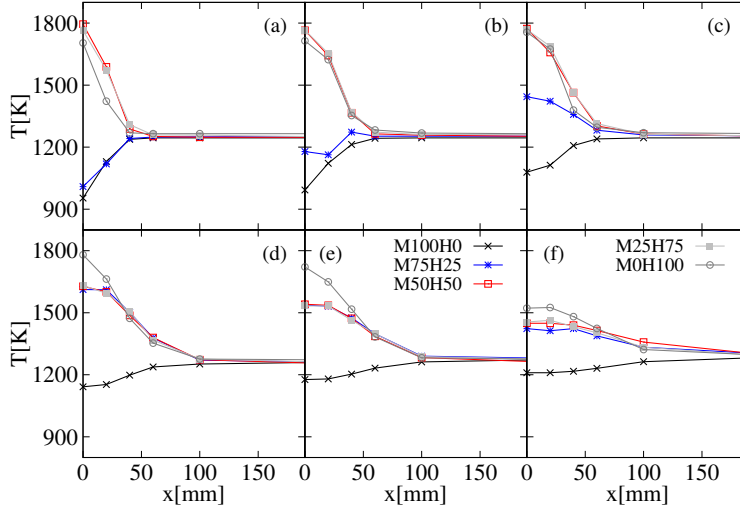


**Figure 3.6:** Averaged temperature measured at (a)  $z=100$  mm, (b)  $z=150$  mm, (c)  $z=200$  mm, (d)  $z=300$  mm, (e)  $z=400$  mm and (f)  $z=600$  mm, varying the  $H_2$  percentage. Averaged experimental uncertainty of 10 K. Test-case T1.

MILD combustion behaviour of a mixture methane/oxygen/nitrogen reacting in a Well Stirred Reactor. For the authors,  $T_{max}$  was the maximum temperature of the system and  $T_{in}$  was the inlet temperature of the reactant mixture to the WSR. Applying this formula to the ULB furnace is not easy, since  $T_{in}$  might be either considered as the air inlet temperature ( $T_{air}$ ) or the reactants temperature once mixed with the recirculating exhausts ( $T_{mix}$ ).  $T_{air}$  is not measured directly, but calculating considering an energy balance on the heat exchanger. On the other side,  $T_{mix}$  is difficult to be evaluated, since it needs the support of CFD simulations to determine the recirculation degree  $k_v$ . In details, the latter was estimated considering the following relation:

$$k_v = \frac{\dot{m}_{rec}}{\dot{m}_a + \dot{m}_f} = \frac{\dot{m}_{mix} - (\dot{m}_a + \dot{m}_f)}{\dot{m}_a + \dot{m}_f}, \quad (3.2)$$

where  $\dot{m}_{mix}$  is the flow rate of the reactants mixed with exhaust gases. This flow rate was calculated as follows. First, the reactive region was identified observing the contour of the species OH and three planes were defined at different axial locations within said region. Second, the flow rate passing



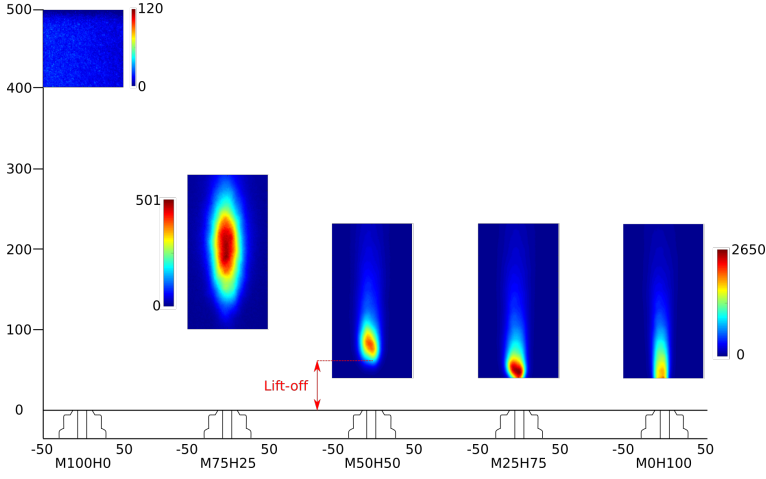


**Figure 3.7:** Averaged  $\text{OH}^*$  distribution varying the  $\text{H}_2$  percentage. The flame lift-off is highlighted. Units in mm and counts. Test-case T1.

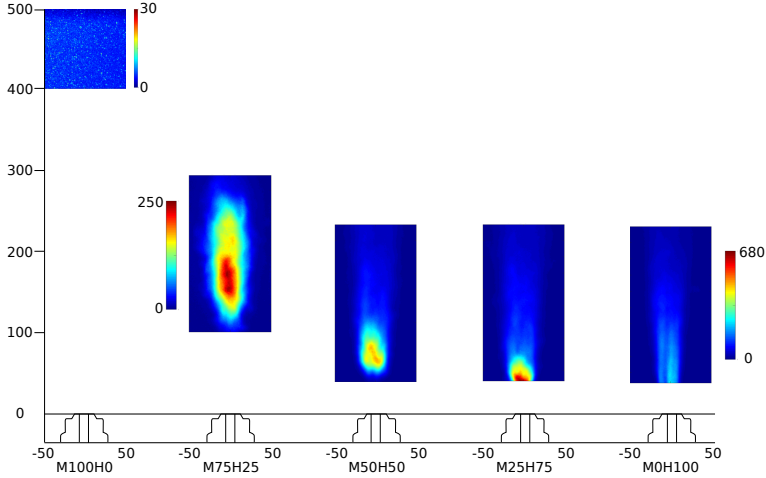


**Figure 3.8:** Standard deviation distribution for  $\text{OH}^*$  varying the  $\text{H}_2$  percentage. Units in mm and counts. Test-case T1.

through a clip of positive velocity (towards the top wall) along these planes was then calculated.  $\dot{m}_{mix}$  was defined as the average between the resulting three values. Once  $k_v$  was known (Table 3.4),  $T_{mix}$  was determined considering an ideal mixing between air, fuel and recirculating exhausts.

Both the approaches were evaluated and reported in Table 3.5. The mixture self-ignition temperature  $T_{si}$  was evaluated following Olchewsky et al. [118]. It must be pointed out that this analysis can be performed only for cases where the reaction zone is located above the first measurement point ( $z > 100$  mm), otherwise the maximum measured temperature might not correspond to the maximum temperature of the system, falsifying the evaluation.

**Table 3.4:** Recirculation ratio  $k_v$  estimated using CFD simulations, varying the hydrogen content. Test-case T1.

	M100H0	M75H25	M50H50	M25H75	M0H100
$k_v$	13	8	7	6	4

The pure methane (M100H0) case shows a very smooth temperature distribution (Figure 3.5) with temperature peak not exceeding 1300 K (Figure 3.6) and a reactive region (Figure 3.7) shifted downstream and most probably attached to the top wall. Indeed, the OH\* signal is not visible in the investigated region ( $z \leq 500$  mm). This case represents an ideal flameless configuration, since no flame is visible and it can be classified as MILD for both definitions (Table 3.5). Indeed, although the maximum temperature might be located above 600 mm, it is safe to consider that it does not go beyond the threshold ( $T_{si} + T_{in}$ ). Furthermore, it is cautionary to consider it lower than the one of M25H75. M0H100 presents an high ignition delay time with a minimum lift-off of 500 mm. Chemistry plays a major role, since combustion becomes chemically controlled ( $\tau_c \gg \tau_{mix}$ ).

Hydrogen has a much higher adiabatic temperature, reactivity, mass and thermal diffusivity compared to methane. Indeed, a progressive addition of hydrogen in methane induces an exponential increase of laminar burning velocity [119] and a more robust sensitivity of turbulent flames to stretch rate [120]. Addition of hydrogen to methane has already proven to be a convenient way to enhance combustion features. This is true in standard non-diluted conditions, for example when adding up to 20% of  $H_2$  in a swirl burner [121], as well as in mild flameless conditions, where the combustion stability and limits of dilution are widened [53] and heat release can be intensified. These properties are a key aspect to understand the transition from pure methane to pure hydrogen. Indeed, the fuel blend

increases progressively its reactivity and the ignition delay time is reduced, as well as the lift-off and eventually losing the flameless/MILD behaviour of the furnace. This is in line with previous studies [56][55]. Indeed, visible structures appear at M75H25 and become progressively more intense and shifted upstream. The OH\* contour for M75H25 (Figure 3.7) occupies a large fraction of the furnace, becoming more localised and intense towards pure hydrogen. The OH\* standard deviation peak (Figure 3.8) is the half of the one on the averaged image. This can be explained looking at the instantaneous images of Figure 3.2, which fluctuate in a space between 100 and 292 mm. The flame lift-off passes from 120 mm (M75H25) to 50 mm (M50H50) and less than 40 mm (M25H75), as shown in Figure 3.7. This can be quantitatively confirmed by the maximum measured temperature of 1612 K at  $z = 200$  mm for M75H25, corresponding to the maximum OH\* intensity, 1795 K at  $z = 100$  mm for M50H50 and 1776 K for M25H75 (Figures 3.5-3.6). For the latter, the authors expect it not to be the real maximum temperature, since the maximum OH\* distribution is located at  $z = 40$  mm. It appears clear, since the flame lift-off decreases, that the entrainment of exhaust gases at the locations where reactions begin is smaller. Then, combustion occurs in less diluted environment. This can be quantitatively confirmed by the recirculation ratio  $k_v$  reported in Table 3.4. Here, a difference classifying the cases as MILD arises, considering the air or the mixed gases temperature as inlet temperature of the ideal WSR. Indeed, in the second case, M50H50 case can be classified as MILD (Table 3.5). However, there are discrepancies between the presence of a visible flame structure region (basis of the flameless definition) starting at M75H25 with the MILD requirement.

The pure hydrogen flame appears attached to the burner exit, indeed OH\* is partially visible (Figure 3.7) and it is characterized by a wider high temperature zone ( $T \geq 1700$  K up to  $z = 400$  mm). This might also due to the higher impulse of the fuel jet due to the high flow rate needed to keep the thermal input power constant. This determines two concurrent jets (air and fuel) and a higher penetration of the fuel along the axis implying a more elongated reaction zone. The maximum temperature is well below the first measurement point, therefore the MILD criteria can not be evaluated. The flame lift-off can be assumed as negligible and the flame becomes mixing controlled, i.e. once the reactants are mixed they burn ( $\tau_c \ll \tau_{mix}$ ).

Figure 3.9 compares the CO<sub>2</sub> and NO emissions varying the hydrogen percentage. Both are on dry basis, while NO emissions were normalized at 3% O<sub>2</sub>. The decrease of CO<sub>2</sub> emissions is more pronounced for large H<sub>2</sub> content.

**Table 3.5:** Classification of the cases as MILD combustion, according to the two different estimations of  $T_{in}$ .  $T_{max}$  refers to the maximum measured temperature. Test-case T1.

$\%H_2[\text{mol}]$	$T_{air,in}[\text{K}]^1$	$T_{mix}[\text{K}]$	$T_{max}[\text{K}]$	$T_{si}[\text{K}]$	MILD <sup>2</sup>	MILD <sup>3</sup>
0	908	1197	1284	885	✓	✓
25	909	1185	1612	866	✓	✓
50	920	1180	1795	840		✓
75	922	1145	1776	830	NA	NA
100	973	1137	1780	824	NA	NA

<sup>1</sup>  $U_{95,T_{air}} \approx 30 \text{ K}$ .

<sup>2</sup>  $T_{in}=T_{air}$ .

<sup>3</sup>  $T_{in}=T_{mix}$ .

On the other hand, pollutant emissions follow the discussion about temperature. Indeed, below M90H10 the system shows single digit emissions. The increment of hydrogen content has a primordial role of enhancing the NNH pathway as well as the thermal route, which both start to become relevant at M50H50 ( $\approx 1800 \text{ K}$ ).

A global energy balance is reported in Table 3.6 to analyse the performances of the furnace, as well as the relative uncertainties. The heat leaving the furnace through the walls ( $P_{walls}$ ) was estimated after measuring the wall temperatures and taking into account radiation and natural convection on the vertical and horizontal walls ( $\approx 27\%$  of the overall energy). The energy loss through the window ( $P_{rad}$ ) ( $\approx 18\%$ ) was calculated considering the radiative energy emitted from the insulation walls leaving the window. The last two components suffers from the biggest uncertainties due to the dependence on the fourth power of temperature. The amount of energy recovered by the air-cooled tubes ( $P_{cool}$ ) was calculated using the measured temperature and mass flow rate of the air entering and leaving the tubes; this energy output accounts for 34% of the losses. Considering the sum of cooling and radiative losses through the window, the process efficiency reaches values of 54% (pure methane) and 57% (M50H50). The power lost through the exhaust gases ( $P_{exh}$ ) decreases increasing the hydrogen

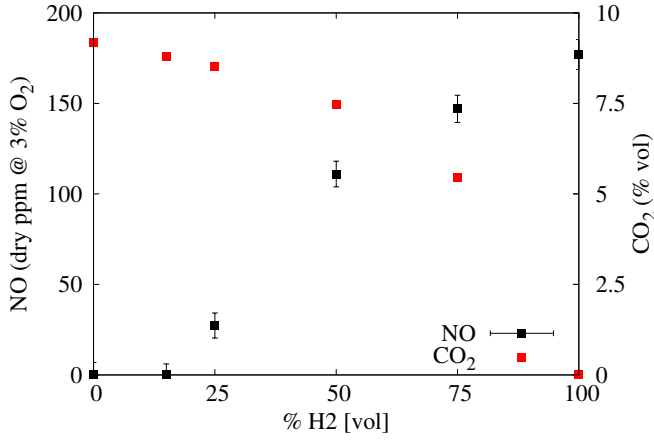


**Figure 3.9:** NO and CO<sub>2</sub> emissions varying the H<sub>2</sub> percentage. CH<sub>4</sub>-H<sub>2</sub> blends. ID25.

content in the fuel in the face of a reduced air mass flow.  $\Delta P$  accounts for the energy loss not considered in the other terms. Sensible heat of air and fuel are neglected. A further study to quantify the uncertainty related to these variables is proposed in Appendix B.

**Table 3.6:** Furnace energy balance for the investigated cases. Test-case T1.

Power [kW]	M100H0	M50H50	M0H100
$P_{th}$	15.00	15.00	15.00
$P_{cool}$	5.10	5.10	5.10
$P_{walls}$	4.11	4.13	4.14
$P_{rad}$	2.79	2.91	2.91
$P_{exh}$	3.00	2.86	2.52
$\Delta P$	0.0	0.0	0.33

**OH\* vs CH\***

Chemiluminescence is the spontaneous electromagnetic radiation that is produced when chemically created excited states return to a lower energy state. In the past years, many studies focused in understanding the important reactions governing this phenomenon. A general mechanism foresees a formation and a release of energy via either collisional quenching with other molecules or spontaneous radiative transition to the ground state. In combustion of hydrocarbon fuels, OH\* formation is mainly provided by reaction with CH, while in pure hydrogen flame it is due to third body reaction with radicals O and H. For CH\*, the formation is due to C<sub>2</sub> and C<sub>2</sub>H (Table 3.7).

**Table 3.7:** Formation (F), quenching (Q) and release (R) reactions for OH\* and CH\*. Only a part of the quenching reactions is reported.

Type	OH* Reactions	CH* Reactions
F	$\text{CH} + \text{O}_2 \rightleftharpoons \text{OH}^* + \text{CO}$	$\text{C}_2 + \text{OH} \rightleftharpoons \text{CH}^* + \text{CO}$
F	$\text{H} + \text{O} + \text{M} \rightleftharpoons \text{OH}^* + \text{M}$	$\text{C}_2\text{H} + \text{O} \rightleftharpoons \text{CH}^* + \text{CO}$
Q	$\text{OH}^* + \text{H}_2\text{O} \rightarrow \text{OH} + \text{H}_2\text{O}$	$\text{CH}^* + \text{H}_2\text{O} \rightarrow \text{CH} + \text{H}_2\text{O}$
Q	$\text{OH}^* + \text{CO}_2 \rightarrow \text{OH} + \text{CO}_2$	$\text{CH}^* + \text{CO}_2 \rightarrow \text{CH} + \text{CO}_2$
Q	$\text{OH}^* + \text{CO} \rightarrow \text{OH} + \text{CO}$	$\text{CH}^* + \text{CO} \rightarrow \text{CH} + \text{CO}$
R	$\text{OH}^* \rightarrow \text{OH} + h\nu$	$\text{CH}^* \rightarrow \text{CH} + h\nu$

Figure 3.10 shows the averaged CH\* distribution varying the H<sub>2</sub> percentage. The position and shape are similar to those of OH\*. However, the maximum number of counts is achieved for M50H50, since the formation of CH\* involves the radicals C<sub>2</sub> or C<sub>2</sub>H and local rich conditions. A relevant noise level was recorded for M100H0, where the reaction zone is not visible, although the noise coming from the wall was already subtracted. Figure 3.11 quantifies the standard deviation ( $\sigma$ ) associated with the averaged images

of Figure 3.10. The same considerations made for  $\text{OH}^*$  (Figure 3.8) are still valid, even if, here, the relative impact of  $\sigma$  is much higher.

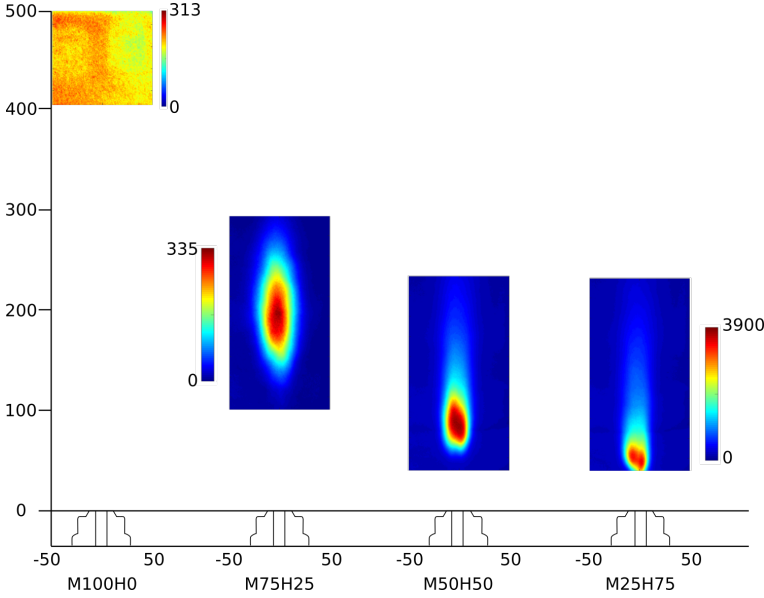


**Figure 3.10:** Averaged  $\text{CH}^*$  distribution varying the  $\text{H}_2$  percentage. Units in mm and counts.  $\text{CH}_4\text{-H}_2$  blends. ID25.

### 3.2.3 Main features of flameless combustion of $\text{CH}_4\text{-H}_2$ mixtures varying the air injector ID

The aim of the second experimental campaign (Test-cases T2-T3 of Table 3.2) was to reduce the temperature peaks and pollutant emissions, retrieving flameless conditions for fuels with high hydrogen content (above 25%). Since hydrogen has high diffusivity and it increases the reactivity of the mixture, the first technique consisted in enhancing the mixing with the exhaust gases (i.e. increasing the recirculation ratio), as well as reducing the residence time of the mixture within the reactive region. To achieve this aim, two different air injector diameters were employed: ID20 and ID16. The first effect was to increase the injection velocity, as shown in Table 3.8. The maximum velocity was achieved with pure methane with ID16, 202 m/s reaching  $\text{Ma} \approx 0.22$ . Table 3.9 shows the important incre-

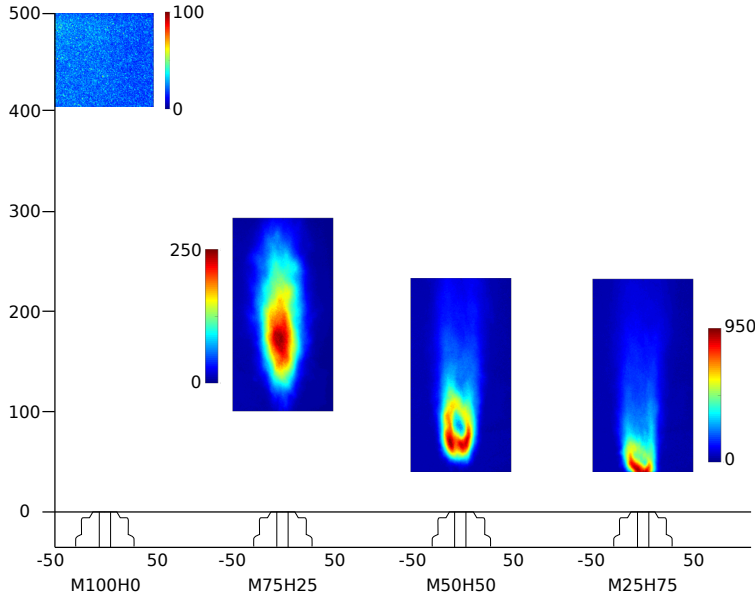


**Figure 3.11:** Standard deviation distribution for  $\text{CH}^*$  varying the  $\text{H}_2$  percentage. Units in mm and counts.  $\text{CH}_4$ - $\text{H}_2$  blends. ID25.

ment of the recirculation ratio  $k_v$  using ID16 at the place of ID25. This is more evident for low hydrogen content, while the discrepancy between the two values becomes null for pure hydrogen, underlying how combustion happens in a region very attached to the burner exit and the entrainment of hot combustion products is much smaller.

Focusing on Figures 3.12-3.13, which compare photographs and contours of temperature for the three injectors for M50H50, the beneficial effect of the increased mixing on the performance of the burner is clear. Indeed, the visible reaction region is progressively shifted downstream and it almost vanishes for ID16, becoming truly “flameless”.

This aspect can be quantitatively confirmed looking at the temperatures and  $\text{OH}^*$  distribution for ID20 (Figures 3.14-3.15) and for ID16 (Figures 3.16-3.17). M75H25 appears to be completely flameless, characterized by smooth temperature profiles and an  $\text{OH}^*$  region wide and positioned above 300 mm, already with ID20. Once ID16 is employed, the temperature peak at M50H50 is lowered from about 1800 K to 1680 K and the  $\text{OH}^*$  region is shifted from 80 mm to 200 mm from the burner exit, corresponding to the maximum temperature point. M25H75 and M0H100 cases



still preserve a very high temperature (1800 K) also with ID16, even if the flame lift-off becomes slightly bigger, i.e. 80 mm (M25H75) and 40 mm (M0H100). In light of that, assuming a direct correspondence between the maximum temperature and maximum OH\*, the usage of ID16 allows to measure the actual maximum temperature for M25H75, but still not for pure hydrogen. The OH\* distributions for ID16 (Figure 3.17) appear not to be perfectly symmetric. However, it must be considered that the gap between air and fuel nozzles is very narrow (2 mm). This means that an alignment tolerance between the two nozzles might implies a deviation respect to the burner axis, which is amplified by the high air momentum.

**Table 3.8:** Air injection velocity varying the air injector ID. Test-cases T1-T2-T3.

Case	$v_{air,25}$ [m/s]	$v_{air,20}$ [m/s]	$v_{air,16}$ [m/s]
M100H0	44.92	88.04	202.06
M75H25	44.22	87.03	198.92
M50H50	43.15	84.91	194.09
M25H75	41.29	81.25	185.72
M0H100	37.27	73.34	167.65

**Table 3.9:** Recirculation ratio  $k_v$  estimated using CFD simulations for air injection diameter ID25 and ID16, varying the hydrogen content. Test-cases T1-T3.

ID [mm]	M100H0	M75H25	M50H50	M25H75	M0H100
25	13	8	7	6	4
16	28	25	18	14	4

The MILD classification, reported in Table 3.10, follows the two possible definitions of  $T_{in}$  defined above. Only M50H50 with ID16 can be considered MILD for both formulations, being its maximum measured temperature 1680 K. Once again, there is not direct correspondence between MILD and

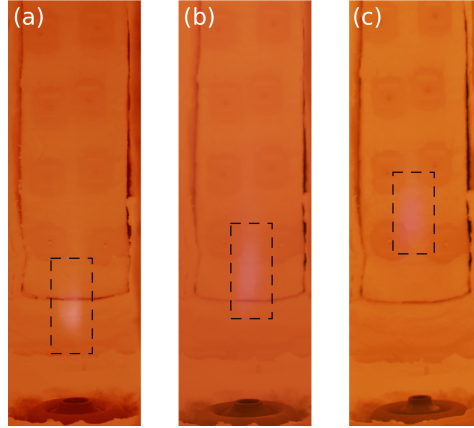


**Figure 3.12:** Photographs of M50H50 for air injector ID25 (a), ID20 (b) and ID16 (c). The visible reaction zone is highlighted. Canon EOS 80D 1/70 s exposure time. Test-cases T1-T2-T3.

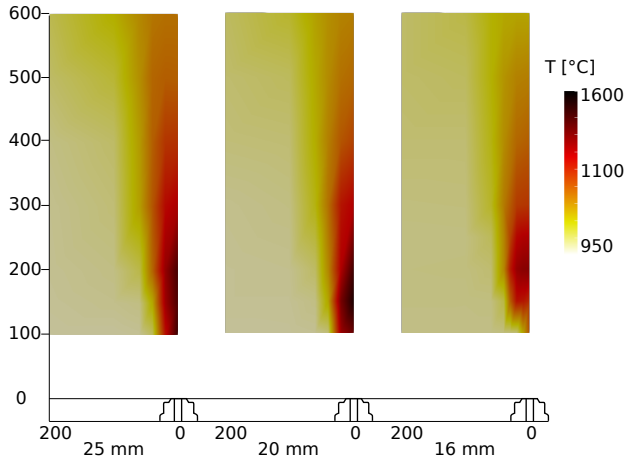


**Figure 3.13:** Contours of temperature measured at different spatial coordinates for M50H50 and ID25, ID20, ID16. The contours represent only a part of the furnace. Units in mm and  $^{\circ}\text{C}$ . Test-cases T1-T2-T3.

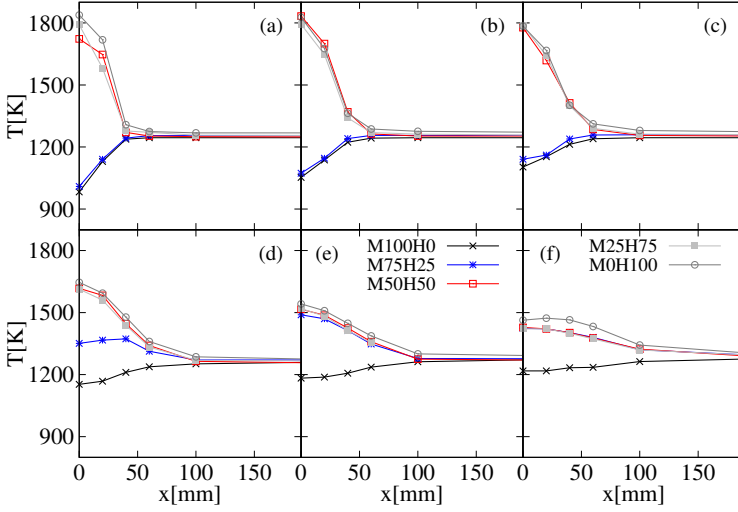


**Figure 3.14:** Averaged temperature measured at (a)  $z=100$  mm, (b)  $z=150$  mm, (c)  $z=200$  mm, (d)  $z=300$  mm, (e)  $z=400$  mm and (f)  $z=600$  mm for ID20, varying the  $H_2$  percentage. Averaged experimental uncertainty of 10 K. Test-case T2.

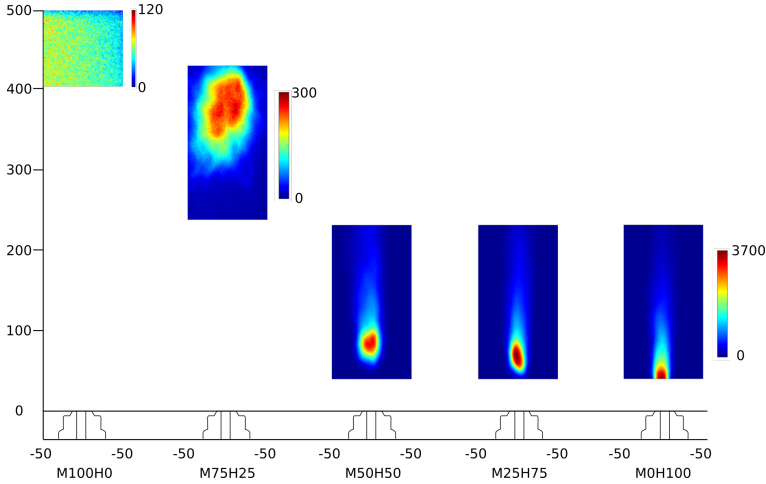


**Figure 3.15:** Averaged  $OH^*$  distribution for ID20, varying the  $H_2$  percentage. Units in mm and counts. Test-case T2.

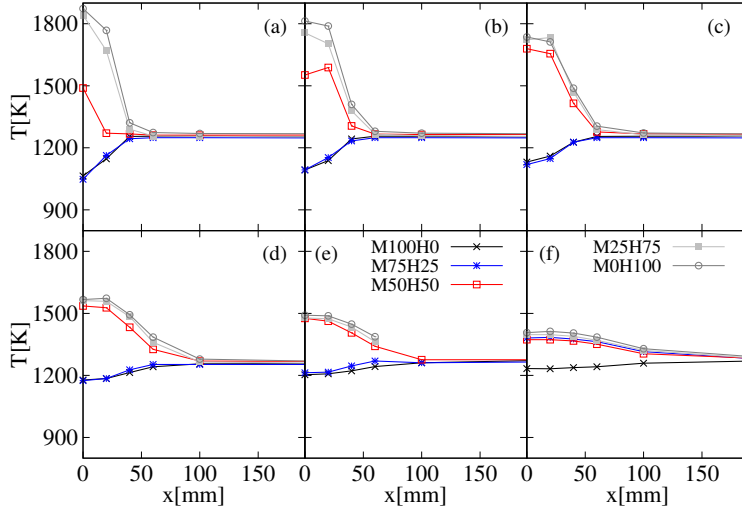


**Figure 3.16:** Averaged temperature measured at (a)  $z=100$  mm, (b)  $z=150$  mm, (c)  $z=200$  mm, (d)  $z=300$  mm, (e)  $z=400$  mm and (f)  $z=600$  mm for ID16, varying the  $H_2$  percentage. Averaged experimental uncertainty of 10 K. Test-case T3.

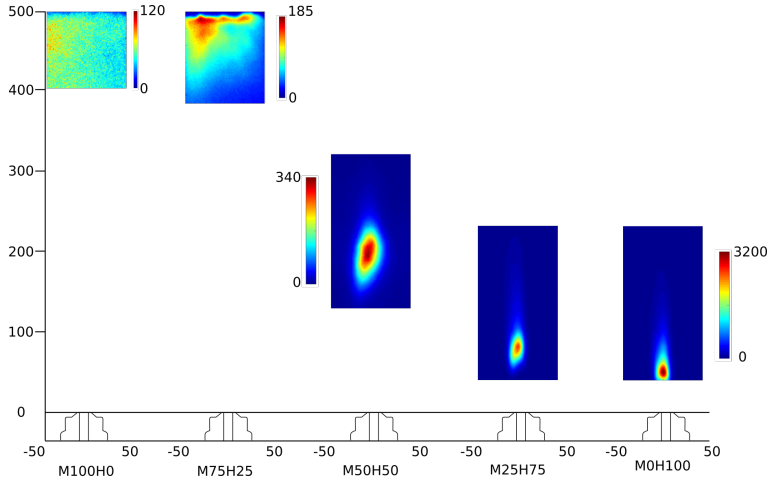


**Figure 3.17:** Averaged  $OH^*$  distribution for ID16, varying the  $H_2$  percentage. Units in mm and counts. Test-case T3.

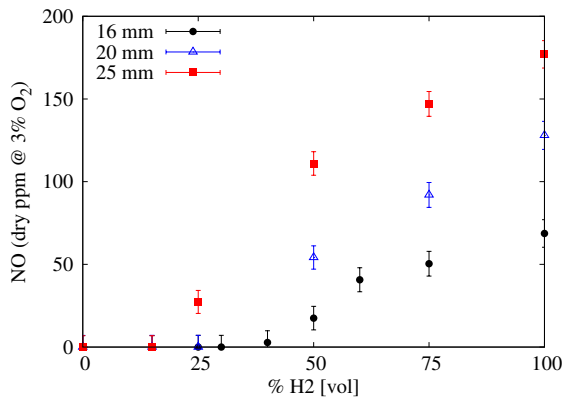


**Figure 3.18:** NO emissions varying the  $H_2$  percentage and the ID air injector. Test-cases T1-T2-T3.

**Table 3.10:** Classification of the cases as MILD combustion, varying the hydrogen content and the air injector ID.

%H <sub>2</sub> [mol]	ID25 <sup>1</sup>	ID25 <sup>2</sup>	ID20 <sup>1</sup>	ID20 <sup>2</sup>	ID16 <sup>1</sup>	ID16 <sup>2</sup>
0	✓	✓	✓	✓	✓	✓
25	✓	✓	✓	✓	✓	✓
50		✓		✓	✓	✓
75	NA	NA	NA	NA	NA	NA
100	NA	NA	NA	NA	NA	NA

<sup>1</sup>  $T_{in}=T_{air}$ .

<sup>2</sup>  $T_{in}=T_{mix}$ .

flameless, since this particular case shows still a slightly visible reactive structure Figure 3.12c. The highest hydrogen content cases still present a maximum temperature below the first measurement point, therefore it was not possible to apply such a criteria.

The NO emissions distribution of Figure 3.18 follows the consideration drawn so far. Indeed, the temperature reduction, achieved increasing the recirculation degree, lowers the thermal pathway, leaving NNH and possibly  $N_2O$  as dominant source of NO. In particular, ID20 and ID16 decrease NO emission by 51% (55 ppm) and 84% (18 ppm), respectively compared with ID25 (111 ppm) for M50H50. A correlation, already partially seen for ID25 (Figure 3.9), can be established between NO emissions and the achievement of flameless conditions. Indeed, when NO is below a certain threshold (i.e. 10 ppm), no visible flame structures were noticed. M50H50 confirms this trend, having 18 ppm and a slightly visible reaction region Figure 3.12.

A further study (Test-case T4), varying the equivalence ratio for an equimolar case (M50H50) is presented in Appendix D.

### 3.2.4 Main features of flameless combustion of $CH_4$ - $H_2$ mixtures varying the fuel lance length

Additional experimental campaigns (Test-cases T5-T6) aimed at further reducing the temperature peak and pollutant emissions for the highest hydrogen contents (above 50%) were carried out using a longer fuel injection lance. Indeed, differently from previous tests, the fuel lance was immersed inside the furnace for a total distance of 25 mm (L25) or 50 mm (L50) respect to the air injector (ID16), as shown in Figure 3.19. Being the fuel injected further downstream in the furnace, it guarantees more time to the air stream to be diluted by the exhaust gases, thus increasing the recirculation degree  $k_v$  from 18 to 20 (L25) and 21 (L50) for M50H50. As a result, the fuel mixture will encounter an oxidizer having a much lower oxygen content. This is quantitatively confirmed by CFD simulations (for details see Chapter 6), comparing the oxygen mass fraction profiles (Figure 3.20) extracted at a relative distance ( $z+ = z - L$ ) of 50 mm and 100 mm from the fuel lance, for four different lance lengths (0, 10, 25, 50 mm).

Figure 3.21 shows the measured axial temperature as a functions of the three lances along  $z+$ , i.e. the relative distance from fuel lance exit. The

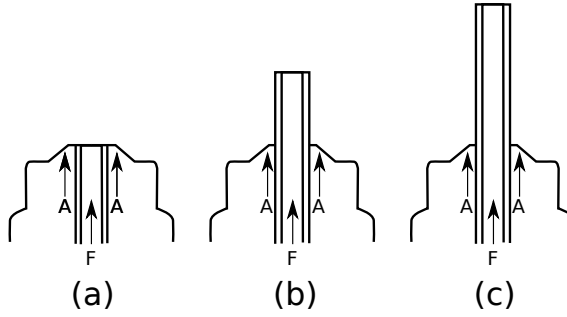


**Figure 3.19:** Conceptual sketch of the injection system, increasing the fuel lance length of 25 mm (L25) (b) and 50 mm (L50) (c) respect to the standard configuration (L0) (a).

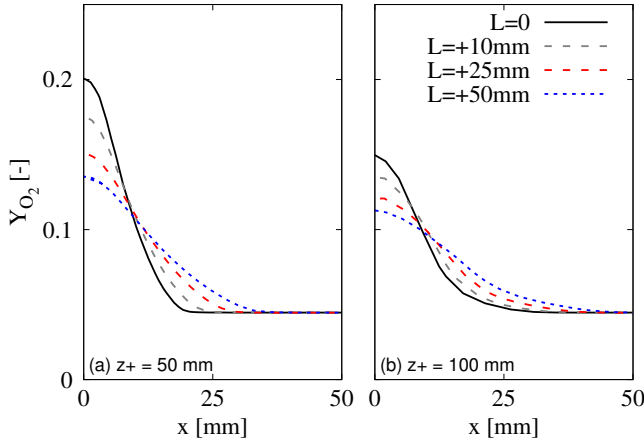


**Figure 3.20:** CFD profiles of oxygen mass fraction, extracted at a relative distance of 50 mm (a) and 100 mm (b) from the fuel lance exit. Four different lance length are compared. M50H50, ID16.

fuel lance L25 has already a strong impact, reducing the measured temperature peak of 25%, 5% and 10% for M50H50, M25H75 and M0H100 cases, respectively. No major differences can be highlighted between L25 and L50, meaning that L25 guarantees already a strong enough oxygen dilution. The same conclusions can be drawn observing the  $\text{OH}^*$  distribution for the same cases adopting L25. The flame lift-off is now calculated respect to the fuel

exit at the end of the flame lance. MILD combustion was achieved up to M25H75 for L25 and L50 also for the strictest condition ( $T_{in} = T_{air}$ ). Indeed, the first measurement point ( $z = 100$  mm) reveals now the maximum temperature for M25H75. Furthermore, no visible flame structures were detected for all the investigated conditions.

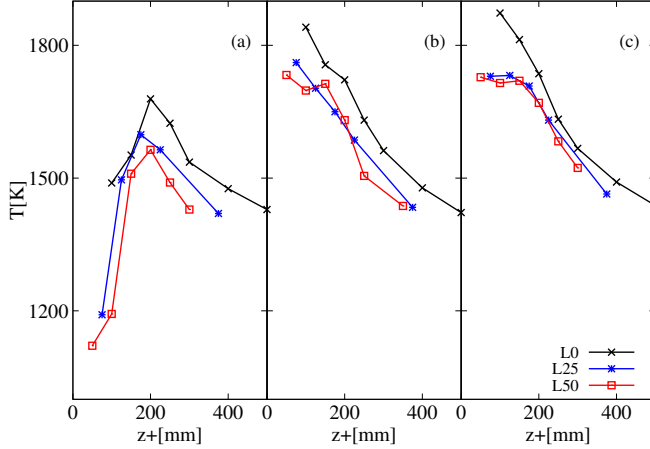


**Figure 3.21:** Averaged temperature profiles extracted along the axis and shown in function of  $z+$  for (a) M50H50 , (b) M25H75 and (c) M0H100. Averaged experimental uncertainty of 10 K. Test-cases T5-T6.

Finally, NO emissions confirmed the consideration done so far. Indeed, using the lance L25 allows a reduction of 54%, 83% and 87% with respect to the standard lance for M50H50, M25H75 and M0H100, respectively. The NNH pathway possibly becomes the only relevant route, since thermal NO are almost suppressed, considering the measured temperatures. Once again, the correlation mentioned above is verified, since no visible flame zone were detected up to M40H60, where NO emissions are below 10 ppm.

A further study (Test-case T7) focused on the dilution of pure hydrogen with nitrogen and it is reported in Appendix D.



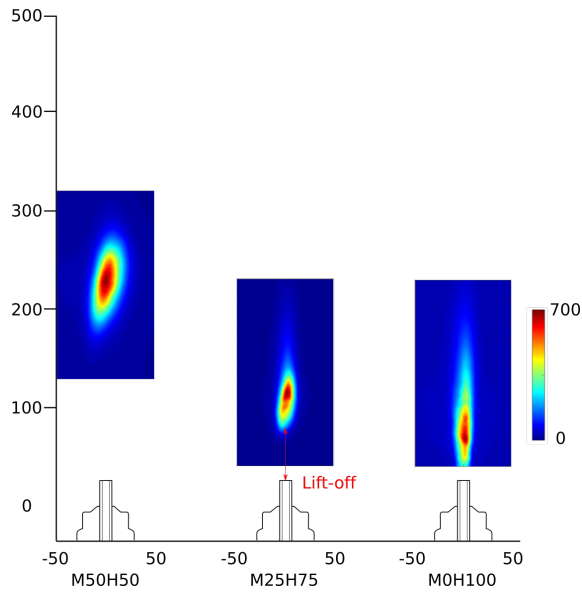


**Figure 3.22:** Averaged OH\* distribution for L25, varying the H<sub>2</sub> percentage. Units in mm and counts. Test-cases T5-T6.

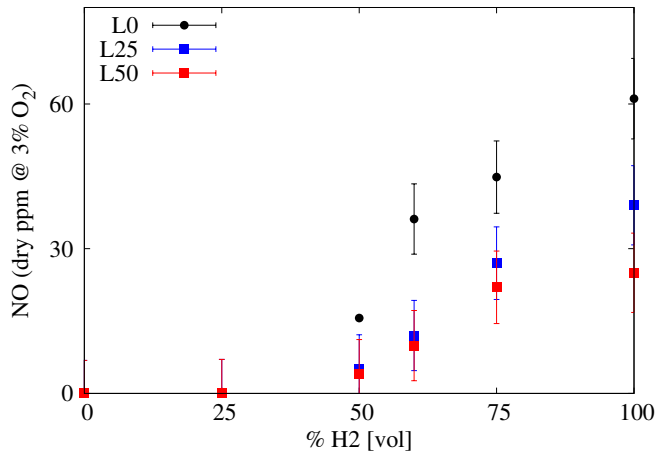


**Figure 3.23:** NO emissions varying the H<sub>2</sub> percentage and the fuel lance length L. Test-cases T5-T6.

### 3.3 Ammonia/Hydrogen blends

The aim of the fourth experimental campaign was two-folded. First, to present first-of-their-kind experimental data from an industrial flameless burner fired with  $\text{H}_2/\text{NH}_3$  blends, over a wide range of operating conditions. This campaign aimed at finding a configuration with optimal trade-off between  $\text{NO}_x$  emission and ammonia slip, while testing fuel flexibility of the furnace. Second, to explain the experimental trends of  $\text{NO}_x$  emissions using a well stirred reactor (WSR) network to model chemistry in diluted conditions.

#### 3.3.1 Pollutant emissions for $\text{NH}_3/\text{H}_2$ blends

The main working parameters, such as power and cooling, were kept constant with respect to the methane/hydrogen flames. Two air injectors were used (ID25 and ID16), standard fuel lance and a span of equivalence ratio  $\phi$  (0.8-1), as reported in Table 3.11. In the following,  $\text{N}_x\text{H}_y$  term represents the fuel mixture of  $x$  %vol. of  $\text{NH}_3$  and  $y$  %vol. of  $\text{H}_2$ .

Test	$P_{th}$ [kW]	$P_{cool}$ [kW]	$\phi$ [-]	$\text{NH}_3$ [%vol]	Air ID [mm]
T1	15	5.1	0.8-1	0-100	25
T2	15	5.1	0.8-1	0-100	16

**Table 3.11:** Operating conditions of the experimental tests on the  $\text{NH}_3\text{-H}_2$  mixtures.

Figure 3.24 shows the intense yellow color typical of ammonia combustion for different  $\text{NH}_3\text{-H}_2$  blends, for the case ID25 and  $\phi = 1$ .

Figures 3.25-3.26 compare averaged experimental temperature profiles extracted at different axial locations and  $\text{OH}^*$  imaging for the N50H50 mixture, varying the air ID and the  $\phi$ . Using ID16 and  $\phi = 0.8$ , the reaction region is located in the region 110-160 mm from the nozzle, with a maximum temperature of around 1750 K, at  $z = 150$  mm. The  $\text{OH}^*$  contour also appears more spread and less intense compared to the other cases. Indeed, ID16 ensures a very high injection velocity ( $\approx 185$  m/s), leading to a high strain rate value close to the burner exit. When the latter is reduced, at a certain axial distance, ignition occurs, leading to a noticeable lift-off. Keeping the same injector, but reducing the air excess ( $\phi = 1$ ), thinner reaction

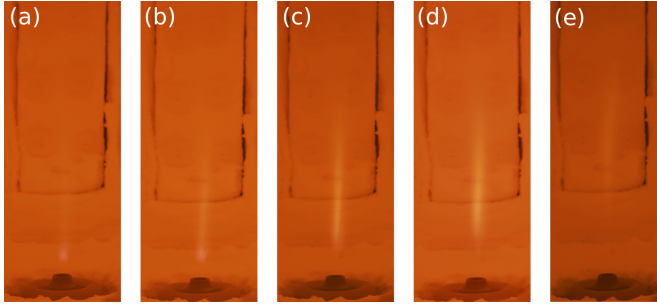


**Figure 3.24:** Photographs of  $\text{NH}_3\text{-H}_2$  combustion for (a) N10H90, (b) N20H80, (c) N40H60, (d) N50H50 and (e) N60H40. ID25,  $\phi = 1$ . Canon EOS 80D 1/70 s exposure time.

layer shifted towards the burner exit is observed. However, for this case, as well as for ID25, the actual maximum temperature is likely to be located below the first available measurement port ( $z = 100$  mm). When the ID25 is employed, the  $\text{OH}^*$  region is shifted even more upstream (between 50-80 mm). Unfortunately, temperatures for case ID25  $\phi = 1$  were not measured, since the suction pyrometer was damaged permanently by the corrosion of the condensing ammonia within the pipe.

Figure 3.27(left) shows the normalized NO and ammonia-slip emissions, varying the ammonia molar fraction and the equivalence ratio for ID25. Differently from nitrogen-free fuels (i.e. methane and hydrogen), when a fuel blend containing ammonia is used, different pathways are involved. With a small amount of  $\text{NH}_3$  (10% in volume), NO emissions grow considerably (from 159 to 827 ppm for  $\phi = 0.8$ ) reaching a peak at between 50% and 60%  $\text{NH}_3$  of 3500 ppm. Moreover, results suggest that the stoichiometry has a major impact on NO formation, confirming literature outcomes from Somarathne et al. [122] and Sorrentino et al. [61]. As expected, the minimum NO emission levels were obtained close to stoichiometric conditions. Under these conditions, NO is less sensitive to the reaction  $\text{O} + \text{NH}_2 = \text{H} + \text{HNO}$  (R31 in Table 3.12) due to a lower availability of the radical O. HNO is then converted to NO via the reaction  $\text{HNO} + \text{H} \rightarrow \text{NO} + \text{H}_2$  (more details Section 3.3.2). Furthermore, going towards  $\phi = 1$ , the peak is shifted progressively towards lower ammonia molar fraction up to 10 % $\text{NH}_3$  for  $\phi = 1$  (137 ppm). Very low NO emissions (single digit) can be achieved for this last condition ( $\phi = 1$ ), for a percentage of ammonia above 50%. The stabilization of pure ammonia combustion was not achieved, since extinction

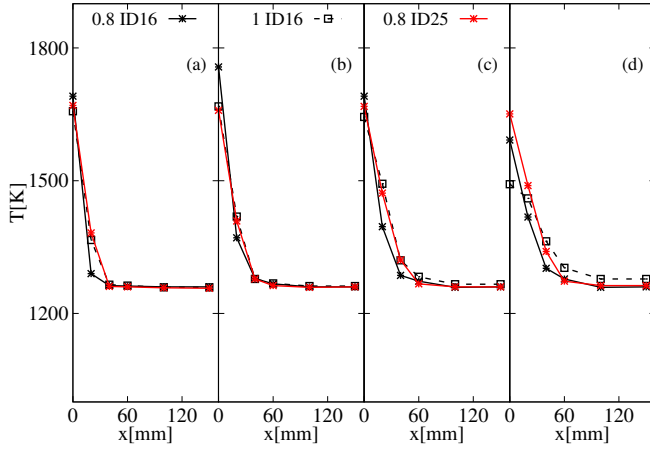


**Figure 3.25:** Averaged temperature measured at (a)  $z=100$  mm, (b)  $z=150$  mm, (c)  $z=200$  mm and (d)  $z=400$  mm for N50H50, varying the air ID and  $\phi$ . Averaged experimental uncertainty of 10 K.

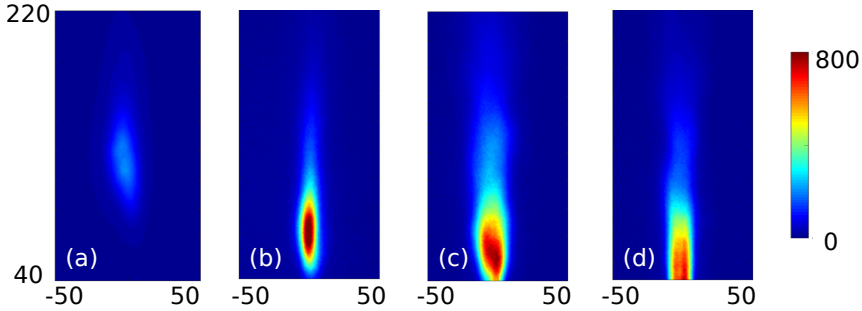


**Figure 3.26:** Averaged  $\text{OH}^*$  distribution for ID16  $\phi=0.8$  (a) and  $\phi=1$  (b) and for ID25  $\phi=0.8$  (c) and  $\phi=1$  (d). Units in mm and counts. N50H50.

occurred above 80%  $\text{NH}_3$ , for all the investigated conditions. In literature, there are example of pure ammonia burning in MILD regime, for instance Sorrentino et al. [61] managed to use pure ammonia in a cyclonic burner, under specific conditions. Further investigations will focus on extending the extinction limit pre-heating ammonia and/or reducing the thermal power to enhance the reactivity and increase the residence time, respectively.

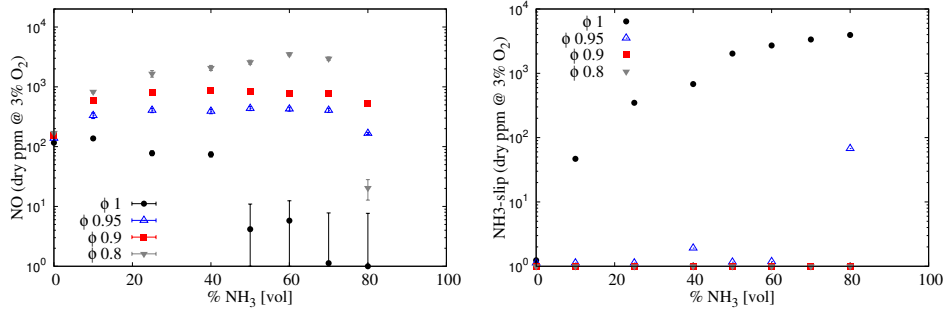


**Figure 3.27:** (Left) NO and (Right) NH<sub>3</sub>-slip emissions varying the NH<sub>3</sub> percentage in the fuel (vol.) and the equivalence ratio  $\phi$  for ID 25 mm. NH<sub>3</sub>-slip averaged relative uncertainty of 8%.

**Table 3.12:** List of sensitive reactions for NH<sub>3</sub>-H<sub>2</sub> blends.

Index	Reaction
R31	$\text{O} + \text{NH}_2 = \text{HNO} + \text{H}$
R39	$\text{NH} + \text{NH}_2 = \text{H} + \text{N}_2\text{H}_2$
R76	$\text{NO} + \text{NH}_2 = \text{N}_2 + \text{H}_2\text{O}$
R80	$\text{NH} + \text{OH} = \text{HNO} + \text{H}$
R85	$\text{NH} + \text{NO} = \text{H} + \text{N}_2\text{O}$
R89	$\text{OH} + \text{N} = \text{H} + \text{NO}$
R90	$\text{O}_2 + \text{N} = \text{O} + \text{NO}$
R91	$\text{NO} + \text{N} = \text{N}_2 + \text{O}$

Finally, reaching conditions close to stoichiometry, unburned ammonia might be found in the exhaust gases (NH<sub>3</sub>-slip). At  $\phi = 1$  (Figure 3.27(right)), NH<sub>3</sub>-slip rapidly increases reaching values about  $\approx 3000$  ppm, while it is almost zero for lean conditions. An optimal window can be found between  $\phi = 0.95$  and  $\phi = 1.00$  with a strong reduction in NO emission (maximum value 400 ppm) as well as low NH<sub>3</sub>-slip. However, It must be pointed out that it is easier to clean the exhaust gases removing ammonia (i.e. by condensation, adsorption) than adopting techniques to abate NO (i.e. DeNO<sub>x</sub>).

The effect of the air injector ID is shown in Figures 3.28 for both NO (left)

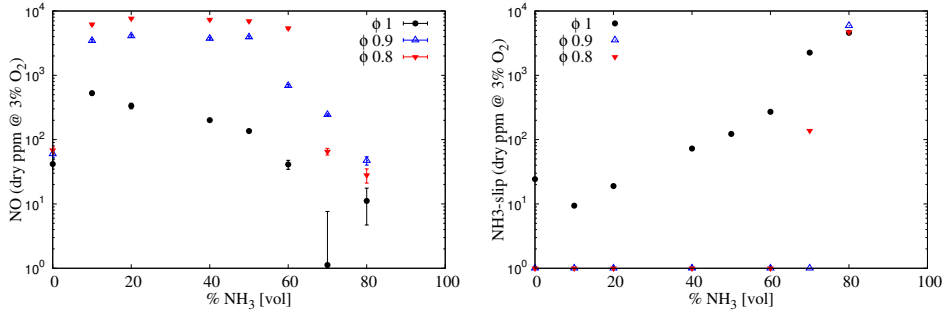


**Figure 3.28:** (Left) NO and (Right) NH<sub>3</sub>-slip emissions varying the NH<sub>3</sub> percentage in the fuel (vol.) and the equivalence ratio  $\phi$  for ID 16 mm. NH<sub>3</sub>-slip averaged relative uncertainty of 8%.

and NH<sub>3</sub>-slip (right) emissions. A higher air inlet velocity tends to increase NO<sub>x</sub> emissions as well. This might be explained considering the following: a higher recirculation ratio  $k_v$  decrease NO since it increases the level of dilution, however a reduced residence time (ID16) might not guarantee a sufficient time to convert NO into N<sub>2</sub>. An in-deep explanation is offered in Section 3.3.2. Analogous trends can be observed varying the equivalence ratio.

### 3.3.2 Characterisation of ammonia/hydrogen blends in WSR with EGR

The aim of this section is to qualitatively explain the pollutant emission trends observed in Figures 3.27-3.28.

As recommended by Medwell et al. [123], an adiabatic, non-isothermal well-stirred reactor was adopted to model the chemistry of a highly diluted and preheated reactive mixture (i.e. MILD-like conditions). In particular, this work focuses on NO<sub>x</sub> formation, aiming to map pollutant emissions in different operating conditions (see Table 3.11), and to qualitatively reproduce the experimental trends. Indeed, being flameless combustion characterized by a slower chemistry, ignition is likely to take place in flame kernels with premixed fuel and oxidizer and relatively low strain rate, i.e. distant from the inlet.

Figure 3.29 shows a schematic representation of the adopted network. The mixing unit takes three streams in input, namely fuel, air and  $k_v$  moles of

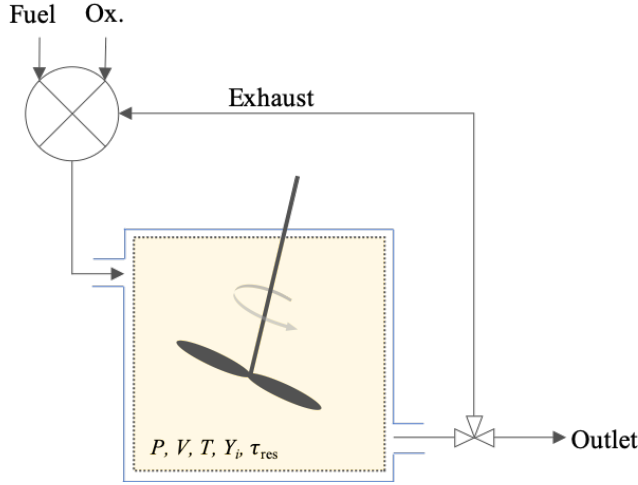


**Figure 3.29:** Schematic representation of the adopted reactor network.

exhaust gases (exhaust gas recirculation-EGR). Each stream is associated with a temperature value, which is set equal to the experiments. In particular, the temperature of exhaust gases flow is set to be equal to the furnace outlet (before the heat exchanger). This allows to avoid modelling of heat losses along the recirculation region, where the mixture may be assumed to be non-reactive (Zieba et al. [124]). As proposed by Medwell et al. [123], intermediate species were included in EGR, since they were found to take part in pre-ignition chemistry in MILD regime Sidey et al. [125]). The complete list of recirculated species in the exhaust gas is:  $\text{NH}_3$ ,  $\text{H}_2$ ,  $\text{O}_2$ ,  $\text{N}_2$ ,  $\text{H}$ ,  $\text{O}$ ,  $\text{H}_2\text{O}$ ,  $\text{OH}$ ,  $\text{HO}_2$ ,  $\text{NO}$ .

The analysis was carried out using the mechanism from Stagni et al. [13]. The network consists in a Matlab script involving the perfectly stirred reactor solver in OpenSMOKE++ by Cuoci et al. [11] to solve canonical reactors with detailed kinetics. The simulation is iteratively repeated until convergence for both the outlet temperature and NO moles fraction is achieved, i.e. residuals are lower than a certain threshold. OpenSMOKE++ [11] also enables the user to perform sensitivity, and rate of production (ROP), analyses. These capabilities were used to identify influential reactions to be further investigated with uncertainty quantification (UQ). The recirculation degree  $k_v$  and the residence time  $\tau_{res}$  of the reactor were estimated using CFD simulations. In particular, the recirculation degree  $k_v$  was estimated as explained in Section 3.2.2, while the residence time of the reactor was

defined as the averaged mixing time scale of the PaSR model ( $\tau_{res} = \tau_{mix}$ ), extracted from CFD simulations within the reactive region delimited by OH contours.

The WSR analysis is not intended to quantitatively predict the experimental data shown in Figures 3.27-3.28, but to provide qualitative information about NO formation in hydrogen-ammonia mixtures. Figure 3.30 shows the NO estimations computed with the WSR network, varying the ammonia molar fraction in the fuel, for two different equivalence ratios (i.e.  $\phi = 0.8$ , 1).

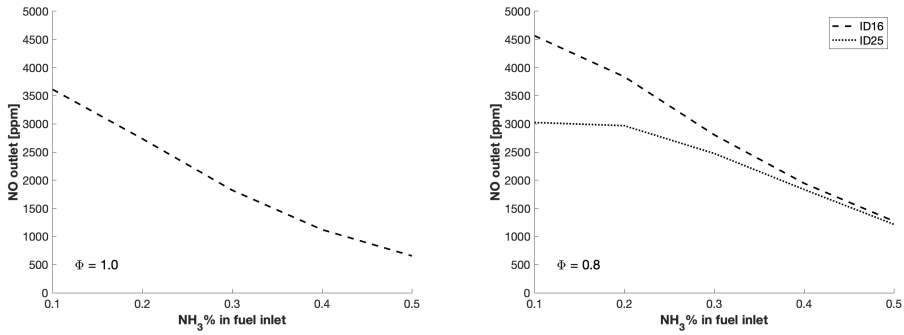


**Figure 3.30:** Pollutant emission estimates from the WSR network, for  $\phi=1.0$  (left) and  $\phi=0.8$  (right) at different fuel composition.

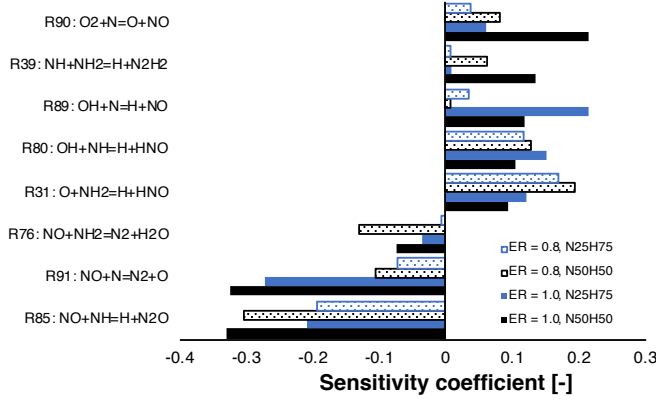
Remarkably, the simplified reactor network is capable of qualitatively reproducing the experimental trends (see Figures 3.27-3.28). In fact, the following conclusions can be withdrawn by looking at Figure 3.30:

- at  $\phi=1$  (see Figure 3.30 left), for the ID16 burner, a peak is observed in correspondence of the N10H90 mixture, then emissions diminish as ammonia concentration in the fuel raises;
- at  $\phi=0.8$  (see Figure 3.30 right), NO emissions increase with respect to stoichiometric conditions;
- at  $\phi=0.8$ , a lower NO production can be achieved using a larger air injector (ID25). This is in line with what was found experimentally (see Figure 3.27). The lower inlet velocity, due to ID25 configuration, reduces the entrainment of exhaust gas ( $k_v$ ), and increases residence



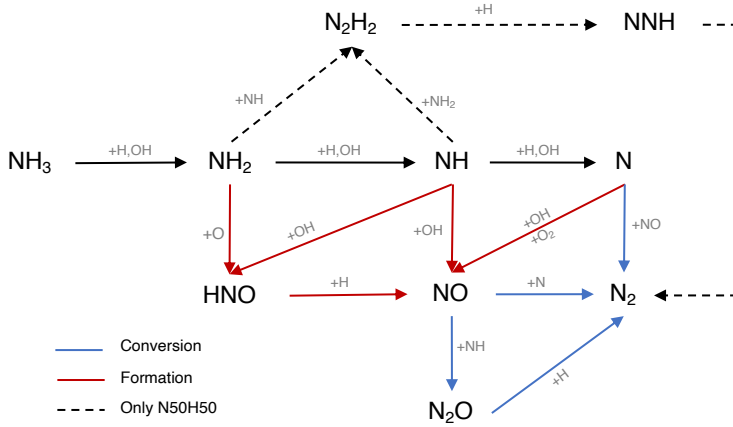
time in the reactive zone ( $\tau_{res}$ ). Globally, this results in reduced emissions.

Figure 3.31 reports the most influential reactions for the mixtures N25H75 and N50H50, at different equivalence ratio, namely 0.8 and 1.0.



**Figure 3.31:** NO sensitivity analysis for NH<sub>3</sub>/H<sub>2</sub> mixtures at different fuel compositions for  $\phi=1$ . ID16.

In particular, reactions involved in the hydrogen core mechanism were discarded *a priori*. The sub-mechanism for thermal NO<sub>x</sub>, involving R89, R90 and R91, was found to be particularly sensitive, especially for stoichiometric mixtures. However, it was not considered for the uncertainty quantification study of Section 6.3, as the authors assumed it to be well-characterized (see Baulch et al. [126]). Interestingly, R85 is the most important reaction with negative sensitivity coefficient. It is also important to point out that NO is very sensitive to R31, which forms HNO, for lean conditions, where more oxygen is available. Indeed, HNO is then converted to NO via  $\text{HNO} + \text{H} = \text{NO} + \text{H}_2$ . This may explain why lean conditions produce higher NO emissions. However, R31 as well as R76, were found to have high sensitivity coefficient for temperature and consequently ruled out from the UQ study of Section 6.3. Regarding other reactions, R80 converts NH into HNO and impact positively the sensitivity, and R39 is only sensitive for higher ammonia content in the fuel than 25%. Indeed, this reaction affects more and more the formation of NO as NH<sub>2</sub>, and NH production increase, due to higher availability of NH<sub>3</sub> as well as lower H and OH radicals concentra-



**Figure 3.32:** ROPA and flux analysis for  $\text{NH}_3\text{-H}_2$  mixtures. ID16.

tions. As a consequence, only R80, R85 and R39 were selected for a further study involving uncertainty quantification (Section 6.3).

In addition, a flux analysis was performed for both N25H75 and N50H50 mixtures (see Figure 3.32), to explain the NO emissions trends. Ammonia reactivity proceeds along  $\text{NH}_2 \rightarrow \text{NH} \rightarrow \text{N}$ , and NO is part of its oxidation. In fact,  $\text{NH}_2$  mainly forms NH and HNO in R31, which gives NO. The NH intermediate has a crucial role, as not only leads to NO through HNO in R80, but also reacts with it in R85 to form  $\text{N}_2\text{O}$ , which is almost completely converted to  $\text{N}_2$  in the termination step  $\text{H} + \text{N}_2\text{O} = \text{N}_2 + \text{OH}$ . In addition, NH is converted to N, which exhibits an analogous behaviour, i.e. it produces NO in R89 and R90, but also reacts with it in R91, again as a termination step. Up to N10H90, hydrogen concentration is so high that the radical pool is extremely rich in H and OH, prompting HNO production (R80) and its next conversion to NO, determining an emissions peak. The latter peak is even more pronounced at  $\phi=0.8$  because of the higher availability of local O radical, prompting the HNO production via R31. As the  $\text{NH}_3$  percentage in the fuel increases (i.e. at N50H50), these pathways weaken, and R39 starts competing. The latter reaction, offers an alternative path to NH, namely  $\text{N}_2\text{H}_2 \rightarrow \text{NNH} \rightarrow \text{N}_2$ , which tends to reduce the NO formation by subtracting NH and  $\text{NH}_2$  from the pool of reactants. So, R39 is part of the reason why richer fuel mixtures in  $\text{NH}_3$  show decreased NO emissions. In fact, this reaction shows a positive impact of NO sensitivity in Figures 3.31 as it competes with  $\text{NH} \rightarrow \text{NO} \rightarrow \text{N}_2\text{O} \rightarrow \text{N}_2$ , which repre-

sents the preferential way for the system to reduce NO emissions. Finally, one possible explanation for the existence of a shifted peak at  $\phi=0.8$  (see Figure 3.27) is the higher oxygen content, which pushes the NO production through HNO in R31 for richer mixtures with respect to stoichiometric conditions, delaying the effect of R39.

### 3.4 Summary and conclusion

In this Chapter a in-depth experimental analysis is reported for the ULB flameless furnace. The aim is to provide a further understanding on the behaviour of non-conventional fuel blends, such as hydrogen/methane and hydrogen/ammonia, in terms of turbulence/chemistry interactions and pollutant emissions.

First, an experimental campaign was conducted to analyse the performance of the burner with a standard air injector diameter (ID25). A progressive addition of hydrogen in methane enhanced combustion features, reducing the ignition delay time and increasing the reactivity of the system. This was confirmed by averaged measured temperature and OH\* chemiluminescence imaging. A threshold of 25% H<sub>2</sub> was defined for detecting visible flame structures, while MILD conditions were achieved up to 50% H<sub>2</sub> according to the formula proposed by Cavaliere et al. [10], considering the inlet temperature as the temperature of the mixture exhausts and reactants.

Second, further experimental campaigns aimed to reduce temperature peaks and pollutant emissions varying the air injector diameter and, therefore, the injection velocity, up to 200 m/s for ID16. This allowed to reach very high recirculation degree  $k_v$ , up to 28 for pure methane. The effect was relevant on both the position of the reaction zone, the maximum temperature of the system and pollutant emissions, with a reduction of 200 K and 84%, respectively, for M50H50 ID16.

Other campaigns focused on using a longer fuel injection lance. The fuel lance was indeed immersed into the furnace for an extra length of 25 mm and 50 mm. Being the fuel injected further downstream in the furnace, it guarantees more time to the air stream to be diluted by the exhaust gases, increasing the recirculation degree. Pollutant emissions were reduced of 87% for pure hydrogen. Minor differences were found between the two length, meaning that L25 provides an already sufficient enough dilution.

MILD conditions were reached up to M25H75 with no visible flame structures.

Finally, a further campaign was performed to confirm the enhanced fuel flexibility of the ULB flameless furnace fired with ammonia/hydrogen blends. Operating configurations in terms of trade-off between NO<sub>x</sub> emissions and ammonia slip could be identified. In fact, ammonia slip emissions are negligible in lean conditions, while they become relevant close to  $\phi = 1$ . The optimal working point was identified for all fuel mixtures at  $\phi = 0.95$ , which allows to reduce NO emissions with respect to leaner conditions, while keeping low NH<sub>3</sub>-slip (below 10 ppm). Additionally, in stoichiometric conditions a peak in NO emissions was observed for both tested injectors (ID16 and ID25), at N10H90 fuel composition. Then, emissions decreased up to extinction, which occurred above N80H20. In general, for lean cases ( $\phi = 0.8$ ), the NO production increased, and a shifted peak towards higher ammonia content in the fuel (N60H40) was observed. Using a bigger air injector (ID25) also help controlling pollutants emissions, as the associated residence time increases enhancing the conversion of NO to N<sub>2</sub>. A simplified reactor network, consisting in a WSR reactor with a mixer unit was built to qualitatively explain these trends. A detailed study, considering sensitivity and flux analysis on NO formation, was performed. It was found out that NO is reduced at stoichiometric condition because of a lower reactivity of the reaction  $O + NH_2 \rightarrow H + HNO$ . Indeed, HNO in turn is converted to NO via the reaction  $HNO + H \rightarrow NO + H_2$ . Furthermore, the presence of two competitive path, i.e.  $N_2H_2 \rightarrow NNH \rightarrow N_2$  and  $NH \rightarrow NO \rightarrow N_2O \rightarrow N_2$  is the key to understand the presence of a peak at varying the ammonia molar fraction in the fuel. The analysis also highlighted the most three impacting reactions (R80, R85 and R39), which should be considered for uncertainty quantification analysis.



## Chapter 4

# Mathematical models

*In this chapter, the theories and models that are used in the following chapters are introduced and described. Firstly, the Reynolds Averaged Navier-Stokes (RANS) approach is presented. Secondly, RANS approaches for turbulent combustion modelling and the closure for the stresses and fluxes are introduced. Thereafter, two combustion models are presented, EDC and PaSR, emphasizing the effect of the mixing and chemical time scales. The radiative properties of gases are then modelled with a weighted-sum-of-grey-gas (WSGG) model which accounts for the mole ratio between  $\text{CO}_2$  and  $\text{H}_2\text{O}$ . The models developed in this thesis have been implemented in the commercial CFD package Ansys Fluent 19.0.*

## 4.1 RANS for turbulent combustion modeling

Reynolds averaging splits any quantity into a mean and fluctuating component as follows:

$$f = \bar{f} + f' \quad \text{with} \quad \bar{f}' = 0. \quad (4.1)$$

In density varying flows, Reynolds averaging introduces many unclosed correlations between any quantity  $f$  and density  $\rho$  fluctuations,  $\overline{\rho' f'}$ . Therefore, Favre averaging (or density-weighted averaging) [127] is usually used to avoid this issue. The Favre averaged quantity is written as:

$$\tilde{f} = \frac{\overline{\rho f}}{\bar{\rho}}. \quad (4.2)$$

Any quantity can be decomposed as follows:

$$f = \tilde{f} + f'' \quad \text{with} \quad \tilde{f}' = 0. \quad (4.3)$$

The Favre-averaged governing equations for low Mach numbers become:  
Mass:

$$\frac{\partial \bar{\rho}}{\partial t} + \frac{\partial \bar{\rho} \tilde{u}_i}{\partial x_i} = 0, \quad (4.4)$$

Momentum:

$$\frac{\partial \bar{\rho} \tilde{u}_j}{\partial t} + \frac{\partial \bar{\rho} \tilde{u}_i \tilde{u}_j}{\partial x_i} = -\frac{\partial \bar{p}}{\partial x_j} + \frac{\partial}{\partial x_i} (\overline{\tau_{ij}} - \widetilde{\rho u_i'' u_j''}), \quad (4.5)$$

Species:

$$\frac{\partial \bar{\rho} \tilde{Y}_k}{\partial t} + \frac{\partial \bar{\rho} \tilde{u}_i \tilde{Y}_k}{\partial x_i} = \frac{\partial}{\partial x_i} \left( \overline{\rho D_{m,k} \frac{\partial Y_k}{\partial x_i}} - \widetilde{\rho u_i'' Y_k''} \right) + \bar{\omega}_k, \quad k = 1, \dots, N, \quad (4.6)$$

Enthalpy:

$$\frac{\partial \bar{\rho} \tilde{h}}{\partial t} + \frac{\partial \bar{\rho} \tilde{u}_i \tilde{h}}{\partial x_i} = \frac{\partial}{\partial x_i} \left( \overline{\rho \alpha \frac{\partial h}{\partial x_i}} - \widetilde{\rho u_i'' h''} \right) + \bar{S}_r. \quad (4.7)$$

The remaining unclosed terms are: Reynolds stresses ( $\widetilde{u_i'' u_j''}$ ), species and enthalpy turbulent fluxes ( $\widetilde{u_i'' Y_k''}$  and  $\widetilde{u_i'' h''}$ ), mean laminar diffusive fluxes for species and enthalpy ( $\overline{\rho D \frac{\partial Y_k}{\partial x_i}}$  and  $\overline{\rho \alpha \frac{\partial h}{\partial x_i}}$ ), viscous stresses  $\overline{\tau_{ij}}$ , and species chemical reaction rate ( $\bar{\omega}_k$ ) and mean radiative source term  $\bar{S}_r$ .

### 4.1.1 Closure for RANS equations

Turbulent fluxes are generally closed using the classical gradient diffusion assumption:

$$\overline{\rho u_i'' \widetilde{Y_k''}} = -\frac{\mu_t}{Sc_t} \frac{\partial \widetilde{Y_k}}{\partial x_i}, \quad (4.8)$$

$$\overline{\rho u_i'' \widetilde{h''}} = -\frac{\mu_t}{Pr_t} \frac{\partial \widetilde{h}}{\partial x_i}, \quad (4.9)$$

where  $Sc_t$  and  $Pr_t$  are the turbulent Schmidt number and Prandtl number, respectively. The molecular diffusion term are generally modelled as:

$$\overline{\rho D_{m,k} \frac{\partial Y_k}{\partial x_i}} \approx \overline{\rho D_{m,k}} \frac{\partial \widetilde{Y_k}}{\partial x_i}, \quad (4.10)$$

$$\overline{\rho \alpha \frac{\partial h}{\partial x_i}} \approx \overline{\rho D_{m,k}} \frac{\partial \widetilde{h}}{\partial x_i}, \quad (4.11)$$

where  $D_{m,k}$  is the molecular diffusion coefficient for species  $k$  in the mixture and  $\alpha$  is the thermal diffusivity. Since  $Sc_t = \mu_t/(\rho D_t)$  ( $D_t$  is the turbulent diffusivity), the molecular diffusion can also be written as  $Sc = \mu/(\rho D_m)$  and therefore  $\rho D_m = \mu/Sc$ .

Reynolds stresses ( $\widetilde{u_i'' u_j''}$ ) are normally described using the Boussinesq's turbulent viscosity hypothesis [128].

$$\overline{\rho u_i'' u_j''} = -\mu_t \left( \frac{\partial \widetilde{u_i}}{\partial x_j} + \frac{\partial \widetilde{u_j}}{\partial x_i} - \frac{2}{3} \frac{\partial \widetilde{u_k}}{\partial x_k} \delta_{i,j} \right) + \frac{2}{3} \overline{\rho k} \delta_{i,j}, \quad (4.12)$$

where  $\mu_t$  is the turbulent dynamic viscosity. The turbulent kinetic energy  $k$  is defined as:

$$k = \frac{1}{2} \sum_{i=1}^3 \overline{u_i'' u_i''}. \quad (4.13)$$

Among the different type of approaches that can be used to close turbulent viscosity in RANS simulation, the two equation  $k$ - $\epsilon$  model [129] is the most used in CFD codes. Turbulent viscosity in  $k$ - $\epsilon$  model is estimated as:

$$\mu_t = \overline{\rho} C_\mu \frac{k^2}{\epsilon}, \quad (4.14)$$



where  $C_\mu$  is a model constant. Turbulent kinetic energy  $k$  and its dissipation rate  $\epsilon$  are calculated by their modelled transport equations:

$$\frac{\partial \bar{\rho} \tilde{k}}{\partial t} + \frac{\partial \bar{\rho} \tilde{u}_i \tilde{k}}{\partial x_i} = \frac{\partial}{\partial x_i} \left[ \left( \mu + \frac{\mu_t}{\sigma_k} \right) \frac{\partial \tilde{k}}{\partial x_i} \right] + P_k - \bar{\rho} \tilde{\epsilon}, \quad (4.15)$$

$$\frac{\partial \bar{\rho} \tilde{\epsilon}}{\partial t} + \frac{\partial \bar{\rho} \tilde{u}_i \tilde{\epsilon}}{\partial x_i} = \frac{\partial}{\partial x_i} \left[ \left( \mu + \frac{\mu_t}{\sigma_\epsilon} \right) \frac{\partial \tilde{\epsilon}}{\partial x_i} \right] + C_{\epsilon 1} \tilde{\epsilon} \tilde{k} - C_{\epsilon 2} \bar{\rho} \tilde{\epsilon}^2. \quad (4.16)$$

The model constants are [128]:

$$C_\mu = 0.09, \quad \sigma_k = 1, \quad \sigma_\epsilon = 1.3, \quad C_{\epsilon 1} = 1.44, \quad C_{\epsilon 2} = 1.92. \quad (4.17)$$

The production term  $P_k$  is given by:

$$P_k = -\overline{\bar{\rho} u_i'' u_j''} \frac{\partial \tilde{u}_i}{\partial x_j}, \quad (4.18)$$

and it can be rewritten using Equation 4.12. The standard  $k$ - $\epsilon$  model is robust, computationally fast and has the potential advantage of generality since it requires no direct empirical input such as a mixing-length specification. Nevertheless, it has the disadvantage of over-estimating the jet spread rate for axisymmetric jets. To overcome this issue a modification of the constant  $C_{\epsilon 1}$  (from 1.44 to 1.60) was proposed by Dally et al. [130]. In the last years, many improved version of the standard  $k$ - $\epsilon$  were defined, such as the Realizable  $k$ - $\epsilon$  [131] for spreading rate of planar and round jets or for flows involving rotation, RNG  $k$ - $\epsilon$  [132] for rotating flows and  $k$ - $\omega$  [133] for cases where the wall effects are predominant.

The mean reaction rates  $\overline{\dot{\omega}_k}$  in species balance equations can be modelled using different combustion models, as presented in Section 4.2.

## 4.2 Combustion model

The interactions between chemical kinetics and turbulent mixing represent the main interest of turbulent combustion modeling. With regard to non-premixed combustion, it is possible to identify two conditions which allow to completely decouple the problem:

- *Infinitely fast chemistry*: the combustion process is dominated by turbulent mixing;

- *Finite rate chemistry*: the combustion process is limited by chemical reactions.

The Eddy Break-up and Eddy Dissipation models were both developed under the hypothesis of infinitely fast chemistry, whereas topological approaches, such as the flamelet model [134] and presumed PDF (Probability Density Function) and transported PDF method [135] were proposed for finite rate chemistry.

Model based on tabulated chemistry techniques [136] were recently developed to account for detailed kinetic mechanisms, saving computational cost. Among them, the Flamelet Generated Manifold model (FGM) [137, 138] is one of the most used and promising. It is a chemistry reduction method that combines the advantages of dimension reduction techniques based on chemical steady-state assumptions and Flamelet models [139]. FGM is based on two main assumptions: the  $n$ -dimensional space of compositions of a combustion system can be represented by a lower-dimensional manifold (tabulated chemistry), and a complex flame structure (laminar or turbulent) can be treated as an ensemble of laminar flames (Flamelet approach). Several works [89, 140, 141] investigated MILD systems using Flamelet approach. Cериello et al [141] investigated also the effect of the internal exhaust gas recirculation on the performances of a tabulated chemistry model through an experimental and numerical study on a cyclonic burner.

On the other side, a reactor-based model, such as the Eddy Dissipation Concept (EDC) by Magnussen [142], has found wide application for the simulation of turbulent reacting flows, especially for cases where kinetics plays a major role, as it appear for MILD/Flameless combustion. MILD combustion processes feature reduced peak temperatures and enhanced mixing phenomena to increase the energy efficiency and reduce the emissions of pollutants. In such systems, the characteristic scales of turbulence  $\tau_\eta$  and chemistry  $\tau_c$  have comparable magnitude, as proven by a Damköhler number ( $\tau_{mix}/\tau_c$ ) approaching unity [143]. Therefore, infinitely fast chemistry models and also the standard flamelet approach are not suited for this combustion regime, as proven by Christo et al. [71] and Parente et al. [31]. EDC has the advantage of incorporating detailed kinetics at a not negligible computational cost, which is however affordable when compared to more sophisticated models such as transported PDF methods. The Partially Stirred Reactor (PaSR) model [77] was proposed as an alternative to EDC. PaSR is conceptually similar to EDC since they both model the combustion process as a sequence of reaction and mixing processes in locally

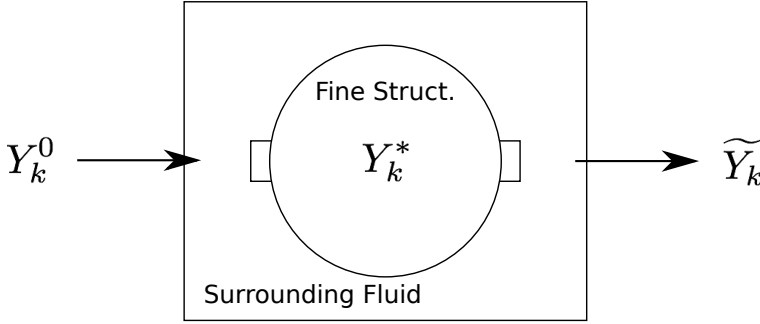


**Figure 4.1:** Conceptual drawing of the EDC model.

uniform regions, i.e. fine structure. In EDC, the dimensions of the fine structures are of the same order of magnitude of the Kolmogorov length scale, whereas in PaSR the reacting volume fraction of the computational cell is expressed as a function of chemical and mixing time scales estimated globally. Details about EDC and PaSR models are provided below.

#### 4.2.1 Eddy Dissipation Concept

The Eddy Dissipation Concept (EDC) was developed by Magnussen [142] and afterwards extended by Gran and Magnussen [144] and Magnussen [145]. EDC separates each computational cell into two zones. One zone is indicated as “fine structure” and another one as “surrounding”. It assumes that combustion takes place in the fine structures where the dissipation of the flow turbulence kinetic energy occurs. In the original model by Magnussen [142], the fine structures were modelled as Perfectly Stirred Reactors (PSR). A conceptual drawing of the EDC model is presented in Figure 4.1.

EDC is based on a cascade model providing the mass fraction of the fine structures,  $\gamma_\lambda$ , and the mean residence time of the fluid within the fine structures  $\tau^*$ , as a function of the flow characteristic scales:

$$\gamma_\lambda = C_\gamma \left( \frac{\nu \epsilon}{k^2} \right)^{1/4}, \quad (4.19)$$

$$\tau^* = C_\tau \left( \frac{\nu}{\epsilon} \right)^{1/2}, \quad (4.20)$$

where  $\nu$  is the kinematic viscosity, while  $C_\gamma$  and  $C_\tau$  are constants in the EDC model [142]. The mean reaction rate (source term in the species transport equation) is expressed as [144]:

$$\overline{\dot{\omega}_k} = -\frac{\bar{\rho}\gamma_\lambda^2}{\tau^*(1-\gamma_\lambda^3)}(\widetilde{Y_k} - Y_k^*). \quad (4.21)$$

The term  $\widetilde{Y_k}$  denotes the averaged mass fraction of the species  $k$  between the fine structures and the surrounding fluid, while  $Y_k^*$  is the mass fraction of species  $k$  in the fine structures. The mean mass fraction  $\widetilde{Y_k}$  can be expressed as a function of  $Y_k^*$  and  $Y_k^0$  (mass fraction of species  $k$  in the surrounding fluid):

$$\widetilde{Y_k} = \gamma_\lambda^3 Y_k^* + (1 - \gamma_\lambda^3) Y_k^0. \quad (4.22)$$

Recently, Evans et al. [74] presented an improved version of the EDC model for MILD combustion with adjusted  $C_\gamma$  and  $C_\tau$  coefficients, whereas Parente et al. [72] proposed functional expression of the EDC coefficients on dimensionless flow parameters, such as Reynolds and Damköhler number.

## 4.2.2 Partially Stirred Reactor

In the PaSR model [77], as in the EDC model, the computational cell is divided into two locally uniform zones: reactive and non reactive. The final concentrations within the cell is determined by the mass exchange between two zones, driven by turbulence. The mean source term provided to the species transport equation is expressed as:

$$\overline{\dot{\omega}_k} = \frac{\kappa \bar{\rho}(Y_k^* - Y_k^0)}{\tau^*}, \quad (4.23)$$

where  $\tau^*$  represents the residence time in the reactive structure. The factor  $\kappa$  provides the partially stirred condition, being the volume fraction of the reactive zone.  $\kappa$  is defined as the ratio between the chemical time scale  $\tau_c$  and the sum of the chemical time scale and the mixing time scale  $\tau_{mix}$ :

$$\kappa = \frac{\tau_c}{\tau_c + \tau_{mix}}. \quad (4.24)$$

To get the value of  $Y_k^*$  in Eq. 4.23, the reactive zone is considered as an ideal reactor (either a PSR or a plug flow reactor, PFR) evolving from  $Y_i^0$ , during a residence time  $\tau^*$ :

$$\frac{dY_k'}{dt} = \frac{\dot{\omega}_k}{\rho}. \quad (4.25)$$

The term  $\omega_k$  is the instantaneous formation rate of species  $k$ . Following a time-splitting approach, the final integration of  $dY'_k/dt$  over the residence time  $\tau^*$  in the reactor is  $Y_k^*$ . In the original formulation proposed by Chomiak [77], the residence time on the reactive fraction ( $\tau^*$ ) was defined as the mixing time scale ( $\tau_{mix}$ ). However, in the present thesis, this definition is adapted to the minimum between  $\tau_c$  and  $\tau_{mix}$  to account for high reactivity cases ( $\tau_c \ll \tau_{mix}$ ). Indeed, the reactants would actually stay in the reactive structure as long as it is needed, which is the minimum of the two time scales. The estimation of the chemical and the mixing time scales becomes crucial to ensure accurate predictions of the model. See Appendix C for a validation of the residence time  $\tau^*$  formulation.

## Estimation of chemical time scale

**Chemical time scale estimation from Jacobian matrix eigenvalues** For the evaluation of chemical time scale, Fox [146] suggested using the eigenvalues of the Jacobian matrix  $\mathbf{J}$  of the chemical source terms. The Jacobian matrix  $\mathbf{J}$  has the dimension of  $k \times k$ , where  $k$  is the number of chemical species in the mechanism. After the decomposition of the Jacobian matrix, the chemical time scale is estimated with the inverse of the eigenvalues is  $\lambda_k$ :

$$\tau_{c,k} = \frac{1}{|\lambda_k|}. \quad (4.26)$$

In Eq. 4.26  $\tau_{c,k}$  is the characteristic time scale of species  $k$ . After removing the dormant species (characterised by infinite time scale values), the largest chemical time scale can be chosen as leading scale for the evaluation of the PaSR parameter  $\kappa$ .

**Chemical time scale estimation from formation rates** The decomposition of the source term Jacobian matrix is accurate but time consuming, especially when large chemical mechanisms are used. The formation rate based characteristic time scale evaluation is a simplified approach. Instead of getting the chemical time scale for each species from the Jacobian matrix decomposition, the ratio of species mass fraction and formation rate in the reactive structure is directly used [147], approximating the Jacobian diagonal terms:

$$\tau_{c,k} = \frac{Y_k^*}{|dY_k^*/dt|}. \quad (4.27)$$

## Estimation of mixing time scale

**Static approach** K  rrholm [148] and Nordin [149] estimated the mixing time scale as a certain fraction of the integral time scale. The latter is a characteristic time scale in turbulent flows and it is related to the eddy break-up time leading from large-scale to Kolmogorov vortices. The mixing time scale is equal to:

$$\tau_{mix} = C_{mix} \frac{k}{\epsilon}, \quad (4.28)$$

where  $k$  is the turbulent kinetic energy  $\epsilon$  is the dissipation rate of the turbulent energy.  $C_{mix}$  is a model constant, which must be conveniently selected by the user. This constant is normally adjusted in a wide range (from 0.001 to 0.3 according to K  rrholm [148]). Kuron et al. [150] invoked the adoption of a dynamic model, given the observed wide variability in the optimal choice of  $C_{mix}$ .

**Fractal-based approach** Another approach is based on the concept of fractal structures in turbulence [151]. According to this theory, the mixing time can be expressed as [152]:

$$\tau_{mix} = \left( \frac{c_\mu}{Re_t} \right)^{\frac{1-\alpha}{2}} \frac{k}{\epsilon}, \quad (4.29)$$

where  $\alpha = \frac{3(D-3)}{1+D}$ ,  $D$  is the fractal dimension,  $C_\mu$  is the constant of the  $k$ - $\epsilon$  model of turbulence and  $Re_t$  is the turbulent Reynolds number ( $\nu_t/\nu$ ). In this approach, the term  $\left( \frac{c_\mu}{Re_t} \right)^{\frac{1-\alpha}{2}}$  is equivalent to the previously defined  $C_{mix}$ . However, the parameter is not any more a constant, but rather a function of  $Re_t$ . It can be shown that a value of  $D=3.5$  corresponds to the Kolmogorov time-scale, whereas adopting  $D=5$  results in the integral time.

**Dynamic approach** An automatic definition of  $\tau_{mix}$  based on local properties of the flow-field using a dynamic approach was proposed by Raman et al. [153]:

$$\tau_{mix} = \tau_\phi = \frac{\widetilde{\phi''^2}}{\widetilde{\epsilon_\phi}}, \quad (4.30)$$

where  $\widetilde{\phi''^2}$  is the variance of the scalar  $\phi$  and  $\widetilde{\epsilon_\phi}$  is its dissipation rate, defined as  $2D_m \left( \widetilde{\partial\phi''/\partial x_i} \right)^2$ , where  $D_m$  is the molecular diffusion coefficient. An equivalent  $C_{mix}$  can also be defined as:

$$C_{mix,eq} = \frac{\tau_\phi}{k/\epsilon}. \quad (4.31)$$

Recognizing that  $C_{mix}$  is not an universal constant, a dynamic estimation of a mixing time shall be based on the resolution of transport equations for the scalar variance and scalar dissipation rate [154]. Being PaSR a reactor model based on the segregation between chemistry and mixing, an estimation of the mixing time is required. To achieve that, a reference scalar must be taken into account. In the present thesis, this scalar is considered as the mixture fraction, in agreement with Senouci et al. [155], strongly simplifying the transport equations for  $\widetilde{\phi''^2}$  and  $\widetilde{\epsilon_\phi}$  [146]. An interesting alternative approach might involve the usage of reacting scalar, but the latter was not investigated in the present work. Following [18], the system of transport equations can be written as:

$$\frac{D\bar{\rho}\widetilde{Z''^2}}{Dt} = \frac{\partial}{\partial x_j} \left( \rho(D_m + D_t) \frac{\partial \widetilde{Z''^2}}{\partial x_j} \right) + 2\rho D_t \left( \frac{\partial \widetilde{Z}}{\partial x_j} \right)^2 - \bar{\rho}\widetilde{\chi}, \quad (4.32)$$

$$\begin{aligned} \frac{D\rho\widetilde{\chi}}{Dt} = & \frac{\partial}{\partial x_j} \left( \rho(D_m + D_t) \frac{\partial \widetilde{\chi}}{\partial x_j} \right) - C_{D1}\bar{\rho}\frac{\widetilde{\chi^2}}{\widetilde{Z''^2}} - C_{D2}\bar{\rho}\frac{\widetilde{\chi\epsilon}}{\widetilde{k}} \\ & + C_{P1}\frac{\widetilde{\chi}}{\widetilde{Z''^2}}P_f + C_{P2}\frac{\widetilde{\chi}}{\widetilde{k}}P_k, \end{aligned} \quad (4.33)$$

where  $Z$  is the mixture fraction,  $\widetilde{Z''^2}$  is the mixture fraction variance  $D_t$  is the turbulent diffusivity,  $\widetilde{\chi}$  is the mixture fraction dissipation rate.  $P_f = -2\bar{\rho}\widetilde{u_k''Z''}(\partial\widetilde{Z}/\partial x_k)$  is the production of scalar fluctuation and  $P_k = -\bar{\rho}\widetilde{u_k''u_i''}(\partial\widetilde{U_i}/\partial x_k)$  is the production of turbulent kinetic energy. The coefficients are listed in Table 4.1, where  $R_\tau = (k/\epsilon)/(\widetilde{Z''^2}/\chi)$  is the mechanical to scalar time-scale ratio.

The combustion and mixing models have been coupled to the main solver via a bespoke subroutine (user-defined function written in C).

**Table 4.1:** Coefficients of the scalar dissipation rate equation by various authors [18].

Author	$C_{P1}$	$C_{P2}$	$C_{D1}$	$C_{D2}$
Chen [156]	0.5	1.45	1.15	0.65
Jones and Musonge [157]	$1.7 R_\tau^{-1}$	1.45	1.0	0.9
Sommer et al. [158]	0.9	0.72	1.1	0.8

### 4.3 Radiation Modeling

Including radiation effects in combustion modelling is very important to achieve good predictions in combustion systems where radiation heat transfer plays a significant role, especially for closed environment (i.e. furnace). Radiation heat transfer in participating media is governed by the radiative transfer equation (RTE), which establishes a relation for the variation of the spectral radiation intensity  $I_\nu$  along a certain path in the medium. Since the scattering effect is negligible in a gas fired furnace, the RTE for an absorbing, emitting, and non-scattering medium [159] is given by:

$$\frac{dI_\nu(\mathbf{r}, \mathbf{s})}{ds} = -\kappa_\nu(\mathbf{r})I_\nu(\mathbf{r}, \mathbf{s}) + \kappa_\nu(\mathbf{r})I_{b\nu}(\mathbf{r}). \quad (4.34)$$

In the above equation,  $I_\nu(\mathbf{r}, \mathbf{s})$  is the spectral radiation intensity at point  $\mathbf{r}$  and direction  $\mathbf{s}$ ,  $I_{b\nu}$  is the blackbody radiation intensity,  $\kappa_\nu$  is the spectral absorption coefficient of the medium.

In flameless furnaces, fuel and air streams are highly diluted by recirculated burnt gases, which contain carbon dioxide and water, increasing the infrared radiative flux [79]. At this purpose, in the present thesis, the Discrete ordinates method (DOM) model, available in ANSYS Fluent, was used for radiation modelling. Indeed, it is a good compromise between accuracy and computational cost [160]. Furthermore, it allows the solution of radiation in semi-transparent media and the possibility to enable the non-grey or multi-bands formulation. Each of the angular space  $4\pi$  at any spatial location is discretized into  $4 \times 4$  solid angles. Then the RTE in each solid angle direction is solved. A total of 200 directions are solved. The details of DOM can be found in [161].

Once the RTE is solved, the radiative heat source of Eq. 4.7 is calculated as:

$$S_r = -\nabla \cdot \mathbf{q} = \int_0^{+\infty} \kappa_\nu(4\pi I_{b\nu} - G_\nu) d\nu = \kappa(4\pi I_b - G), \quad (4.35)$$



where the second equality only holds in the case of a grey medium. Here,  $\mathbf{q}$  is the radiative heat flux vector, and  $G$  is the incident radiation given by:

$$G = \int_0^{+\infty} \int_{4\pi} I_\nu d\Omega d\nu = \int_{4\pi} I d\Omega. \quad (4.36)$$

The term  $\nabla \cdot \mathbf{q}$  can be directly substituted into the enthalpy Eq. 4.7 to account for heat sources (or sinks) due to radiation. However, the solution of the RTE and the radiative heat source, Eqs. 4.34 and 4.35, also require the integration over the wavenumber  $\nu$ . In the present thesis, this will be carried out with the weighted-sum-of-grey gas (WSGG) model, considering that the medium is formed with a mixture of  $\text{H}_2\text{O}$  and  $\text{CO}_2$ .

### 4.3.1 Absorption coefficient

The WSGG model, originally proposed by Hottel and Sarofim [162] for calculation of the total emissivity ( $\epsilon$ ) as a weighted sum of  $J$  grey gases and one clear gas, is written as:

$$\epsilon = \sum_{j=0}^J a_j [1 - \exp(-\kappa_j S_m P(Y_{\text{CO}_2} + Y_{\text{H}_2\text{O}}))], \quad (4.37)$$

where  $S_m$  is the total pathlength. Each gas represents spectral regions which have an absorption coefficient within a specific range which is assumed to be described by a constant value,  $\kappa_j$ . The weight  $a_j$  is the fraction of the blackbody radiation that belongs to the spectral regions of the gas and they are given as a polynomial function of the temperature  $T$ :

$$a_j = \sum_{i=0}^J b_{ij} \left( \frac{T}{T_{ref}} \right)^{j-1}, \quad (4.38)$$

where  $b_{ij}$  is the polynomial constants of the model and  $T_{ref} = 1200$  K. The part of the spectrum, in which the combustion gases do not emit, is considered as a clear gas, having an absorption coefficient  $\kappa_0 = 0$ . Its weight is determined from energy conservation considerations as:

$$a_0 = 1 - \sum_{j=0}^J a_j. \quad (4.39)$$

In ANSYS Fluent, the coefficients proposed by Smith et al. [163] are used. However, a common way of applying the WSGG model in CFD modelling is to make a grey approximation and calculate a total absorption coefficient (Eq. 4.40) to solve the spectrally integrated RTE.

$$\kappa = -\frac{\ln(1 - \epsilon)}{S_m}, \quad (4.40)$$

where the pathlength is computed according to the domain based method recommended by Hottel and Saforim [162],

$$S_m = \frac{3.6V}{A}, \quad (4.41)$$

where  $V$  is the volume of the domain and  $A$  is the corresponding surface area.

An alternative approach is the non-grey or multi-bands formulation [159], where an RTE is solved for each of the grey gases and the clear gas. Emitted blackbody radiation, corresponding to each equation, is given by the total blackbody radiation times the weight of the gas. In this formulation the non-correlated recurrence relation can be applied and for gas  $j$  the discretized RTE becomes:

$$I_{j,n} = I_{j,n-1} \exp(-\kappa_j \Delta s P(Y_{CO_2} + Y_{H_2O})) + a_j I_{b,j,n-1/2} (1 - \exp(-\kappa_j \Delta s P(Y_{CO_2} + Y_{H_2O}))) \quad (4.42)$$

where  $\Delta s$  is the length of the computational cell ranging from  $n - 1$  to  $n$ . The intensity of each gas along a path  $S_m$  is calculated successively for the  $n$  cells with Eq. 4.42, and then the total intensity is obtained as the sum of the individual intensities of the gases.

In the present thesis, both the simplified approach proposed by ANSYS Fluent and the multi-bands formulation are used. The latter was set following Bordbar et al. [164], who proposed different coefficients to account for various ratio of  $H_2O$  to  $CO_2$  concentrations, considering four grey gases ( $J = 4$ ) and one clear gas.



## Chapter 5

# Validation of the PaSR model in a Jet in Hot Co-flow flame

*The aim of this Chapter is to provide answers to important challenges encountered when simulating MILD/flameless combustion. The study is conducted in the framework of the Adelaide Jet in Hot Co-flow burner, where the co-flow is used to dilute the reactants, mimicking exhaust gas recirculation, necessary to obtain MILD combustion. First, the Partially Stirred Reactor (PaSR) combustion model, described in Chapter 4, is benchmarked for a wide set of configurations, with particular focus on the choice of the mixing model. Second, a discussion about the choice of modeling strategies to predict NO emissions, focusing on the role of NNH route, is given. Finally, a correlation between the Heat Release Rate (HRR) and species mole fraction and net reactions rate is studied.*

*This chapter is partially based on the following publications:*

**M. Ferrarotti**, Z. Li, A. Parente, “On the role of mixing models in the simulation of MILD combustion using finite-rate chemistry combustion models”, Proceedings of the Combustion Institute, 37 (4), 4531-4538, 2018.

Z. Li, **M. Ferrarotti**, A. Cuoci, A. Parente, “Finite-rate chemistry modelling of non-conventional combustion regimes using a partially-stirred reactor closure: Combustion model formulation and implementation details”, *Applied Energy*, 225, 637-655, 2018.

**M. Ferrarotti**, R. Amaduzzi, D. Bascherini, C. Galletti, A. Parente, “Heat Release Rate Markers for the Adelaide Jet in Hot Coflow Flame”, *Frontiers in Mechanical Engineering* 6, 2020.

S. Iavarone, M. Caferio, **M. Ferrarotti**, F. Contino, A. Parente, “A multiscale combustion model formulation for NO<sub>x</sub> predictions in hydrogen enriched jet flames”, *International Journal of Hydrogen Energy*, 44, 23436-23457, 2019.

**Author’s contribution to the publication** “*A multiscale combustion model formulation for NO<sub>x</sub> predictions in hydrogen enriched jet flames*”: The author optimized the PaSR model and helped in running the CFD simulations and post-processing the results.

## 5.1 Introduction and literature review

In the past years, lab-scale setups e.g. jet in hot co-flow(JHC) burners were commonly used to mimic exhaust gas recirculation process in furnace, necessary to obtain MILD combustion. The configuration of these burner flames is simple and it is very suitable for detailed measurements. Among them, the Adelaide Jet in Hot Co-flow (AJHC) [14] burner and the Delft Jet in Hot Co-flow (DJHC) [110] have received significant attention from the combustion community, serving as reference data sets for the validation of turbulent combustion models. Nevertheless the JHC configuration has some limit in emulating MILD conditions. Indeed, the fluid dynamic pattern is much more simplified, being the internal recirculation replaced by a co-flow. Furthermore, being the JHC an open-air flame, radiation does not play a major role, differently from furnaces.

From a modeling validation point of view, intensive work has been done, using these data-sets as references. Christo and Dally [71] assessed the performance of different combustion models by modelling the AJHC flames, including the steady flamelet model, the eddy dissipation concept (EDC), and transported probability density function (PDF) model, and concluded that the EDC model produced better results than the flamelet model.

Kim et al. [165] used a conditional moment closure (CMC) model to predict the flame structure and NO formation. In this work, a new approach was proposed to describe the three stream mixing in terms of a single mixture fraction, but it is not accurate downstream where interaction between fuel and fresh air becomes significant in a JHC flame. Ihme and See [166] proposed a flamelet-model for application to three-stream combustion systems in LES framework. The oxidizer split was introduced as an additional scalar to predict the mixing between two oxidizer streams and the fuel stream and used to identify flamelets of different mixture composition. It was concluded that this approach significantly improves predictions for the flame structure and the flow field in the AJHC burner system compared to the single-mixture-fraction FPV model.

EDC was widely used to simulated JHC configurations. Despite conceptual advantages of the model, EDC faces a thorny problem. Indeed, a temperature over-prediction is commonly reported in MILD regime [72, 74, 167–169]. A widely adopted remedy is to use a strongly modified set of constants for the fine structure mass fraction and residence time ( $C_\gamma$  and  $C_\tau$ ), which are key ingredients of EDC [74, 168, 169]. Recently, Ertesvg [170]

presented an extensive survey of proposed modified values revealing uncertainty of the choice, which causes lack of generality of such approach. Yet, a case-dependent character of such procedure is not satisfactory for a general applicability of the model. Therefore, some approaches aiming at generalisation of the EDC were recently presented. Parente et al. [72] proposed functional expressions for the EDC constants dependent on dimensionless flow parameters (Reynolds and Damköhler numbers) simulating the Adelaide JHC flames. They took into account specific features of the MILD combustion mode and applied the proposed changes globally and locally. This approach was further improved by Evans et al. [171] who used more accurate approaches for the determination of the chemical time-scale. Li et al. suggested the possible usage of Partially Stirred Reactor (PaSR) sub-model to account for finite-rate chemistry in the fine structures for AJHC flames, both in RANS [78] and LES [16].

The present Chapter focuses on three aspects: (i) optimization and validation of the PaSR model for AJHC flames, pointing out the main key modeling features, (ii) to assess the best approach to evaluate NO emissions and (iii) to study the correlation between HRR and species mole fraction or reaction rate in MILD combustion. To the author's knowledge, there is not, to date, a comprehensive study showing the impact of the mixing time-scale formulation, in the framework of RANS simulations of non-premixed combustion, using detailed chemistry and fine-rate chemistry combustion models. Different fuel-jet Reynolds numbers (5k, 10k and 20k) and different co-flow oxygen dilution levels (3%, 6% and 9%) are investigated.

## 5.2 Description of the AJHC Database

The Adelaide Jet in Hot Co-flow (AJHC) burner 5.1 has an insulated and cooled central jet ( $ID = 4.2$  mm) that provides an equimolar mixture of  $CH_4$  and  $H_2$  (50%-50%). An annulus pipe ( $ID = 82$  mm) with a secondary burner is mounted upstream. It provides hot combustion products, which are further mixed with air and nitrogen to control the oxygen levels. The wind tunnel, on which the burner is mounted, has a  $254\text{ mm} \times 254\text{ mm}$  cross section [14]. A scheme of the experimental facility is illustrated in Figure 5.1. More details about the experiments carried out by Dally et al. in the Adelaide JHC burner can be found in [14]. The experimental dataset includes different oxygen levels in the co-flow (3%, 6% and 9%, as mass fraction) at different fuel-jet Reynolds number (5k, 10k and 20k).

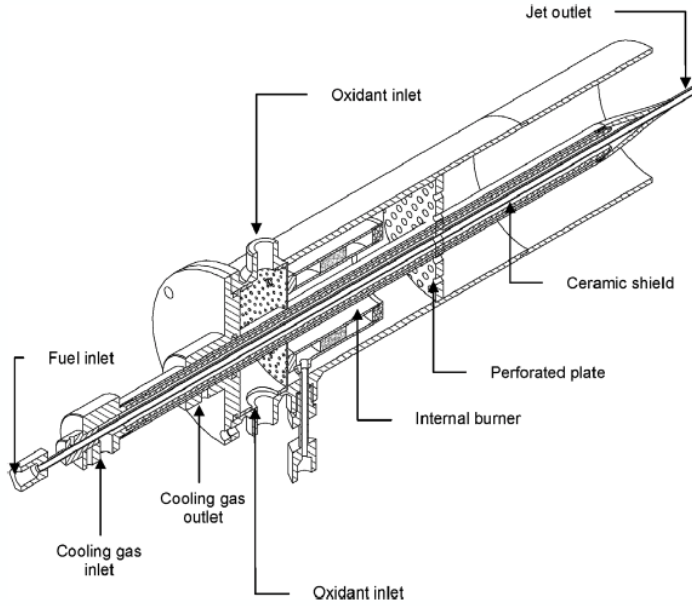


**Figure 5.1:** Schematic of the Adelaide Jet in Hot Co-flow burner, taken from [14].

The central jet, annulus and wind tunnel gas temperatures and velocities (for the  $Re = 10k$  case) are presented in Table 5.1 . In the current study, 5 cases with the combination of different co-flow oxygen contents and fuel jet Reynolds numbers are investigated, as highlighted in Table 5.2. The other conditions are not considered since no experimental data is provided for them.

**Table 5.1:** Physical properties of the jet (Central jet velocity is for the  $Re=10k$  case).

Profiles	Fuel Jet	Co-flow	Tunnel
Velocity	58.74 m/s	3.2 m/s	3.3 m/s
Temperature	294 K	1300 K	294 K

Dally et al. [14] measured temperature and species ( $CH_4$ ,  $H_2$ ,  $O_2$ ,  $CO_2$ ,



**Table 5.2:** List of the investigated cases for AJHC.

Co-flow O <sub>2</sub>	3%	6%	9%
Re = 5k	✓		
Re = 10k	✓	✓	✓
Re = 20k	✓		

CO, H<sub>2</sub>O, OH, N<sub>2</sub> and NO) mass fraction were taken at the centerline as well as at different axial locations  $z = 30/60/120/200$  mm (Figure 5.2 right) via the single-point Raman-Rayleigh-laser-induced fluorescence technique. The above-mentioned scalars were measured instantaneously and simultaneously [14]. The mean and standard deviation values are available for validation. The experimental profiles used for comparison include both the mean values and the error bar with 99.5% confidence interval associated with a Student's distribution for the true mean value [172].

### 5.3 Numerical setup

RANS simulations were carried out using the ANSYS Fluent 19.0 solver. The computational domain starts from the AJHC burner exit and extends 1 m further downstream. A 2D simple sketch of the domain investigated in the numerical modeling is shown in Figure 5.2 left. A two-dimensional axisymmetric grid of about 35k quadrilateral cells was employed (Figure 5.2 right), applying a large refinement across the reaction zone to well capture gradients of composition and temperature. Two additional grids were considered to evaluate the Grid Convergence Index (GCI), which was lower than 3% for temperature and major species. A mass-flow boundary condition was applied for the fuel inlet [14], while velocity-inlet conditions were considered for the air tunnel and the co-flow, as reported in Table 5.1. Uniform boundary conditions for species mass fractions and temperature [14] were employed, while a non-uniform boundary condition was considered only for NO mass fraction when analysing pollutant formation. The latter was taken from the mean sampled experimental value at 4 mm downstream of the jet exit, as suggested by the study of Christo et al. on the same experimental facility [71].

Inlet diffusion was taken into account because of the presence of hydrogen in



## 5.4 Results and discussion

In this section, the results of RANS simulations are compared to experimental temperatures and major and minor species extracted at several axial locations, i.e., 30/60/120 mm in radial direction and along the centerline. The simulated cases are reported in Table 5.2. The section is structured as follows: first, a sensitivity analysis to test the effect of the turbulence modeling and kinetic scheme is presented, second a parametric analysis compares the mixing time scale definitions, as explained in Chapter 4. Thereafter, the NO emissions modeling strategies and the correlations between HRR and species or reaction rate are reported as well.

### 5.4.1 Preliminary Analysis

The goal of this preliminary sensitivity analysis was to test the effect of the turbulence modeling and kinetic scheme for the case  $Re = 10k$  and 3%  $O_2$ , adopting a static  $C_{mix} = 0.5$ . Figure 5.3 shows a comparison between the measured and calculated temperature profiles, obtained with the different combinations of turbulence models and chemical schemes. It appears clear that the jet decays and spreads with increasing axial distance. However, the decay and spread rates are over-estimated by standard and realizable  $k-\epsilon$  models. Best predictions, in both radial and axial directions, were obtained by applying the modified  $k-\epsilon$  version ( $C_{\epsilon 1} = 1.6$ ) as suggested by Dally et al. [130]. This is in accordance with Christo and Dally [71], who firstly employed the modified  $k-\epsilon$  model in simulating the AJHC flames. The modified  $k-\epsilon$  and RSM turbulence models employ the same equation for the dissipation rate of turbulent kinetic energy ( $\epsilon$ ). Indeed, they show similar results at all axial distances, even if the latter has a tendency to underpredict temperature along the centerline. From a kinetic point of view, the differences between KEE and GRI-2.11 based on temperature profiles are minor and below 3% in all cases, thus justifying the further use of the KEE mechanisms, which only consists of 17 species with respect to the 33 of GRI-2.11. Results showed that the KEE mechanism coupled with modified  $k-\epsilon$  ( $C_{\epsilon 1} = 1.6$ ) provides the best compromise between accuracy and computational cost. Indeed, the choice of the modified  $k-\epsilon$  with KEE only worsen by 2% the global predictions of RMS, with a gain in CPU time of 30%. This combination will be used throughout the study.

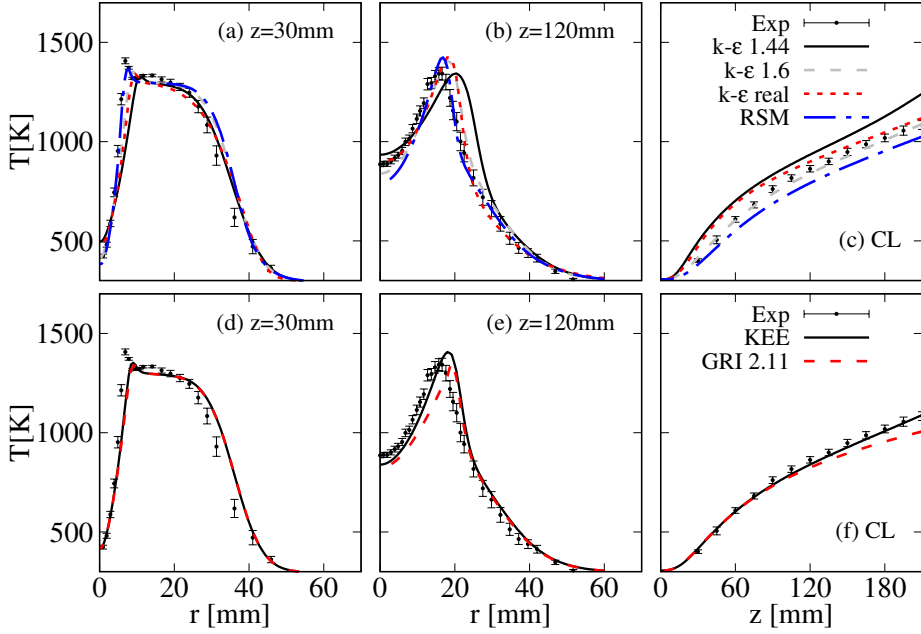


**Figure 5.3:** Sensitivity analysis of turbulence models (using KEE) and kinetic schemes (using  $k-\epsilon$   $C_{\epsilon 1}=1.6$ ) on the mean temperature profiles, at  $z=30$  mm (a-d),  $z=120$  mm (b-e) and along the centerline (c-f). Case  $Re=10k$  and 3%  $O_2$ , adopting  $C_{mix}=0.5$ .

#### 5.4.2 Effect on the choice of the mixing model

The objective of this section is to assess the effectiveness of the approaches for the estimation of the mixing time-scales of the PaSR model, as proposed in Chapter 4. A static, fractal-based and dynamic models were then used to evaluate  $\tau_{mix}$ . The chemical time scale was estimated from the formation rates, considering  $CH_4$ ,  $H_2$ ,  $CO_2$ ,  $O_2$  and  $H_2O$  as target species and uniform boundary conditions were used.

In a first attempt, a static approach was applied (Eq. 4.28) to determine the  $C_{mix}$  that best represents the experimental data for the case  $Re = 10k$  and 3%  $O_2$ . Figure 5.4 compares different  $C_{mix}$  together with EDC-2016 [72], in terms of radial temperature profiles at different axial locations and along the centerline. It can be observed that determining an appropriate value for this parameter is paramount to get accurate results. All the models offer

good prediction for  $z = 30$  mm, but only  $C_{mix} = 0.5$  allows to reduce the typical temperature over-prediction observed at  $z = 120$  mm, resulting in very good predictions of the peak temperature (only 4% relative deviation). Figure 5.4 also shows that with  $C_{mix} = 0.5$  a very accurate representation of the centerline temperature is obtained. EDC-2016 seems to behave like  $C_{mix} = 0.3$ , indeed it performs well at  $z = 30$  and 60 mm, but it over-estimates at  $z = 120$  mm. Discrepancies can still be noticed for  $r > 25$  mm at  $z = 30$  and 60 mm. This region is experimentally characterized by high Root Mean Square (RMS) error values and a sufficient level of accuracy can be achieved only performing a LES study [16]. The same considerations can be drawn looking at the water mass fraction predictions of Figure 5.5.

Despite the very good predictions, this PaSR static approach has several drawbacks. Indeed,  $C_{mix}$  is not a function of local variables, being arbitrarily chosen and constant in every cell of the domain. This implies that a model sensitivity must be always carried out to use this model, since no *a priori* method can be used to infer the value of  $C_{mix}$ . This might limit the use of such an approach for expensive 3D simulations.

The second approach tested in this work is based on a fractal representation of the mixing time-scale (Eq. 4.29). The improvement consists in the fact that  $C_{mix,eq}$  becomes a function of the local  $Re_t$ . However, the fractal dimension  $D$  in Eq. 4.29 still needs to be guessed. Figure 5.6 shows that the best model results are achieved with  $D = 4.4$  and are in line with the ones obtained with  $C_{mix} = 0.5$ . As predictable, decreasing the time-scale to the Kolmogorov one ( $D = 3.5$  and  $D = 4$ ) leads to temperature over-predictions, especially at  $z = 120$  mm.

Finally, the dynamic model based on the scalar mixing time-scale (Eq. 4.30) is applied. In this case, a dynamic  $C_{mix,eq}$  (Eq. 4.31) is obtained from the solution of two transport equations for the mixture fraction variance and dissipation rate (Eq. 4.32-4.33). Such an approach, potentially provides a local optimal mixing scale, with no need for user input. For sake of clarity, the different dynamic models tested in the present work are indicated as “Dyn Chen”, “Dyn JM” and “Dyn Sommer”, following Table 4.1. The dynamic approaches and the static one are compared in Figure 5.7, in terms of mean temperature and important minor species mass fractions, such as CO and OH. No major differences can be observed along the centerline and at  $z = 120$  mm, while the dynamic models improve the predictions at 30 mm and 60 mm. Thus, results confirm that using a local adapted mixing time-scale leads to temperature predictions comparable to the ones

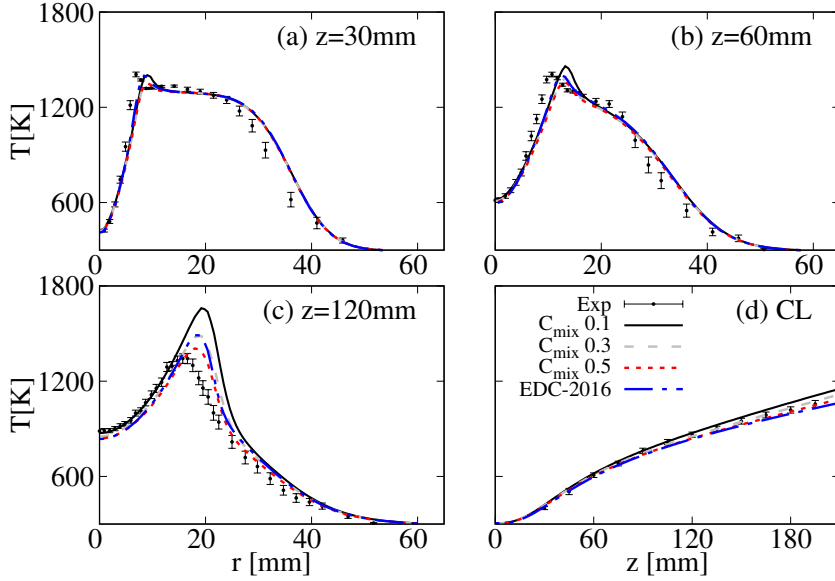


**Figure 5.4:** Sensitivity analysis of  $C_{mix}$  using a static approach on the mean temperature profiles, at  $z=30$  mm (a),  $z=60$  mm (b),  $z=120$  mm (c) and along the centerline (d). Case  $Re=10k$  and 3%  $O_2$ . Modified  $k-\epsilon$  and KEE.

provided by the constant  $C_{mix}$  and fractal approaches, without the need of fine tuning the constants. Moreover, the dynamic models strongly improve the chemical species predictions, at all locations. This is clear from the analysis of the results at  $z = 30$  mm (Figure 5.7), which indicates a strong improvement of OH and CO predictions. Using “Dyn JM”, the relative error on the peak predictions of OH and CO is lowered to 6% and 25% respectively, with respect to 75% and 60% obtained with  $C_{mix} = 0.5$ . The same conclusion is observed at the centerline for CO mass fraction. No major differences can be noticed between the three dynamic models. The analysis of the CO radial profiles in Figure 5.12 shows the existence of a second peak,  $z \approx 30$  mm, in the experimental data. This is due to the non-zero CO concentration in the hot co-flow, that is convected downstream. Because uniform boundary conditions are adopted in the current simulations, this second peak can not be captured.

The scaled CPU time associated to the various mixing models are estimated taking the static  $C_{mix} = 0.1$  as reference in Table 5.3. Even though using  $C_{mix} = 0.1$  reduces the CPU time, this would lead to non-negligible over-

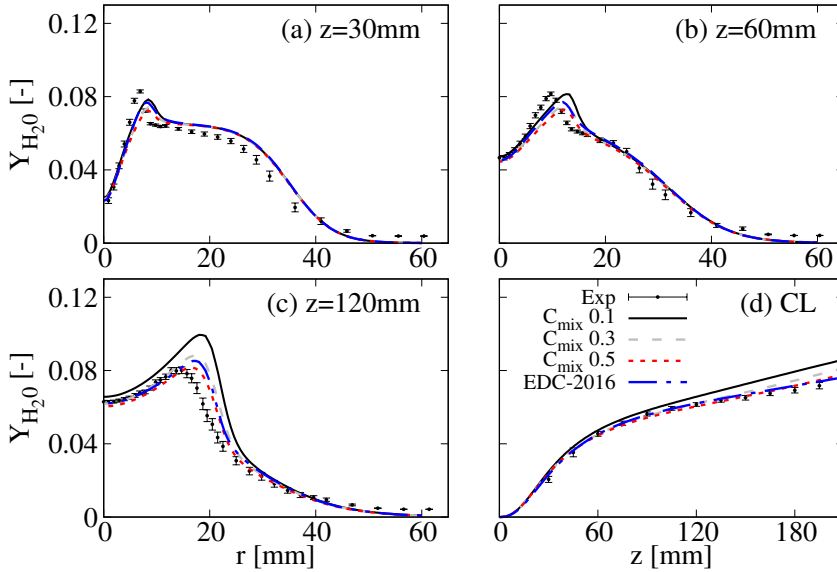


**Figure 5.5:** Sensitivity analysis of  $C_{mix}$  using a static approach on the mean  $H_2O$  profiles, at  $z=30$  mm (a),  $z=60$  mm (b),  $z=120$  mm (c) and along the centerline (d). Case  $Re=10k$  and 3%  $O_2$ . Modified  $k-\epsilon$  and KEE.

prediction of mean temperature and species mass fraction at  $z = 120$  mm (see Figures 5.4-5.5). On the other hand, the dynamic models do not have a strong impact on the required CPU time compared to the best static model scenario, since only three additional transport equations for a conserved scalar need to be solved.

**Table 5.3:** CPU time consumption of various mixing models.

Model	$C_{mix} = 0.1$	$C_{mix} = 0.5$	Fractal	Dynamic
CPU time	1	1.4	1.45	1.6

To highlight the differences between the models, an equivalent  $C_{mix}$  is defined as  $C_{mix,eq} = \tau_{mix}/(k/\epsilon)$ , where  $\tau_{mix}$  is the mixing scale provided by the different approaches and it is shown in Figure 5.8. The use of a fractal model with  $D = 4.4$  provides a  $C_{mix,eq}$  profile very close to a constant one

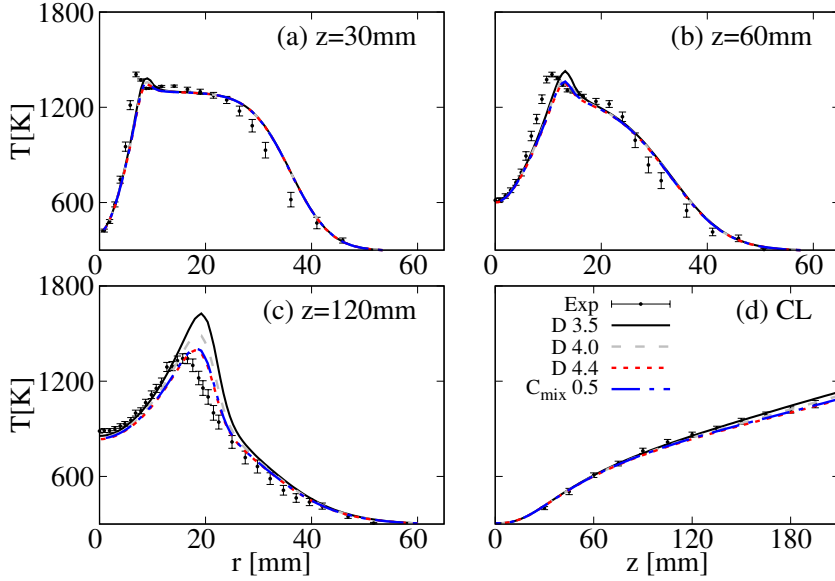


**Figure 5.6:** Sensitivity analysis of  $D$  using a fractal approach on the mean temperature profiles, at  $z=30$  mm (a),  $z=60$  mm (b),  $z=120$  mm (c) and along the centerline (d). Case  $Re=10k$  and 3%  $O_2$ . Modified  $k-\epsilon$  and KEE.

( $C_{mix} = 0.5$ ), with only slight changes due to the variation of  $Re_t$  (Eq. 4.29). Thus, the fractal approach is not able to provide local optimal values of the mixing constant, resulting in the same level of under-prediction and over-prediction. This suggests that the choice of  $Re_t$  to parametrize the mixing constant in the fractal model is not optimal, at least in the present framework. The use of a dynamic approach, based on local value of scalar variance and dissipation rate, results in a distribution of  $C_{mix,eq}$  capable of capturing not only the interaction between fuel and co-flow, but also the breakup of large eddies into smaller ones downstream the fuel jet. In particular, for the dynamic models, the profile (Figure 5.8a) decreases radially in correspondence of the maximum temperature zone, while it increases moving downstream along the axial direction (Figure 5.8b). This particular behaviour explains the ability of the model to improve the predictions at all axial locations with respect to the other approaches, due to the possibility of estimating local optimal values of  $C_{mix,eq}$  and  $\tau_{mix}$ . In particular, the increasing trend shown in Figure 5.8b explains the ability of the model to capture the experimental data above  $z = 100$  mm axial



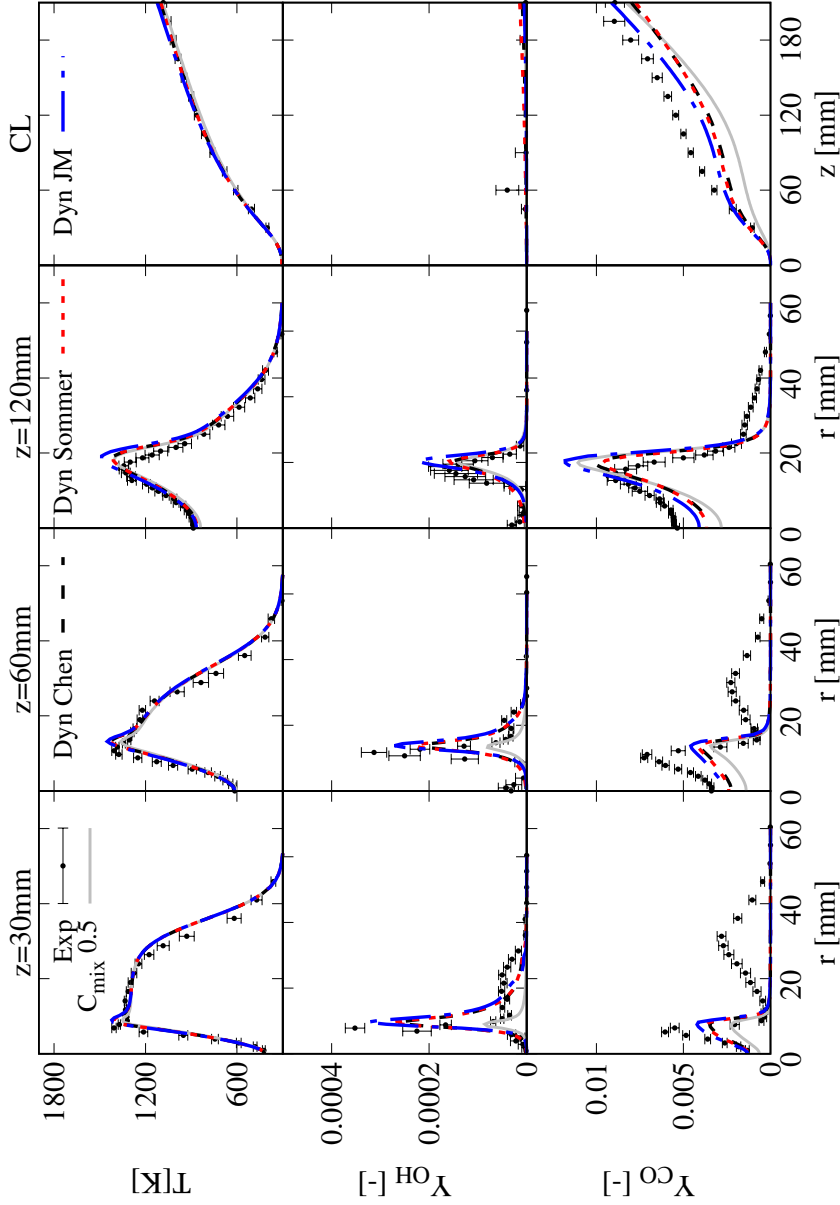


**Figure 5.7:** Comparison between different mixing models based on mean temperature, mean CO and OH mass fraction profiles. Re=10k and 3% O<sub>2</sub> in the co-flow. Modified k- $\epsilon$  and KEE.

distance from the burner, with remarkably accuracy. Among the dynamic model variants, the "JM" provides higher  $C_{mix,eq}$  values, corresponding to lower  $\kappa$  in PaSR model.

Finally, Figure 5.9 compares the best performing case in RANS (KEE with both "Dyn Sommer" and "Dyn JM") and the LES predictions of Li et al. [16]. In their LES study, the authors used PaSR model with KEE kinetic scheme, considering the mixing time scale as the geometrical mean of the sub-grid velocity stretch time and the Kolmogorov time scale. RANS is able to deliver results whose accuracy is comparable with the one achieved by Li et al. [16] with LES, at a much lower computational cost. However, LES manages to alleviate the over-prediction noticed in RANS for  $r > 25$  mm at  $z = 30$  and  $60$  mm and on the peak at  $z = 120$  mm.

For the purpose of investigating how the model performs for varied configurations, a comparison adjusting the oxygen content in the co-flow to 3% (HM1 flame), 6% (HM2 flame) and 9% (HM3 flame) was conducted comparing different dynamic models. Figure 5.8c shows a little sensitivity of  $C_{mix,eq}$  varying the oxygen mass fraction for "Dyn Chen" at  $z = 120$  mm. Temperature predictions are reported in Figure 5.10. All the dynamic models are able to reproduce correctly the shape and peak position of the temperature profiles at different oxygen levels. In particular, two models ("Dyn Chen" and "Dyn Sommer") provides comparable predictions, alleviating the slight over-prediction at  $z = 120$  mm for the three oxygen contents provided by "Dyn JM". For instance, the relative error on the peak predictions is lowered to 1% with respect to 7% at  $z = 120$  mm and  $Y_{O_2} = 6\%$ . Capturing the OH radical mass fraction distribution is very important, as it can be used as flame marker. In Figure 5.11 the experimental and numerical profiles of OH mass fraction are shown, for different  $O_2$  levels in the co-flow (3%, 6% and 9%). The analysis confirms what was already pointed out for  $Y_{O_2} = 3\%$ , even if slight under-predictions are observed at  $z = 60$  mm and  $120$  mm going towards a more conventional flame behaviour (i.e. 6% and 9%). Similar considerations can be drawn from the analysis of a minor species mass fraction, such as CO (Figure 5.12). "Dyn JM" is the mixing model that provides the best predictions of CO mass fraction for all the positions and oxygen contents. However, none of the models can accurately reproduce the centerline profile. The results shown above refer to cases with a fixed Reynolds number, varying the  $O_2$  content in the co-flow. This means that the mixing time is not strongly affected, as clearly shown in Figure 5.8c. However, the chemical time scale changes due to the change of the oxidizing atmosphere. The contour plots showing the

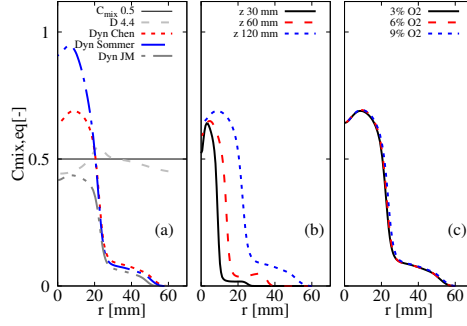


**Figure 5.8:** Radial  $C_{mix}$  distribution as a function of (a) different mixing models ( $z=120$  mm,  $Re=10k$ , 3%  $O_2$ ), (b) axial position ( $Re=10k$ , 3%  $O_2$ , “Dyn Chen”) and (c)  $Y_{O_2}$  in the co-flow ( $Re=10k$ , “Dyn Chen”,  $z=120$  mm).

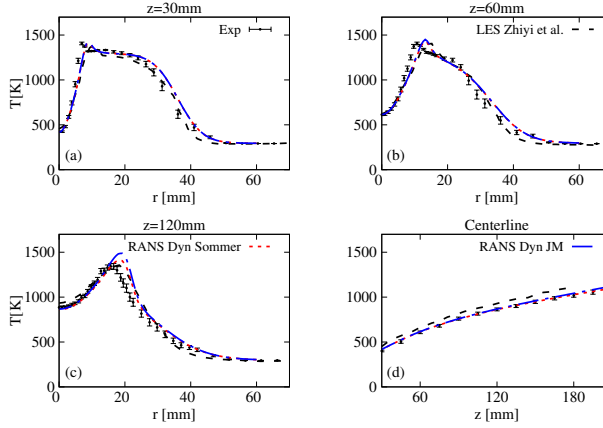


**Figure 5.9:** Comparison between RANS and LES (Li et. al [16]).  $Re=10k$ , 3%  $O_2$ . Modified  $k-\epsilon$  and KEE.

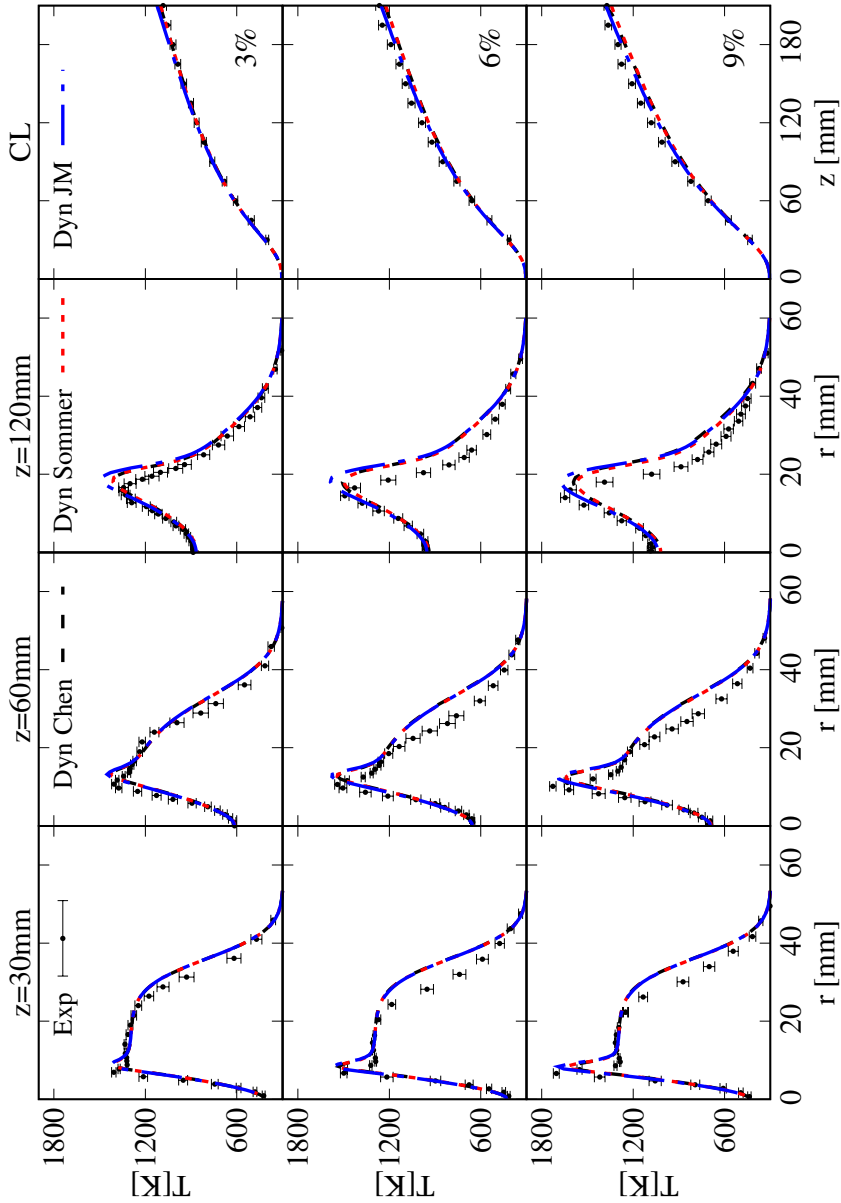


**Figure 5.10:** Comparison between different mixing models based on mean temperature for different co-flow oxygen levels (3%, 6% and 9%).  $Re=10\text{ k}$ . Modified  $k-\epsilon$  and KEE.

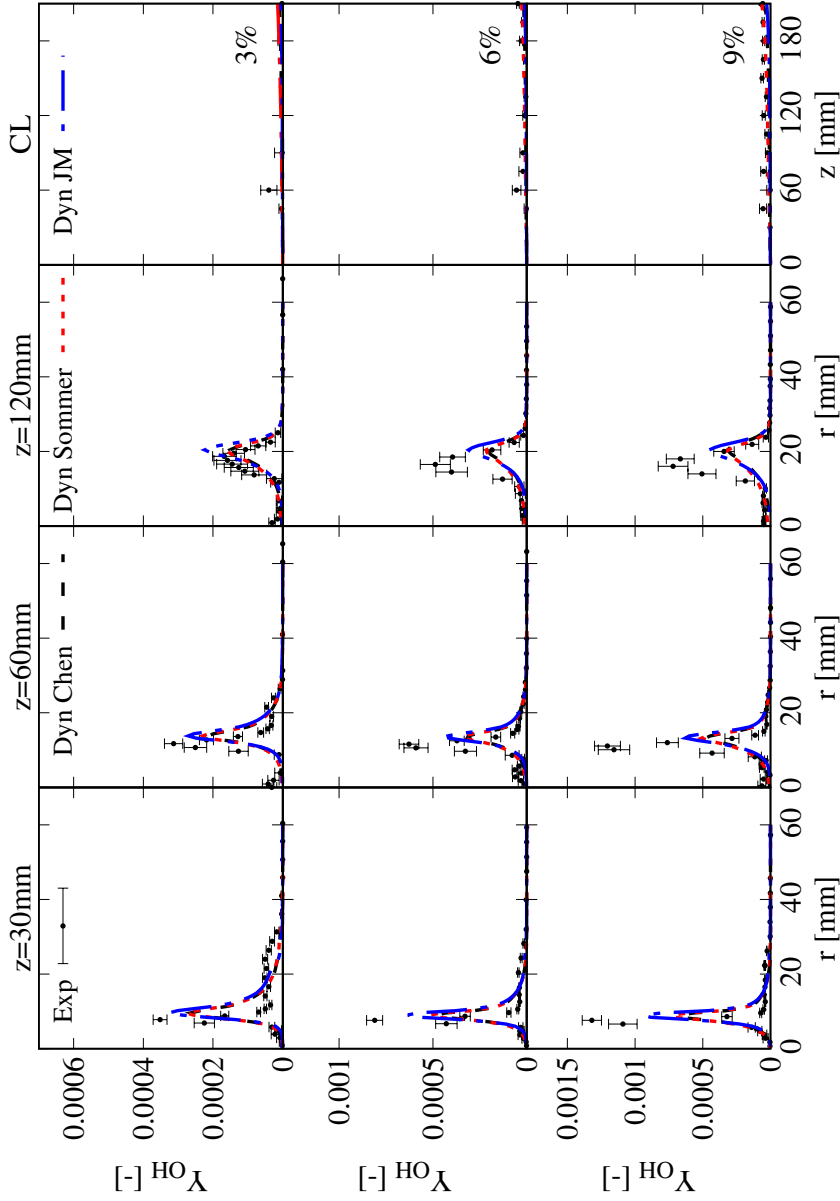


**Figure 5.11:** Comparison between different mixing models based on mean OH mass fraction for different co-flow oxygen levels (3%, 6% and 9%).  $Re=10$  k. Modified  $k-\epsilon$  and KEE.

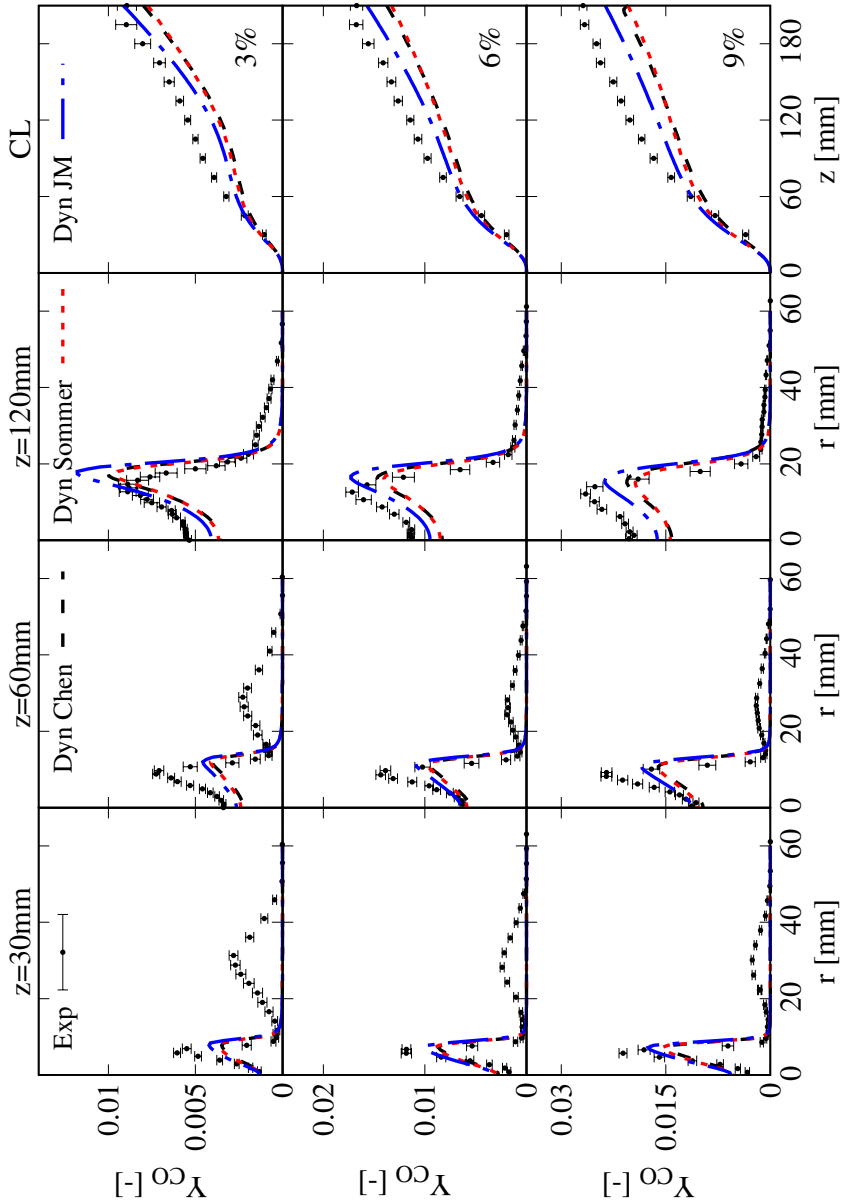


**Figure 5.12:** Comparison between different mixing models based on mean CO mass fraction for different co-flow oxygen levels (3%, 6% and 9%).  $Re=10\text{ k}$ . Modified  $k-\epsilon$  and KEE.

chemical time scale distributions for the three  $O_2$  level cases (3%, 6% and 9%) are compared in Figure 5.13. With increasing oxygen content, more oxygen is available to mix with the fuel stream, and the reaction process is enhanced. This can be well indicated by the expansion of the reactive region in the flow, which is characterized by chemical time scales ( $\tau_c$ ) much smaller than the fixed threshold value of 0.1s.

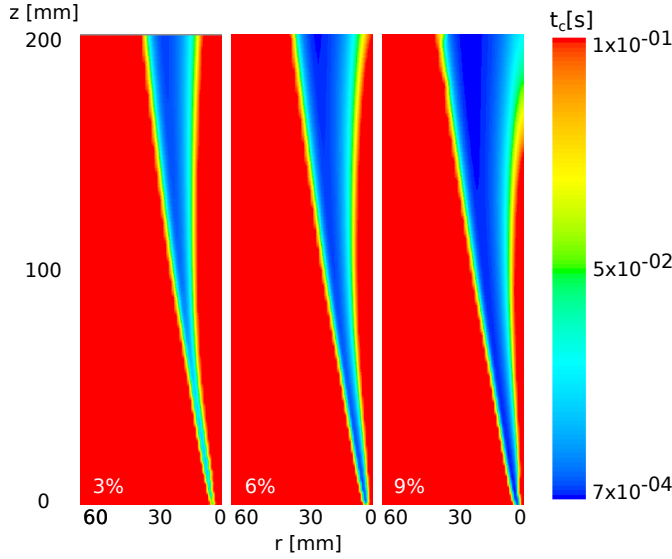


**Figure 5.13:** Chemical time scale ( $\tau_c$ ) distribution for different co-flow oxygen levels (3%, 6% and 9%).  $Re=10$  k. Modified  $k-\epsilon$ , KEE and “Dyn JM”. Only the area of interest of the simulation domain is shown.

For the purpose of investigating how the model performs for varied flow field, cases with different fuel jet Reynolds numbers are simulated, fixing co-flow oxygen content to 3%. The mean temperature profiles and species distribution (OH and CO) are presented in Figures 5.14-5.15-5.16, separately. At  $Re = 5k$ , the mean temperature profiles (Figure 5.14) are well predicted using all the dynamic models or a static model with  $C_{mix} = 0.5$  (not shown here for sake of clarity). However, the error in CO and OH predictions at  $z = 30$  mm is reduced from 90% to 2% and from 50% to 15%, respectively, using the “Dyn JM” model, with respect to a static case. At  $Re = 20$  k, the experimental data show a strong temperature reduction for increasing distance from the burner nozzle, at  $z = 120$  mm, due to the

partial extinction of the flame caused by the increased jet velocity, as documented in [72]. All the dynamic models allow to well capture the profiles at  $z = 30$  mm, while only “Dyn Sommer” helps reducing the temperature, CO and OH over-prediction at  $z = 120$  mm, catching well the first region of the flame.

The  $C_{mix,eq}$  distribution with various fuel jet Reynolds numbers can be appreciated in Figure 5.17. The  $Re = 5k$  case shows a pronounced shear layer between the co-flow and fuel jet. This layer is progressively reduced when increasing the Reynolds number to 10k and 20k. The reason is that the increased fuel jet velocity reduces the inter-facial area and diminishes mixing [175]. For a fully developed turbulent pipe flow, the turbulent intensity has a negative correlation with the Reynolds number, meaning that higher Reynolds number jet breaks up later than the one with lower Reynolds number [176]. Therefore, a larger mixing scale is found for the case with higher Reynolds number, thus resulting in higher  $\tau_{mix}$  value and lower values of reacting fractions. This justifies the reduction of the temperature levels going from  $Re = 5k$  to  $Re = 20k$ , as seen in Figure 5.14.

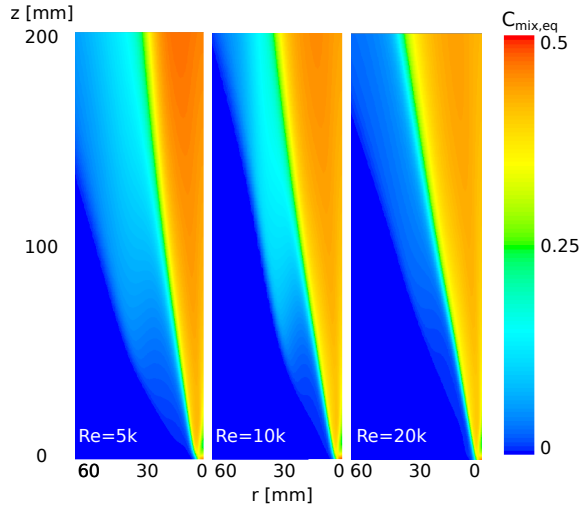


**Figure 5.17:** Mixing time constant  $C_{mix,eq}$  distribution for the different fuel jet Reynolds number cases (5k, 10k and 20k). Only the area of interest of the simulation domain is shown.



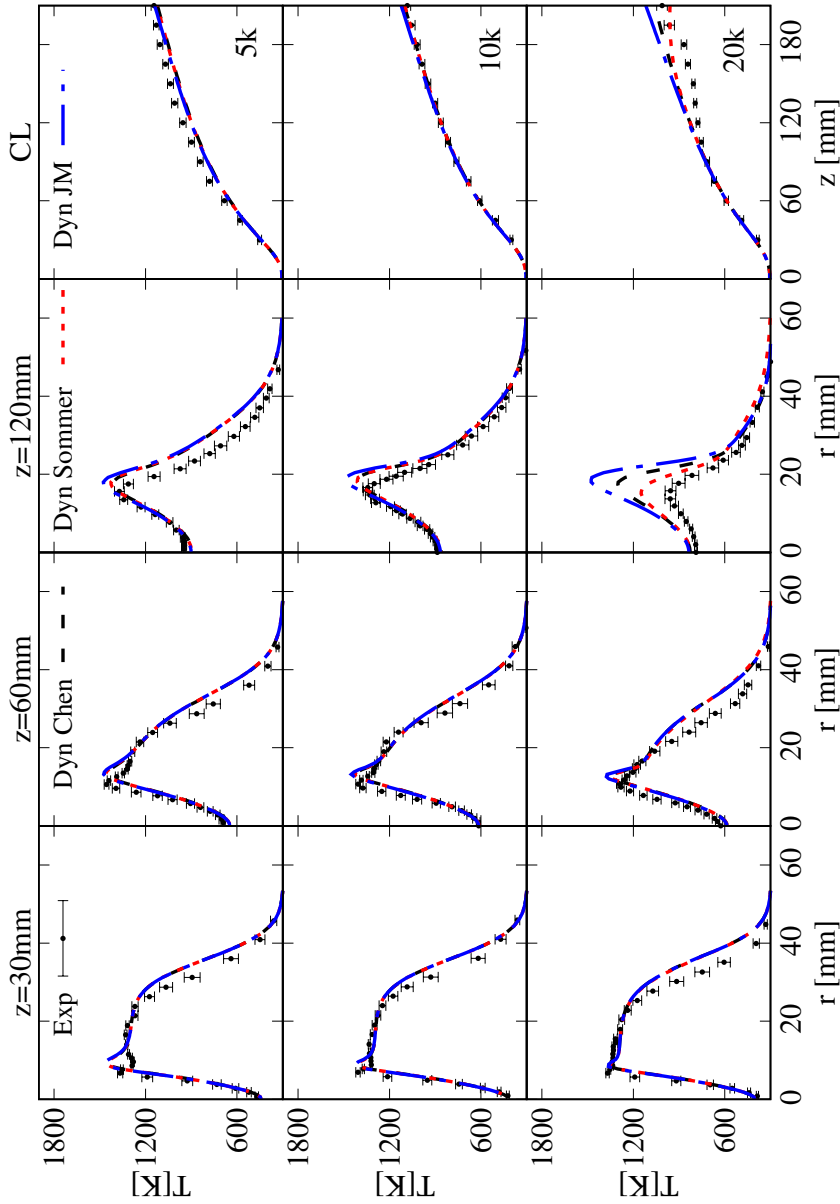


**Figure 5.14:** Comparison between different mixing models based on mean temperature for different fuel jet Reynolds number (5k, 10k and 20k). Modified  $k-\epsilon$  and KEE.

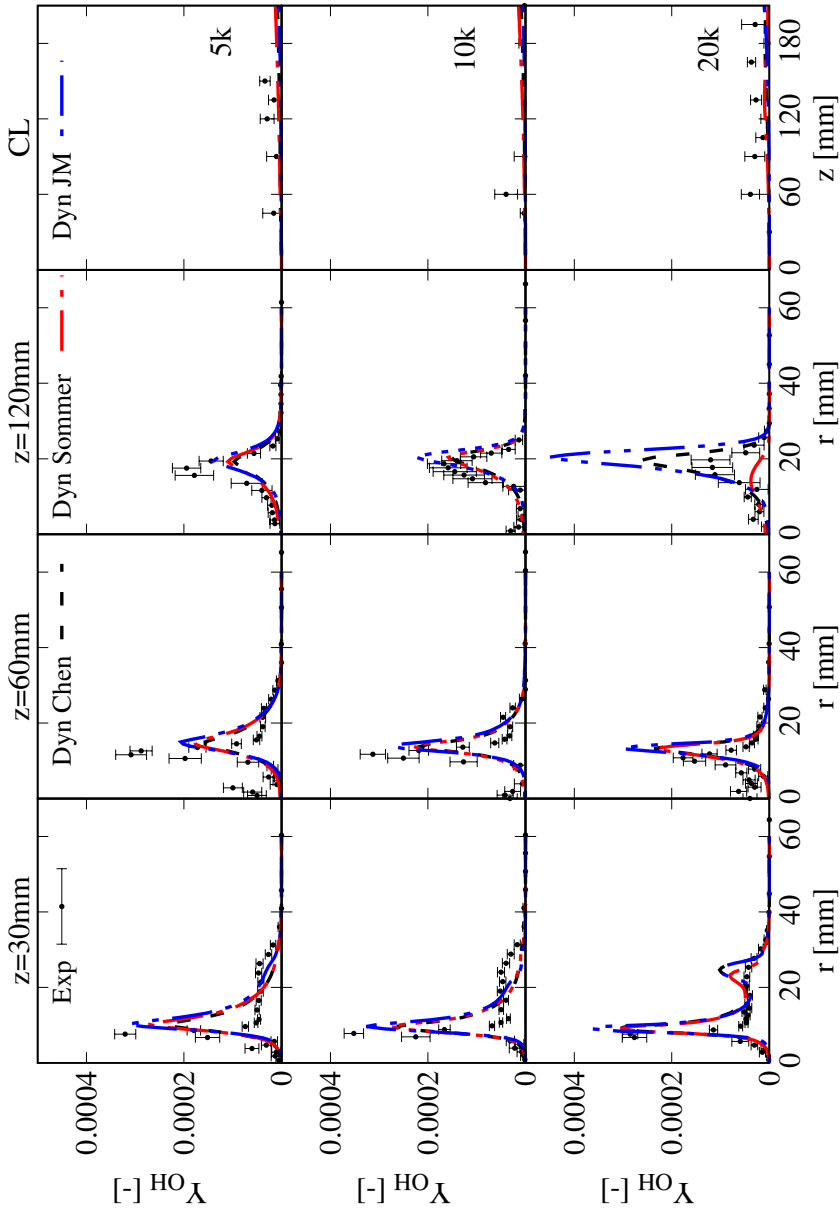


**Figure 5.15:** Comparison between different mixing models based on mean OH mass fraction for different fuel jet Reynolds number (5k, 10k and 20k). Modified  $k-\epsilon$  and KEE.

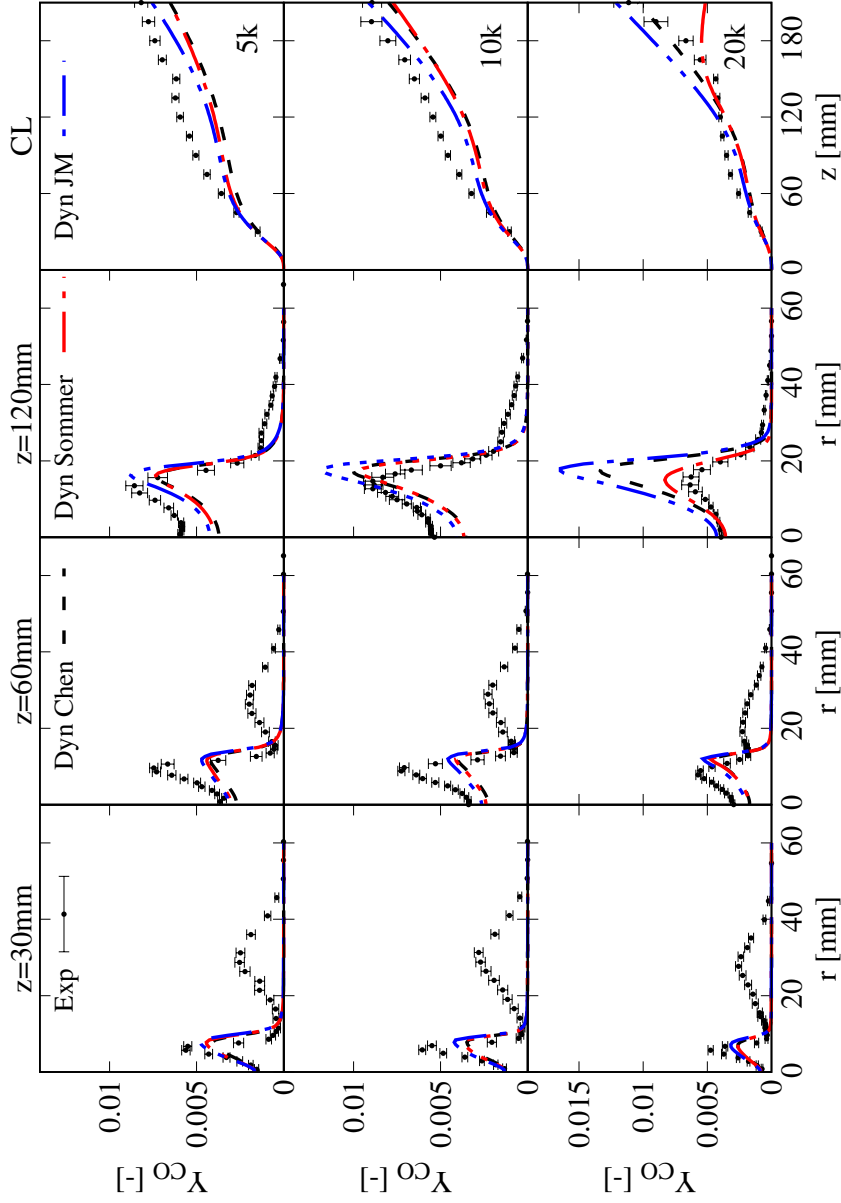


**Figure 5.16:** Comparison between different mixing models based on mean CO mass fraction for different fuel jet Reynolds number (5k, 10k and 20k). Modified  $k-\epsilon$  and KEE.

### 5.4.3 NO predictions

This section analyses different strategies to quantify NO emission in the AJHC burner. First, the ANSYS Fluent post-processing tool was applied on the case “Dyn JM” coupled with KEE, shown in the previous section, being one of the most performing in terms of temperature and OH predictions. Predicting accurately the latter might paramount to achieve accurate NO predictions. Thermal NO emissions were modeled using a Finite Rate (FR) approach obtained from the Zeldovich scheme by assuming steady state for the N radicals:

$$\frac{d[NO]_{th}}{dt} = k_{th}[N_2][O], \quad (5.1)$$

where the  $k_{th}$  is the kinetic rate constant, which follows an Arrhenius expression,  $[NO]$ ,  $[N_2]$  and  $[O]$  are the concentration of nitric oxide, nitrogen and O radical, respectively. The O radical concentration was taken directly from the detailed kinetic mechanism. Prompt NO formation is modeled according to De Soete [177]:

$$\frac{d[NO]_{pr}}{dt} = k_{pr}[FUEL][N_2][O_2]^\alpha f, \quad (5.2)$$

where  $f$  is a correction factor that depends on the number of carbon atoms per molecule of the hydrocarbon fuel and on the fuel/air equivalence ratio,  $k_{pr}$  is the kinetic rate constant,  $[NO]$ ,  $[FUEL]$ ,  $[N_2]$  and  $[O_2]$  are the concentration of nitric oxide, hydrocarbon fuel, nitrogen and oxygen, respectively, and  $\alpha$  is the oxygen reaction order, which depends on the  $O_2$  mole fraction in the flame. The NO formed via the  $N_2O$ -intermediate route is instead modeled via the following reaction rate expression:

$$\frac{d[NO]_{N_2O}}{dt} = k_f[N_2O][O] - k_b[NO]^2, \quad (5.3)$$

where  $k_f$  and  $k_b$  are the kinetic rate constants for the forward and the backward reaction, respectively, of the reaction  $N_2O + O \rightleftharpoons NO + NO$ . The quasi-steady-state assumption is considered or the calculation of the  $N_2O$  concentration. Regarding the NNH pathway, a one-step global reaction rate was proposed by Konnov et al. [7]:

$$\frac{d[NO]_{NNH}}{dt} = k_0 \exp\left(-\frac{T_a}{T}\right)[N_2][O]X_H, \quad (5.4)$$

where  $k_0$  is the pre-exponential factor,  $T_a$  is the activation temperature,  $[N_2]$ ,  $[O]$  and  $X_H$  are the concentration of nitrogen, O radicals and the mole

fraction of H radicals, respectively. As mentioned in Chapter 1, Konnov et al. [7] derived a range of uncertainty for the activation temperature  $T_a$ , i.e.,  $T_a = 3600 \pm 600$  K. However, a later study by Klippenstein et al. [5] has quantified with negligible uncertainty such heat of formation (Figure 1.5). A one-step global reaction rate for the NNH pathway is not featured in the ANSYS Fluent post-processing tool. Thus, it was implemented by means of a bespoke User Defined Function (UDF) according to Equation 5.4.

Figure 5.18 shows the experimental and numerical NO mass fraction profiles at different axial positions ( $z = 60, 120$  and  $200$  mm), varying the sets of kinetic parameters considered for the NNH route: the nominal value proposed by Konnov et al. [7], Hayhurst et al. [8] and Klippenstein et al. [5]. A negligible difference, of the order of tenth of ppm, can be appreciated among the predictions coming from the implemented kinetic rates of the NNH route. This result can be explained by the minimal relevance of the NNH pathway compared to the prompt NO, which resulted to be the exclusive source of NO when the ANSYS Fluent post-processing tool is used.

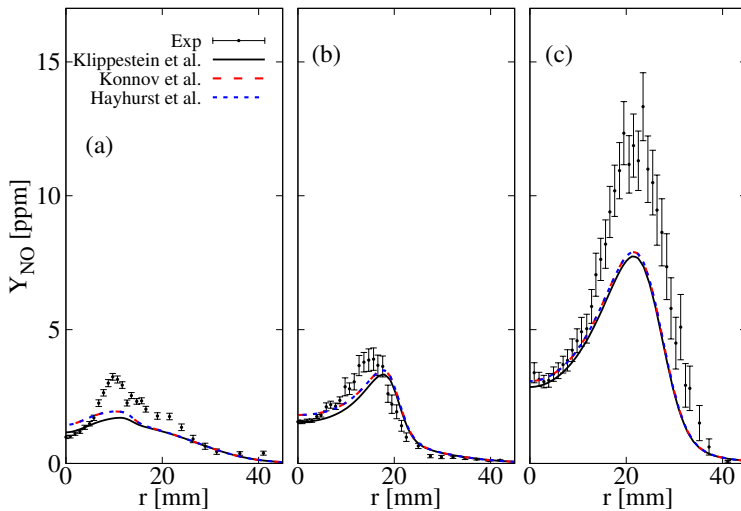


**Figure 5.18:** Experimental and numerical NO mass fraction profiles at axial locations  $z=60$  mm (a),  $z=120$  mm (b), and  $z=200$  mm (c). “Dyn JM” and KEE.

In fact, Figure 5.19 shows the prominent amount of NO emitted by the

prompt route, and the negligible amount coming from all the other pathways, including NNH, when the post-processing tool is used. These results show the inability of one-step global reaction rates to describe NO profiles, which involves pathways with fast intermediates, whose formation is strictly linked to the radical pool resulting from the fuel oxidation kinetics. Improved predictions of NO formed via the NNH route, as well as the prompt route, may require the use of a detailed NO mechanism, either coupled or uncoupled with the fuel oxidation chemistry. For this reason, the analysis targeted the simulations with “Dyn JM” and GRI-2.11 (49 species and 279 elementary reactions), which avoids the use of the post-processing tool for NO. The sets of kinetic parameters proposed by Hayhurst et al. [8] and Klippenstein et al. [5] were considered and implemented in GRI-2.11 by changing the parameters of the following reactions:  $\text{H} + \text{N}_2 \rightleftharpoons \text{NNH}$  and  $\text{NNH} + \text{O} \rightleftharpoons \text{NH} + \text{NO}$ , because these reactions are considered the rate-limiting steps of NO formation via NNH.

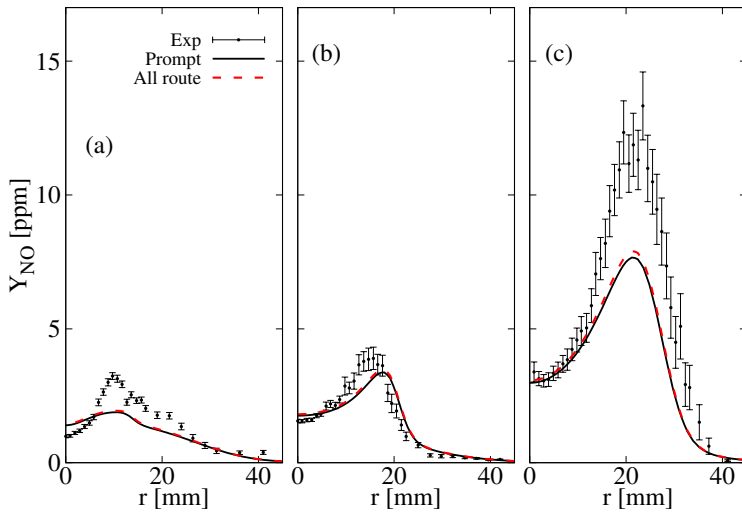


**Figure 5.19:** Experimental and numerical NO mass fraction profiles at axial locations  $z=60$  mm (a),  $z=120$  mm (b), and  $z=200$  mm (c). “Dyn JM” and KEE.

The results are reported in Figure 5.20. A significant difference can be noticed among the predictions coming from the implemented kinetic rates for the NNH route. The modification that follows the kinetics proposed by Hayhurst et al. [8] leads to a good prediction of NO at axial locations  $z =$

60 mm and  $z = 200$  mm, but to a slight over-estimation of NO at  $z = 120$  mm. The kinetic parameters implemented in the GRI-2.11 scheme lead to predictions included in the range determined by the other two sets of parameters, as expected. It is clear that the use of a one-step global rate scheme for all the NO formation pathways lacks the necessary chemical accuracy and furthermore overshadows the importance of the NNH pathway in this combustion regime, as well as the interactions of this pathway with the other NO routes.

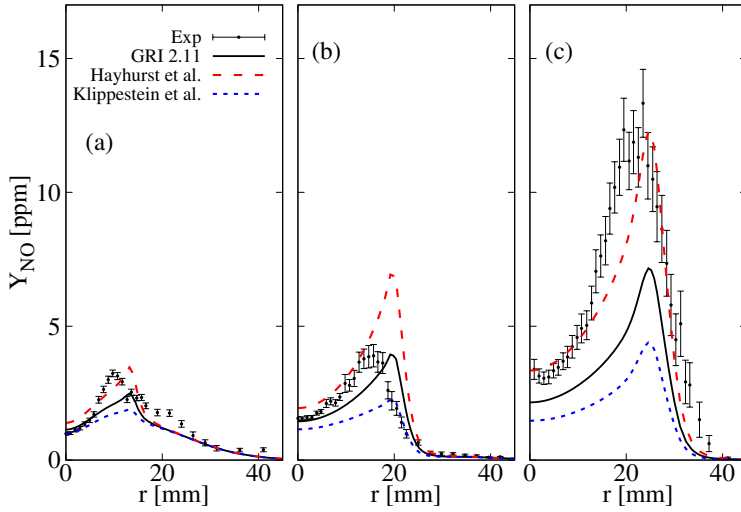


**Figure 5.20:** Experimental and numerical NO mass fraction profiles at axial locations  $z=60$  mm (a),  $z=120$  mm (b), and  $z=200$  mm (c). “Dyn JM” and full GRI-2.11.

A second strategy to overcome the under-estimation of NO was then investigated [3]. It consists of an engineering adjustment of the PaSR model to account for the different time scales of the fuel-oxidizer reactions and NO formation pathways, such as thermal and NNH. It has been observed that the production of NO via NNH occurs both in flame and post-flame zones [178]. For the slowest NO pathways, a large chemical time scale  $\tau_c$  may be considered and, thus,  $\tau_c \gg \tau_{mix}$  may be assumed, resulting in values of  $\kappa = \tau_c / (\tau_c + \tau_{mix})$  approaching unity. Accordingly, a different  $\kappa$  for the NO species was adopted and set equal to 1 in the whole domain (Figure 5.21). Similar predictions are obtained at axial location  $z = 60$  mm, whereas higher predictions are achieved at the other axial locations,

resulting in an over-estimation at  $z = 120$  mm and a better prediction at  $z = 200$  mm, where the NO peak is increased by a factor 1.7. The predictions of temperature and OH mass fraction (not reported here) are nearly coincident at all axial locations, indicating that the use of a different  $\kappa$  for NO affects the NO predictions solely.

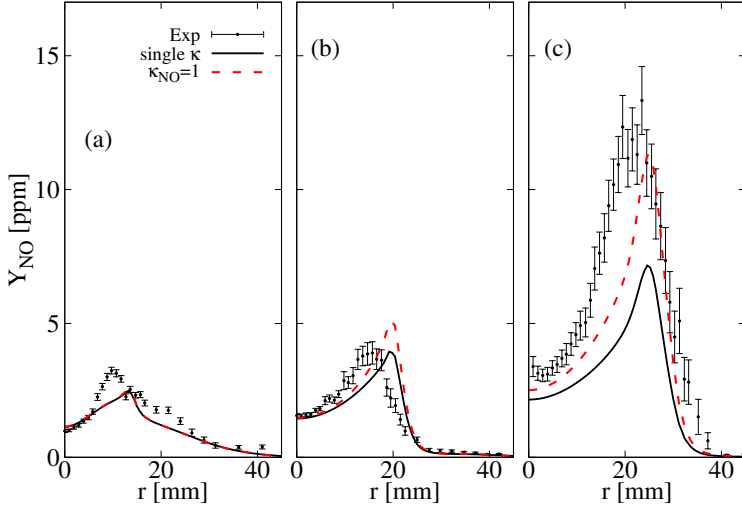


**Figure 5.21:** Experimental and numerical NO mass fraction profiles at axial locations  $z=60$  mm (a),  $z=120$  mm (b), and  $z=200$  mm (c). “Dyn JM” and full GRI-2.11 and: a single  $\kappa$  for all the species (blue solid lines);  $\kappa_{NO}=1$  and the “standard”  $\kappa$  for all the species but NO (red dashed lines).

To determine which NO formation pathways benefited from the adjustment of  $\kappa_{NO}$ , the impact of each pathway on the NO formation before and after the modification was assessed, taking the rate-limiting reactions of each pathway out of the GRI-2.11 scheme, one-at-a-time. Figure 5.22(left) shows the contribution of each pathway to the NO emission peak at axial location  $z = 200$  mm for the case where a single  $\kappa$  applies for all the species, and for the case where  $\kappa_{NO} = 1$  is used. For both cases, the biggest contributor to NO formation is the NNH route, followed by thermal, prompt, and  $N_2O$  routes. Figure 5.22(right) shows that all the pathways were impacted by the adjustment of  $\kappa_{NO}$  and that the highest increase corresponds to the thermal route.

Looking at Equation 4.23, it is clear that a unique value of  $\kappa$  (and  $\tau^*$ , as



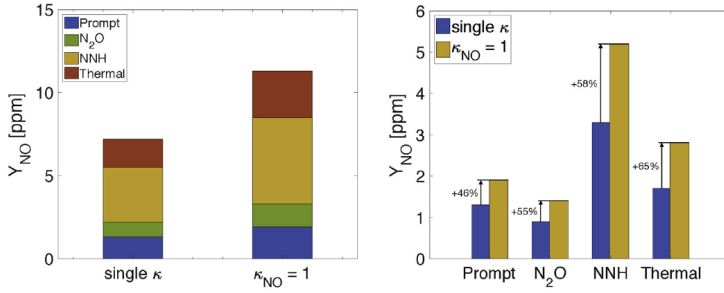


**Figure 5.22:** (Left) Contribution of each pathway to the peak of NO formation at  $z=200$  mm with a single  $\kappa$  and with  $\kappa_{NO}=1$ . (Right) Effect of  $\kappa_{NO}=1$  on the formation of NO from each route. “Dyn JM” and full GRI-2.11.

a consequence) is required to ensure mass conservation since the following expression:

$$\sum_k^N \bar{\dot{\omega}}_k = \frac{\kappa \bar{\rho} \sum_{k=1}^N (Y_k^* - Y_k^0)}{\tau^*}, \quad (5.5)$$

equals zero in each computational cell. Using optimized values of  $\kappa$  for individual species introduces an error in the total mass balance. The sum of the mean source terms, see Eq. 5.5, was calculated within each computation cell via the Fluent UDF, and its volume integral over the whole CFD domain was estimated. When the total of the source term is estimated considering two values of  $\kappa$  ( $\kappa_{NO} = 1$  and the standard value for all the other species), the integral value differs from the single- $\kappa$  value by 0.3%. The negligible mass imbalance is explained by the minimal concentrations of the NO in the domain (order of ppm). On the other hand, the mass imbalance would be significantly high if NO would be a main species of the fuel oxidation chemistry (i.e. NH<sub>3</sub>), thus making the proposed PaSR modifications unfeasible.

#### 5.4.4 HRR marker analysis

The aim of this study is to add further understanding on the adequacy of the various Heat Release Rate (HRR) markers (see Section 1.3.2) under diluted condition of a methane/hydrogen-air mixture for both MILD and not-MILD conditions. To this purpose, the “Dyn JM” coupled with

GRI-2.11 (excluding nitrogen-containing species) was considered, since an accurate evaluation of the radical pool is required to investigate the correlation with HRR. A sub-mechanism assembled by Kathrotia et al. [179] and used also by Doan et al. [180] was added to the main mechanism, to account for the conventional HRR-marker OH ( $A^2 \Sigma^+$ ), namely OH\*. OH\* is generally accepted as a marker for the flame-front structure and heat release rate, therefore its inclusion in the mechanism should enhance the description of the phenomena. The OH\* sub-mechanism consists of twelve reactions, whose Arrhenius terms are taken from Kathrotia et al. [179] and Tamura et al. [181]. The resulting mechanism contains 32 chemical species and 187 reactions. CH\* was not considered in the analysis.

HRR, chemical species mole fractions ( $X_\alpha$ , where  $\alpha$  is the species index) and net reaction rates ( $\dot{\omega}_r$ , where  $r$  is the reaction index) values were sampled along the radial direction at various axial distances from the burner nozzle ( $z$ ). Each sampled profile is 50 mm long starting from the burner axis. Obtained data were used to estimate the metric  $Z(\nu)$  at each axial location as proposed by [62], to appreciate how much a scalar  $\nu$  is representative of the HRR. In particular,  $Z(\nu)$  for the radial segment  $s$  is defined as:

$$Z_s(\nu) = \sum_{n=1}^{N_p} \left( \frac{|HRR_{n,s}|}{\max_s(|HRR|)} - \frac{|\nu_{n,s}|}{\max_s(|\nu|)} \right)^2. \quad (5.6)$$

In the equation above,  $N_p$  indicates the number of points of the radial segment.  $\max_s(|HRR|)$  and  $\max_s(\nu)$  are the maximum HRR and  $\nu$  of that segment, respectively, while  $\nu$  can be any scalar of interest. For the current case, it is either the mole fraction of the  $\alpha$  chemical species  $X_\alpha$ , or the reaction rate  $\dot{\omega}_r$ .  $Z_s(\nu)$  was normalized as  $Z_s^+ = 100 \cdot Z_s / \max(Z_s)$ , as explained by Nikolaou et al. [62]. The Z-metric gives an idea on how well a normalized scalar reproduces the spatially matched normalized HRR. At each radius, the lowest values of  $Z_s^+(\nu)$  will identify the scalars that best correlate with the HRR. It is worth to repeat that the fractional contribution of a reaction to the HRR is not a good way to identify the best HRR markers. As a consequence, the Z-metric was chosen as benchmark for comparison, being a more rigorous technique. If the chosen scalar is the net reaction rate, it may have positive and negative contributions to  $Z$ , thus giving ambiguous results. However, the top-correlating reactions have either only positive or negative contributions, without influencing the adequacy of the above definition. The results were first obtained in terms of mole fractions and reactions. Then, the analysis was also performed substituting to  $\nu$  appropriate combinations of mole fractions to verify if there

are products of species concentrations that may be more suitable for HRR identification.

### Analysis on the HM1 case

Figure 5.23 shows  $Z_s^+(X_\alpha)$  values for the HM1 case ( $Re = 10k$  and co-flow  $Y_{O_2} = 3\%$ ), calculated according to Eq. 5.6 when  $\nu = X_\alpha$ , namely for all the 32 species of the employed mechanism. Furthermore, the products in mole fractions of OH and CH<sub>2</sub>O firstly proposed by Paul et al. [64], and of H and CH<sub>2</sub>O suggested by Nikolaou et al. [62] were also taken into consideration. Six graphics, one for the respective axial location,  $z$ , collect only the first twelve values of  $Z_s^+(X_\alpha)$  in ascending order. According to Eq. 5.6, the lowest values are representative of best correlations with HRR. At this point, it is worth to remember that MILD combustion is achieved in the first 100 mm downstream of the burner exit for the HM1 case [14]. After that, the entrained oxygen from the surrounding changes the combustion behaviour.

As shown in Figure 5.23, for  $z = 30$  mm all the species exhibit rather low values of  $Z_s^+(X_\alpha)$ , never exceeding 5. O, H, and the conventional HRR-markers OH and OH\* provide the lowest values. At this axial location the flame brush is quite thin and the low  $Z_s^+(X_\alpha)$  for most of the scalars can be attributed to this reason. Figure 5.23 show a different species ranking for  $z = 60$  mm and  $z = 90$  mm: for the former H, OH\* provide lower values of  $Z_s^+$ , while O and OH are better correlated in the latter. However, at these locations, a clear selection of the best potential HRR markers cannot be made. Besides,  $Z_s^+(X_\alpha)$  is generally low (under 10) for all the listed species suggesting that different scalars could be used to detect the reaction zone. Nevertheless, this behaviour changes moving further from the jet nozzle: at  $z = 120$  mm (Figure 5.23d) the gap between the four radicals, O, OH, OH\*, H and the others becomes higher while the values of  $Z_s^+(X_\alpha)$  grow. This difference is clear in Figure 5.23e where O, OH, OH\* are unambiguously the top-three markers, while H usually presents a slightly lower matching with the HRR. At  $z = 550$  mm (Figure 5.23f) and higher distance (not reported here) HRR decreases and so all the correlations are lost rapidly. It is interesting to note that the formyl radical, HCO, conventionally used as marker with LIF techniques, displays higher values among the correlated species. Moreover, contrary to what proposed by Najm et al. [63], the product of OH and CH<sub>2</sub>O mole fractions is not a good HRR marker, since

its  $Z_s^+$  is not within the top-five species. This finding may be due to the different chemical pathway followed when methane is diluted with hydrogen and is consistent with results from [179].

Figure 5.24 adds further insights in this behaviour, showing the normalized  $Z$ -metric obtained in terms of reactions rates instead of species concentrations. Hence, in Eq. 5.6 the scalar  $\nu$  is substituted with the kinetic reaction rate,  $\dot{\omega}_r$  (where the subscript  $r$  indicates the reaction). What stands out is that several reactions from the added  $\text{OH}(A^2\Sigma^+)$  sub-mechanism appear among the top correlated reactions at many axial locations, while the reactions  $\text{O} + \text{CH}_3 \rightleftharpoons \text{H} + \text{CH}_2\text{O}$ ,  $\text{OH} + \text{CH}_2\text{O} \rightleftharpoons \text{HCO} + \text{H}_2\text{O}$  suggested by [63] and [64] and the reaction  $\text{H} + \text{CH}_2\text{O} \rightleftharpoons \text{HCO} + \text{H}_2$  proposed by [62] are not present among the ones reported. This may be due to the fuel enrichment with hydrogen, since the cited literature refers to methane-only configurations. This is in line with the previous observations on mole fractions, which do not identify formaldehyde and formyl radical among the markers. Third-body reactions are present in the top ranking positions throughout the flame. The excitation reaction  $\text{H} + \text{O} + \text{M} \rightleftharpoons \text{M} + \text{OH}^*$  [179], together with  $\text{CH} + \text{O}_2 \rightleftharpoons \text{OH}^* + \text{CO}$ , is responsible for the formation of the common HRR marker [65, 180]. At  $z = 60$  mm and  $z = 90$  mm (Figure 5.24b,c) the third-body reaction of oxygen,  $2\text{O} + \text{M} \rightleftharpoons \text{O}_2 + \text{M}$ , shows the lowest values of  $Z_s^+(\omega_r)$  and remains in the top-seven markers. A conspicuous number of reactions involving the hydrogen peroxide,  $\text{H}_2\text{O}_2$ , and the hydroperoxyl radical,  $\text{HO}_2$ , replace the previous ones in the last sampled segment at  $z = 550$  mm (Figure 5.24f). Moreover, at this axial location, the reactions  $\text{H} + \text{HO}_2 \rightleftharpoons 2\text{OH}$  and  $\text{H} + \text{HO}_2 \rightleftharpoons \text{O} + \text{H}_2\text{O}$  do not appear, even though their reaction rates were found to be good HRR indicators by [62] for lean to near-stoichiometric methane-air mixtures and especially at low value of HRR.

### Analysis on the HM3 case

Figure 5.25 reports  $Z_s^+(X_\alpha)$  relative to the co-flow oxygen concentration of 9%, i.e. HM3 flame. With this configuration the flame is visible since its beginning and MILD conditions are not reached. Unlike Figure 5.23a,b,c,d, O, OH,  $\text{OH}^*$  radicals show unambiguously greater correlation with HRR if compared to the other species. O and OH present slightly higher  $Z_s^+(X_\alpha)$  values throughout the entire domain. As previously underlined, at long distances HRR decays and  $Z_s^+(X_\alpha)$  increases fast for all the species. It is

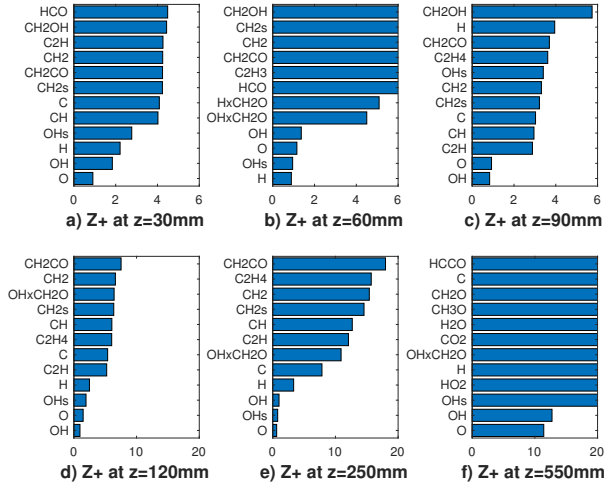


**Figure 5.23:** HM1 case: best correlated species at various axial locations. Lower  $Z_s^+(X_\alpha)$  values mean better correlation.

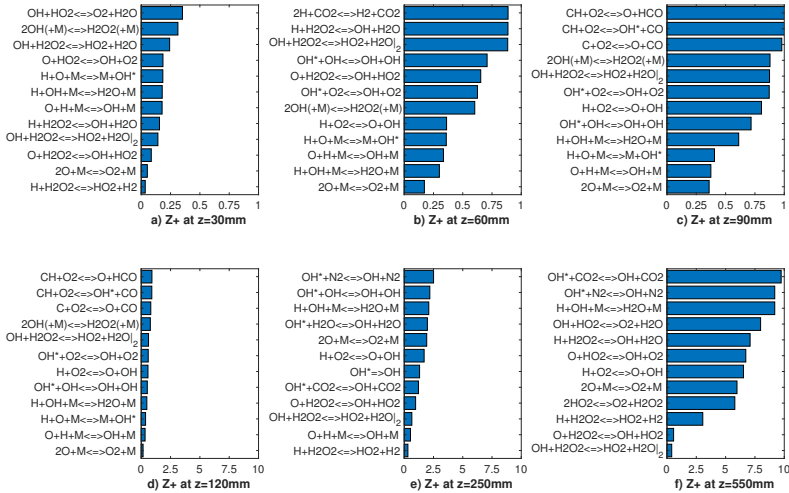


**Figure 5.24:** HM1 case: best correlated net reaction rates at various axial locations. Lower  $Z_s^+(\dot{\omega}_r)$  values mean better correlation.

interesting to note that this last phenomena emerges a bit before if compared to the HM1 case. Indeed, in the HM1 configuration the combustion is somewhat slowed down due to MILD conditions. This leads to a slightly longer flame for  $Y_{O_2} = 3\%$ , explaining why the correlations drop down later with respect to the HM3 case. The product of OH and  $CH_2O$  mole fractions appears as well in Figure 5.25, always having a higher  $Z_s^+(X_\alpha)$  value.

It is clear that the influence of oxygen concentration plays a significant role in determining the best HRR-markers. For the HM3 case the distinction between the top three markers O, OH, OH\* and the others is noticeable from the beginning of the combustion process, whereas, for the 3%  $O_2$  case, this distinction becomes clearer only downstream of 100 mm of flame, probably due to the higher level of entrained oxygen from surroundings.

Looking now at Figure 5.26, it is interesting to note that values of  $Z_s^+(\dot{\omega}_r)$  are generally lower up to 90 mm if compared with the HM1 case. The OH\* formation reaction appears again as a good indicator of heat release as several reactions from the sub-mechanism are listed. Also in this case, for  $z = 250$  mm and  $z = 550$  mm (Figure 5.26), reactions involving hydroperoxyl radical show a very good agreement with the HRR. In the latter,  $OH + H_2O_2 \rightleftharpoons HO_2 + H_2O$  and  $O + H_2O_2 \rightleftharpoons OH + HO_2$  cover the first positions, suggesting that their rates could be good HRR markers at this location with the % co-flow oxygen concentration.

## Combinations of mole fractions

Figures 5.27-5.28 report  $Z_s^+(\nu)$  calculated substituting to  $\nu$  respectively species mole fractions  $X_\alpha$  and their combinations. It is noteworthy that several combinations present values lower than the lowest ones recorded in Figures 5.23- 5.25. The product of O and OH shows a very good agreement with the HRR and is the solution of choice till  $z = 120$  mm (Figure 5.23). These notable results may suggest that for MILD combustion under the conditions of interest, an appropriate combination of species can identify the reaction zone more precisely than a single species, thus with less uncertainty on the choice of the right scalar. Just above the combination  $O \times OH$  (here  $x$  is the product symbol), combinations of H, O, OH and OH\* show also a very good correlation metric. At higher distances, combinations of these 3 radicals with the major species  $H_2O$  and  $CO_2$  are ranked first. As expected, this change occurs first for the HM3 configuration (fig. 5.28).

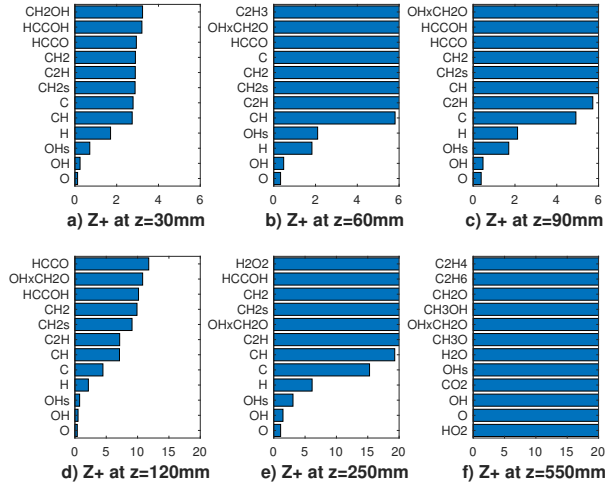


**Figure 5.25:** HM3 case: best correlated species at various axial locations. Lower  $Z_s^+(X_\alpha)$  values mean better correlation.

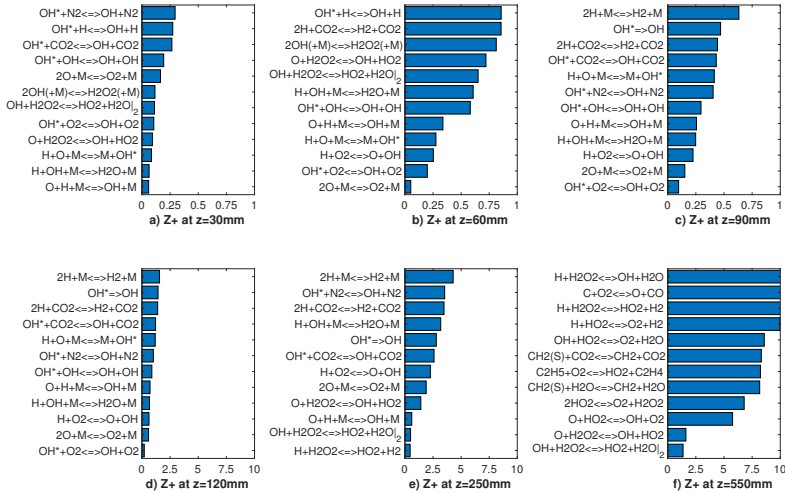


**Figure 5.26:** HM3 case: best correlated net reaction rates at various axial locations. Lower  $Z_s^+(\dot{\omega}_r)$  values mean better correlation.

The distributions of HRR, mole fraction and combinations are reported and compared in Figure 5.29. The 6 graphics correspond to 3 positions of the 2 cases studied, i.e.,  $z = 60$  mm,  $z = 120$  mm and  $z = 550$  mm, respectively. Only radial profiles of the top two species and the top-two combinations are drawn together with the HRR. All these scalars are normalized with respect to their own maximum. It is worth noting that both species mole fractions and combinations capture the HRR peak very well in Figure 5.29a,b,d,e. The main difference is associated to the tails of the curves, for low values of HRR. In particular, using the mole fraction products allows to have a higher correlation in these branches and capture the near-zero HRR behaviour. This might also suggest a good detection of local extinction. Different considerations should be done for Figure 5.29c,f. At  $z = 550$  mm, the HRR curve is wider and, as stated previously, the sole species are not a very good HRR marker, especially for the HM3 case.

Looking to the contour plots (Figure 5.30) reported as a qualitative example, it is possible to identify the 3 zones previously underlined. Two black dotted lines divide this zones at  $z = 150$  mm and  $z = 450$  mm. For each part, the best HRR marker combination is reported.

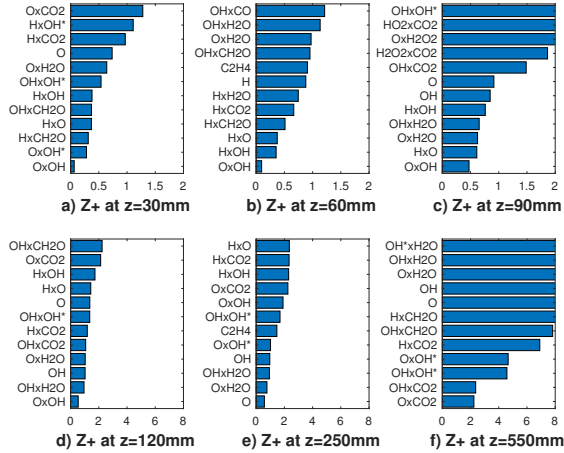


**Figure 5.27:** HM1 case: best correlated markers at various axial locations. Lower  $Z_s^+(\nu)$  values mean better correlation. Here  $\nu$  comprehends both  $X_\alpha$  and their combinations.



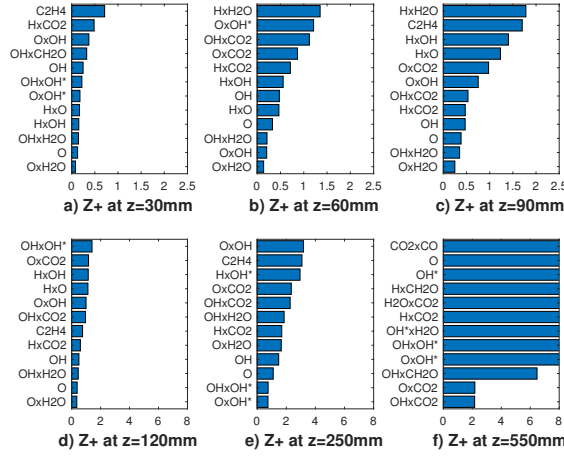


**Figure 5.28:** HM3 case: best correlated markers at various axial locations. Lower  $Z_s^+(\nu)$  values mean better correlation. Here  $\nu$  comprehends both  $X_\alpha$  and their combinations.

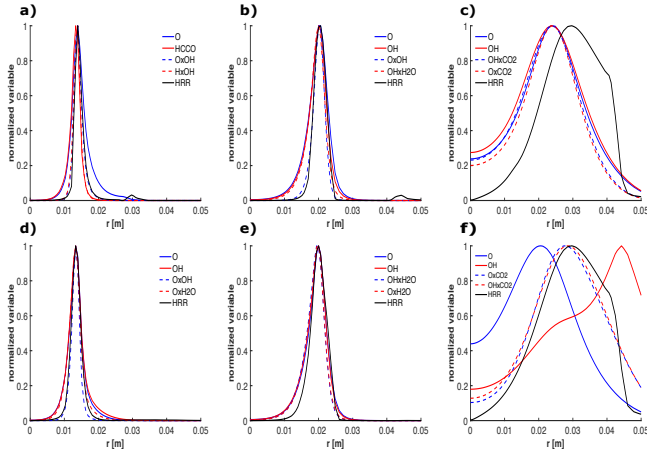


**Figure 5.29:** Trends of normalized HRR, top-two mole fractions and combinations at 60 mm, 120 mm and 550 mm respectively. First row refers to HM1 case, second row to HM3.

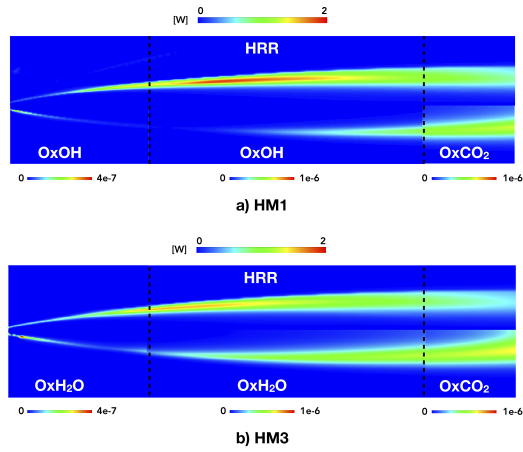


**Figure 5.30:** HM1 and HM3 contour plots of HRR compared to species products contours. The three zones are split as follows: from 0 to 150 mm, from 150 mm to 450 mm and from 450 mm to 550 mm.

## 5.5 Summary and conclusions

In this Chapter, an extensive numerical analysis on the Adelaide Jet in Hot Co-flow is reported. The aim is to provide understandings to clarify three important aspects characterizing MILD combustion: 1) turbulence/chemistry interaction modeling and the parameters involved, 2) NO emission and 3) choice of a suitable marker which correlates the best with the HRR.

First, a set of RANS simulations were run using the Partially Stirred Reactor (PaSR) approach, investigating different mixing model formulations: a static model based on a fraction of the integral time-scale, a fractal-based and a dynamic model based on the resolution of transport equations for scalar variance and dissipation rate. The proposed approaches were validated at different fuel-jet Reynolds numbers (5k, 10k and 20k) and different co-flow oxygen dilution levels (3%, 6% and 9%). A parametric study identified a  $C_{mix}=0.5$  as the best performing, when adopting a static model, reducing the temperature over-prediction at  $z = 120$  mm (4% relative error at 10k and 3% O<sub>2</sub>). A dynamic mixing model was coupled for the first time to the PaSR combustion model. The model outperforms both the static and fractal models, leading to very accurate predictions in terms of mean temperature, CO and OH mass fraction for a wide range of conditions. To the author's knowledge this level of accuracy was not yet reached for the simulation of the AJHC burner using a RANS formulation and without a fine tuning of the model parameters. While the static and fractal-based models show very large sensitivity to the choice of parameters, the three different dynamic formulations produce similar results, providing the robustness and soundness of the proposed approach.

Second, a study about the role of combustion models and kinetic mechanisms on the prediction of NO formation was conducted. A forward propagation of the uncertainty in the kinetics of the NNH route on the predictions of NO was carried out. For the simulation with "Dyn JM" and KEE, the predictions obtained using the post-processing tool of ANSYS Fluent 19.0 were insensitive to the variability of the kinetic parameters of the one-step global rate for the NNH route. The exclusive impact of the prompt route on the simulated NO emissions was shown. On the contrary, the predictions of NO obtained from the simulation with the "Dyn JM" and GRI-2.11 scheme showed considerable sensitivity to the uncertainty in the kinetic parameters of the rate-limiting reactions of the NNH pathways. The analysis proved

that the use of a one-step global rate scheme for the NO formation pathways, as supposed in the post-processing tool, lacks the necessary chemical accuracy and dims the importance of the NNH pathways in this combustion regime. Subsequently, two different values for the volume fraction  $\kappa$  of the PaSR model were considered. Such an approach aims at accounting for the different time scales of the oxidation reactions and the reactions involved in the NO chemistry. An elevated chemical scale was supposed for the NO species. Accordingly,  $\kappa$  was set to a unitary value for the NO species. This implementation augmented the estimation of the NO mean source term coming from the PaSR closure and resulted in higher predictions of NO emissions. A subsequent analysis showed that the adjustment enhanced the formation of NO by all the routes and was especially beneficial for the thermal and NNH routes. However, such an approach leads to a small mass imbalance, which may become significant approaching N-containing fuels (i.e.  $\text{NH}_3$ ). For these fuels, this might be solved adding an artificial mass conservation correction. Furthermore, a detailed uncertainty quantification on the most sensitive reaction might be performed to further improve the accuracy of the predictions.

Finally, an analysis about the choice of a Heat Release Rate (HRR) marker for MILD (HM1 flame) and not MILD (HM3 flame) conditions was conducted. Correlations between HRR and both species mole fractions and reaction rates were investigated at various axial locations along the radial direction. Considering the HM1 case, the radical OH is always one of the four top markers in the first 120 mm of reaction zone. Further downstream from the burner, the top-three markers are O, OH, OH\* radicals. The reaction rates that better correlate with the HRR are shown to belong mostly to reactions of the OH\* sub-mechanism and involve primarily these radicals together with other species such as H,  $\text{O}_2$ ,  $\text{HO}_2$ ,  $\text{H}_2\text{O}_2$ ,  $\text{H}_2\text{O}$ , CO and  $\text{CO}_2$ . For the HM3 configuration, a very good agreement between the top-three radicals O, OH, OH\* and the HRR was found right from the first axial location, suggesting that a higher oxygen level allows better correlation with the HRR. Even though conventional HRR markers, such as OH and OH\* perform well along most of the flame, a better detection of the reaction zone may be achieved using appropriate combinations of species. Considering the change of the combustion behaviour due to the entrained oxygen from the air stream, different parts of the flame should be detected by different markers. For the HM1 case, the combination of O and OH mole fractions seems to be the right choice for the MILD region while beyond  $z = 150$  mm, the HRR is well captured by the product  $\text{O} \times \text{CO}_2$ , for both the

configurations. Finally, only in the region far from the nozzle, i.e the last 150 mm of the studied domain, the low and wide values of HRR are better captured by combinations of O and OH with carbon dioxide.

## Chapter 6

# CFD analysis of the ULB flameless furnace

*This chapter presents a detailed numerical simulation analysis to define the key aspects in simulating a flameless furnace varying the composition of the fuel. Simulations were carried out in a RANS approach using the PaSR combustion model in ANSYS Fluent. A first study analysed three methane/hydrogen blends, focusing on the effect of kinetic schemes, mixing time scale definition as well as turbulence and radiation modeling on the prediction of temperature profiles and pollutant emissions. Afterwards, the ammonia/hydrogen blends were also validated. An uncertainty quantification analysis was also performed to determine the most impacting reactions in the NO formation, leading to improved pollutant emission predictions.*

*This chapter is partially based on the following publication:*

**M. Ferrarotti**, M. Fürst, E. Cresci, W. De Paepe, A. Parente, “Key Modeling Aspects in the Simulation of a Quasi-industrial 20 kW Moderate or Intense Low-oxygen Dilution Combustion Chamber”, *Energy Fuels*, 2018, 32, 10228-10241.

**M. Ferrarotti**, A. Bertolino, R. Amaduzzi, A. Parente, “On the influence of kinetic uncertainties on the accuracy of numerical modelling of an industrial flameless furnace fired with NH<sub>3</sub>/H<sub>2</sub> blends: a numerical and experimental study”, *Frontiers in Energy Research*, Under review.

**M. Ferrarotti**, W. De Paepe, A. Parente, “Reactive structures and pollutant emissions for methane/hydrogen mixtures in flameless regime”, Combustion&Flames, In preparation.

**Author’s contribution to the publications** The author performed all the CFD simulations and post-processed the data for both methane/hydrogen and ammonia/hydrogen cases. The uncertainty quantification study based on WSR, simulating ammonia/hydrogen blends, was performed by A. Bertolino. Nevertheless, the author contributed on the methodology to follow.

## 6.1 Introduction

As discussed in Chapter 4, the modelling of turbulent reacting flows is one of the most challenging problems. The difficulty of the problem is due to the simultaneous presence of different physical phenomena, such as turbulence, combustion, thermal radiation and to their interactions. Compared to the jet-in-hot-coflow flames (Chapter 5), flameless combustion in a furnace is more complex in terms of fluid dynamics fluid patterns (example in Figure 6.1), combustion characteristics and heat transfer.

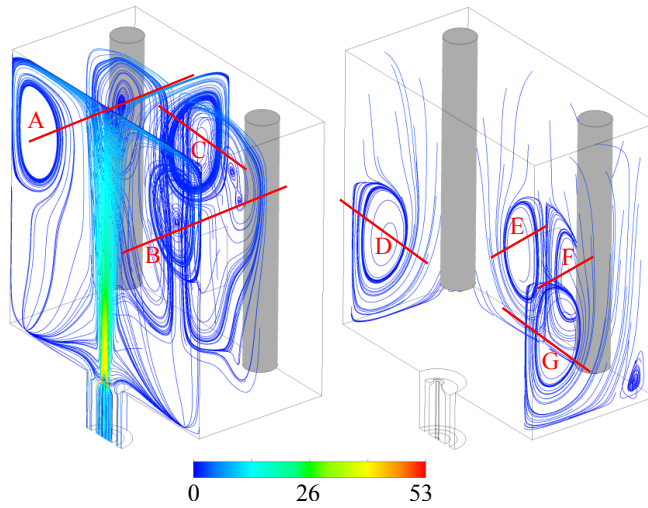


**Figure 6.1:** Streamlines, colored according to the velocity magnitude for pure methane combustion in the ULB furnace. Units in meters per second.

In the ULB furnace, combustion is sustained by a continuous entrainment of recirculated exhaust gases into the air stream. The dilution level varies over space and depending of operational parameters (injection diameter and configuration) and fuel composition. Since the furnace is a closed system, radiative heat transfer is significantly affected by the high temperature walls and therefore has to be taken into account, differently from a JHC system. Furthermore, flameless/MILD combustion is characterised a relatively low Damköhler number, due to a stronger competition between chemistry and mixing. As a consequence, detailed kinetic chemistry must be considered in



an affordable way. A numerical model, therefore, has to be robust enough to work in very different conditions, varying fuel blends, from conventional to renewable, as well as providing a fair estimate of the pollutant emissions.

In this chapter, the PaSR model, optimized in the AJHC burner (Chapter 5), is applied to the simulations of the ULB furnace. Some of the most representative cases of Chapter 3 are extracted and validated numerically.

## 6.2 Methane/hydrogen blends

Three different cases, presented in Chapter 3, are here studied numerically, i.e. pure hydrogen, pure methane and an equimolar blend with an air injector diameter of ID16 and equivalence ratio  $\phi = 0.8$ . The simulations were performed in ANSYS Fluent 19.3, using a RANS approach.

### 6.2.1 Numerical details

#### Domain and grid

Due to the presence of the window in only one side of the furnace, a faithful computational domain should consider half domain, as a result of the symmetry of the problem. The window properties can be included in ANSYS Fluent imposing a semi-transparent wall boundary condition, which means that radiation approaching the window can exit, but no radiation from the surroundings can enter the domain. The latter is anyway negligible.

During the present work, two sets of computational grids were created, contemplating or not the presence of the window. The domain considered for both sets has an air injection diameter of ID 16 mm. All the computational grids were first created with tetrahedrons and then converted into polyhedrons. This operation allows for the reduction of the number of cells and improvement of convergence and accuracy, because the number of neighbours is higher than those of tetrahedrons. Particular attention was paid refining the fuel–air mixing zone (Figure 6.2). Preliminary simulations dealt with the grid independency study, adopting the two set of grids. The number of cells ranges between 450k to 1300k cells for the case with window (180° domain) and between 114k to 320k cells for the case without window (45° domain). For the latter, the cooling surface also incorporates the energy loss by radiation through the window. The selected grids consist

of 216k cells for the case without window and 850k cells for the case with window. They can be considered as a good compromise between accuracy and computational time. More details are available in Appendix C. A second comparison was aimed at understanding the effect of the window on the reactive zone. The grid without window offers a fair compromise between accuracy (Appendix C) and computational cost in an area far from the window, allowing the use of only a  $45^\circ$  section of the geometry (216k cells instead of 850k). This domain is used hereafter (Figure 6.2).



**Figure 6.2:** Computational domain and grid resolution from the selected grid (case without window).

### Boundary conditions and physical model

Differently from combustion air, the fuel pipe is not directly pre-heated across the heat exchanger. Nevertheless, the fuel lance is immersed in a high temperature environment, therefore the fuel blend is partially indirectly pre-heated. This increment is of the order of 50-70 K, which has a marginal effect on the combustion performances considering the ratio between air and fuel flow rate. To summarize, fuel was assumed to be fed into the furnace at 343 K. Fuel and air mass flow, as well as inlet air temperature are taken from Tables 3.3-3.5. The cooling surfaces were modeled using

a constant negative heat flux condition, whose value is set in accordance with the furnace energy balance (Table 3.6) and it also incorporates the energy loss by radiation through the window. Energy loss through the external wall were also imposed according to Table 3.6. Different turbulence models were considered in the analysis coupled with enhanced wall functions: standard  $k-\epsilon$ , modified  $k-\epsilon$  ( $C_{\epsilon 1}=1.6$ ), realizable  $k-\epsilon$  and Reynolds stress model (RSM). PaSR was used as combustion model. The chemical time scale was evaluated from the species formation rate, while a static and a dynamic approach were both considered for the mixing time scale. Two kinetic schemes were considered to investigate chemistry accuracy on the results: GRI-2.11 (31 species and 175 reactions for the version without NOx chemistry) and KEE (17 species, 58 reactions). In the present work, no chemiluminescence species sub-models ( $\text{OH}^*/\text{CH}^*$ ) were considered. The discrete ordinate (DO) radiation model was used, in combination with the weighted-sum-of-gray-gases (WSGG) model. The WSGG was used in two ways: via the default approach proposed by ANSYS Fluent, which considers a grey approximation to solve one spectrally integrated RTE with the coefficient proposed by Smith et al. [163] or via a multi bands approach, which solves an RTE for each of the grey gases. For the latter approach, the coefficient proposed by Bordbar et al. [164] were considered (for details see Section 4.3.1).

## 6.2.2 Results

This section shows the main findings about modeling reactive structures and pollutant emissions for methane/hydrogen blends. In particular, three cases were simulated in details, namely M100H0, M50H50 and M0H100.

### M100H0

A first numerical simulation was run with KEE and  $C_{mix}=0.5$ <sup>1</sup> to ensure the closure and validation of the global energy and mass balances. Figure 6.3 presents the measured and computed profiles of wall temperatures along the vertical direction  $z$  on the central plane. The averaged relative error is below 1%. This, together with the validation of the temperature value at the outlet, reported in Table 6.1 (error below 1%), confirms the closure of the energy balance. A similar conclusion can be drawn for the

---

<sup>1</sup>value suggested from the analysis of Chapter 5

mass balance, looking at the  $O_2$  and  $CO_2$  mass fractions at the outlet (Table 6.1).

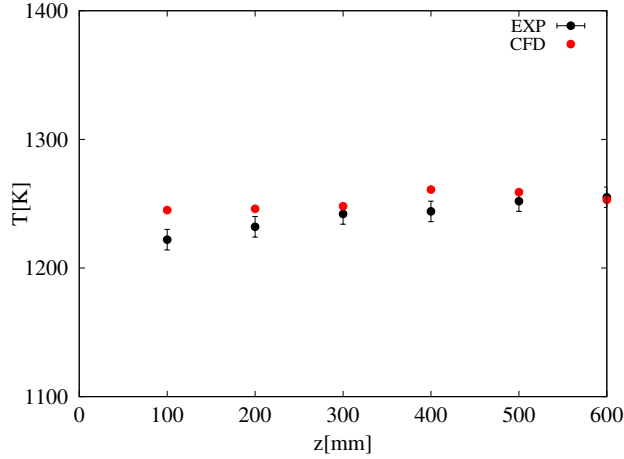


**Figure 6.3:** Comparison of the measured and computed wall temperature profiles at six different points along the  $z$  coordinate.

**Table 6.1:** Comparison of the measured and computed temperature,  $O_2$  and  $CO_2$  (on a dry basis) mole fraction values at the outlet.

Case	$T_{ex}$ [K]	$Y_{O_2}$ [%]	$Y_{CO_2}$ [%]
Exp	$1240 \pm 7$	$4.53 \pm 0.2$	$9.25 \pm 0.3$
CFD	1233	4.59	8.93

A first sensitivity analysis was aimed at understanding the chemistry accuracy needed to describe the oxidation of pure methane. To this purpose, Figure 6.4 compares KEE and GRI-2.11 varying the mixing constant value ( $C_{mix}$ ), in terms of temperature profiles obtained at different axial locations. Standard  $k-\epsilon$  was used as turbulence model. As already pointed out in Section 3.2.3, the reactive region is shifted upstream almost in correspondence of the top wall. Indeed, after the reactants are mixed with the exhaust gases (between 100 and 200 mm), the profiles remain flat and smooth. A first sign of ignition can be observed at  $z = 600$  mm. Since,

$\tau_c \gg \tau_{mix}$ , the mixing constant has no effect on the predictions, as long as chemistry is accurate enough. Indeed, only GRI-2.11 can catch the temperature increment at  $z = 600$  mm. This peculiar aspect is confirmed by the contour plot (Figure 6.5) of the volume fraction of the reactive zone ( $\kappa$ ) of PaSR (a) and the Damköhler ( $Da = \tau_{mix}/\tau_c$ ) distribution (b). The  $\kappa$  parameter is close to unity everywhere, while  $Da$  has a maximum value lower than unity, i.e. 0.02.

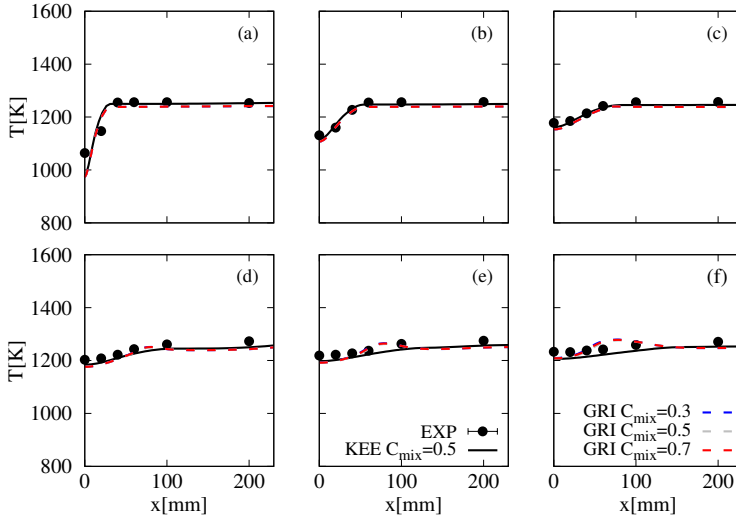


**Figure 6.4:** Sensitivity of temperature predictions to kinetic scheme and PaSR constant  $C_{mix}$  for pure methane. (a)  $z=100$  mm, (b)  $z=200$  mm, (c)  $z=300$  mm, (d)  $z=400$  mm, (e)  $z=500$  mm and (f)  $z=600$  mm. Averaged experimental uncertainty of 10 K, which is the radius of the marker. M100H0,  $\phi=0.8$  and ID16. Std  $k-\epsilon$ .

Li et al. [16] proposed an implicit approach for PaSR simulating AJHC in LES. They showed that imposing  $\kappa$  equals to unity, so without closure model, the results were comparable to the ones obtained computing  $\tau_{mix}$  and  $\tau_c$ . Figure 6.6 compares a static approach ( $C_{mix} = 0.5$ ) and an implicit PaSR, imposing  $\kappa = 1$ . No differences can be noticed among the two formulations. However, differently from LES, in RANS a residence time  $\tau^*$  still has to be defined, implying the calculation of the two time scales.

One tool that can be helpful in understanding the nature of the chem-

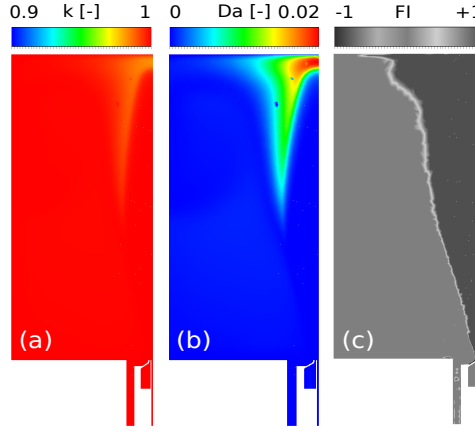


**Figure 6.5:** Contour of  $\kappa$  (a), Damköhler number (b) and flame index (c) for M100H0,  $\phi=0.8$ , ID16. Std k- $\epsilon$ ,  $C_{mix}=0.5$ , GRI-2.11.

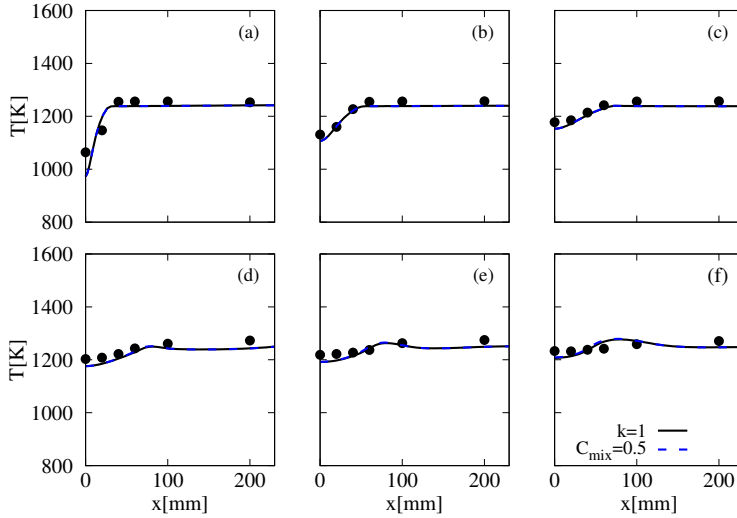


**Figure 6.6:** Sensitivity of temperature predictions to the  $\kappa$  parameter for pure methane. (a)  $z=100$  mm, (b)  $z=200$  mm, (c)  $z=300$  mm, (d)  $z=400$  mm, (e)  $z=500$  mm and (f)  $z=600$  mm. Averaged experimental uncertainty of 10 K, which is the radius of the marker. M100H0,  $\phi=0.8$  and ID16. Std k- $\epsilon$ .

istry/turbulence interactions is the so-called normalized flame index, introduced by Yamashita et al. [182] and defined by Knudsen and Pitsch [183] as:

$$\xi = \frac{\nabla Y_F \cdot \nabla Y_O}{|\nabla Y_F \cdot \nabla Y_O|} \quad (6.1)$$

By definition, the index takes the value of  $\xi = +1$  for premixed flames and  $\xi = -1$  for non-premixed ones. It evaluates if the fuel and oxidizer gradients are aligned. This tool can be useful to assess the ability of the model to capture the premixed nature of the combustion process under MILD/flameless conditions. Figure 6.5 (c) shows that a non-premixed region is almost exclusively restricted to the injection zone, while in the core of the furnace the index is  $+1$ , indicating a premixed region behaviour.

## M50H50

As discussed in Chapter 3, hydrogen has a relevant role in reducing the ignition delay time and increasing the reactivity of the system respect to pure methane. The aim of this section is to define the key parameters in investigating a methane-hydrogen blend. Damköhler number (Figure 6.7) is now one order of magnitude larger (0.2) compare to pure methane, approaching unity, and  $\kappa$  becomes 0.5 in the reactive region. As a results, an implicit approach ( $\kappa = 1$ ) can not be used and chemistry and mixing have both great importance. The flame index (Figure 6.8(a)) shows that, leaving aside a small non-premixed region at the burner exit, combustion can be considered as premixed for this particular configuration, in correspondence of the OH region (Figure 6.8(b)). Interestingly, measured OH\* and predicted OH show very good agreement.

A more detailed kinetic mechanism is needed to capture correctly ignition, (Figure 6.9). Indeed, GRI-2.11 reduces the temperature under-estimation of KEE at  $z = 150$  mm (relative error from 7% to 2%) and 200 mm (relative error from 8% to 3%). Indeed, GRI-2.11 offers a higher level of accuracy, having more intermediate species, a more recent thermodynamic database and being validated and optimized against a wide database. After the ignition region, where only thermodynamics and transport are involved, the two models provide similar results and they are in good agreement with experimental results (relative error below 1%).

Figure 6.10 offers a sensitivity on the choice of the mixing time scale ( $\tau_{mix}$ ) formulation, varying the  $C_{mix}$  among the static version or the scalar dissi-

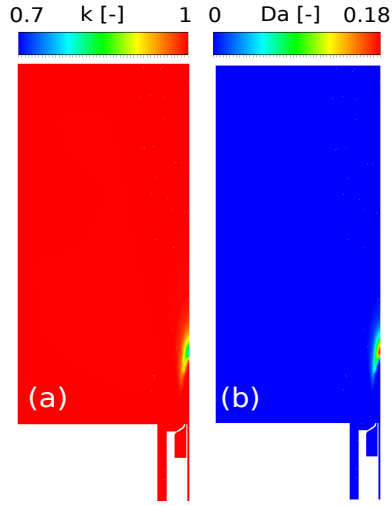


**Figure 6.7:** Contour of  $\kappa$  (a), Damköhler number and (b) for M50H50,  $\phi=0.8$ , ID16. Std k- $\epsilon$ ,  $C_{mix}=0.3$ , GRI-2.11.

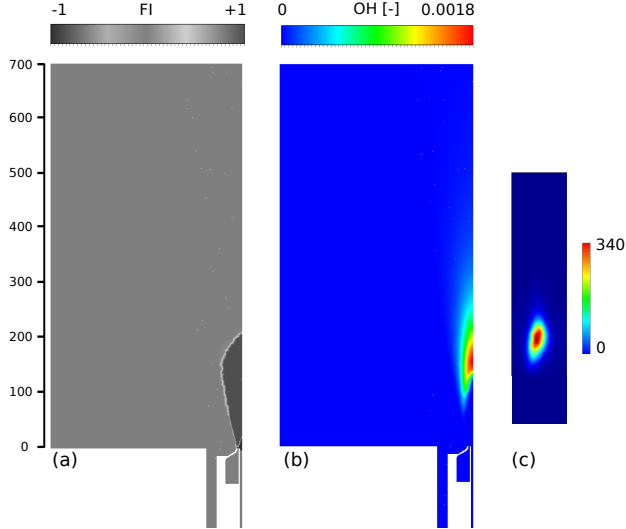


**Figure 6.8:** Contour of flame index (a), predicted OH (b) and experimental OH\* (c) for M50H50,  $\phi=0.8$ , ID16. Std k- $\epsilon$ ,  $C_{mix}=0.3$ , GRI-2.11.



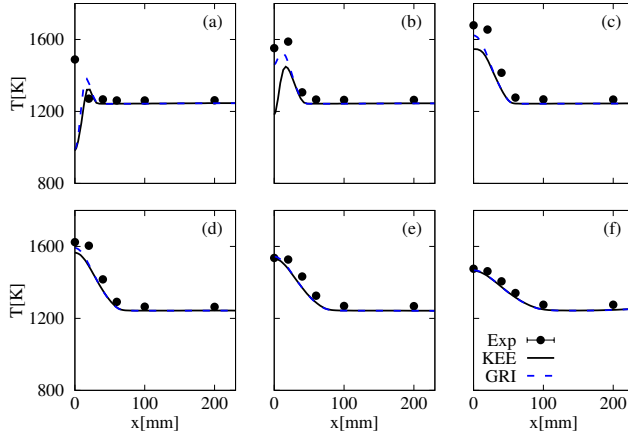


**Figure 6.9:** Sensitivity of temperature predictions to kinetic scheme for M50H50,  $\phi=0.8$ , ID16. (a)  $z=100$  mm, (b)  $z=150$  mm, (c)  $z=200$  mm, (d)  $z=250$  mm, (e)  $z=300$  mm and (f)  $z=400$  mm.  $C_{mix}=0.5$ , std k- $\epsilon$ . Averaged experimental uncertainty of 10 K, which is the radius of the marker.

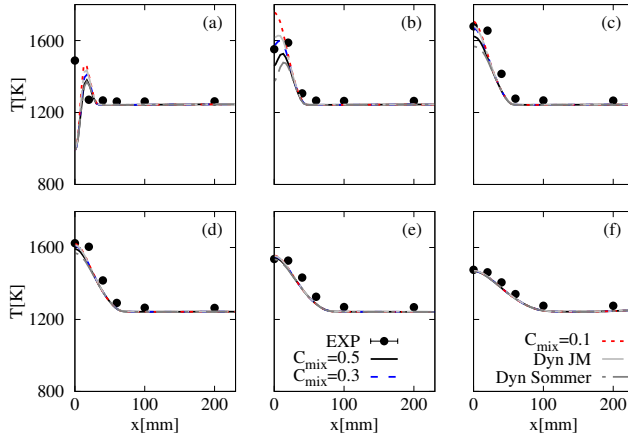


**Figure 6.10:** Sensitivity of temperature predictions to different  $\tau_{mix}$  definitions for M50H50,  $\phi=0.8$ , ID16. (a)  $z=100$  mm, (b)  $z=150$  mm, (c)  $z=200$  mm, (d)  $z=250$  mm, (e)  $z=300$  mm and (f)  $z=400$  mm. GRI-2.11, std k- $\epsilon$ . Averaged experimental uncertainty of 10 K, which is the radius of the marker.

pation rate definition among the dynamic ones (“Dyn JM” or “Dyn Sommer”). The latter were the best performing models in the AJHC (Chapter 5). The analysis clearly shows that the definition of  $\tau_{mix}$  is crucial to obtain good results. However, setting a  $C_{mix}$  value requires a priori knowledge about the physics of the system. Indeed, the use of a low mixing time scale ( $C_{mix} = 0.1$ ), closer to the Kolmogorov scale, may slightly improve prediction at  $z = 100$  mm (Figure 6.10a) over-estimating at  $z = 150$  mm (relative error of 13 %), as shown in Figure 6.10b. Moving towards the integral time scale helps in catching ignition properly. Best results are achieved with  $C_{mix} = 0.3$  (relative error below 1% at  $z = 150$  and 200 mm). A dynamic formulation of  $\tau_{mix}$  would allow to overcome the drawbacks of choosing a mixing constant a priori. Indeed, it provides an automatic estimation of the mixing time scale. The two tested versions provide results which are in line with  $C_{mix} = 0.3$  (“Dyn JM”) and  $C_{mix} = 0.5$  (“Dyn Sommer”). Unfortunately, data about in-flame species mass fraction are not available for this installation. However, considering the results of Chapter 5, it is reasonable to believe that the dynamic models would lead to an improvement compared to the static models. Furthermore, the scalar dissipation transport equations proposed by Jones and Musonge [157] and Sommers et al. [158] are based on analytical considerations assuming homogeneous turbulence and 2D configurations. These assumptions are likely violated in the present case, where the flow structure is 3D and turbulence is shear-driven. As a consequence, the coefficients used in “Dyn JM” and “Dyn Sommer” for the scalar dissipation rate transport equation might not be optimal. An interesting future work may deal with an uncertainty quantification of these coefficients.

The effect of the turbulence model was also studied, comparing standard  $k-\epsilon$ ,  $k-\epsilon$  with  $C_{\epsilon,1}=1.6$ , realizable  $k-\epsilon$  and RSM, while keeping the optimal  $C_{mix}$  value (0.3). Figure 6.11 shows a comparison in terms of predicted temperature profiles. The modification of  $C_{\epsilon,1}$  implies an even delayed ignition, causing major over-prediction at  $z = 250$  and 300 mm. No major differences can be noticed between the other models, reason why standard  $k-\epsilon$  was considered hereafter, in light of the lower computational time and stability.

So far, no model combinations seem to faithfully reproduce the pre-ignition zone ( $z = 100$  mm), therefore the discrepancies cannot be attributed neither to turbulence modeling neither to chemistry. At this purpose, a sensitivity study varying the air inlet turbulence intensity, set as boundary condition was carried out (Figure 6.12), but without improvement.

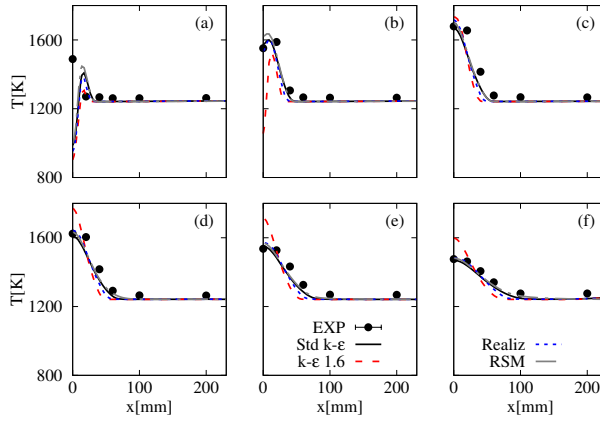


**Figure 6.11:** Sensitivity of temperature predictions to different turbulence models for M50H50,  $\phi=0.8$ , ID16. (a)  $z=100$  mm, (b)  $z=150$  mm, (c)  $z=200$  mm, (d)  $z=250$  mm, (e)  $z=300$  mm and (f)  $z=400$  mm. GRI-2.11,  $C_{mix}=0.3$ . Averaged experimental uncertainty of 10 K, which is the radius of the marker.

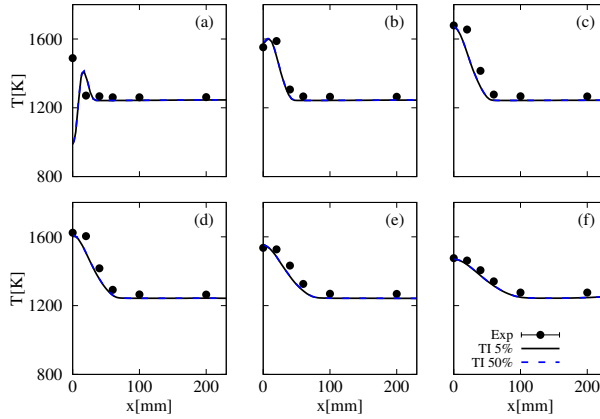


**Figure 6.12:** Sensitivity of temperature predictions to inlet air turbulence intensity for M50H50,  $\phi=0.8$ , ID16. (a)  $z=100$  mm, (b)  $z=150$  mm, (c)  $z=200$  mm, (d)  $z=250$  mm, (e)  $z=300$  mm and (f)  $z=400$  mm. GRI-2.11,  $C_{mix}=0.3$ , std k- $\epsilon$ . Averaged experimental uncertainty of 10 K, which is the radius of the marker.

Finally, the formulation of the WSGG model was also put under investigation (Figure 6.13). Beside the default approach proposed by ANSYS Fluent, a multi bands formulation was also considered. The former, considers a grey approximation to solve one spectrally integrated RTE with the coefficient proposed by Smith et al. [163]. On the contrary, the latter solves an RTE of each of the grey gases (four plus one clear gas), adopting the coefficient proposed by Bordbar et al. [164], which accounts for higher  $\text{H}_2\text{O}$  to  $\text{CO}_2$  ratios. A multi bands approach helps in improving the performances of the numerical model in the recirculation region (high  $\text{H}_2\text{O}$  to  $\text{CO}_2$  ratios), with relative error almost negligible, as well as in the pre-ignition zone ( $z = 100$  mm). However, it over-estimates the temperature peak with respect to the 1WSGG formulation.

The investigation, reported above, has touched almost every key aspects of simulating a turbulent combustion flame in a furnace. The author concludes that a RANS approach does not allow to catch the pre-ignition zone ( $z = 100$  mm) with sufficient accuracy. A further investigation using Large Eddy Simulations (LES) or Detached Eddy Simulations (DES) might clarify this aspect, shedding light on the gases flow field and turbulence-chemistry interactions.

## M0H100

As mentioned in Chapter 3, a pure hydrogen flame shows a reaction region attached to the burner exit and it becomes mixing controlled ( $\tau_c \ll \tau_{mix}$ ). This aspect is qualitatively confirmed by the contours of Figure 6.14. The volume fraction of the reactive zone ( $\kappa$ ) assumes values much lower compared to methane and its definition can be rewritten as  $\kappa = \tau_c / (\tau_c + \tau_{mix}) \approx \tau_c / \tau_{mix}$ . As a consequence, the Damköhler number is far from unity (22) and the flame index shows that main core of combustion is non-premixed, while there is still a small structure premixed on the sides.

Figure 6.15 compares three detailed kinetic schemes using a static  $C_{mix}$  (0.5): KEE, GRI-2.11. The temperature predictions seem not to be affected by the accuracy in representing chemistry, but differences might arise in predicting minor species and pollutants. All the schemes over-predict at  $z = 100$  mm (relative error of 7% or 130 K) and they consider a thinner reactive region compared to experimental data. Nevertheless, ignition starts upstream, attached to the burner exit, where there are no available data to compare with.

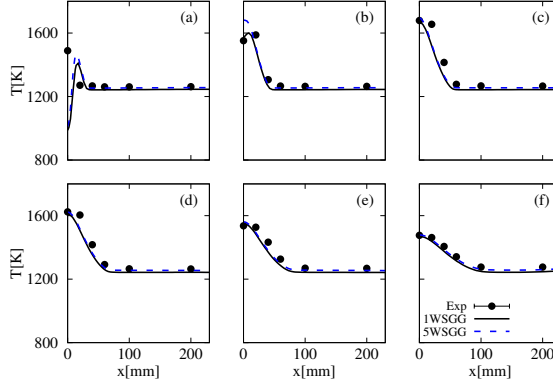


**Figure 6.13:** Sensitivity of temperature predictions to radiation modeling for M50H50,  $\phi=0.8$ , ID16. (a)  $z=100$  mm, (b)  $z=150$  mm, (c)  $z=200$  mm, (d)  $z=250$  mm, (e)  $z=300$  mm and (f)  $z=400$  mm. GRI-2.11,  $C_{mix}=0.3$ , std k- $\epsilon$ . Averaged experimental uncertainty of 10 K, which is the radius of the marker.

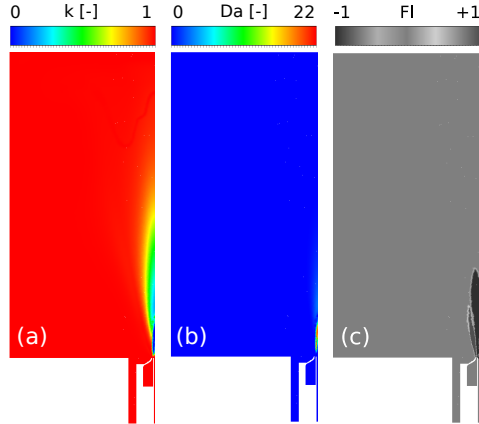


**Figure 6.14:** Contour of  $\kappa$  (a), Damköhler number and (b) flame index for M0H100,  $\phi=0.8$ , ID16. Std k- $\epsilon$ ,  $C_{mix}=0.5$ , KEE.

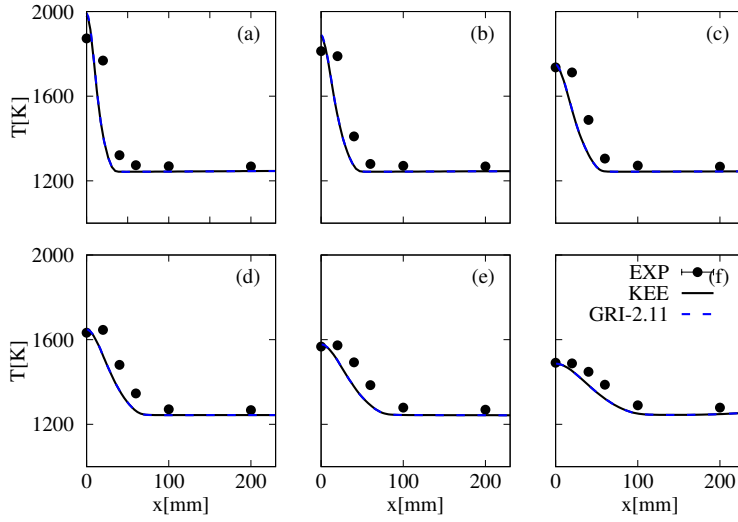


**Figure 6.15:** Sensitivity of temperature predictions to different kinetic schemes for M0H100,  $\phi=0.8$ , ID16. (a)  $z=100$  mm, (b)  $z=150$  mm, (c)  $z=200$  mm, (d)  $z=250$  mm, (e)  $z=300$  mm and (f)  $z=400$  mm.  $C_{mix}=0.5$ , std k- $\epsilon$ . Averaged experimental uncertainty of 10 K, which is the radius of the marker.

A comparison between different definitions for  $\tau_{mix}$ , i.e. static and dynamic, is shown in Figure 6.16. Reducing the  $C_{mix}$  constant or adopting a dynamic approach worsen the over-prediction at  $z = 100$  mm. As for M50H50, a sensitivity to the turbulence modeling was also conducted (Figure 6.17). All the investigated models over-predict the first measured points (Figure 6.17(b)-(c)), while only standard k- $\epsilon$  and realizable reduce the error for axial coordinate  $z < 200$  mm. Figure 6.16(a) compares the axial profile of temperature, also for a region ( $z < 100$  mm) where no experimental data are available. In this region, all the two-equations models collide on a profile, while RSM predicts slightly lower values. Thus, no under-predictions can be noticed for the modified k- $\epsilon$  ( $C_{\epsilon 1} = 1.6$ ) in the pre-ignition region, differently from M50H50. This might be due to the fact that ignition occurs at the burner exit.

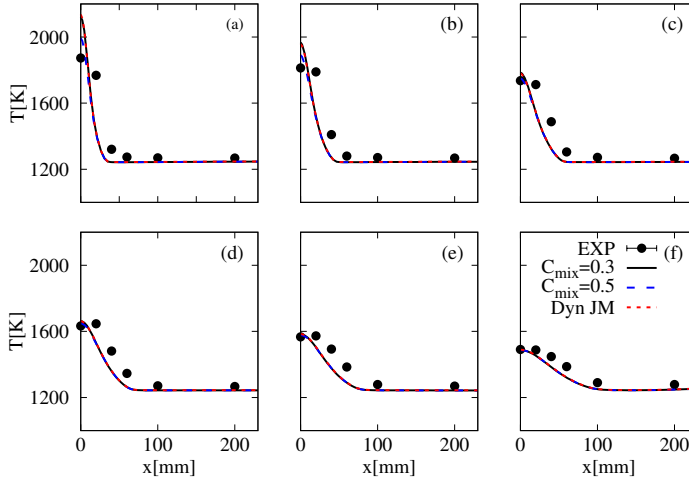


**Figure 6.16:** Sensitivity of temperature predictions to different  $\tau_{mix}$  definitions for M0H100,  $\phi=0.8$ , ID16. (a)  $z=100$  mm, (b)  $z=150$  mm, (c)  $z=200$  mm, (d)  $z=250$  mm, (e)  $z=300$  mm and (f)  $z=400$  mm. GRI-2.11, std k- $\epsilon$ . Averaged experimental uncertainty of 10 K, which is the radius of the marker.

Despite the investigated parameters, some aspects of pure hydrogen flame could not be caught, in the current investigation. More experimental points might be beneficial in reducing this uncertainty for  $z < 100$  mm. As for M50H50 case, these discrepancies might be related to the RANS framework,

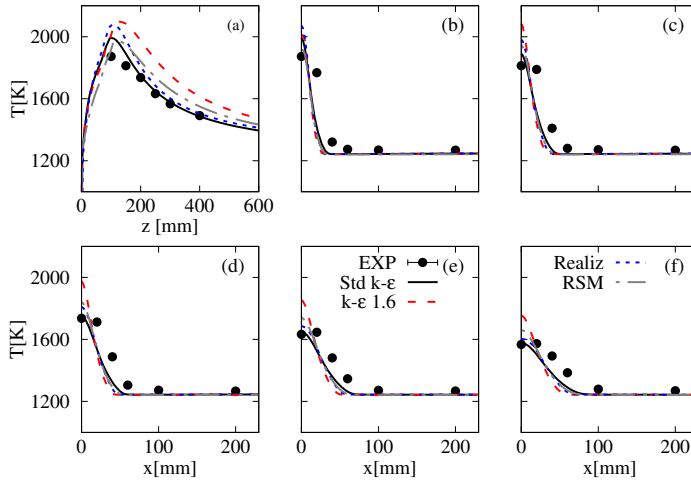


**Figure 6.17:** Sensitivity of temperature predictions to different turbulence models for M0H100,  $\phi=0.8$ , ID16. (a) axial, (b)  $z=100$  mm, (c)  $z=150$  mm, (d)  $z=200$  mm, (e)  $z=250$  mm and (f)  $z=300$  mm. GRI-2.11,  $C_{mix}=0.5$ . Averaged experimental uncertainty of 10 K, which is the radius of the marker.



therefore additional investigations in LES are required.

## NO emissions

Finally, this section also compares different approaches to quantify NO emissions for the methane/hydrogen blends. The strategy follows the methodology already presented by Iavarone et al. [3] for the Adelaide JHC. First, the ANSYS Fluent post-processing tool was applied considering the thermal, prompt,  $\text{N}_2\text{O}$  and NNH routes, using the best performing  $C_{mix}$  for each case and the GRI-2.11 (without NOx chemistry). For the NNH route, the reaction rate for  $\text{NNH} + \text{O} = \text{NH} + \text{NO}$  proposed by Konnov et al. [7] and Klippenstein et al. [5] were both used and compared. Beside that, the complete GRI-2.11 (with NOx chemistry) was also considered. The latter considers an intermediate reaction rate between Konnov and Klippenstein for the NNH pathway.

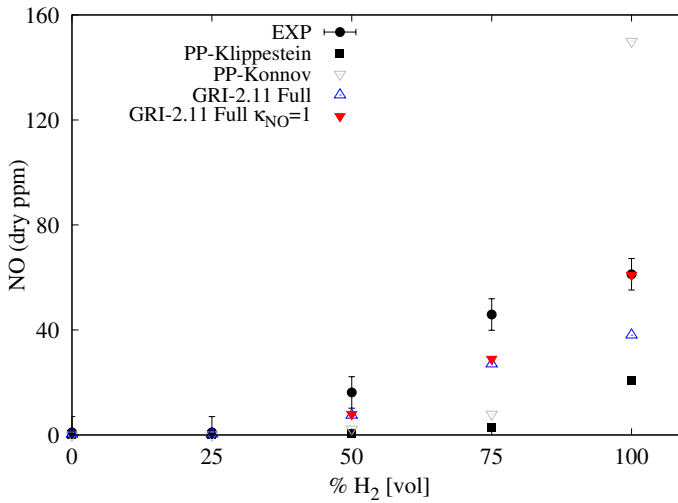


**Figure 6.18:** Measured and predicted NO emissions on dry basis in the exhaust gases, using different methods. PP means post-processing tool. ID16,  $\phi=0.8$ .

For M100H0 and M75H25, all the predictions are close to the experimental value ( $\approx 1$  ppm), while differences start to arise from M50H50. The two

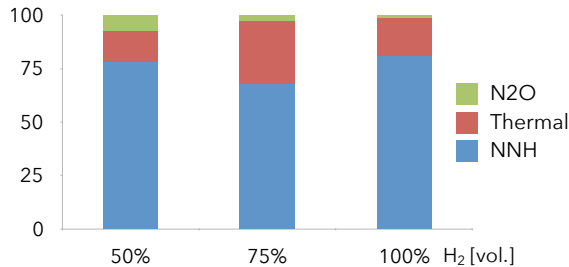


**Figure 6.19:** Percentage contribution of each pathway to NO emissions varying the hydrogen content in the fuel blend using a brute-force sensitivity analysis. GRI-2.11, ID16.

post-processing methods predict a very similar value (0.7 and 2.3 ppm for Klippestein and Konnov, respectively) far from the measured one (16.2 ppm). Better performances can be achieved using the full GRI-2.11 for both M50H50 and M25H75. For pure hydrogen, the two post-processing methods lead to opposite results: on one hand, the kinetic proposed by Klippestein et al. [5] under-estimates NO (21 versus 62 ppm), while on the other hand, the kinetic proposed by Konnov et al. [7] shows a major over-prediction (150 ppm). To sum up, the higher the hydrogen percentage, the more important the effect of the uncertainty on the NNH kinetic in a post-processing framework. The usage of the full GRI-2.11 helps to alleviate the under-prediction (35 ppm versus 62 ppm for M0H100). A strategy to further mitigate this under-prediction was also investigated, as tested in Chapter 5. It consists of an engineering adjustment of the PaSR model (Iavarone et al. [3]) to account for the different time scales of the fuel-oxidizer reactions and NO formation pathways. Accordingly, a different  $\kappa$  for the NO species was adopted and set equal to 1 in the whole domain. This adjustment proved to be very effective since the NO predictions are in excellent agreement with experimental data for pure hydrogen (60 ppm versus 62 ppm). However, using such an approach introduces an error in the total mass balance of 0.4 %, as already documented in [3].

Figure 6.19 shows the percentage contribution of each route in forming NO varying the hydrogen content in the fuel blend. This analysis was conducted considering the impact of each pathway on the NO formation before and after taking out the rate-limiting reactions of each pathway from the full GRI-2.11 scheme, one-at-a-time (brute-force sensitivity). NNH route confirms to be the most important in presence of hydrogen. It is responsible for

78% of NO emissions for M50H50, 68% for M25H75 and 81% for M0H100. Thermal NO<sub>x</sub> starts to be relevant at M25H75 (30%), considering the rise in temperature observed in Figure 3.16. Even if for M0H100 temperature continues to rise, the thermal contribution lowers to 18%, considering the massive growth of NNH route, due to the major presence of radical H. Finally, N<sub>2</sub>O route counts 7% for M50H50 and then becomes progressively negligible.

## 6.3 Ammonia/hydrogen blends

This section is focused on the influence of existing uncertainties in detailed kinetic mechanisms on NO predictions in RANS simulations.

A first validation for temperature profiles is presented for case N50H50 ID16  $\phi = 1$ . Here, a value of 0.5 was employed for  $C_{mix}$  in the PaSR model, together with standard k- $\epsilon$  for turbulence. Figure 6.20 shows the comparison between measured and predicted temperature profiles along the axis (a) and at different axial positions (b, c, d). The results from two different kinetic mechanisms, developed for ammonia combustion, i.e. Stagni et al. [13] and Glarborg et al. [4] are reported. Looking at Figure 3.26, the reaction region (maximum of OH\* counts) is located between 110 and 160 mm from the burner exit. However, the two models predict a late ignition compared to experimental data, as they under-predict the temperature peak at 100 mm away from the inlet. The above-mentioned under-prediction corresponds to a 2% and 1% relative error for Stagni et al. [13] and Glarborg et al. [4] models, respectively.

Even tough, both mechanisms performed well on temperature profiles, strong differences were detected for pollutant emissions estimates. Regarding NO<sub>x</sub>, a pronounced overestimation was observed using both models (see “Stagni2020-original” and “Glarborg2018” in Figure 6.21). In particular, for  $\phi = 1$  (Figure 6.21 left), Glarborg et al. [4] predicts much higher values, i.e. 13580 and 5300 ppm at N25H75 and N50H50, respectively, versus 9473 and 2851 ppm for the mechanism from Stagni et al. [13]. Anyway, even using the latter model, predictions are still far from the experimental data (460 ppm and 160 ppm for N25H75 and N50H50, respectively). For  $\phi = 0.8$  (Figure 6.21 right), a better agreement with experimental data is observed, even tough the model under-predicts the NO emissions for N50H50.

In order to verify the major role of an accurate kinetic sub-model in this

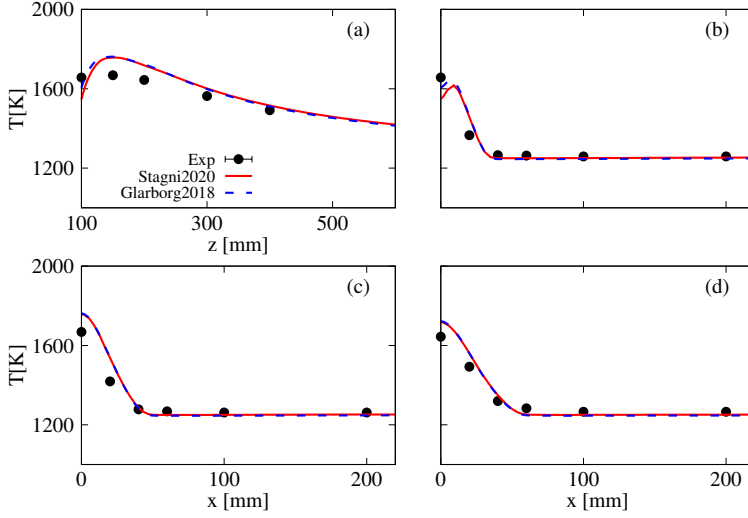


**Figure 6.20:** Sensitivity of temperature predictions to different kinetic schemes, Stagni et al. [13] and Glarborg et al. [4]. (a) Axial, (b)  $z=100$  mm, (c)  $z=150$  mm and (d)  $z=200$  mm.  $C_{mix}=0.5$ , std  $k-\epsilon$ . Averaged experimental uncertainty of 10 K. N50H50,  $\phi=1$ , ID16.

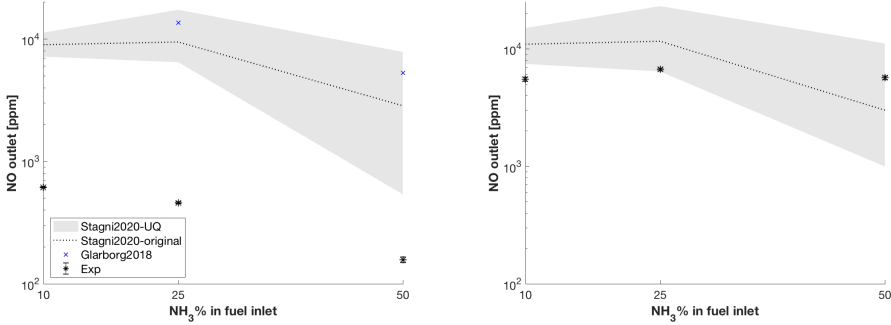


**Figure 6.21:** Dry NO pollutant emissions predicted using different kinetic schemes. The gray area represents the uncertainty propagation of the LHS study for Stagni et al. [13]. ID16,  $\phi=1$  (left) and  $\phi=0.8$  (right). Relative experimental uncertainty 2%.

chemistry-controlled regime (flameless), a fundamental analysis was carried out through the WSR network (Section 3.3.2), using the Stagni et al. [13]

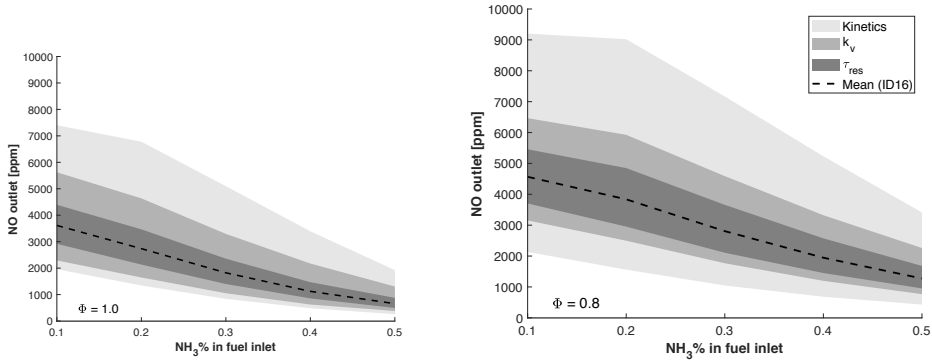


**Figure 6.22:** Effect of the recirculation degree ( $k_v$ ), the residence time, and kinetics uncertainties on the pollutant emission estimates from the WSR network, for equivalence ratio of 1.0 (left) and 0.8 (right) at different fuel composition. ID16.

kinetic scheme. In particular, as the adopted  $k_v$  and  $\tau_{res}$  values, for each fuel composition, are average quantities extracted from the reactive zone in RANS simulations, a sensitivity analysis was performed by multiplying and dividing them by a factor of 2. The model responses are reported in Figure 6.22 for ID16, where a higher sensitivity to the recirculation degree than to residence time is observed. Figure 6.22 also shows a much greater impact on the NO variance due to the kinetic model. For this reason, only the uncertainty related to kinetic was considered for an uncertainty quantification study. Section 3.3.2 identified reactions R39, R80 and R85 as the most sensitive to NO emissions and their uncertainty factors are reported in Table 6.2, based on literature information. Thus, these reactions

**Table 6.2:** Details about identified sensitive reactions.

Index	Reaction	$f$	Ref.
R39	$\text{NH} + \text{NH}_2 = \text{H} + \text{N}_2\text{H}_2$	0.18	[184]
R80	$\text{NH} + \text{OH} = \text{HNO} + \text{H}$	0.7	[185]
R85	$\text{NH} + \text{NO} = \text{H} + \text{N}_2\text{O}$	0.65	[186]

were addressed as random variables, propagating their uncertainty through the WSR. So, for each combination of operating conditions, NOx emissions were represented as a region, rather than a curve. This was achieved

using a Latin Hypercube Sampling (LHS) (Iman et al. [187] and Florian et al. [188]) approach for the pre-exponential factors of the selected reactions, within their estimated uncertainties. The maximum and minimum pre-exponential factors ( $A_{min}$  and  $A_{max}$ ) were calculated considering the definition of the uncertainty factor  $f$  (see Baulch et al. [189]), reported in Table 6.2:

$$f = \log_{10}\left(\frac{k_{max}}{k_{min}}\right) = \log_{10}\left(\frac{k_{nom}}{k_{min}}\right), \quad (6.2)$$

where  $k$  represents the kinetic rate constant for a certain reaction and the subscript "nom" means nominal value. However, considering the pre-exponential factor as the only uncertain parameter, one could write:

$$f = \log_{10}\left(\frac{A_{max}}{A_{min}}\right). \quad (6.3)$$

Performing a LHS study using RANS simulations would have been prohibitive from a computational point of view. For this reason, the WSR network was used instead. By analysing the system responses to input variations, Arrhenius parameters combinations, corresponding to both maximum and minimum of the NO formation distribution, could be identified (Figure 6.23). To achieve that, a total number of 500 samples were considered from the cube shaped by three coordinates, namely the pre-exponential factors of reactions R39, R80, and R85, which are uncertain random variables of the kinetic model.

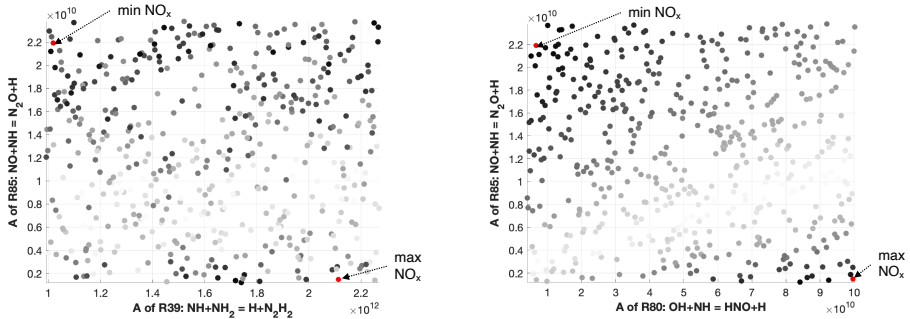


**Figure 6.23:** Latin Hypercube Sampling samples for reactions R80, R85 and R39. Here, the grey scale represents in black the points with maximum NO deviation from the nominal mechanism, in white the points with minimum NO deviation.

The results from the LHS study on the WSR network were then tested in CFD simulations. This means performing additional simulations using the set of kinetic parameters corresponding to the maximum and minimum NO emissions on the LHS chart (Figure 6.23). The uncertainty propagation associated with R39-80-85 on the NO emissions is shown in Figure 6.21 (see “Stagni2020-UQ”). At  $\phi = 1$ , the lower band moves towards the experimental values, allowing a massive reduction compared to the original model from Stagni et al. [13]. This is true especially for N50H50, where NO emissions decrease from 2851 ppm to 539 ppm. On the contrary, temperature profiles in the furnace (not shown here) remain almost constant, meaning that the effect of the kinetic of the three reactions is relevant only for NO. Much better results were achieved at  $\phi = 0.8$ , where the uncertainty bounds almost intersects the experimental data region for N10H90 and contains it for N25H75 and N50H50.

## 6.4 Summary and conclusion

A detailed numerical analysis was conducted to extend the validation of an existing turbulence/chemistry interaction sub-model (PaSR), for non-conventional fuels and conditions. The commercial software ANSYS Fluent 19.3 was used in a framework RANS approach.

For M100H0, it was found that the Damköhler number is well below unity, implying a decoupling between chemistry and mixing. The flame index indeed revealed a premixed combustion behaviour. As a consequence, the choice of the mixing time scale had not impact on the temperature predictions. On the contrary, adopting a more refined kinetic schemes (GRI-2.11 instead of KEE) allowed to catch ignition at  $z = 600$  mm.

If hydrogen (M50H50) is introduced in the fuel blend, the reaction region is shifted upstream towards the burner exit and the Damköhler number approach unity. This means that there is a strong interplay between chemistry and turbulence. On one side, GRI-2.11 allowed to capture correctly the ignition, lowering the relative error from 7% to 2% at  $z = 150$  mm and from 8% to 3% at  $z = 200$  mm compared to KEE. On the other side, the proper choice of the mixing time scale constant  $C_{mix}$  was paramount to further reduce these discrepancies. A  $C_{mix} = 0.3$  was found to be the best compromise. Beside the static approach, dynamic models were also tested to automatically define the mixing constant without the need for tuning.

Results were in line with those obtained by  $C_{mix} = 0.3$ . However, an under-prediction at  $z = 100$  mm was remarked which was not alleviated neither by the choice of the turbulence modeling neither by boundary conditions or radiation model. The author believes this is due to RANS limit and an LES or DES simulation might solve the issue.

Simulating a pure hydrogen flame (M0H100) implies a Damköhler number well higher unity and a partially non-premixed combustion behaviour as shown by the flame index. Temperature predictions seemed not to be affected by the accuracy in representing chemistry. Despite the turbulence models and  $C_{mix}$  values tested, the model over-predicted the first measured point ( $z = 100$  mm).

Different approaches were used to evaluate NO molar fraction at the outlet, comparing the post-processing tool with the complete kinetic scheme (with NO chemistry). The full GRI-2.11 allowed to reduce the under-prediction achieved with the post-processing tool. Furthermore, an engineering approach, considering  $\kappa=1$  for NO, allowed to fill the gap between experiments and prediction for M0H100. Finally, a brute-force sensitivity revealed the contribution of each pathway to NO emissions. It was found out that NNH is the most important route, responsible alone for the 81% of NO production for M0H100, followed by thermal NOx and the  $N_2O$  route.

Finally, an equimolar blend of ammonia and hydrogen (N50H50) was validated numerically using the air injector ID16 and  $\phi=0.8$ . The agreement between temperature measurements and estimations was found to be satisfactory, and nearly insensitive to the adopted kinetics, i.e. Stagni et al. [13] and Glarborg et al. [4]. However, in terms of NOx emissions, substantial differences between predictions with the two mechanisms were observed. In light of this pronounced difference, the error in pollutant emissions can be partially attributed to the uncertainties intrinsically embedded in the kinetic sub-model. In spite of the great over-prediction at  $\phi = 1$ , the mechanism from Stagni et al. [13] was found to be more accurate. To reduce this discrepancy, a Latin Hypercube Sampling (LHS) method was adopted to propagate the uncertainty of a sub-set of reactions (R39-80-85) to NO production/emissions using a well-stirred reactor network (WSR). Two kinetic mechanisms were determined from Stagni et al. [13], representing the maximum and the minimum of the NO distribution. At  $\phi = 1$ , the lower band moves towards the experimental values, allowing a massive reduction compared to the original model from Stagni et al. [13]. Much better results were achieved at  $\phi = 0.8$ , where the uncertainty bounds almost intersects



the experimental data region for N10H90 and contains it for N25H75 and N50H50. In conclusion, a significant part of the discrepancy between the measured and predicted pollutant emissions is associated to inherent uncertainties in recent kinetic mechanisms for ammonia/hydrogen combustion. In fact, the latter were found to be reliable for temperature prediction, while over-predicting NO emission significantly. Thus, this work indicates the need to improve existing  $\text{NH}_3/\text{H}_2$  models, especially in diluted conditions. In particular, specific reactions (i.e. R39-80-85) need better characterization, to improve models of practical systems. This is particularly true for stoichiometric conditions, where the discrepancies between numerical models predictions and experiments was found to be most significant.

## Chapter 7

# Reduced-order model from CFD simulations

*Although CFD tools have significantly progressed in recent years, their use in real time is still unrealistic. In this context, the availability of physics-based reduced-order models (ROMs) becomes very attractive, to embed the critical aspects of a detailed simulations into simplified relationships between the inputs and outputs that can be used in real time. With this idea in mind, a first-of-its-kind digital twin for a furnace operating in flameless conditions is presented in this chapter. It is based on CFD simulations combining Proper Orthogonal Decomposition (POD) and Kriging. Firstly, POD is used for data compression and then Kriging is used to find a response surface for the unexplored operating condition. The influence of the number of training simulations used for the development of the ROM has been performed and a leave-k-out analysis has also been carried out to determine how many and which simulations are needed.*

*This chapter is partially based on the following publication:*

G. Aversano, **M. Ferrarotti**, A. Parente, “Digital twin of a combustion furnace operating in flameless conditions: reduced-order model development from CFD simulations”, Accepted for publication in the “Proceedings of the Combustion Institute” 2020.

**Author's contribution to the publication** The author contributed in reviewing the relevant literature and in choosing the methodology to follow. Furthermore, he analysed and selected the most relevant physical parameters of the ULB furnace, which are the basis for the reduce order model development. The author optimised the CFD model and conducted all simulations in ANSYS Fluent 19.0. He also contributed in judging the physicality of the results obtained with the ROM.

## 7.1 Introduction and literature review

Although CFD are becoming more and more reliable, their use in real time is still unrealistic, especially for combustion regimes such as flameless/MILD combustion, whose description requires the use of detailed kinetic mechanisms and advanced turbulence-chemistry interactions approaches, as seen in the previous Chapters. In this context, the availability of physics-based reduced-order models (ROMs) becomes very attractive, to embed the critical aspects of a detailed simulations into simplified relationships between the inputs and outputs that can be used in real time. The development of virtual models, also referred to as *digital twins*, of industrial systems opens up a number of opportunities, such as the use of data to anticipate the response of a system and brainstorm malfunctioning, and the use of simulations to develop new technologies, i.e. virtual prototyping.

A definition of digital twins is “an integrated multi-physics, multi-scale, probabilistic simulation of an as-built system, enabled by digital thread, that uses the best available models, sensor information, and input data to mirror and predict activities/performance over the life of its corresponding physical twin” [190]. Combining CFD simulations with experiments and real-time data coming from sensors of a real industrial system to foresee a change in its state is possible only if the prediction of the system’s state becomes instantaneous [81]. To do so, a set of training simulations must be generated beforehand, for a wide enough range of possible operating conditions. A physics-based ROM can be then developed by using unsupervised learning to extract the key latent features in the data, for which a response surface is subsequently found by a supervised learning technique. Once the mapping between inputs and outputs is embedded in a ROM, the system state can be predicted for new operating conditions, based on real-time data coming from sensors. Aversano et al. [191] showed that the combination of an unsupervised data compression method, i.e. Proper Orthogonal Decomposition (POD), with a supervised interpolation technique, i.e. Kriging, could be effectively used for the reconstruction and prediction of two-dimensional laminar methane flames. In the present work, this methodology was extended and applied to the development of a first-of-its-kind digital twin for a furnace operating in flameless combustion conditions. The aim is to predict the full state of the furnace (spatial fields of temperature and main chemical species mass fractions) as well as of important scalar quantities at locations of interest (wall temperature, OH peak value and location, flame length and exhaust gas composition

including pollutants), within a prescribed accuracy. The design space consisted of a design parameter, the air injector diameter, and two measured inputs, the fuel composition (mixture of  $\text{H}_2/\text{CH}_4$  in molar basis) and the equivalence ratio.

The remainder of this chapter is organized as follows. The methods used for the ROM development are described in Section 7.2, while the description of the case study is reported in Section 7.2.3. The sensitivity to the training data of the data compression process and of POD+Kriging are presented in Section 7.3.1 and 7.3.2, respectively. The performances of the developed digital twin are finally discussed in Section 7.4.

## 7.2 Methods

### 7.2.1 Proper Orthogonal Decomposition

Consider a snapshot matrix  $\mathbf{Y}$  of size  $(m \times n)$ , where each row of  $\mathbf{Y}$  is a vectorized 2D or 3D spatial field of some variable of interest such as temperature, or a concatenation of more than one field, coming from one CFD simulation. Thus,  $m$  is the number of available simulations and  $n$  is the number of grid points times the number of considered variables. In combustion-related problems,  $n \gg m$ . Proper Orthogonal Decomposition (POD) seeks  $\mathbf{Z}$  of size  $(m \times k)$  and  $\mathbf{A}$  of size  $(n \times k)$  with  $k \ll n$  (hence the reduction), such that the functional  $f(\mathbf{Z}, \mathbf{A}) = \frac{1}{2} \|\mathbf{Y} - \mathbf{Z}\mathbf{A}^T\|^2$  is minimized, subject to  $\mathbf{A}^T \mathbf{A} = \mathbf{I}$ , where  $\mathbf{I}$  is the identity matrix. This problem can be solved by computing the singular value decomposition (SVD) of the matrix  $\mathbf{Y}$ , which corresponds to finding the eigenvectors of the matrix  $\mathbf{C} = \frac{1}{m-1} \mathbf{Y}^T \mathbf{Y}$ . These eigenvectors are the columns of  $\mathbf{A}$ . A low-rank approximation of  $\mathbf{Y}$  is found as follows  $\mathbf{Y} \approx \mathbf{Z}\mathbf{A}^T = \mathbf{Y}\mathbf{A}\mathbf{A}^T$ , where the columns of  $\mathbf{A}$  of size  $(n \times k)$  are the POD modes, also referred to as spatial shapes or *eigenflames* [191], and  $\mathbf{Z}$  of size  $(m \times k)$  is the matrix of POD coefficients. Each column of  $\mathbf{Z}$  are the  $k$  coefficients for the retained  $k$  POD modes so that one particular simulation, or row of  $\mathbf{Y}$ , can be expressed as a weighted sum of different data-driven eigenflames:  $\mathbf{y}(\mathbf{x}) = \sum_{i=1}^k \mathbf{a}_i z_i(\mathbf{x})$ .

### 7.2.2 Kriging

Kriging is an interpolation method in which every realization  $z(\mathbf{x})$  (e.g. the POD coefficients) is expressed as a combination of a trend function and a residual [192]:

$$z(\mathbf{x}) = \mu(\mathbf{x}) + s(\mathbf{x}). \quad (7.1)$$

The trend function  $\mu(\mathbf{x})$  is a low-order polynomial regression and provides a global model in the input space.

The residuals  $s(\mathbf{x})$  are modeled by a Gaussian process with a kernel or correlation function that depends on a set of hyper-parameters to be evaluated by Maximum Likelihood Estimation (MLE) [193, 194].

### 7.2.3 Data-set

To generate the samples required for development of the furnace ROM, CFD simulations were carried out using the commercial software Ansys Fluent 19.0. A constant input power of 20 kW was fixed, while the cooling flow rate was set to reach a furnace outlet temperature of  $T_{out} = 1000$  °C. A 45° degrees angular sector of the 3D geometry of the furnace was considered, as a result of the symmetry of the problem, without considering the window. More details about the grid can be found in Chapter 6. The standard  $k-\epsilon$  turbulence model was used in combination with the PaSR model [77] for turbulence-chemistry interactions. Following the findings of Chapters 5 and 6, a  $C_{mix}$  of 0.5 was set to determine the mixing time scale in PaSR. Keeping in mind the objective of running a large set of CFD simulations, the KEE kinetic scheme was used as a fair compromise between accuracy and computational cost. The author is aware that such a choice penalizes more the cases having an hydrogen molar fraction of about 50%, as shown in Chapter 6. Following the same logic, the NO modeling was handled by the post-processing tool of ANSYS Fluent, which includes the thermal, prompt,  $N_2O$  and NNH pathways as described in Chapters 5-6. The discrete ordinate (DO) radiation model was used, in combination with the weighted-sum-of-gray-gases (WSGG) model, using the coefficients proposed by Smith et al. [163].

Three input parameters were considered to generate the simulation samples: fuel composition in mole fractions (mixture of methane/hydrogen), equivalence ratio and air injection geometry. A design of experiments (DoE) was

established using latin hypercube sampling, varying the input parameters in the range 0-100 % ( $\text{H}_2$  molar fraction), 0.7-1 (equivalence ratio  $\phi$ ) and 16-20-25 mm (air injector ID size). A total of 45 simulations were carried out. The variables of interest selected for the generation of the furnace ROM were temperature, major species ( $\text{CH}_4$ ,  $\text{H}_2$ ,  $\text{O}_2$ ,  $\text{H}_2\text{O}$  and  $\text{OH}$ ), minor species ( $\text{CO}$  and  $\text{OH}$ ), and pollutants ( $\text{NO}$ ).

Before generating a digital twin based on CFD simulations, it is key to ensure that the numerical simulations are a good representation of reality. The computational model used in this work was validated in the Adelaide Jet in Hot Co-flow in Chapter 5, fed with an equimolar methane-hydrogen mixture, and in the very same furnace in Chapter 6 for similar operating conditions.

## 7.3 Reduced order model development

The furnace ROM was developed based on the methodology shown in Figure 7.1. The approach, introduced by Aversano et al. [191], allows to distinguish between invariant information, the POD modes, and system-dependent ones, the POD coefficients. The POD modes are kept constant, as they represent the intrinsic system physics. The POD coefficients, on the other hand, are used to represent the system variability due to changes in the boundary conditions. This relationship is modelled by means of non-linear regression approaches, Kriging in the present case. The accuracy of the reduced-order model is then dependent on the degree of reduction imposed during the POD decomposition as well as on the training data used to identify the POD modes and coefficients. These aspects are critically discussed in the next sections of the present study. The maximum number of POD modes that could be extracted from the data-set was  $m - 1$ , where  $m$  is the total number of available simulations. In the present study, the data-set related to one particular field (e.g. temperature) consisted of a matrix of size  $(m \times l)$ , with  $m = 45$  and  $l = N_c$ , where  $N_c$  is the number of cells of the grid<sup>1</sup>. Thus, a total of 44 POD modes could be identified and used to encode each simulation (i.e. a vector of 216,360 real numbers for ID16) into a set of 44 coefficients, for which a Kriging response surface was found. The ROM developed in the present work requires the training of a reduced set of scalars (from 216,360 to 44 for ID16) from the POD de-

---

<sup>1</sup>216,360 for ID16. It slightly varies in function of the selected air ID.

composition, for which the supervised Kriging method is used. Once built, the evaluation of the ROM is almost instantaneous and can be used in real time, while each of the 45 numerical simulations required 1440 CPU hours on 20 cores.

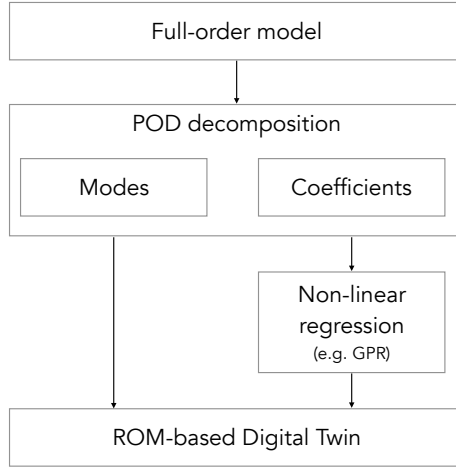


**Figure 7.1:** Reduced-order model generation: identification of invariant and system-dependent information.

### 7.3.1 Reconstruction of test data

The set of training data to be used for the generation of the reduced-order model out of the 45 available CFD simulations was determined using the sampling strategy described by Aversano et al. [191], as this method allows to associate an importance index to each available simulation, based on the influence they have on the reduced POD basis. To assess the importance of the training data size on the POD basis and understand if enough data had been collected for ROM development, a leave- $k$ -out cross validation analysis was performed, where  $k$  was the number of simulations left out from the overall available training data set. Each time,  $k$  simulations were left out and the error associated to the reconstruction of left-out simulations from the POD basis was evaluated.

Figure 7.2 shows the average normalized root mean squared errors (NRMSE) across all the available thermo-chemical variables, for the re-



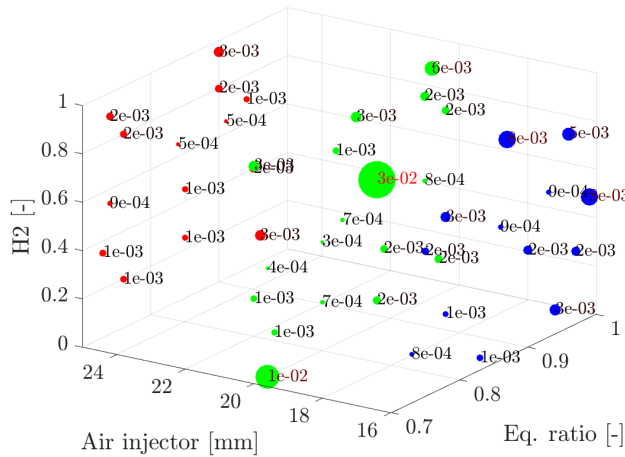


**Figure 7.2:** Leave-one-out reconstruction errors, visualized in the input parameter space. The sizes of the circles are proportional to the error. Different colours are used for the 3 different values of the air injector size.

construction of one particular left-out simulation. This corresponds to a leave-one-out (LOO) analysis. In this case, the total number of possible design of experiments (DoE) was equal to the number of available simulations, making it possible to visualise the NMRSE in the design space. Figure 7.2 allows to identify the design points impacting most the POD reconstruction error. It can be observed that very few design points had a considerable impact on the quality of the POD reconstruction. When  $k > 1$ , the total number of possible DoE is given by:  $m!/(m-k)! k!$ , where  $m$  is the total number of available simulations and  $k$  is the number of simulations to leave out each time. In the present case,  $m = 45$  while  $k$  ranges between 1 and 5, thus leading to a very large number of combinations (exceeding 1 million), for  $k = 5$ . Therefore, only a random subset of all the possible combinations was considered. For a given value of  $k$ , the leave- $k$ -out errors were estimated from random subsets of different sizes. Based on a sensitivity study, the size of the subset was chosen to be 250, as the leave- $k$ -out errors were converging for this value. The analysis was carried out for an increasing value of  $k$ , as reported in Figure 7.3, where the average NRMSE and its standard deviation for the reconstruction of the test data are reported. Two observations can be made. First, the aver-

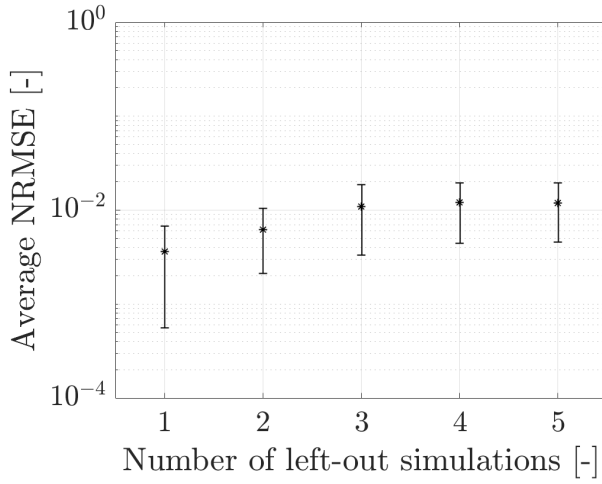


**Figure 7.3:** Average NRMSE for the reconstruction of an increasing number of left-out simulations. Vertical bars represent the standard deviation of the error associated to different combinations of  $k$  left out simulations.

age reconstruction error increases when more simulations are left out of the training data, as expected, and converges at a value of roughly 1%, indicating the ability of the POD basis to reconstruct the test data. Second, the standard deviation of the reconstruction error decreases when  $k$  increased, indicating that for high values of  $k$  the ROM is more sensitive to the size of the training data than to the location of the training simulations in the input parameter space.

### 7.3.2 Prediction of new data

The leave- $k$ -errors for the reconstruction of the left-out data can be used to identify the most relevant simulations for the definition of a reduced basis, as shown in the previous section. However, in the context of predictive ROMs, it is more robust to base the leave- $k$ -out approach on the prediction of the left-out data in order to assess how the developed ROM generalizes to new data [195]. Thus, this section presents the leave- $k$ -out errors relative to the prediction of the left-out data by building a ROM from the included (not left out) simulations. Figure 7.4 shows the average normal-

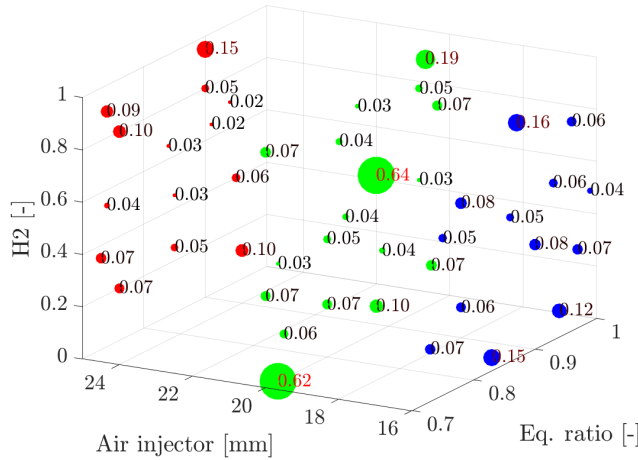


**Figure 7.4:** Leave-one-out reconstruction errors, visualized in the input parameter space. The sizes of the circles are proportional to the error. Different colours are used for the 3 different values of the air injector size.

ized root mean squared errors (NRMSE) associated to the prediction of each particular simulation (spatial fields of temperature and main chemical species), when that particular simulation was left out. Although relatively high prediction errors were observed for simulations that had a low influence on the POD basis, some of the highest LOO errors were observed for the prediction of the simulations that had the highest influences on the POD basis as well. Thus, the evaluation of these influences can be taken into consideration as a fast preliminary method to assess the quality of the training data and detect the regions in the input space where more observations are needed. Figure 7.5 shows the average NRMSE for the prediction of an increasing number of left-out simulations, similarly to what was done in Figure 7.3. As the LOO prediction errors of Figure 7.4 indicated the most influential simulations that should always be included in the training set, the leave- $k$ -out errors of Figure 7.5 were estimated taking this into account. Thus, only the simulations whose influence was  $< 15\%$  with respect to the most important simulation were taken into consideration as possible test data. Predictably, the prediction errors were greater for higher values of left-out simulations,  $k$ . Interestingly, as observed for the reconstruction errors, the standard deviation of the mean prediction NRMSE decreased

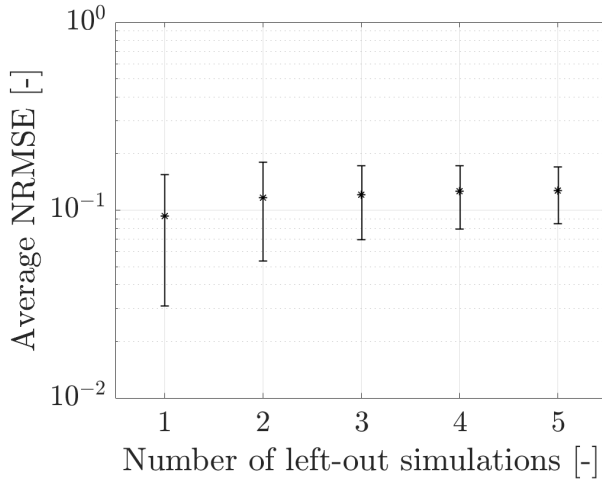


**Figure 7.5:** Average NRMSE for the prediction of an increasing number of left-out simulations. Vertical bars represent the standard deviation of the error associated to different combinations of  $k$  left out simulations.

when  $k$  was increased. In the context of stationary systems, it is of major interest to look at quantities that can be immediately compared to sensory data rather than at the full spatial fields. Therefore, leave- $k$ -out errors for the prediction of scalar and integral quantities such as wall temperature, flame length and exhaust gas composition are reported in Figure 7.6. The flame length was estimated as the distance from the inlet (on a vertical axis) at which the OH mass fraction decreased to less than 5% of its maximum value. The wall temperature was measured at the following axial coordinates  $z$  (in mm): 100, 200, 300, 400, 500, 600. Figure 7.6 shows that the prediction error for the wall temperatures, flame length and OH peak location slightly increase when increasing  $k$  from  $k = 1$  to  $k = 5$ . Nevertheless, the average NRMSE never exceeds 2%, which is remarkable. Higher NRMSE were obtained for the prediction of the OH peak value, around 10%, but this can be considered acceptable considering the lower concentrations and more localised distribution of OH compared to other scalars. Similarly to Figure 7.5, the standard deviations in Figure 7.6 decrease for higher values of  $k$ . Low standard deviations for the prediction errors are a preferable characteristic of a ROM, to guarantee a lower upper bound for the prediction error. The fact that the developed digital twin can provide

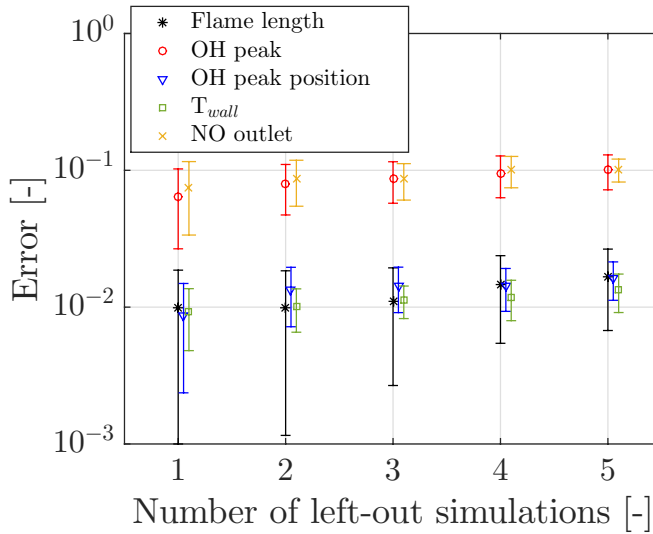


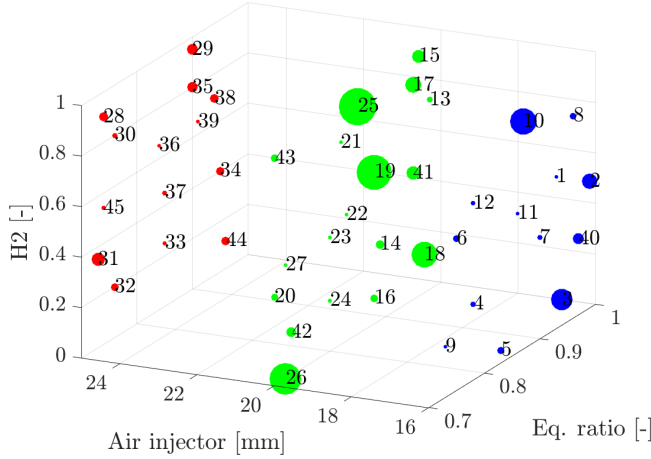
**Figure 7.6:** Leave- $k$ -out relative errors for the prediction of scalar quantities such as wall temperature, flame length, value and location of the  $Y_{OH}$  peak. Vertical bars represent standard deviations of the error associated to different combinations of  $k$  left out simulations.

access to quantities difficult to measure with physical sensors is a very interesting feature of the approach and opens a number of opportunities for the soft-sensing [196] and control of combustion technologies using models, in this case ROMs.

## 7.4 ROM developed from the training data-set determined by leave-k-out analysis

A ROM was developed based on the simulations determined by the leave- $k$ -out analysis of the previous Section. The errors of Figure 7.6 were considered relatively low even for  $k = 4$ , suggesting that the use of a training set of size  $m - 4$ , i.e. 41, could lead to satisfactory performances as well, especially for the prediction of the scalar and integral quantities. Thus, a value of  $k = 4$  was chosen and all simulations except the four-dimensional set characterised by the minimum leave- $k$ -out error (simulations 1, 22, 28

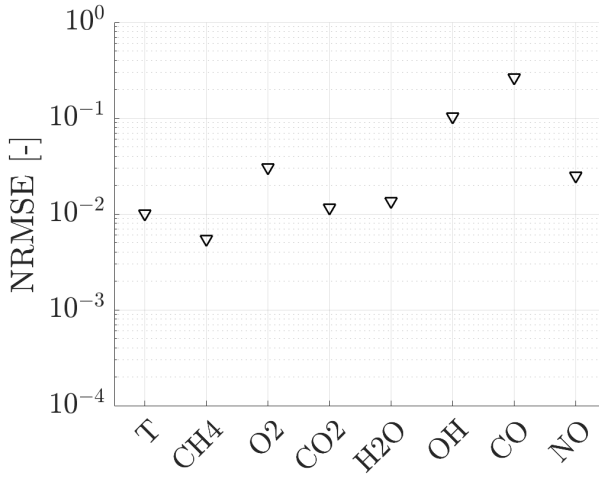
and 39 of Figure 7.7) were employed as training data-set to find both the reduced POD basis, and train a Kriging model for the prediction of the POD scores. The left-out simulations were used as test data, to assess the ROM's predictive capabilities.



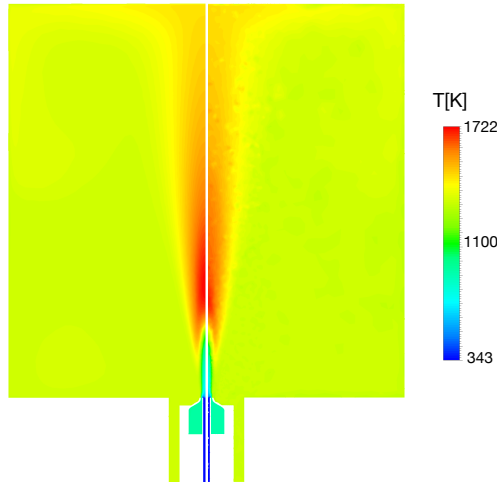
**Figure 7.7:** List of CFD cases varying the three operating conditions.

Figure 7.8 reports the overall NRMSE for all the variables for the prediction of the test data. The fields of temperature and the main chemical species mass fractions and pollutants were predicted with an error below 10%, whereas higher prediction errors were obtained for CO and OH. This was expected, considering the order of magnitude (ppm) and the much more localised distribution of CO and OH with respect to other scalar. Indeed, a relatively modest error on the location of the peak might become a high NRMSE, thus representing a more challenging target for the ROM.

Figure 7.9 and Figure 7.10 compare the true temperature and OH field, respectively, to the ROM predictions, for different unexplored operating conditions. It can be observed how the ROM is able to accurately capture their distribution within the furnace, providing a solution which closely matches the CFD one, with no evident difference. Table 7.1 reports the errors for the prediction of different scalar quantities such as flame length, position and value of the OH peak and exhaust gas composition, for the four left-out simulations. Errors on the wall temperatures, flame length and OH mass fraction peak location are remarkably low, below 5% for all cases,



**Figure 7.8:** NRMSE for the prediction of the test data by a ROM based on POD and Kriging.



**Figure 7.9:** (left) True temperature field from CFD simulation for ID16, 60% H<sub>2</sub> and  $\phi=0.93$ . (right) Predicted temperature field for the same operating conditions.

with respect to the true values for the left-out simulations. The prediction of the OH mass fraction peak location values shows higher prediction errors.

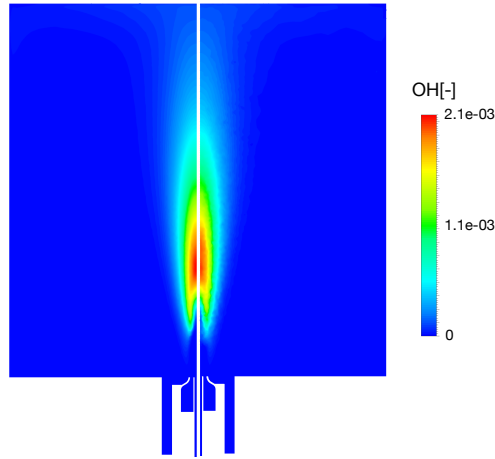


**Figure 7.10:** (left) True OH field from CFD simulation for ID25, 65%  $H_2$  and  $\phi=0.91$ . (right) Predicted OH field for the same operating conditions.

Nevertheless the error never exceeds 10%, with respect to the true values.

(Error on)	Sim. 1	Sim. 2	Sim. 3	Sim. 4
$T_{wall}$	0%	3%	1%	0%
FLAME LENGTH	9%	0%	1%	0%
POS. OF $Y_{OH}$ PEAK	2%	0%	0%	0%
VALUE OF $Y_{OH}$ PEAK	9%	5%	7%	1%
$Y_{H_2O}$ OUTLET	1%	3%	4%	1%
$Y_{CO_2}$ OUTLET	5%	1%	5%	1%
$Y_{CO}$ OUTLET	3%	0%	0%	1%
$Y_{NO}$ OUTLET	5%	3%	1%	1%

**Table 7.1:** Digital twin's prediction errors for different scalar quantities of the furnace such as wall temperature, flame length , position of the peak of  $Y_{OH}$ , value of the peak of  $Y_{OH}$ , furnace outlet mass fractions of  $H_2O$ ,  $CO_2$  and  $CO$ .



## 7.5 Summary and conclusions

In the present work, the first-of-its-kind digital twin for a furnace operating in flameless combustion conditions was developed and validated. A reduced-order model (ROM) based on the combination of Proper Orthogonal Decomposition (POD) and Kriging was developed for the prediction of three-dimensional spatial fields of temperature and chemical species (major, minor and pollutants), as a function of three input parameters, the fuel composition (a mixture of methane and hydrogen from pure methane to pure hydrogen), the equivalence ratio and the air injector diameter. Forty-five three-dimension CFD simulations were carried out to generate samples for the ROM. Numerical simulations were also validated against available experimental data on the furnace, for different fuel mixture compositions. During the construction of the ROM, POD was used for data compression, thus to represent the original data with a reduced number of features, the POD scores. Kriging was used to find a response surface for these scores at unexplored operating conditions. The influence of each simulation on the reduced basis found by POD was estimated, so to identify the most important simulations to retain as training data for the ROM. The influence of the number of training simulations used for the development of the ROM was also assessed. A leave- $k$ -out analysis was carried out to determine how many and which simulations were needed for the training of the ROM, and estimate how the developed ROM would generalize to new data. Results showed that the developed ROM could predict the fields of temperature and  $\text{CO}_2$ ,  $\text{O}_2$ ,  $\text{H}_2\text{O}$ ,  $\text{CH}_4$  mass fractions, at unexplored operating conditions, reliably with an overall prediction error lower than 10%. Higher errors ( $< 20\%$ ) were observed for the prediction of minor species, e.g.  $\text{CO}$ , and radicals, e.g.  $\text{OH}$  radicals. In addition, the prediction of scalar quantities at specific locations was characterised by even lower reconstruction errors, below 5%. The latter included wall temperatures, flame length,  $\text{OH}$  peak value and location, as well as exhaust gas composition and temperature, proving the potential of the method for soft sensing and real-time predictions of system change when changing operating conditions.

In the present work, a ROM combining sensor data with CFD simulations was developed. It was also proved that the RANS-based simulations are a good representation of reality. Nevertheless, CFD might have different level of fidelities, considering LES or RANS with detailed or reduced kinetic schemes. A future work might combine simulations with different level of accuracy to improve the overall ROM predictions. The goal is to model the

level of discrepancy between these different type of simulations to build a ROM able to intrinsically consider the error committed passing from LES to RANS and from a detailed to a reduced kinetic scheme. Furthermore, an interesting aspect would involve the extension of the ULB furnace ROM to other furnaces. Here, the key point is to extract, within the modes, universal features from the ULB furnace ROM, to be used in different systems running a reduced number of ad-hoc simulations. However, at this purpose, the ROM shall be derived differently, being the modes function of the grid size.



## Chapter 8

# Conclusions and future work

*In this final chapter, the main conclusions of this PhD thesis are summarised. Special focus is placed on the comparison between the main objective and the final results. This allows to see which goals have been achieved. Then, future perspectives and improvement are given.*

## 8.1 Summary and conclusions

In the next years, the world will face a major change to reduce the carbon footprint and pollutant emissions. However, a reliable energy storage should permit a synchronization between energy production and demand. Power-to-Fuel option or chemical storage can be the key for a sustainable energy system, creating synthetic “green” fuels, whose composition is a blend of  $\text{CH}_4$ ,  $\text{H}_2$ ,  $\text{CO}$  and  $\text{NH}_3$ . To achieve Power-to-Fuel, the development of a high efficiency technology, coupled with virtually zero pollutant emissions, stable working conditions with different load and fuel and significant energy saving is required. In the last years, a so-called MILD or flameless combustion has drawn attention for its ability of meeting the mentioned targets. However, the studies available in literature are conducted on Jet in hot co-flow-like systems or they face conventional fuels, such as natural gas or methane. The examples using non-conventional fuels are scarce and limited to few operating conditions.

With this aim in mind, the investigations carried out in this PhD thesis tackled the following aspects. On one side, experimentally investigate the potential use of flameless combustion to burn in an efficient and low-pollutant way non-conventional fuels. On the other, the optimization of an affordable numerical model capable of reproducing the main features of this combustion mode, such as reaction zone position, maximum temperature and pollutant emissions. Finally, the development of a reduced order model or digital twin of the furnace, capable of predicting new operating condition with almost negligible delay.

A detailed experimental campaign was conducted to analyse the performance of the flameless burner with a standard air injector diameter. A progressive addition of hydrogen in methane enhanced combustion features, reducing the ignition delay time and increasing the reactivity of the system, possibly losing its flameless behaviour. Indeed, this was confirmed by measured temperature profiles and  $\text{OH}^*$  chemiluminescence imaging. A threshold of 25%  $\text{H}_2$  was defined for reaching MILD conditions, even if visible flame structures were remarked. Pollutant emissions for this fuel blend were still moderate (25 ppm). This is in line with the goal of introducing “green” hydrogen into the natural gas pipeline (up to 20%) to reduce  $\text{CO}_2$  emissions. A second experimental campaign aimed to reduce temperature peaks and pollutant emissions varying the air injector diameter and therefore the injection velocity, up to 200 m/s for ID16. This allowed to

reach very high recirculation degree,  $k_v$ , up to 28 for pure methane. The effect was relevant on both the position of the reaction zone and the maximum temperature of the system, as well as on pollutant emissions, with a reduction of 200 K and 84%, respectively, for M50H50 ID16. A further campaign focused on using a longer fuel injection lance. The fuel lance was indeed immersed into the furnace for an extra length of 25 mm and 50 mm. Being the fuel injected further downstream in the furnace, it guarantees more time to the air stream to be diluted by the exhaust gases, increasing the recirculation degree. Pollutant emissions were reduced of 87% for pure hydrogen respect to the case with a standard fuel lance. Minor differences were found between the two length, meaning that L25 provides already a good level of dilution. MILD conditions were reached up to M25H75 with no visible flame structures. Finally, an additional campaign focused on studying pollutant emissions when adopting ammonia/hydrogen blends. This first-of-its-kind analysis showed that NO increases rapidly when a small amount of ammonia (10%) is introduced in pure hydrogen, reaching a peak which varies according to the equivalence ratio. Results suggests also that stoichiometry has a major impact on NO emissions. An optimal window, minimizing both NO and  $\text{NH}_3$ -slip emissions can be defined when using  $\phi = 0.9$ . Differently from the methane/hydrogen cases, higher injection velocities increases the pollutant emissions drastically. This might be due to a reduced residence time, which does not allow a sufficient conversion of NO towards  $\text{N}_2$ . To qualitatively describe the observed trends, a reactors network, consisting of a well stirred reactor coupled with a mixing unit, was considered. The analysis highlighted the most important reactions correlated to NO formation and the reason of the NO reduction at stoichiometry condition.

On the other hand, an existing numerical model based on Partially Stirred reactor (PaSR) was firstly tested and optimized on a simplified burner, emulating MILD combustion (Adelaide Jet in Hot Co-flow). First, a set of RANS simulations were run to investigate different mixing model formulations: a static model based on a fraction of the integral time-scale, a fractal-based and a dynamic model based on the resolution of transport equations for scalar variance and dissipation rate. The proposed approaches were validated at different fuel-jet Reynolds numbers (5k, 10k and 20k) and different co-flow oxygen dilution levels (3%, 6% and 9%). The dynamic mixing model outperforms both the static and fractal models, leading to very accurate predictions in terms of mean temperature, CO and OH mass fraction for a wide range of conditions. Second, a study about the role of

combustion models and kinetic mechanisms on the prediction of NO formation was also conducted. Finally, an analysis about the choice of a Heat Release Rate (HRR) marker for MILD (HM1 flame) and not MILD (HM3 flame) conditions was carried out.

Once having awareness of the capability of the proposed numerical model, simulations were conducted to define the key aspects in simulating a flameless furnace, testing its limits simulating different fuel blends. For pure methane, it was found that the Damköhler number is well below unity, implying a decoupling between chemistry and mixing. Indeed, the choice of the mixing time scale has not impact on the temperature predictions. On the contrary, adopting a more refined kinetic schemes (GRI-2.11 instead of KEE) allows to catch ignition. If hydrogen is introduced in the fuel blend, the reaction region is shifted upstream towards the burner exit and the Damköhler number approach unity, while flameless/MILD conditions are still kept. This means that there is a strong interplay between chemistry and turbulence. A temperature under-prediction at  $z = 100$  mm was remarked, which was not alleviated neither by the choice of the turbulence modeling neither by radiation modeling. The author believes this is due to RANS limits and an LES or DES simulation might solve the issue. Simulating a pure hydrogen flame implies a Damköhler number well higher unity and the flame index shows that combustion is non-premixed. Temperature predictions seemed not to be affected by the accuracy in representing chemistry. Despite the turbulence models and the mixing time scale formulations tested, the model over-predicts the first measured point ( $z = 100$  mm). Different approaches were used to evaluate NO molar fraction at the outlet, comparing the post-processing tool with the complete kinetic scheme considering the NO chemistry. However, an important under-prediction was remarked for the pure hydrogen case. Finally, an equimolar blend of ammonia and hydrogen was validated numerically using the air injector ID 16 mm and  $\phi = 0.8$ . The agreement between temperature measurements and estimations was found to be satisfactory, and nearly insensitive to the adopted kinetics. However, in terms of NOx emissions, substantial differences between predictions with the mechanisms were observed. In light of this pronounced difference, the error in pollutant emissions can be partially attributed to the uncertainties intrinsically embedded in the kinetic sub-models. To reduce this discrepancy, a Latin Hypercube Sampling (LHS) method was adopted to propagate the uncertainty of a sub-set of reactions to NO production/emissions using a Well-Stirred Reactor network (WSR). Two kinetic mechanisms were determined from Stagni et al. [13], represent-

ing the maximum and the minimum of the NO distribution and tested back on the CFD simulations, leading to a substantial improvement.

Finally, the first-of-its-kind digital twin for a furnace operating in flameless combustion conditions was created and validated. A reduced-order model (ROM) based on the combination of Proper Orthogonal Decomposition (POD) and Kriging was developed for the prediction of three-dimensional spatial fields of temperature and chemical species (major, minor and pollutants), as a function of three input parameters, the fuel composition (a mixture of methane and hydrogen from pure methane to pure hydrogen), the equivalence ratio and the air injector diameter. Results showed that the developed ROM could predict, in negligible delay, the fields of temperature and  $\text{CO}_2$ ,  $\text{O}_2$ ,  $\text{H}_2\text{O}$ ,  $\text{CH}_4$  mass fractions, at unexplored operating conditions, reliably with an overall prediction error lower than 10%.

## 8.2 Recommendations

The present thesis has made significant progress in testing the fuel flexibility of flameless combustion, both from an experimental and a numerical perspective. However, there are still some aspects, which deserve a further understanding. The following recommendations are made to advance this field beyond the stage reached in this thesis.

Simultaneous imaging of flow field using PIV and temperature field with two-dimensional Rayleigh imaging or Background Oriented Schlieren (BOS) would provide both qualitative and quantitative information about the mixing between fuel, oxidizer and exhaust gases as well as the flame-flow interactions. In addition OH-PLIF,  $\text{CH}_2\text{O}$ -PLIF would provide more information to clarify the turbulence/chemistry interactions and the topology of the autoignition structures. NO-PLIF would increase the understanding of NO formation for methane/hydrogen blends and about the oxidation of  $\text{NH}_3$ . Measurement ports closer to the burner exit ( $z < 100$  mm) together with flow field imaging (PIV) might clarify the position of the ignition region for fuel with very high hydrogen content. This would be beneficial also for numerical validation.

An experimental campaign might be conducted to investigate extinction limits for ammonia/hydrogen blends towards pure ammonia. In particular, it shall consider: pre-heating of the fuel blend and/or reducing the



thermal power to enhance the reactivity and increase the residence time, respectively.

From a numerical modeling point of view, a complete Large Eddy Simulation (LES) study of the furnace is needed to add more information about the flow field and to clarify all doubts about the choice of the turbulence model. This approach would also allow to overcome the limitations of the RANS framework remarked simulating the equimolar blend methane/hydrogen and pure hydrogen.

As clearly stated from the kinetic uncertainty quantification study simulating ammonia/hydrogen blends, there is a need to improve existing  $\text{NH}_3/\text{H}_2$  sub-models, especially in diluted conditions. In particular, specific reactions (i.e. R39-80-85) need better characterization, to improve models of practical systems.

Finally, a future work developing a ROM might combine simulations with different level of accuracy (RANS vs LES) to improve the overall ROM predictions. The goal is to model the level of discrepancy between these different type of simulations to build a ROM able to intrinsically consider the error committed passing from LES to RANS and from a detailed to a reduced kinetic scheme. Furthermore, an interesting aspect would involve the extension of the ULB furnace ROM to other furnaces. Here, the key point is to extract, within the modes, universal features from the ULB furnace ROM, to be used in different systems running a reduced number of ad-hoc simulations.

# Appendices



## Appendix A

# Correlations used to calculate the furnace energy balance

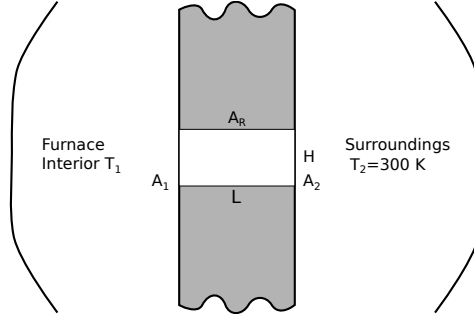
This section contains the correlations used in Section 2.4 to quantify the energy balance of the furnace.

Figure 2.8 shows an idealized sketch to estimate the radiative power transmitted through the window ( $P_{rad}$ ). The solution of the problems relies on the following assumptions: (1) steady-state conditions, (2) furnace interior and exterior surroundings are large, isothermal surfaces, (3) furnace insulation layers are adiabatic and diffuse-gray with uniform radiosity. The open-end ideal surfaces ( $A_1$  and  $A_2$ ) and the two sides of the insulation (both named as  $A_R$ ) form a diffuse-gray enclosure.

The hypothetical areas  $A_1$  and  $A_2$  behave as black surfaces at the respective temperatures of the large surroundings to which they are exposed. Since  $A_R$  is adiabatic, it behaves as a re-radiating surface and its emissivity has no effect on the analysis. The net radiation leaving  $A_1$  can be finally written as

$$P_{rad} = \frac{E_{b1} - E_{b2}}{\frac{1 - \epsilon_1}{\epsilon_1 A_1} + \frac{1}{A_1 F_{12} + [(1/A_1 F_{1R}) + (1/A_2 F_{2R})]^{-1}} + \frac{1 - \epsilon_2}{\epsilon_2 A_2}}, \quad (\text{A.1})$$

where  $F_{ij}$  is the view factor between surfaces  $i$  and  $j$  and  $\epsilon_i$  is the emis-



**Figure A1:** Idealized problem to quantify the radiative power transmitted through the window.

sivity of the surface  $i$ <sup>1</sup>.  $E_{bi}$  is the black body emissive power  $\sigma T_i^4$ , where  $\sigma = 5.67 \times 10^{-8} \text{ W/m}^2 \text{ K}^4$ . The view factor  $F_{12}$  can be determined using the following relation between aligned parallel rectangles [17], as shown in Figure A2. Using the summation rule on  $A_1$ , one could finally find:

$$\bar{X} = X/L, \bar{Y} = Y/L$$

$$F_{ij} = \frac{2}{\pi \bar{X} \bar{Y}} \left\{ \ln \left[ \frac{(1 + \bar{X}^2)(1 + \bar{Y}^2)}{1 + \bar{X}^2 + \bar{Y}^2} \right]^{1/2} + \bar{X}(1 + \bar{Y}^2)^{1/2} \tan^{-1} \frac{\bar{X}}{(1 + \bar{Y}^2)^{1/2}} + \bar{Y}(1 + \bar{X}^2)^{1/2} \tan^{-1} \frac{\bar{Y}}{(1 + \bar{X}^2)^{1/2}} - \bar{X} \tan^{-1} \bar{X} - \bar{Y} \tan^{-1} \bar{Y} \right\}$$

**Figure A2:** View factors for aligned parallel rectangles [17].

$$F_{1R} = 1 - F_{12}, \quad (\text{A.2})$$

and from symmetry of the enclosure  $F_{2R} = F_{1R}$ .

The energy loss through the walls ( $P_{walls}$ ) considers a natural convection and radiative heat exchange as:

$$P_{walls} = A(h_{conv} + h_{rad})(T_{walls} - T_{sur}), \quad (\text{A.3})$$

---

<sup>1</sup> $\epsilon_2$  can be assumed equal to 1, being the surrounding

where  $A$  is the external furnace wall surface,  $T_{walls}$  is the external wall temperature,  $T_{sur}$  is the temperature of the surroundings air and  $h_{rad}$  and  $h_{conv}$  are the radiative and convective heat transfer coefficients, respectively. The former can be expressed as:

$$h_{rad} = \epsilon \sigma F_{12} (T_{walls} + T_{sur}) (T_{walls}^2 + T_{sur}^2), \quad (\text{A.4})$$

where  $\epsilon$  is the emissivity of the wall, taken equals to 0.8,  $\sigma$  is the Stefan-Boltzmann constant,  $F_{12}$  is the view factor between the wall and the surrounding ( $F_{12} = 1$ ). The convective heat transfer coefficient  $h_{conv}$  is a function of the Nusselt number ( $Na$ ) and it is defined differently, considering vertical walls (Eq. A.5), horizontal walls with hot surface up (Eq. A.7) or horizontal walls with hot surface down (Eq. A.8), according to [17].

- Vertical walls:

$$h_{conv} = \frac{k}{L} \overline{Nu}_L = \frac{k}{L} \left[ 0.825 + \frac{0.387 Ra_L^{1/6}}{[1 + (0.492/Pr)^{9/16}]^{4/9}} \right] \quad Ra_L < 10^9, \quad (\text{A.5})$$

where  $Pr$  is the Prandtl number ( $\mu$  cp/k),  $k$  is the thermal conductivity,  $cp$  the specific heat at constant pressure,  $\mu$  the viscosity and  $L$  is the characteristic length. The Rayleigh number ( $Ra_L$ ) is defined as a function of the Prandtl and Grashof numbers:

$$Ra_L = Gr_L Pr = \frac{g \beta (T_{walls} - T_{sur}) L^3}{\nu \alpha}, \quad (\text{A.6})$$

where  $g$  is the gravitational acceleration,  $\beta$  is the volumetric thermal expansion coefficient,  $\nu$  is the kinematic viscosity and  $\alpha$  is the thermal diffusivity.

- Horizontal walls with hot surface up:

$$h_{conv} = \frac{k}{L} \overline{Nu}_L = \frac{k}{L} 0.15 Ra_L^{1/3} \quad 10^7 < Ra_L < 10^{11}. \quad (\text{A.7})$$

- Horizontal walls with hot surface down:

$$h_{conv} = \frac{k}{L} \overline{Nu}_L = \frac{k}{L} 0.27 Ra_L^{1/4} \quad 10^5 < Ra_L < 10^{10}. \quad (\text{A.8})$$

# Appendix B

## Uncertainty quantification

This Appendix contains the uncertainty quantification study performed on the experimental campaign described in Section 2.5. Quantify the uncertainty on experimental data is also very important to determine reliable boundary conditions for CFD simulations. A further study might further investigate this aspect. The study follows the recommendations suggested by Pochet et al. [109].

In a first step, only the uncertainties of the furnace measurands that do not need post-processing techniques to be derived are investigated. Afterwards, the uncertainty quantification methodology is applied to the furnace measurands that cannot be used directly, but that require post-processing techniques, see Figure B1.

**Inlet flow rate uncertainties** In this furnace the fuel and air flow rates are controlled by MFCs. Being the control device of a continuous flow, in addition to a measuring device, a MFC do not offer repeated measurements of the same physical quantity, hence no Type A uncertainties are available for them. Therefore, each MFC flow uncertainty,  $u_{\dot{n},x}$  will be composed of the manufacturer-provided Type B uncertainties. MFCs are manufactured by Brooks, and their uncertainties are accuracy, repeatability, and temperature-pressure-age drift, as reported in the summary in Table B1. The  $x$ th MFC uncertainty is obtained as:

$$u_{\dot{n},x} = \sqrt{u_{lin}^2 + u_{drift,p}^2 + u_{drift,Tspan}^2 + u_{drift,Tzero}^2 + u_{repeat}^2}. \quad (\text{B.1})$$

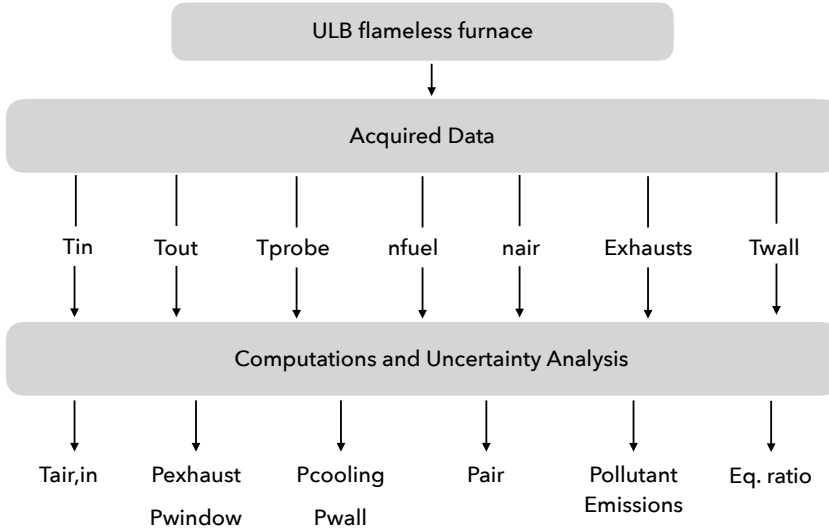


**Figure B1:** Graphical visualization of the measurand uncertainties that need post-processing.

**Table B1:** MFC uncertainty data summary. SP set-point, FS full-scale.

MFC (Brooks SLA-585XX)	Uncertainty
Linearity	$\pm 0.9\%$ SP
Linearity	$\pm 0.18\%$ FS <sup>1</sup>
Repeatability	$\pm 0.2\%$ FS
Temperature zero drift	$\pm 0.05\%$ FS/K
Temperature span drift	$\pm 0.05\%$ FS/K
Pressure drift	$\pm 0.429\%$ SP/bar

<sup>1</sup> if SP < 20% FS.

The total flow entering the burner and related uncertainty is obtained from the MFC flows and uncertainties:

$$\dot{n} = \sum_x^{MFCs} \dot{n}_x, \quad u_{\dot{n}} = \sqrt{\sum_x^{MFCs} u_{\dot{n}_x}^2}. \quad (\text{B.2})$$



However, the composition of each MFC flow is uncertain: the MFCs are hooked up to bottled gas of below 100% purity. If a bottle is of  $Pu\%$  purity, it means that it contains at least  $Pu\%$  of the prescribed gas. Therefore, to translate that in terms of uncertainty, there is a given probability distribution of the gas purity between  $Pu\%$  and 100%. The uncertainty on its real content becomes therefore  $u_{Pu} = (100 - Pu)/\sqrt{3} \%$ . The total uncertainty on the species flow delivered by the MFC is:

$$u_{\dot{n},x,tot} = \sqrt{u_{\dot{n},x}^2 + u_{Pu}^2}. \quad (\text{B.3})$$

For the gases mentioned in Chapter 3, the bottle purity is the following: 99.5% for  $\text{CH}_4$ , 99.9% for  $\text{H}_2$  and 99.99% for  $\text{NH}_3$ .

Focusing only on the cooling air and the combustion air flow rates, additional uncertainty sources must be considered. Indeed, the two fans supply the furnace with outdoor air, therefore the dry air composition and air moisture content might influence the measure. Precise dry air composition is 78.08%  $\text{N}_2$ , 20.95%  $\text{O}_2$ , 0.93%  $\text{Ar}$  and 0.04%  $\text{CO}_2$  in molar percentages. Compared to the generally assumed 79%  $\text{N}_2$  - 21%  $\text{O}_2$ , the only difference for oxygen is 0.05% molar. Argon and carbon dioxide being inert, it does not induce any combustion error to consider them as nitrogen. Considering a false composition of 79%  $\text{N}_2$  21%  $\text{O}_2$  instead of 79.05%-20.95% is equivalent as using a 100% purity nitrogen bottle and a 99.52% purity oxygen bottle, as this impurity englobes the possibility of having the real concentration of 79.05%-20.95%.

The fans supply air at 300 mbarg and it is directly sent to the furnace at a temperature that can vary seasonally between 20-30°C for combustion air and between 30-40°C for cooling air. The experimental campaigns were conducted during winter with an outdoor temperature between 4-13 °C. An averaged outdoor temperature of 10°C and a relative humidity of 70% are considered for this study. This represents a partial water vapour pressure of 850 Pa. Considering a polytropic compression with a compression ratio of 1.3, the partial water vapour pressure ramps up to 1100 Pa, while the saturation pressure is 4200 Pa at 30°C (combustion air), while it is 7390 Pa at 40°C (cooling air). As a consequence, water does not condense and it represents the 0.84% content in air in molar basis. Therefore, it is taken into account in the uncertainty analysis as an impurity of 0.84%.

The final uncertainty formulation for cooling and combustion air can be re-written considering the mass flow rate ( $u_{\dot{n},air}$ ), the dry air composition

( $u_{comp}$ ) and the moisture content ( $u_{moist}$ ) uncertainties as:

$$U_{95,air} = 1.96 \sqrt{u_{n,air}^2 + u_{comp}^2 + u_{moist}^2}. \quad (B.4)$$

Table B2 reports the uncertainty on fuel and air mass flow rates with a 95% probability interval ( $U_{95,x} = 1.96 \cdot u_x$ ), referred to equivalence ratio  $\phi=0.8$ . Uncertainty related to hydrogen are lower compared to methane, considering a much higher purity level. This is qualitatively visible from the Figure B2. On the other hand, the combustion air total uncertainty lowers going towards pure methane, considering the higher flow rate.

**Table B2:** Uncertainty quantification for the fuel, combustion air and cooling air, varying the H<sub>2</sub> content. Flow rates in Nm<sup>3</sup>/h.

Case	Fuel	$U_{fuel}$ (%)	Air	$U_{air}$ (%)	Cool	$U_{cool}$ (%)
100% H <sub>2</sub>	5.01	0.87	14.89	1.64	20.15	1.83
50% H <sub>2</sub>	2.30	0.74	17.25	1.54	20.15	1.83
0% H <sub>2</sub>	1.51	1.05	17.95	1.52	20.15	1.83

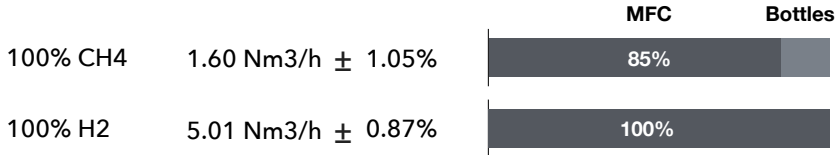


**Figure B2:** Relative impact of MFC and impurities on the final fuel uncertainty. For sake of clarity only the pure component cases are reported.

Figure B3 shows the relative impact on the final uncertainty for combustion air (100% H<sub>2</sub> and 100% CH<sub>4</sub>) and cooling air (identical in the two cases). It appears clear that the uncertainties related to temperature drift (zero and span) as well as the component related to the air moisture are not negligible for both combustion air and cooling air. In the latter, considering air enters at a higher temperature (40°C) the drift sources are the 43% of the total MFC uncertainty. This suggests some improvement that might be done

on the facility to alleviate those uncertainties. For instance introducing a cooler after the fans to reduce the temperature down to 15 °C, partially condensing the water vapour.

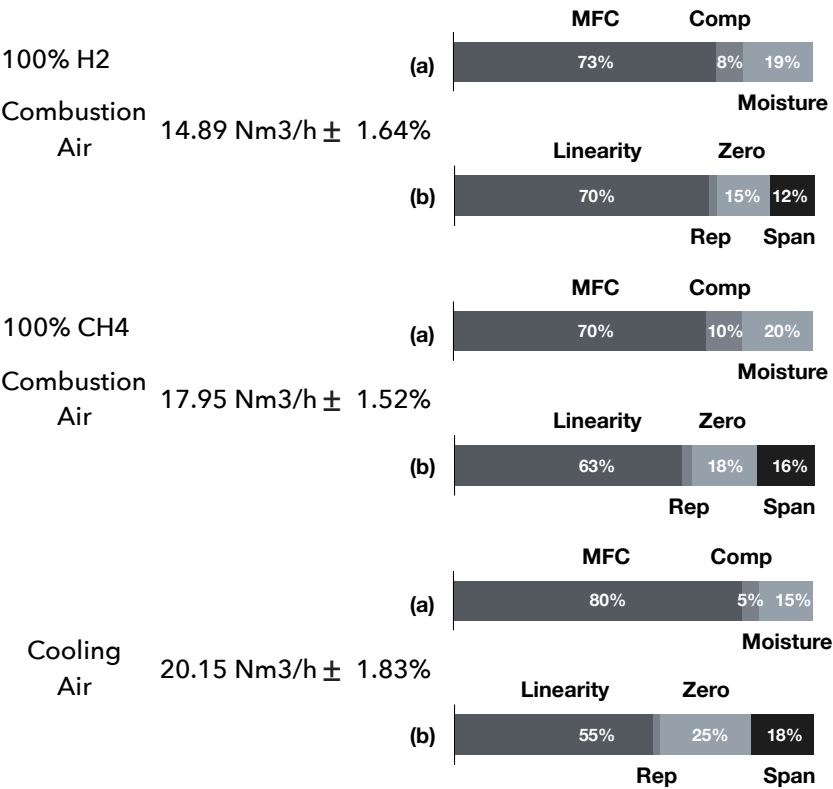


**Figure B3:** Relative impact of MFC, dry air composition and air moisture (a) on the final combustion air and cooling air uncertainties. (b) Relative impact of each sources of Table B1 on the MFC uncertainty. Two examples are reported for combustion air (100% H<sub>2</sub> and 100% CH<sub>4</sub>).

**Equivalence ratio** Chapter 3 shows the importance of the equivalence ratio on the pollutant emissions, especially for mixture ammonia/hydrogen. As a consequence, it is really important to reduce its uncertainty. The latter can be quantify considering the general formula for variables that cannot be

measured directly (Eq. 2.18), referring to the equivalence ratio definition (Eqs. 2.6-2.5). It follows that the nominal value has an uncertainty of  $\approx 1.8\%$  ( $\phi = 0.80 \pm 0.02$ ).

**Air inlet temperature** As seen in Chapter 2, the air inlet temperature cannot be measured directly, but it is evaluated based on an energy balance on the heat exchanger, based on Eq. 2.10. The heat exchanger efficiency was considered as  $0.90 \pm 0.05$ . The JANAF tables were used to quantify the specific heat at constant pressure  $cp$ :

$$cp = R \cdot \left( \frac{a_1}{T^2} + \frac{a_2}{T} + a_3 + a_4T + a_5T^2 + a_6T^3 + a_7T^4 \right). \quad (\text{B.5})$$

However, the coefficient  $a_i$  were considered with no uncertainty. Applying Eq. 2.18, one could retrieve an uncertainty for the inlet air  $U_{95}$  varying between 3.2% and 3.4% ( $\approx 30$  K) for the different methane/hydrogen blends.

**Energy balance** This section aims to quantify the uncertainty on the powers involved in the energy balance of the furnace and shown in Chapter 2. The values were reported in Table B3 for different methane/hydrogen blends. Eq. 2.18 was applying on the equations Eq. 2.4 for  $P_{th}$ , Eq. 2.8 for  $P_{cool}$  and  $P_{exh}$ , Eq. 2.11 for  $P_{rad}$  and Eq. 2.13 for  $P_{walls}$ . To solve those equations, uncertainties were only considered on the measured temperatures, flow rates and efficiency of the heat exchanger. The final values containing uncertainty information are reported in Table B3. The uncertainty on the thermal input power follows the trend already observed for the fuel mass flow rate uncertainty, varying between 0.7% and 1.1%. The cooling and walls losses are characterised by an uncertainty of 2.2% and 5.9%, respectively. For the latter, the major source comes from the radiative heat exchange. An increasing uncertainty is observed for the enthalpy of the exhaust gases, being the 4.1% for pure methane and the 4.4% for pure hydrogen. Finally, the radiative heat exchange through the window suffers from the biggest uncertainty 7.6%, due to the dependence on the fourth power of temperature.

**Table B3:** Energy balance with uncertainty quantification ( $U_{95}$ ) for the investigated cases.

Power [kW]	0% H <sub>2</sub>	50% H <sub>2</sub>	100% H <sub>2</sub>
$P_{th}$	$15.00 \pm 0.17$	$15.00 \pm 0.11$	$15.00 \pm 0.13$
$P_{cool}$	$5.10 \pm 0.11$	$5.10 \pm 0.11$	$5.10 \pm 0.11$
$P_{walls}$	$4.11 \pm 0.26$	$4.13 \pm 0.26$	$4.14 \pm 0.26$
$P_{rad}$	$2.79 \pm 0.21$	$2.91 \pm 0.21$	$2.91 \pm 0.22$
$P_{exh}$	$3.00 \pm 0.12$	$2.86 \pm 0.12$	$2.52 \pm 0.11$
$\Delta P$	$0.0 \pm 0.40$	$0.0 \pm 0.40$	$0.33 \pm 0.40$

## Appendix C

# Additional information about numerical modeling

**Computational grid** Due to the presence of the window in only one side of the furnace, a faithful computational domain should consider half domain, as a result of the symmetry of the problem. The window properties can be included in ANSYS Fluent imposing a semi-transparent wall boundary condition, which means that radiation approaching the window can exit, but no radiation from the surroundings can enter the domain. The latter is anyway negligible. During the present work, two sets of computational grids were created, contemplating or not the presence of the window. The domain considered for both sets an air injection diameter of ID 16 mm. All the computational grids were first created with tetrahedrons and then converted into polyhedrons. This operation allows for the reduction of the number of cells and improvement of convergence and accuracy, because the number of neighbours is higher than those of tetrahedrons. Particular attention was paid refining the fuel–air mixing zone (Figure 6.2). Preliminary simulations dealt with the grid independency study adopting the two set of grids. The number of cells ranges between 450k to 1300k cells for the case with window (180° domain) and between 114k to 320k cells for the case without window (45° domain). For the latter, the cooling surface also incorporates the energy loss by radiation through the window. The simulations considered a 40%-60% CH<sub>4</sub>-H<sub>2</sub> fuel blend at stoichiometric condition. Figure C1 offers a comparison between the set of grids without window, based on temperature predictions for ID16. The selected grids consist of 216k cells for the case without window (45° domain) and 850k cells for

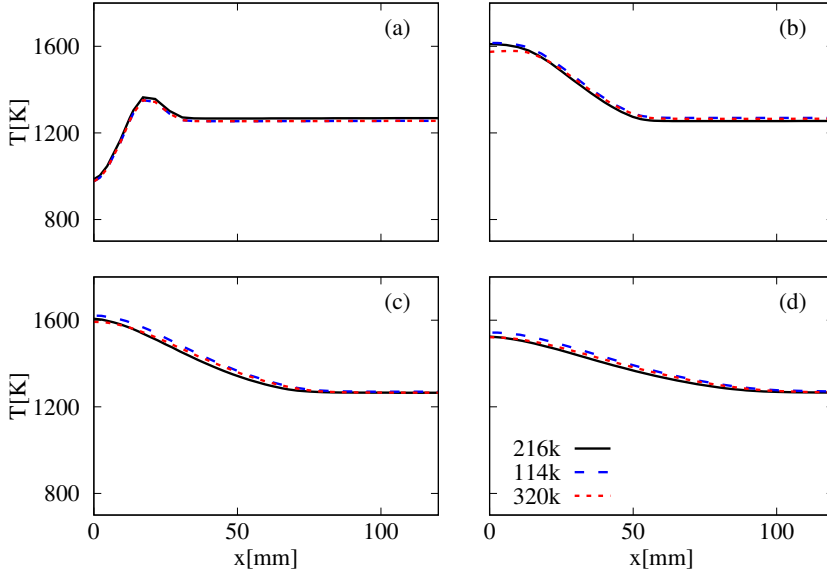


**Figure C1:** Predicted temperature profiles for the coarse, medium and fine grids, varying the axial location (a)  $z=100$  mm, (b)  $z=200$ , (c)  $z=300$  mm and (d)  $z=400$  mm for a 40%-60%  $\text{CH}_4\text{-H}_2$  fuel blend and  $\phi=1$ . ID16, case without window.

the case with window ( $180^\circ$  domain). They can be considered as a good compromise between accuracy and computational time.

A second comparison was aimed at understanding the effect of the window on the reactive zone. Figure C2-C3 compare CFD temperature predictions for the cases with and without window. The grid without window offers a fair compromise between accuracy (maximum relative error of 4% at  $z = 200$  mm) and computational cost in an area far from the window, allowing the use of only a  $45^\circ$  domain (216k cells instead of 850k). The main differences are located only in the area close to the window, where there is a sudden temperature drop, due to the localised heat loss (Figure C3).

**PaSR residence time formulation** In Chapter 4, the author defined the PaSR residence time as the minimum between  $\tau_c$  and  $\tau_{mix}$  to account for high reactivity cases ( $\tau_c \ll \tau_{mix}$ ). Indeed, the reactants would actually stay in the reactive structure as long as it is needed, which is the minimum

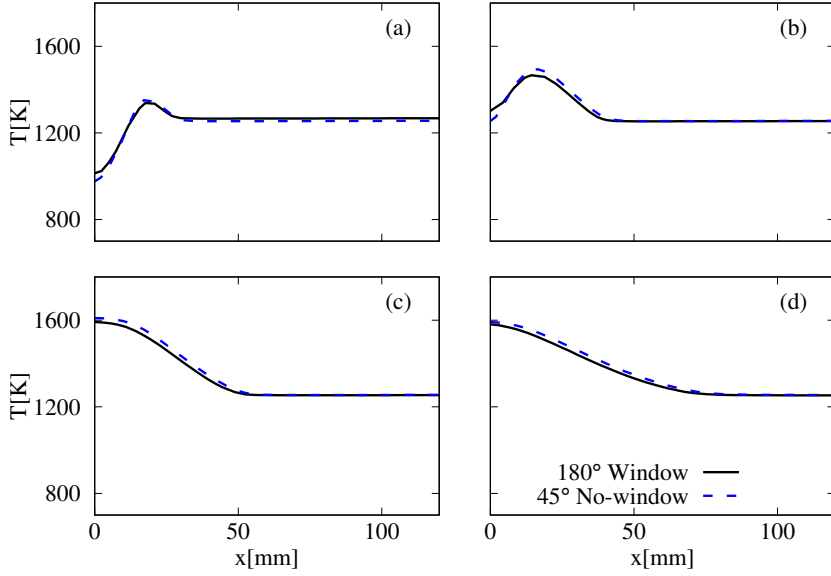


**Figure C2:** Predicted temperature profiles for the case with window and without window, varying the axial location (a)  $z=100$  mm, (b)  $z=200$  mm, (c)  $z=300$  mm and (d)  $z=400$  mm for a 40%-60%  $\text{CH}_4\text{-H}_2$  fuel blend and  $\phi=1$ . ID16.

of the two time scales. This formulation extends the work of Chomiak [77], who defined the residence time  $\tau^*$  as the mixing time scale ( $\tau_{mix}$ ). This section aims at validate such an assumption on two test cases, such as the AJHC (Chapter 5) and the ULB furnace (Chapter 6).

On one hand, no differences can be notices between the two formulations of  $\tau^*$  ( $\min(\tau_c, \tau_{mix})$  or  $\tau_{mix}$ ) simulating the AJHC for temperature, CO and OH mass fractions (Figure C4).

On the other hand, considering the local minimum between  $\tau_c$  and  $\tau_{mix}$  helps in alleviating the temperature under-prediction simulating the ULB furnace for M50H50 at  $z = 150$  mm and  $z = 200$  mm (Figure C5). The effect is even more relevant for M0H100 (Figure C6), proving that defying  $\tau^*$  as  $\min(\tau_c, \tau_{mix})$  is more effective than the definition proposed by Chomiak [77] for cases where the chemical time scale is locally lower than the mixing time scale.



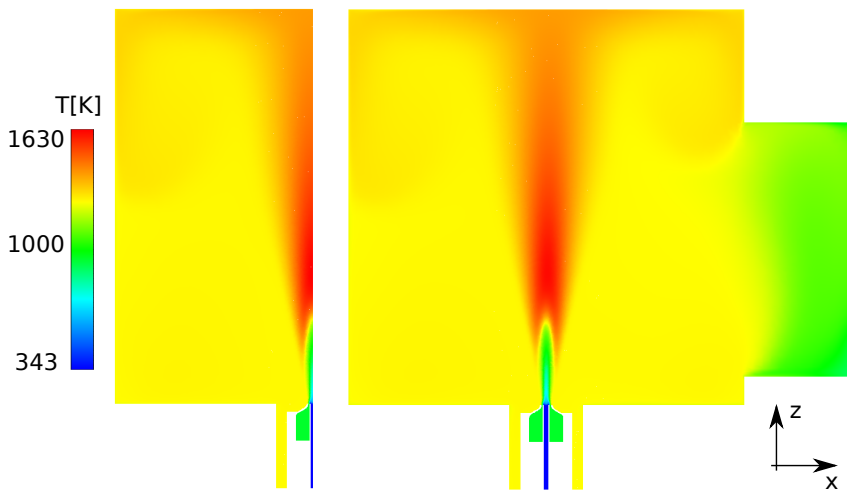


**Figure C3:** Contour of temperature for a 45° domain without window (left) and a 180° domain with window (right) on the symmetry plane. Case 40%-60% CH<sub>4</sub>-H<sub>2</sub> fuel blend and  $\phi=1$ . ID16.

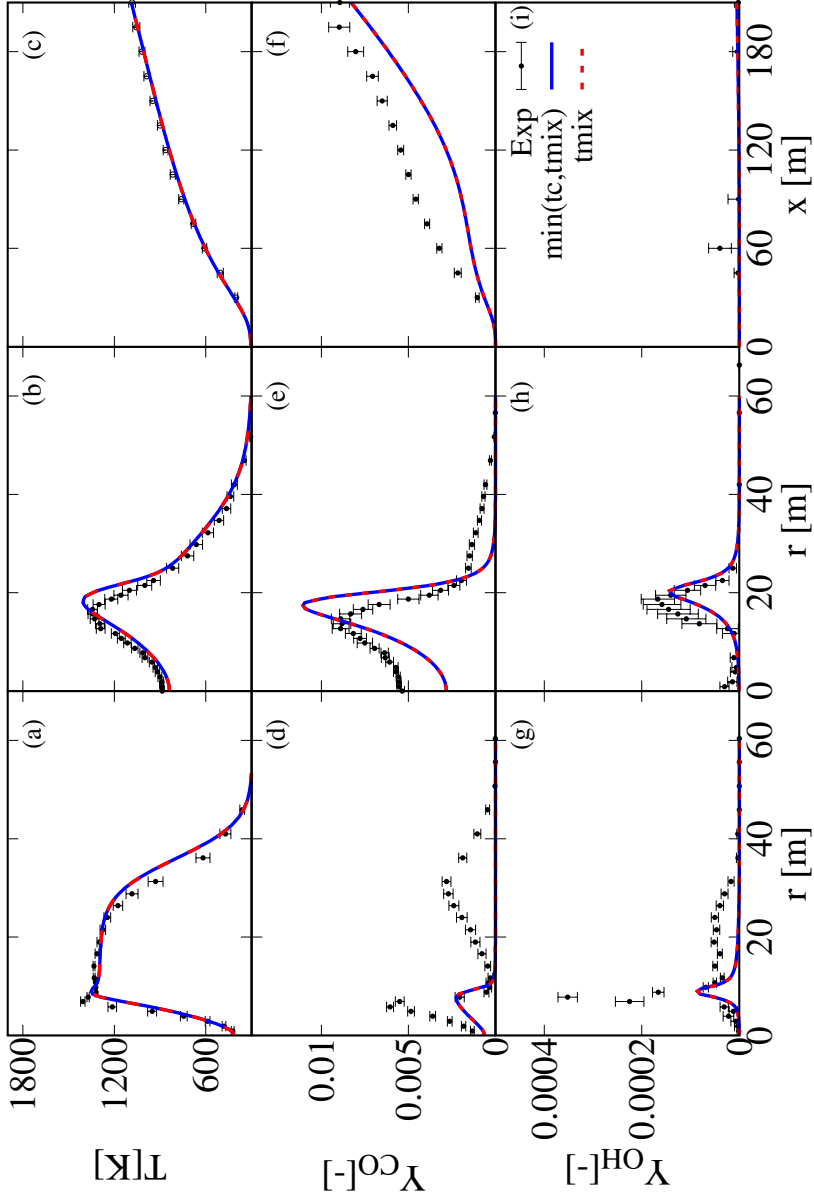


**Figure C4:** Comparison between two different formulations of  $\tau^*$  based on mean temperature, mean CO and OH mass fraction profiles. Re=10k and 3% O<sub>2</sub> in the co-flow. AJHC, Modified k- $\epsilon$  and KEE.

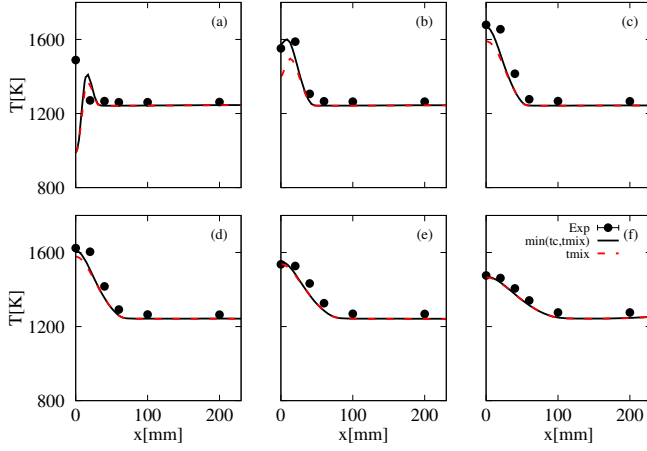


**Figure C5:** Comparison between two different formulations of  $\tau^*$  for M50H50, ULB furnace. (a)  $z=100$  mm, (b)  $z=150$  mm, (c)  $z=200$  mm, (d)  $z=250$  mm, (e)  $z=300$  mm and (f)  $z=400$  mm. GRI-2.11,  $C_{mix}=0.3$ , std k- $\epsilon$ . Averaged experimental uncertainty of 10 K, which is the radius of the marker.

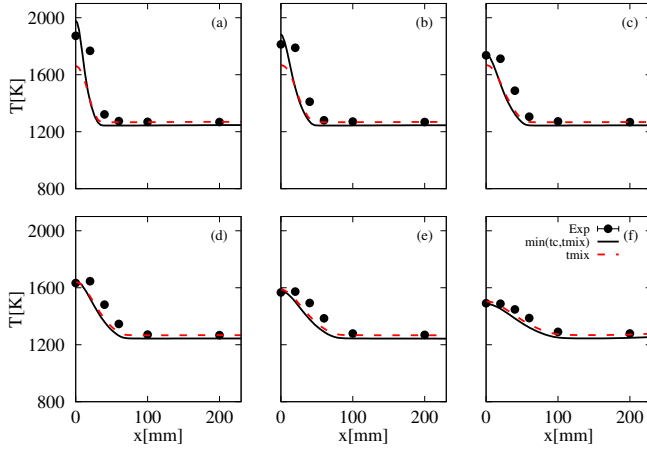


**Figure C6:** Comparison between two different formulations of  $\tau^*$  for M0H100, ULB furnace. (a)  $z=100$  mm, (b)  $z=150$  mm, (c)  $z=200$  mm, (d)  $z=250$  mm, (e)  $z=300$  mm and (f)  $z=400$  mm. GRI-2.11,  $C_{mix}=0.3$ , std k- $\epsilon$ . Averaged experimental uncertainty of 10 K, which is the radius of the marker.

## Appendix D

# Additional experimental studies for CH<sub>4</sub>-H<sub>2</sub>

The goal of this section is to offer additional experimental studies performed with methane/hydrogen blends.

### D.1 Effect of equivalence ratio

A further study (Test-case T4 of Table 3.2), varying the equivalence ratio for an equimolar case (M50H50) CH<sub>4</sub>-H<sub>2</sub>, is here presented in terms of OH\* chemiluminescence imaging and pollutant emissions for the air injector ID16. Two aspects appear clear looking at Figures D1-D2. The reactive region is shifted close to the burner exit and it is more stretched at stoichiometric condition. The pollutant emissions reach a maximum for  $\phi = 0.8$ . Increasing the air excess (lower equivalence ratio) might enhance the NO formation from thermal, N<sub>2</sub>O and NNH pathways, because of the intensified O radical pool. Nevertheless, global temperature decreases inside the furnace, decreasing the reactivity as well. The global result is a decreasing trend increasing the air excess. On the other side, the mentioned pathways are less enhanced going towards stoichiometry, where prompt route seems not to be particularly relevant.

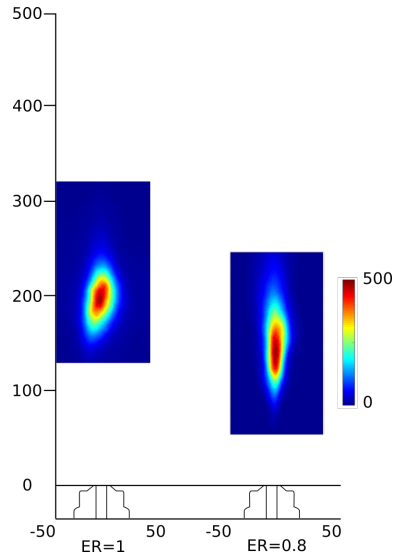


**Figure D1:** Averaged  $\text{OH}^*$  distribution varying the equivalence ratio. Test-case T4. Units in mm and counts.

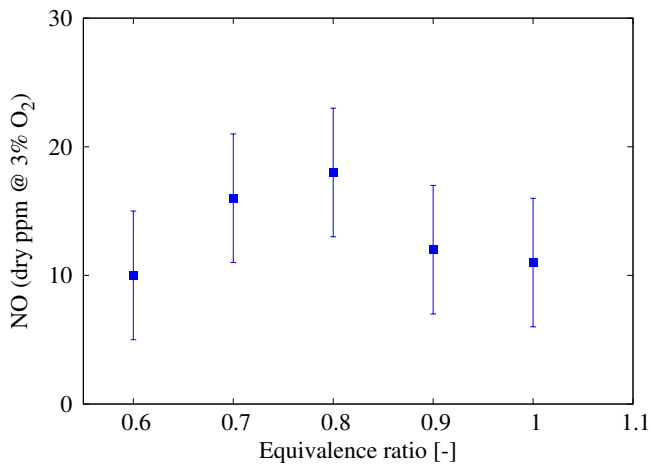


**Figure D2:** Pollutant emission varying the equivalence ratio. Test-case T4.

## D.2 Dilution effect on a pure hydrogen flame

A last campaign (Test-case T7 of Table 3.2) focused on reducing pollutant emissions for hydrogen flames. The most effective set-up, i.e. ID16 and a longer fuel lance (L25) was used coupled with a dilution of the fuel. A pure nitrogen dilution was imagined to reduce the reactivity of hydrogen and increase the recirculation degree. This was an attempt to reproduce a real Exhaust Gas Recirculation (EGR). Indeed, for hardware limits, it was not possible to physically recirculate those gases into the air stream, as it happens for gas turbine or piston engine. As a consequence, nitrogen was

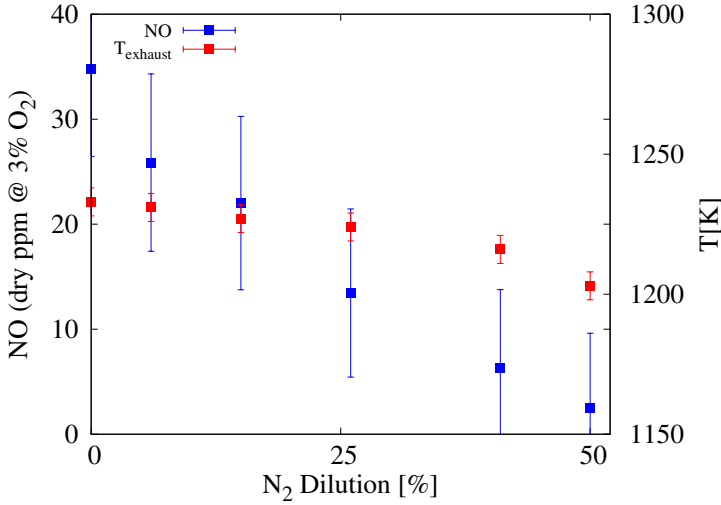


**Figure D3:** Pollutant emissions in function of the nitrogen dilution level. Test-case T7.

added to the fuel stream, being aware that this would increase the fuel flow rate and therefore the fuel velocity, affecting the mixing with air. Figure D3 shows the pollutant emissions and the exhaust temperature<sup>1</sup> in function of the nitrogen dilution level. The first effect of dilution is to reduce the outlet temperature (keeping the same cooling power) and most probably to reduce the in-flame temperature peak, smoothing its distribution. On the other hand, NO emissions are drastically reduced (reduction of 35% with 15% of N<sub>2</sub> dilution) up to single digit for a dilution level higher then 40%. Indeed,

<sup>1</sup>before entering the heat exchanger

this is related to the lower temperatures involved and the lower local molar fraction of radicals involved in forming NO, i.e. H for the NNH pathway.

# List of publications

**M. Ferrarotti**, W. De Paepe, A. Parente, “Reactive structures and pollutant emissions for methane/hydrogen mixtures in flameless regime”, *Combustion&Flames*, In preparation.

**M. Ferrarotti**, A. Bertolino, R. Amaduzzi, A. Parente, “On the influence of kinetic uncertainties on the accuracy of numerical modelling of an industrial flameless furnace fired with  $\text{NH}_3/\text{H}_2$  blends: a numerical and experimental study”, *Frontiers in Energy Research*, Under review.

R. Amaduzzi, **M. Ferrarotti** and A. Parente, “Evaluation of Hydrogen-Enrichment of Methane Combustion in a Quasi-Industrial Flameless Combustion Chamber ”, *Frontiers in Energy Research*, Under review.

G. Aversano, **M. Ferrarotti**, A. Parente, “Digital twin of a combustion furnace operating in flameless conditions: reduced-order model development from CFD simulations”, Accepted for publication in the ”Proceedings of the Combustion Institute” 2020.

**M. Ferrarotti**, R. Amaduzzi, D. Bascherini, C. Galletti, A. Parente, “Heat Release Rate Markers for the Adelaide Jet in Hot Coflow Flame”, *Frontiers in Mechanical Engineering* 6, 2020.

R. Amaduzzi, G. Ceriello, **M. Ferrarotti**, G. Sorrentino, A. Parente, “Evaluation of Modeling Approaches for MILD Combustion Systems With Internal Recirculation”, *Frontiers in Mechanical Engineering*, 6, 2020.

S. Iavarone, M. Cafiero, **M. Ferrarotti**, F. Contino, A. Parente, “A multiscale combustion model formulation for  $\text{NO}_x$  predictions in hydrogen enriched jet flames”, *International Journal of Hydrogen Energy*, 44, 23436-23457, 2019.

**M. Ferrarotti**, M. Fürst, E. Cresci, W. De Paepe, A. Parente, “Key Modeling Aspects in the Simulation of a Quasi-industrial 20 kW Moderate or



Intense Low-oxygen Dilution Combustion Chamber”, *Energy Fuels*, 2018, 32, 10228-10241.

**M. Ferrarotti**, Z. Li, A. Parente, “On the role of mixing models in the simulation of MILD combustion using finite-rate chemistry combustion models”, *Proceedings of the Combustion Institute*, 37 (4), 4531-4538, 2018.

Z. Li, **M. Ferrarotti**, A. Cuoci, A. Parente, “Finite-rate chemistry modelling of non-conventional combustion regimes using a partially-stirred reactor closure: Combustion model formulation and implementation details”, *Applied Energy*, 225, 637-655, 2018.

R. Longo, M. Furst, A. Bellemans, **M. Ferrarotti**, M. Derudi, A. Parente, “CFD dispersion study based on a variable Schmidt formulation for flows around different configurations of ground-mounted buildings”, *Building and Environment*, 154, 336-347, 2019.

R. Longo, **M. Ferrarotti**, C. Garcia-Sanchez, M. Derudi, A. Parente, “Advanced turbulence models and boundary conditions for flows around different configurations of ground-mounted buildings”, *Journal of wind engineering and industrial aerodynamics*, 167, 160-182, 2017.

# Bibliography

- [1] Intergovernmental Panel on Climate Change, Global Warming of 1.5°C, Special Report (2018).
- [2] R. Pachauri, L. Mayer, IPCC, Climate Change 2014, Tech. rep., IPCC, Geneva, Switzerland (2015).
- [3] S. Iavarone, Uncertainty Quantification for Scale-Bridging Modeling of Multiphase Reactive Flows, Ph.D. thesis, ULB (2019).
- [4] P. Glarborg, J. A. Miller, B. Ruscic, S. J. Klippenstein, Modeling nitrogen chemistry in combustion (2018). doi:10.1016/j.pecs.2018.01.002.
- [5] S. J. Klippenstein, L. B. Harding, P. Glarborg, J. A. Miller, The role of NNH in NO formation and control, Combustion and Flame 158 (4) (2011) 774–789. doi:10.1016/j.combustflame.2010.12.013.
- [6] J. W. Bozzelli, A. M. Deant, 0 + NNH: A Possible New Route, International Journal of Chemical Kinetics 27 (1995) 1097–1109.
- [7] A. A. Konnov, G. Colson, J. De Ruyck, NO formation rates for hydrogen combustion in stirred reactors, Fuel 80 (1) (2001) 49–65. doi:10.1016/S0016-2361(00)00060-0.
- [8] A. N. Hayhurst, E. M. Hutchinson, Evidence for a new way of producing NO via NNH in fuel-rich flames at atmospheric pressure, Combustion and Flame 114 (1-2) (1998) 274–279. doi:10.1016/S0010-2180(97)00328-3.
- [9] J. A. Wüning, J. G. Wüning, Flameless oxidation to reduce thermal no-formation, Progress in Energy and Combustion Science 23 (1) (1997) 81–94. doi:10.1016/s0360-1285(97)00006-3.

- [10] A. Cavaliere, M. De Joannon, Mild combustion, *Progress in Energy and Combustion Science* 30 (4). doi:10.1016/j.pecs.2004.02.003.
- [11] A. Cuoci, A. Frassoldati, T. Faravelli, E. Ranzi, OpenSMOKE++: An object-oriented framework for the numerical modeling of reactive systems with detailed kinetic mechanisms, *Computer Physics Communications* 192 (2015) 237–264. doi:10.1016/j.cpc.2015.02.014.
- [12] E. Ranzi, A. Frassoldati, R. Grana, A. Cuoci, T. Faravelli, A. Kelley, C. Law, Hierarchical and comparative kinetic modeling of laminar flame speeds of hydrocarbon and oxygenated fuels, *Progress in Energy and Combustion Science* 38 (4) (2012) 468 – 501. doi:<https://doi.org/10.1016/j.pecs.2012.03.004>.  
URL <http://www.sciencedirect.com/science/article/pii/S0360128512000196>
- [13] A. Stagni, C. Cavallotti, S. Arunthanayothin, Y. Song, O. Herbinet, F. Battin-Leclerc, T. Faravelli, An experimental, theoretical and kinetic-modeling study of the gas-phase oxidation of ammonia, *Reaction Chemistry & Engineering* 5 (4) (2020) 696–711. doi:10.1039/c9re00429g.
- [14] B. B. Dally, A. N. Karpetis, R. S. Barlow, Structure of turbulent non-premixed jet flames in a diluted hot coflow, *Proceedings of the Combustion Institute* 29 (1) (2002) 1147–1154. doi:10.1016/S1540-7489(02)80145-6.
- [15] C. Galletti, M. Ferrarotti, A. Parente, L. Tognotti, Reduced NO formation models for CFD simulations of MILD combustion, *International Journal of Hydrogen Energy* 40 (14) (2015) 4884–4897. doi:10.1016/j.ijhydene.2015.01.172.
- [16] Z. Li, A. Cuoci, A. Parente, Large Eddy Simulation of MILD combustion using finite rate chemistry: Effect of combustion sub-grid closure, *Proceedings of the Combustion Institute* 37 (4) (2019) 4519–4529. doi:10.1016/j.proci.2018.09.033.
- [17] F. P. Incropera, *Fundamentals of Heat and Mass Transfer*, 6th Edition, Wiley, New York, USA, 2010.
- [18] J. P. H. Sanders, I. Gökalp, Scalar dissipation rate modelling in variable density turbulent axisymmetric jets and diffusion flames, *Physics of Fluids* 10 (4) (1998) 938–948. doi:10.1063/1.869616.

## BIBLIOGRAPHY

- [19] I. E. Agency, Key World Energy Statistics, Tech. rep., IEA, Paris, France (2017).
- [20] O. Edenhofer, R. Pichs-Madruga, Y. Sokona, C. Field, V. Barros, T. Stocker, Q. Dahe, J. Minx, K. Mach, G.-K. Plattner, S. Schlmer, G. Hansen, M. Mastrandrea, Meeting Report of the Intergovernmental Panel on Climate Change Expert Meeting on Geoengineering., IPCC Working Group III Technical Support Unit, Potsdam Institute for Climate Impact Research, Potsdam, Germany (2012) 99.
- [21] I. Glassman, A. Yetter, Combustion, Academic Press, Burlington, 2008, Ch. 8-Environm, pp. 409–494.
- [22] Framework Convention on Climate Change, Adoption of the Paris Agreement (2015) (Last accessed 17/04/2019).  
URL <https://unfccc.int/resource/docs/2015/cop21/eng/109r01.pdf>
- [23] H. Kobayashi, A. Hayakawa, K. D. A. Somarathne, E. C. Okafor, Science and technology of ammonia combustion, Proceedings of the Combustion Institute 37 (1) (2019) 109–133. doi:10.1016/j.proci.2018.09.029.
- [24] Zeldovich, Y., The oxidation of nitrogen in combustion and explosions, Acta Physicochimica URSS 21 (1946) 577–628.
- [25] J. M. Beér, Minimizing NOx emissions from stationary combustion; reaction engineering methodology, Chemical Engineering Science 49 (24 PART A) (1994) 4067–4083. doi:10.1016/S0009-2509(05)80006-5.
- [26] C. Fenimore, Formation of nitric oxide in premixed hydrocarbon flames, Proc. Combust. Inst. 13 (1971) 373–380.
- [27] M. R. Roomina, R. W. Bilger, Conditional Moment Closure (CMC) predictions of a turbulent methane-air jet flame, Combustion and Flame 125 (3) (2001) 1176–1195. doi:10.1016/S0010-2180(01)00237-1.
- [28] P. Glarborg, J. A. Miller, R. J. Kee, Kinetic modeling and sensitivity analysis of nitrogen oxide formation in well-stirred reactors, Combustion and Flame 65 (2) (1986) 177–202. doi:10.1016/0010-2180(86)90018-0.

- [29] L. V. Moskaleva, M. C. Lin, The spin-conserved reaction  $\text{CH} + \text{n}_2\text{H} + \text{NCN}$ : A major pathway to prompt no studied by quantum/statistical theory calculations and kinetic modeling of rate constant, *Proceedings of the Combustion Institute* 28 (2) (2000) 2393–2401. doi:10.1016/S0082-0784(00)80652-9.
- [30] G. Szego, B. B. Dally, G. Nathan, Scaling of NOx emissions from a laboratory-scale mild combustion furnace, *Combust. Flame* 154 (2008) 281–295.
- [31] A. Parente, C. Galletti, L. Tognotti, A simplified approach for predicting NO formation in MILD combustion of  $\text{CH}_4\text{-H}_2$  mixtures, *Proceedings of the Combustion Institute* 33 (2) (2011) 3343–3350. doi:10.1016/j.proci.2010.06.141.
- [32] P. C. Malte, D. T. Pratt, Measurement of atomic oxygen and nitrogen oxides in jet-stirred combustion, *Symposium (International) on Combustion* 15 (1) (1975) 1061–1070. doi:10.1016/S0082-0784(75)80371-7.
- [33] P. Glarborg, A. D. Jensen, J. E. Johnsson, Fuel nitrogen conversion in solid fuel fired systems, *Progress in Energy and Combustion Science* 29 (2) (2003) 89–113. doi:10.1016/S0360-1285(02)00031-X.
- [34] M. Yumura, T. Asaba, Y. Matsumoto, H. Matsui, Thermal decomposition of ammonia in shock waves, *International Journal of Chemical Kinetics* 12 (7) (1980) 439–450. doi:10.1002/kin.550120702.
- [35] J. Bian, J. Vandooren, P. J. Van Tiggelen, Experimental study of the structure of an ammonia-oxygen flame, *Symposium (International) on Combustion* 21 (1) (1988) 953–963. doi:10.1016/S0082-0784(88)80327-8.
- [36] R. K. Lyon, Thermal DeNOx Controlling nitrogen oxides emissions by a noncatalytic process, *Environmental Science & Technology* 21 (3) (2002) 231–236. doi:10.1021/es00157a002.
- [37] S. Song, R. K. Hanson, C. T. Bowman, D. M. Golden, A shock tube study of the product branching ratio of the  $\text{NH}_2 + \text{NO}$  reaction at high temperatures, *Journal of Physical Chemistry A* 106 (40) (2002) 9233–9235. doi:10.1021/jp020943d.

## BIBLIOGRAPHY

- [38] J. A. Miller, C. T. Bowman, Mechanism and modeling of nitrogen chemistry in combustion, *Prog. Energy Combust. Sci.* 15 (1989) 287–338.
- [39] A. Milani, A. Saponaro, Diluted combustion technologies, *IFRF Combustion Journal* 32.
- [40] F. J. Weinberg, Combustion Temperatures: The future?, *Nature* 233 (0) (1971) 239–241.
- [41] M. Katsuki, T. Hasegawa, The science and technology of combustion in highly preheated air, *Symposium (International) on Combustion* 27 (2) (1998) 3135–3146.
- [42] A. Milani, J. Wunning, Flameless Oxidation Technology, *Advanced Combustion and Aerothermal Technologies* (2007) 343–352.
- [43] V. K. Arghode, A. Gupta, Effect of flow field for colorless distributed combustion (CDC) for gas turbine combustion, *Applied Energy* 87 (5) (2010) 1631–1640. doi:10.1016/j.apenergy.2009.09.032.
- [44] V. K. Arghode, A. K. Gupta, K. M. Bryden, High intensity colorless distributed combustion for ultra low emissions and enhanced performance, *Applied Energy* 92 (2012) 822–830. doi:10.1016/j.apenergy.2011.08.039.
- [45] H. Tsuji, A. K. Gupta, T. Hasegawa, M. Katsuki, K. Kishimoto, M. Morita, *High Temperature Air Combustion*, CRC Press, 2002. doi:<https://doi.org/10.1201/9781420041033>.
- [46] T. Plessing, N. Peters, J. G. Wunning, Laseroptical investigation of highly preheated combustion with strong exhaust gas recirculation, *Symposium (International) on Combustion* 27 (2) (1998) 3197–3204. doi:10.1016/S0082-0784(98)80183-5.
- [47] G. M. Choi, M. Katsuki, Advanced low NO<sub>x</sub> combustion using highly preheated air, *Energy Convers. Manag.* 42 (2001) 639–652.
- [48] M. Flamme, Low NO<sub>x</sub> combustion technologies for high temperature applications, *Energy Conversion and Management* 42 (15-17). doi:10.1016/S0196-8904(01)00051-6.

- [49] M. Flamme, New combustion systems for gas turbines (NGT), *Applied Thermal Engineering* 24 (11-12) (2004) 1551–1559. doi:10.1016/j.applthermaleng.2003.10.024.
- [50] S. Kruse, B. Kerschgens, L. Berger, E. Varea, H. Pitsch, Experimental and numerical study of mild combustion for gas turbine applications, *Applied Energy* 148. doi:10.1016/j.apenergy.2015.03.054.
- [51] B. B. Dally, E. Riesmeier, N. Peters, Effect of fuel mixture on moderate and intense low oxygen dilution combustion, *Combustion and Flame* 137 (4) (2004) 418–431. doi:10.1016/j.combustflame.2004.02.011.
- [52] R. Weber, J. P. Smart, W. V. Kamp, On the (mild) combustion of gaseous, liquid, and solid fuels in high temperature preheated air, *Proceedings of the Combustion Institute* 30 II. doi:10.1016/j.proci.2004.08.101.
- [53] M. Derudi, A. Villani, R. Rota, Sustainability of mild combustion of hydrogen-containing hybrid fuels, *Proceedings of the Combustion Institute* 31 II. doi:10.1016/j.proci.2006.08.107.
- [54] P. Sabia, M. de Joannon, S. Fierro, A. Tregrossi, A. Cavaliere, Hydrogen-enriched methane mild combustion in a well stirred reactor, *Experimental Thermal and Fluid Science* 31 (5). doi:10.1016/j.expthermflusci.2006.04.016.
- [55] M. Ayoub, C. Rottier, S. Carpentier, C. Villiermaux, A. M. Boukhalfa, D. Honore, An experimental study of mild flameless combustion of methane/hydrogen mixtures, *International Journal of Hydrogen Energy* 37 (8) (2012) 6912–6921. doi:10.1016/j.ijhydene.2012.01.018.
- [56] G. Mosca, Experimental and Numerical Study of MILD Combustion, Ph.D. thesis, University of Mons (2017).
- [57] P. Sabia, G. Sorrentino, P. Bozza, G. Ceriello, R. Ragucci, M. De Joannon, Fuel and thermal load flexibility of a MILD burner, *Proceedings of the Combustion Institute* 37 (4). doi:10.1016/j.proci.2018.09.003.

- [58] A. Chinnici, Z. F. Tian, J. H. Lim, G. J. Nathan, B. B. Dally, Thermal performance analysis of a syngas-fuelled hybrid solar receiver combustor operated in the MILD combustion regime, *Combustion Science and Technology* 191 (1). doi:10.1080/00102202.2018.1452381.
- [59] A. F. Colorado, B. A. Herrera, A. A. Amell, Performance of a Flameless combustion furnace using biogas and natural gas, *Bioresource Technology* 101 (7) (2010) 2443–2449. doi:10.1016/j.biortech.2009.11.003.
- [60] S. E. Hosseini, M. A. Wahid, A. A. Abuelnuor, Biogas flameless combustion: A review, in: *Applied Mechanics and Materials*, Vol. 388, 2013. doi:10.4028/www.scientific.net/AMM.388.273.
- [61] G. Sorrentino, P. Sabia, P. Bozza, R. Ragucci, M. de Joannon, Low-NO<sub>x</sub> conversion of pure ammonia in a cyclonic burner under locally diluted and preheated conditions, *Applied Energy* 254 (x) (2019) 1–7. doi:10.1016/j.apenergy.2019.113676.
- [62] Z. Nikolaou, N. Swaminathan, Heat release rate markers for premixed combustion, *Combustion and Flame* 161 (12) (2014) 3073 – 3084. doi:https://doi.org/10.1016/j.combustflame.2014.05.019.
- [63] H. Najm, P. Paul, C. Mueller, P. Wyckoff, On the adequacy of certain experimental observables as measurements of flame burning rate, *Combustion and Flame* 113 (3) (1998) 312 – 332. doi:https://doi.org/10.1016/S0010-2180(97)00209-5.
- [64] P. Paul, H. Najm, Planar laser-induced fluorescence imaging of flame heat release rate, *Proceedings of the Combustion Institute* 27 (1) (1998) 43 – 50. doi:https://doi.org/10.1016/S0082-0784(98)80388-3.
- [65] J. Sidey, E. Mastorakos, Visualization of mild combustion from jets in cross-flow, *Proceedings of the Combustion Institute* 35 (3) (2015) 3537 – 3545. doi:https://doi.org/10.1016/j.proci.2014.07.028.
- [66] M. Roder, T. Dreier, C. Schulz, Simultaneous measurement of localized heat-release with oh/ch2o-lif imaging and spatially integrated oh\* chemiluminescence in turbulent swirl flames, *Proceedings of the Combustion Institute* 34 (2) (2013) 3549 – 3556. doi:https://doi.org/10.1016/j.proci.2012.06.102.



- [67] C. Vagelopoulos, J. Frank, An experimental and numerical study on the adequacy of  $\text{CH}$  as a flame marker in premixed methane flames, *Proceedings of the Combustion Institute* 30 (1) (2005) 241 – 249. doi:<https://doi.org/10.1016/j.proci.2004.08.243>.
- [68] I. Mulla, A. Dowlut, T. Hussain, Z. Nikolaou, S. Chakravarthy, N. Swaminathan, R. Balachandran, Heat release rate estimation in laminar premixed flames using laser-induced fluorescence of  $\text{CH}_2\text{O}$  and  $\text{H}$ -atom, *Combustion and Flame* 165 (2016) 373 – 383. doi:<https://doi.org/10.1016/j.combustflame.2015.12.023>.
- [69] A. Fayoux, K. Zhringer, O. Gicquel, J. Rolon, Experimental and numerical determination of heat release in counterflow premixed laminar flames, *Proceedings of the Combustion Institute* 30 (1) (2005) 251 – 257. doi:<https://doi.org/10.1016/j.proci.2004.08.210>.
- [70] Y. Minamoto, N. Swaminathan, Scalar gradient behaviour in MILD combustion, *Combustion and Flame* 161 (4) (2014) 1063–1075. doi:[10.1016/j.combustflame.2013.10.005](https://doi.org/10.1016/j.combustflame.2013.10.005).
- [71] F. Christo, B. Dally, Modeling turbulent reacting jets issuing into a hot and diluted coflow, *Combustion and Flame* 142 (1) (2005) 117 – 129. doi:<https://doi.org/10.1016/j.combustflame.2005.03.002>.
- [72] A. Parente, M. R. Malik, F. Contino, A. Cuoci, B. B. Dally, Extension of the Eddy Dissipation Concept for turbulence/chemistry interactions to MILD combustion, *Fuel* 163 (2016) 98–111. doi:[10.1016/j.fuel.2015.09.020](https://doi.org/10.1016/j.fuel.2015.09.020).
- [73] B. F. Magnussen, The eddy dissipation concept, a bridge between science and technology, in: *Eccomas Thematic Conf on Computat Combust*, 2005.
- [74] M. J. Evans, P. R. Medwell, Z. F. Tian, Modeling Lifted Jet Flames in a Heated Coflow using an Optimized Eddy Dissipation Concept Model, *Combustion Science and Technology* 187 (7) (2015) 1093–1109. doi:[10.1080/00102202.2014.1002836](https://doi.org/10.1080/00102202.2014.1002836).
- [75] A. Parente, M. R. Malik, F. Contino, A. Cuoci, D. Dally, Characteristics and mechanistic analysis of CO formation in MILD regime with simultaneously diluted and preheated oxidant and fuel, *Fuel* 163 (2016) 98–111.

- [76] N. Romero-Anton, X. Huang, H. Bao, K. Martin-Eskudero, E. Salazar-Herran, D. Roekaerts, New extended eddy dissipation concept model for flameless combustion in furnaces, *Combustion and Flame* 220 (2020) 49–62. doi:10.1016/j.combustflame.2020.06.025.  
URL <https://doi.org/10.1016/j.combustflame.2020.06.025>
- [77] J. Chomiak, *Combustion: A Study in Theory, Fact and Application*, Abacus Press/Gorden and Breach Science Publishers, United States, 1990.
- [78] Z. Li, A. Cuoci, A. Sadiki, A. Parente, Comprehensive numerical study of the Adelaide Jet in Hot-Coflow burner by means of RANS and detailed chemistry, *Energy* 139 (2017) 555–570. doi:10.1016/j.energy.2017.07.132.
- [79] N. Lallemand, A. Sayre, R. Weber, Evaluation of emissivity correlations for H<sub>2</sub>O-CO<sub>2</sub>-N<sub>2</sub>/AIR mixtures and coupling with solution methods of the radiative transfer equation, *Progress in Energy and Combustion Science* 22 (6) (1996) 543–574. doi:10.1016/S0360-1285(96)00010-X.
- [80] Z. Liu, N. Meyendorf, N. Mrad, The role of data fusion in predictive maintenance using digital twin, *AIP Conference Proceedings* 1949 (April 2018). doi:10.1063/1.5031520.
- [81] T. H. Uhlemann, C. Schock, C. Lehmann, S. Freiburger, R. Steinhilper, The Digital Twin: Demonstrating the Potential of Real Time Data Acquisition in Production Systems, *Procedia Manufacturing* 9 (2017) 113–120. doi:10.1016/j.promfg.2017.04.043.
- [82] M. Ferrarotti, M. Fürst, E. Cresci, W. de Paepe, A. Parente, Key Modeling Aspects in the Simulation of a Quasi-industrial 20 kW Moderate or Intense Low-oxygen Dilution Combustion Chamber, *Energy & Fuels* 32 (10) (2018) 10228–10241. doi:10.1021/acs.energyfuels.8b01064.  
URL <https://doi.org/10.1021/acs.energyfuels.8b01064>
- [83] B. D. Stojkovic, T. D. Fansler, M. C. Drake, V. Sick, High-speed imaging of OH\* and soot temperature and concentration in a stratified-charge direct-injection gasoline engine, *Proceedings of the Combustion Institute* 30 II (2) (2005) 2657–2665. doi:10.1016/j.proci.2004.08.021.

- [84] V. Nori, J. Seitzman, Evaluation of chemiluminescence as a combustion diagnostic under varying operating conditions, 46th AIAA Aerospace Sciences Meeting and Exhibit (January) (2008) 1–14. doi:10.2514/6.2008-953.
- [85] X. Song, Q. Guo, C. Hu, Y. Gong, G. Yu, OH Chemiluminescence Characteristics and Structures of the Impinging Reaction Region in Opposed Impinging Diffusion Flames, *Energy and Fuels* 30 (2) (2016) 1428–1436. doi:10.1021/acs.energyfuels.5b02721.
- [86] Y. Ikeda, J. Kojima, T. Nakajima, Local chemiluminescence measurements of OH\*, CH\* and C2\* at turbulent premixed flame-fronts, in: *Smart control of turbulent combustion*, Springer Japan, Tokyo, 2001.
- [87] Y. Hardalupas, C. S. Panoutsos, A. M. Taylor, Spatial resolution of a chemiluminescence sensor for local heat-release rate and equivalence ratio measurements in a model gas turbine combustor, *Experiments in Fluids* 49 (4) (2010) 883–909. doi:10.1007/s00348-010-0915-z.
- [88] A. S. Veríssimo, A. M. Rocha, M. Costa, Operational, combustion, and emission characteristics of a small-scale combustor, *Energy and Fuels* 25 (6) (2011) 2469–2480. doi:10.1021/ef200258t.
- [89] X. Huang, Measurements and model development for flameless combustion in a Lab-scale furnace, Ph.D. thesis, TUDelft (2018).
- [90] M. Weidmann, D. Honoré, V. Verbaere, G. Boutin, S. Grathwohl, G. Godard, C. Gobin, R. Kneer, G. Scheffknecht, Experimental characterization of pulverized coal MILD flameless combustion from detailed measurements in a pilot-scale facility, *Combustion and Flame* 168 (2016) 365–377. doi:10.1016/j.combustflame.2016.01.029.
- [91] F. Xing, A. Kumar, Y. Huang, S. Chan, C. Ruan, S. Gu, X. Fan, Flameless combustion with liquid fuel: A review focusing on fundamentals and gas turbine application, *Applied Energy* 193 (2017) 28–51. doi:10.1016/j.apenergy.2017.02.010.  
URL <http://dx.doi.org/10.1016/j.apenergy.2017.02.010>
- [92] P. R. Medwell, B. B. Dally, Experimental observation of lifted flames in a heated and diluted coflow, *Energy and Fuels* 26 (9) (2012) 5519–5527. doi:10.1021/ef301029u.

- [93] B. Zhou, M. Costa, Z. Li, M. Aldén, X. S. Bai, Characterization of the reaction zone structures in a laboratory combustor using optical diagnostics: From flame to flameless combustion, *Proceedings of the Combustion Institute* 36 (3) (2017) 4305–4312. doi:10.1016/j.proci.2016.06.182. URL <http://dx.doi.org/10.1016/j.proci.2016.06.182>
- [94] T. S. Cheng, C. Y. Wu, Y. H. Li, Y. C. Chao, Chemiluminescence measurements of local equivalence ratio in a partially premixed flame, *Combustion Science and Technology* 178 (10-11) (2006) 1821–1841. doi:10.1080/00102200600790755.
- [95] M. M. Tripathi, S. R. Krishnan, K. K. Srinivasan, F. Y. Yueh, J. P. Singh, Chemiluminescence-based multivariate sensing of local equivalence ratios in premixed atmospheric methane-air flames, *Fuel* 93 (2012) 684–691. doi:10.1016/j.fuel.2011.08.038. URL <http://dx.doi.org/10.1016/j.fuel.2011.08.038>
- [96] IEA, *World Energy Outlook 2019*, Tech. rep., Paris, France (2019).
- [97] Hydrogen Europe, *Hydrogen Europe Vision on the Role of Hydrogen and Gas Infrastructure on the Road Toward a Climate Neutral Economy*, Tech. rep. (2019). URL <https://hydrogeneurope.eu/>
- [98] A. Hayakawa, Y. Arakawa, R. Mimoto, K. D. A. Somarathne, T. Kudo, H. Kobayashi, Experimental investigation of stabilization and emission characteristics of ammonia/air premixed flames in a swirl combustor, *International Journal of Hydrogen Energy* 42 (19) (2017) 14010–14018. doi:10.1016/j.ijhydene.2017.01.046.
- [99] A. Valera-Medina, D. G. Pugh, P. Marsh, G. Bulat, P. Bowen, Preliminary study on lean premixed combustion of ammonia-hydrogen for swirling gas turbine combustors, *International Journal of Hydrogen Energy* 42 (38) (2017) 24495–24503. doi:10.1016/j.ijhydene.2017.08.028.
- [100] A. Valera-Medina, R. Marsh, J. Runyon, D. Pugh, P. Beasley, T. Hughes, P. Bowen, Ammonia-methane combustion in tangential swirl burners for gas turbine power generation, *Applied Energy* 185 (2017) 1362–1371. doi:10.1016/j.apenergy.2016.02.073.

- [101] D. Pugh, P. Bowen, A. Valera-Medina, A. Giles, J. Runyon, R. Marsh, Influence of steam addition and elevated ambient conditions on NO<sub>x</sub> reduction in a staged premixed swirling NH<sub>3</sub>/H<sub>2</sub> flame, *Proceedings of the Combustion Institute* 000 (2018) 1–9. doi:10.1016/j.proci.2018.07.091.
- [102] H. J. Burbano, J. Pareja, A. A. Amell, Laminar burning velocities and flame stability analysis of H<sub>2</sub>/CO/air mixtures with dilution of N<sub>2</sub> and CO<sub>2</sub>, *International Journal of Hydrogen Energy* 36 (4) (2011) 3232–3242. doi:10.1016/j.ijhydene.2010.11.089.
- [103] R. Sankaran, H. G. Im, Effects of hydrogen addition on the Markstein length and flammability limit of stretched methane/air premixed flames, *Combustion Science and Technology* 178 (9) (2006) 1585–1611. doi:0.1080/00102200500536217.
- [104] A. N. Lipatnikov, J. Chomiak, Turbulent flame speed and thickness: Phenomenology, evaluation, and application in multi-dimensional simulations, *Progress in Energy and Combustion Science* 28 (1) (2002) 1–74. doi:10.1016/S0360-1285(01)00007-7.
- [105] Y. Zhang, Z. Huang, L. Wei, J. Zhang, C. K. Law, Experimental and modeling study on ignition delays of lean mixtures of methane, hydrogen, oxygen, and argon at elevated pressures, *Combustion and Flame* 159 (3) (2012) 918–931. doi:10.1016/j.combustflame.2011.09.010.
- [106] T. Lieuwen, V. McDonell, D. Santavicca, T. Sattelmayer, Burner development and operability issues associated with steady flowing syngas fired combustors, *Combustion Science and Technology* 180 (6) (2008) 1169–1192. doi:10.1080/00102200801963375.
- [107] B. J. McBride, S. Gordon, M. Reno, Coefficients for calculating thermodynamic and transport properties of individual species, Tech. rep., NASA Lewis Research Center, Cleveland, United States (1993).
- [108] Joint Committee For Guides In Metrology, Evaluation of measurement data Guide to the expression of uncertainty in measurement, International Organization for Standardization Geneva ISBN 50 (September) (2008) 134. doi:10.1373/clinchem.2003.030528.

## BIBLIOGRAPHY

- [109] M. Pochet, H. Jeanmart, F. Contino, Uncertainty quantification from raw measurements to post-processed data: A general methodology and its application to a homogeneous-charge compressionignition engine, *International Journal of Engine Research* doi:10.1177/1468087419892697.
- [110] E. Oldenhof, M. Tummers, E. V. Veen, D. Roekaerts, Role of entrainment in the stabilisation of jet-in-hot-coflow flames, *Combust. Flame* 158 (2011) 1553–1563.
- [111] G. G. Szegő, Experimental and Numerical Investigation of a Parallel Jet MILD Combustion Burner System in a Laboratory-scale Furnace, PhD Thesis 2010 (July) (2010) 168.
- [112] J. Mi, P. Li, B. B. Dally, Importance of initial momentum rate and air-fuel premixing on moderate or intense low oxygen dilution (MILD) combustion in a recuperative furnace, *Energy Fuels* 23 (2009) 5349–5356.
- [113] I. B. Özdemir, N. Peters, Characteristics of the reaction zone in a combustor operating at mild combustion, *Experiments in Fluids* 30 (6) (2001) 683–695. doi:10.1007/s003480000248.
- [114] A. S. Veríssimo, A. M. Rocha, M. Costa, Experimental study on the influence of the thermal input on the reaction zone under flameless oxidation conditions, *Fuel Processing Technology* 106 (2013) 423–428. doi:10.1016/j.fuproc.2012.09.008.
- [115] G. Mosca, D. Lupant, MILD Combustion of Biogas on a 30 kW and 200 kW Lab Furnaces: scale effects and influence of the geometrical configuration, in: 37th IEA Combustion Task Leaders Meeting, At St. Andrews, 2015.
- [116] G. Sorrentino, U. Göktolga, M. De Joannon, J. Van Oijen, A. Cavaliere, P. De Goey, An experimental and numerical study of MILD combustion in a Cyclonic burner, *Energy Procedia* 120 (2017) 649–656. doi:10.1016/j.egypro.2017.07.173.
- [117] C. J. Dasch, One-dimensional tomography: a comparison of Abel, onion-peeling, and filtered backprojection methods, *Applied Optics* 31 (8) (1992) 1164–1152.

- [118] K. Olchewsky, C. Fuller, M. Holton, P. Gokulakrishnan, Autoignition temperature measurements of hydrogen mixtures, 10th U.S. National Combustion Meeting 2017-April (May).
- [119] M. Ilbas, A. P. Crayford, I. Yilmaz, P. J. Bowen, N. Syred, Laminar-burning velocities of hydrogen-air and hydrogen-methane-air mixtures: An experimental study, *International Journal of Hydrogen Energy* 31 (12) (2006) 1768–1779. doi:10.1016/j.ijhydene.2005.12.007.
- [120] M. Fairweather, M. P. Ormsby, C. G. Sheppard, R. Woolley, Turbulent burning rates of methane and methane-hydrogen mixtures, *Combustion and Flame* 156 (4) (2009) 780–790. doi:10.1016/j.combustflame.2009.02.001.
- [121] R. W. Schefer, Hydrogen enrichment for improved lean flame stability, *International Journal of Hydrogen Energy* 28 (10) (2003) 1131–1141. doi:10.1016/S0360-3199(02)00199-4.
- [122] K. D. K. A. Somarathne, S. Hatakeyama, A. Hayakawa, H. Kobayashi, Numerical study of a low emission gas turbine like combustor for turbulent ammonia/air premixed swirl flames with a secondary air injection at high pressure, *International Journal of Hydrogen Energy* 42 (44) (2017) 27388–27399. doi:10.1016/j.ijhydene.2017.09.089.
- [123] P. R. Medwell, M. J. Evans, Q. N. Chan, V. R. Katta, Laminar Flame Calculations for Analyzing Trends in Autoignitive Jet Flames in a Hot and Vitiated Coflow, *Energy and Fuels* 30 (10) (2016) 8680–8690. doi:10.1021/acs.energyfuels.6b01264.
- [124] M. Zieba, A. Brink, A. Schuster, M. Hupa, G. Scheffknecht, Ammonia chemistry in a flameless jet, *Combustion and Flame* 156 (10) (2019) 1950–1956. doi:10.1016/j.combustflame.2009.07.002.  
URL <http://dx.doi.org/10.1016/j.combustflame.2009.07.002>
- [125] J. Sidey, E. Mastorakos, R. L. Gordon, Simulations of autoignition and laminar premixed flames in methane/air mixtures diluted with hot products, *Combustion Science and Technology* 186 (4-5) (2014) 453–465. doi:10.1080/00102202.2014.883217.  
URL <http://dx.doi.org/10.1080/00102202.2014.883217><https://doi.org/10.1080/00102202.2014.883217>

# BIBLIOGRAPHY

- [126] D. L. Baulch, C. J. Cobos, R. A. Cox, P. Frank, G. Hayman, T. Just, J. A. Kerr, T. Murrells, M. J. Pilling, J. Troe, R. W. Walker, J. Warnatz, Evaluated kinetic data for combustion modeling. supplement i, *Journal of Physical and Chemical Reference Data* 23 (6) (1994) 847–848. [arXiv:https://doi.org/10.1063/1.555953](https://doi.org/10.1063/1.555953), doi: 10.1063/1.555953.  
URL <https://doi.org/10.1063/1.555953>
- [127] A. Favre, Statistical equations of turbulent gases, *Problems of hydrodynamics and continuummechanics* (1969) 231–266.
- [128] S. B. Pope, *Turbulent flows*, Cambridge University Press, 2000.
- [129] W. P. Jones, B. E. Launder, The prediction of laminarization with a two-equation model of turbulence, *International Journal of Heat and Mass Transfer* 15 (2) (1972) 301–314. doi:10.1016/0017-9310(72)90076-2.
- [130] B. B. Dally, D. F. Fletcher, A. R. Masri, Flow and mixing fields of turbulent bluff-body jets and flames, *Combustion Theory and Modelling* 2 (2) (1998) 193–219. doi:10.1088/1364-7830/2/2/006.
- [131] T. Shih, W. Liou, A. Shabbir, Z. Yang, J. Zhu, A new k-epsilon eddy viscosity model for high reynolds number turbulent flows, *Computers & Fluids*, 24 (3) (1995) 227–238. doi:10.1016/0045-7930(94)00032-T.
- [132] V. Yakhot, S. Orszag, S. Thangam, T. Gatski, C. Speziale, Development of turbulence models for shear flows by a double expansion technique, *Physics of Fluids* 4 (7) (1992) 1510–1520.
- [133] D. Wilcox, Re-assessment of the scale-determining equation for advanced turbulence models, *AIAA Journal* 26 (11) (1988) 1299–1310.
- [134] N. Peters, *Turbulent Combustion*, Cambridge University Press, 2001.
- [135] S. B. Pope, Lagrangian pdf methods for turbulent flows, *Annual review of fluid mechanics* 26 (1) (1994) 23–63.
- [136] J. Lamouroux, M. Ihme, B. Fiorina, O. Gicquel, Tabulated chemistry approach for diluted combustion regimes with internal recirculation and heat losses, *Combustion and Flame* 161 (8) (2014) 2120–2136. doi:10.1016/j.combustflame.2014.01.015.  
URL <http://dx.doi.org/10.1016/j.combustflame.2014.01.015>



- [137] J. A. Van Oijen, L. P. H. De Goey, Modelling of Premixed Laminar Flames using Flamelet- Generated Manifolds, *Combustion Science and Technology* 161 (1) (2000) 113–137. doi:10.1080/00102200008935814.  
URL <http://www.tandfonline.com/loi/gcst20{%}5Cnhttp://dx.doi.org/10.1080/00102200008935814{%}5Cnhttp://{%}5Cnwww.tandfonline.com/>
- [138] J. A. van Oijen, A. Donini, R. J. Bastiaans, J. H. ten Thije Boonkkamp, L. P. de Goey, State-of-the-art in premixed combustion modeling using flamelet generated manifolds, *Progress in Energy and Combustion Science* 57 (2016) 30–74. doi:10.1016/j.pecs.2016.07.001.  
URL <http://dx.doi.org/10.1016/j.pecs.2016.07.001>
- [139] N. Peters, Laminar diffusion flamelet models in non-premixed turbulent combustion, *Progress in Energy and Combustion Science* 10 (3) (1984) 319–339. doi:10.1016/0360-1285(84)90114-X.
- [140] E. Abtahizadeh, P. De Goey, J. Van Oijen, Development of a novel flamelet-based model to include preferential diffusion effects in autoignition of CH<sub>4</sub>/H<sub>2</sub> flames, *Combustion and Flame* 162 (11) (2015) 4358–4369. doi:10.1016/j.combustflame.2015.06.015.  
URL <http://dx.doi.org/10.1016/j.combustflame.2015.06.015>
- [141] G. Ceriello, G. Sorrentino, A. Cavaliere, P. Sabia, M. de Joannon, R. Ragucci, The role of dilution level and canonical configuration in the modeling of MILD combustion systems with internal recirculation, *Fuel* 264 (June 2019). doi:10.1016/j.fuel.2019.116840.
- [142] B. Magnussen, On the structure of turbulence and a generalized eddy dissipation concept for chemical reaction in turbulent flows, in: *AIAA Aerospace Science Meeting*, St. Louis, Missouri, USA, 1981.
- [143] A. Parente, C. Galletti, L. Tognotti, Effect of the combustion model and kinetic mechanism on the MILD combustion in an industrial burner fed with hydrogen enriched fuels, *International Journal of Hydrogen Energy* 33 (24) (2008) 7553–7564. doi:10.1016/j.ijhydene.2008.09.058.
- [144] I. Granm, B. Magnussen, A numerical study of a bluff-body stabilized diffusion flame. part 2. influence of combustion modeling and

## BIBLIOGRAPHY

- finite-rate chemistry, *Combustion Science and Technology* 110 (16) (1996) 191–217.
- [145] B. Magnussen, The eddy dissipation concept a bridge between science and technology, in: *Eccomas Thematic Conference on Computational Combustion*, Lisbon, Portugal, 2005.
- [146] O. R. Fox, *Computational Models for Turbulent Reacting Flows*, Cambridge University Press, Cambridge, U.K., 2003.
- [147] J. Chomiak, A. Karlsson, Flame liftoff in diesel sprays, *Symposium (International) on Combustion* 26 (2) (1996) 2557–2564. doi:10.1016/S0082-0784(96)80088-9.
- [148] F. Karrholm, Numerical modelling of diesel spray injection, turbulence interaction and combustion, Ph.D. thesis, Chalmers University of Technology (2008).
- [149] P. A. N. Nordin, Complete chemistry modeling of diesel spray combustion, Ph.D. thesis, Chalmers University of Technology, Sweden (2001).
- [150] M. Kuron, E. R. Hawkes, Z. Ren, J. C. Tang, H. Zhou, J. H. Chen, T. Lu, Performance of transported pdf mixing models in a turbulent premixed flame, *Proceedings of the Combustion Institute*, 36 (2) (2017) 1987–1995.
- [151] K. R. Sreenivasan, C. Meneveau, The fractal facets of turbulence, *Journal of Fluid Mechanics* 173 (1) (1986) 357. doi:10.1017/S0022112086001209.
- [152] V. I. Golovitchev, P. K. Tretjakov, C. N. Raffoul, Evaluation of drag reduction of blunt bodies at supersonic speeds by counter-flow combustion, *32nd AIAA Fluid Dynamics Conference and Exhibit* doi:10.2514/6.2002-3296.
- [153] V. Raman, H. Pitsch, A consistent LES/filtered-density function formulation for the simulation of turbulent flames with detailed chemistry, *Proceedings of the Combustion Institute* 31 II (2007) 1711–1719. doi:10.1016/j.proci.2006.07.152.

- [154] M. Stöllinger, S. Heinz, Evaluation of scalar mixing and time scale models in PDF simulations of a turbulent premixed flame, *Combustion and Flame* 157 (9) (2010) 1671–1685. doi:10.1016/j.combustflame.2010.01.015.
- [155] M. Senouci, A. Bounif, M. Abidat, N. M. Belkaid, C. Mansour, I. Gokalp, Transported-PDF (IEM, EMST) micromixing models in a hydrogen-air nonpremixed turbulent flame, *Acta Mechanica* 224 (12) (2013) 3111–3124. doi:10.1007/s00707-013-0911-5.
- [156] J. Y. Chen, Second-order conditional modeling of turbulent non-premixed flames with a composite PDF, *Combustion and Flame* 69 (1) (1987) 1–36. doi:10.1016/0010-2180(87)90018-6.
- [157] W. P. Jones, P. Musonge, Closure of the Reynolds stress and scalar flux equations, *Physics of Fluids* 31 (12) (1988) 3589–3604. doi:10.1063/1.866876.
- [158] T. P. Sommer, R. M. C. So, Y. G. La, A near-wall two-equation model for turbulent heat fluxes, *International Journal of Heat and Mass Transfer* 35.
- [159] M. Modest, *Radiative heat transfer*, McGraw-Hill, New York, USA, 2003.
- [160] ANSYS-FLUENT, *Theory Guide v.19.0*, Tech. rep. (2019).
- [161] W. Fiveland, Discrete-ordinates solutions of the radiative transport equation for rectangular enclosures, *ASME Transactions Journal of Heat Transfer* 106 (1984) 699–706.
- [162] H. Hottel, A. Sarofim, *Radiative Transfer*, New York, USA, 1967.
- [163] T. F. Smith, Z. F. Shen, J. N. Friedman, Evaluation of Coefficients for the Weighted Sum of Gray Gases Model, *Journal of Heat Transfer* 104 (4) (1982) 602. doi:10.1115/1.3245174.
- [164] H. Bordbar, G. C. Fraga, S. Hostikka, An extended weighted-sum-of-gray-gases model to account for all CO<sub>2</sub> H<sub>2</sub>O molar fraction ratios in thermal radiation, *International Communications in Heat and Mass Transfer* 110 (December 2019) (2020) 104400. doi:10.1016/j.icheatmasstransfer.2019.104400.

## BIBLIOGRAPHY

- [165] S. H. Kim, K. Huh, B. B. Dally, Conditional moment closure modeling of turbulent nonpremixed combustion in diluted hot coflow, *Proceedings of the Combustion Institute* 30 (1) (2005) 751–757.
- [166] M. Ihme, Y. C. See, LES flamelet modeling of a three-stream MILD combustor: Analysis of flame sensitivity to scalar inflow conditions., *Proceedings of the Combustion Institute* 33 (1) (2011) 1309–1317.
- [167] M. T. Lewandowski, A. Parente, J. Pozorski, Generalised Eddy Dissipation Concept for MILD combustion regime at low local Reynolds and Damköhler numbers . Part 1 : Model framework development, *Fuel* (February) (2020) 117743. doi:10.1016/j.fuel.2020.117743.
- [168] A. De, E. Oldenhof, P. Sathiah, D. Roekaerts, Numerical simulation of Delft-Jet-in-Hot-Coflow (DJHC) flames using the eddy dissipation concept model for turbulence-chemistry interaction, *Flow, Turbulence and Combustion* 87 (4) (2011) 537–567. doi:10.1007/s10494-011-9337-0.
- [169] J. Aminian, C. Galletti, S. Shahhosseini, L. Tognotti, Numerical investigation of a MILD combustion burner: Analysis of mixing field, chemical kinetics and turbulence-chemistry interaction, *Flow, Turbulence and Combustion* 88 (4) (2012) 597–623. doi:10.1007/s10494-012-9386-z.
- [170] I. S. Ertesvag, Analysis of some recently proposed modifications to the eddy dissipation concept (edc), *Combustion Science and Technology* 192 (6) (2020) 1108–1136. doi:10.1080/00102202.2019.1611565.
- [171] M. J. Evans, C. Petre, P. R. Medwell, A. Parente, Generalisation of the eddy-dissipation concept for jet flames with low turbulence and low Damköhler number, *Proceedings of the Combustion Institute* 37 (4) (2019) 4497–4505. doi:10.1016/j.proci.2018.06.017.
- [172] W. L. Oberkampf, M. F. Barone, Measures of agreement between computation and experiment: Validation metrics, *Journal of Computational Physics* 217 (1) (2006) 5–36. doi:10.1016/j.jcp.2006.03.037.
- [173] R. Bilger, S. Starner, R. Kee, On reduced mechanisms for methane-air combustion in non-premixed flames, *Combust Flame* 80 (1990) 135–149.

- [174] C. T. Bowman, R. K. Hanson, D. F. Davidson, W. C. Gardiner, V. Lissianski, G. P. Smith, D. M. Golden, M. Frenklach, M. Goldenberg, GRI-2.11, [http://www.me.berkeley.edu/gri\\_mech/](http://www.me.berkeley.edu/gri_mech/).
- [175] A. Ghasemi, V. Roussinova, R. Balachandar, R. Barron, Reynolds number effects in the near-field of a turbulent square jet, *Experimental Thermal and Fluid Science* 61 (2015) 249–258.
- [176] F. Russo, N. Basse, Scaling of turbulence intensity for low-speed flow in smooth pipes., *Flow Measurement and Instrumentation* 52 (2016) 101–114.
- [177] G. G. De Soete, Overall reaction rates of NO and N<sub>2</sub> formation from fuel nitrogen, *Symposium (International) on Combustion* 15 (1) (1975) 1093–1102. doi:10.1016/S0082-0784(75)80374-2.
- [178] J. E. Harrington, G. P. Smith, P. A. Berg, A. R. Noble, J. B. Jeffries, D. R. Crosley, Evidence for a new no production mechanism in flames, *Symposium (International) on Combustion* 26 (2) (1996) 2133–2138. doi:10.1016/S0082-0784(96)80038-5.
- [179] T. Kathrotia, U. Riedel, A. Seipel, K. Moshhammer, A. Brockhinke, Experimental and numerical study of chemiluminescent species in low-pressure flames, *Applied Physics B* 107 (3) (2012) 571–584. doi:10.1007/s00340-012-5002-0.
- [180] N. Doan, N. Swaminathan, Y. Minamoto, Dns of mild combustion with mixture fraction variations, *Combustion and Flame* 189 (2018) 173 – 189. doi:<https://doi.org/10.1016/j.combustflame.2017.10.030>.
- [181] M. Tamura, P. Berg, J. Harrington, J. Luque, J. Jeffries, G. Smith, D. Crosley, Collisional quenching of ch(a), oh(a), and no(a) in low pressure hydrocarbon flames, *Combustion and Flame* 114 (3) (1998) 502 – 514. doi:[https://doi.org/10.1016/S0010-2180\(97\)00324-6](https://doi.org/10.1016/S0010-2180(97)00324-6).
- [182] H. Yamashita, M. Shimada, T. Takeno, A numerical study on flame stability at the transition point of jet diffusion flames, *Symposium (International) on Combustion* 26 (1) (1996) 27–34. doi:10.1016/S0082-0784(96)80196-2.

## BIBLIOGRAPHY

- [183] E. Knudsen, H. Pitsch, A general flamelet transformation useful for distinguishing between premixed and non-premixed modes of combustion, *Combustion and Flame* 156 (3) (2009) 678–696. doi:10.1016/j.combustflame.2008.10.021.
- [184] D. F. Davidson, K. Kohse-Höinghaus, A. Y. Chang, R. K. Hanson, A Pyrolysis Mechanism for Ammonia, *Int. J. Chem. Kinet* 22 (1990) 513–535.
- [185] N. Cohen, K. R. Westberg, Chemical Kinetic Data Sheets for High-Temperature Reactions. Part II, *J. Phys. Chem. Ref. Data* 20 (6).
- [186] J. D. Mertens, A. Y. Chang, R. K. Hanson, C. T. Bowman, A shock tube study of the reactions of NH with NO, O<sub>2</sub>, and O, *International Journal of Chemical Kinetics* 23 (2) (1991) 173–196. doi:10.1002/kin.550230208.
- [187] R. L. Iman, W. J. Conover, Small sample sensitivity analysis techniques for computer models, with an application to risk assessment, *Communications in Statistics - Theory and Methods* 9 (17) (1980) 1749–1842. doi:10.1080/03610928008827996.
- [188] A. Florian, An efficient sampling scheme: Updated Latin Hypercube Sampling, *Probabilistic Engineering Mechanics* 7 (2) (1992) 123–130. doi:10.1016/0266-8920(92)90015-A.
- [189] D. L. Baulch, C. T. Bowman, C. J. Cobos, R. A. Cox, T. Just, J. A. Kerr, M. J. Pilling, D. Stocker, J. Troe, W. Tsang, R. W. Walker, J. Warnatz, Evaluated Kinetic Data for Combustion Modeling: Supplement II, *Journal of Physical and Chemical Reference Data* 34 (3). doi:10.1063/1.1748524.
- [190] E. H. Glaessgen, D. T. Branch, D. S. Stargel, The Digital Twin Paradigm for Future NASA and U . S . Air Force Vehicles (2019) 1–14.
- [191] G. Aversano, A. Bellemans, Z. Li, A. Coussement, O. Gicquel, A. Parente, Application of reduced-order models based on PCA & Kriging for the development of digital twins of reacting flow applications, *Computers and Chemical Engineering* 121 (2019) 422–441. doi:10.1016/j.compchemeng.2018.09.022.

- [192] P. G. Constantine, E. Dow, Q. Wang, Active Subspace Methods in Theory and Practice, *SIAM Journal of Scientific Computation* 36 (4) (2014) 1500–1524.
- [193] S. N. Lophaven, J. Søndergaard, H. B. Nielsen, *Kriging Toolbox* (2002) 1–28.
- [194] M. Seeger, Gaussian processes for machine learning., *International journal of neural systems* 14 (2) (2004) 69–106. doi:10.1142/S0129065704001899.
- [195] G. C. Cawley, N. L. C. Talbot, On Over-fitting in Model Selection and Subsequent Selection Bias in Performance Evaluation, *Journal of Machine Learning Research* 11 (2010) 2079–2107.
- [196] B. Gabrys, S. Strandt, Data-driven Soft Sensors in the Process Industry, *Computers & Chemical Engineering*.